Title

Forming Infrastructural Materials by Mechanical Compaction of Lunar and Martian Regolith Simulants

Author

Chow, Brian Justin

Publication Date

2016

UNIVERSITY OF CALIFORNIA, SAN DIEGO

Forming Infrastructural Materials by Mechanical Compaction of Lunar and Martian Regolith Simulants

A dissertation submitted in partial satisfaction of the
requirement for the degree Doctor of Philosophy

in

Structural Engineering

by

Brian Justin Chow

Committee in charge:

Professor Yu Qiao, Chair
Professor Francesco Lanza di Scalea
Professor John S. McCartney
Professor Joanna McKittrick
Professor P. Benson Shing

The Dissertation of Brian Justin Chow is approved and it is acceptable in quality and form for publication on microfilm and electronically:

Chair

University of California, San Diego

2016

DEDICATION

In recognition of the responsibilities she shouldered, pervading all aspects of life; for whose life-long dedication and service to society I constantly strive to emulate; and in the face of which I shall always feel as though I am all but a mere novice; this thesis is dedicated to my mother, Grace Y. Lin.

EPIGRAPH

You can forget what I told you.
It all comes down to just using it.

Jiddu Bezares-Chávez

TABLE OF CONTENTS

LIST OF ABBREVIATIONS

°C	degrees Celsius
at%	atomic percent
BPO	benzoyl peroxide
cal	calorie
CHNS/O	carbon hydrogen nitrogen sulfur / oxygen
cm	centimeter
EDX	energy dispersive X-ray
EGA	evolved gas analysis
EVA	ethylene vinyl acetate
g	gram
GPa	gigapascal
h	hour
HCl	hydrochloric acid
IOH	inorganic-organic hybrid
J	joule
JSC	Johnson Space Center

K	Kelvin
kcal	kilocalorie
kg	kilogram
m	meter
mA	milliampere
mC	millicoulomb
ml	milliliter
MMA	methyl methacrylate
mm	millimeter
mo	month
mol	mole
MPa	megapascal
MS	mass spectrometer
NaOH	sodium hydroxide
NaPC	sodium perchlorate
npOx	nanoparticulate iron oxide
Pa	pascal
PEKK	polyetherketoneketone

PES	polyethersulfone
PMMA	polymethylmethacrylate
PS	polystyrene
PSU	polysulfone
PVC	polyvinylchloride
R_C	Rockwell C hardness
s	second
SEM	scanning electron microscope
TEM	transmission electron microscope
TGA	thermogravimetric analysis
TS-PMMA	thermosetting polymethylmethacrylate
wt%	weight percent
XRD	X-ray diffraction

Note: Common Latin phrases or abbreviations appear in *italics* and are not listed here.

LIST OF FIGURES

LIST OF TABLES

ACKNOWLEDGEMENTS

First and foremost, I would like to thank Professor Yu Qiao for his mentorship. Without his combination of guidance and flexibility, the course of this research would have never taken its current form. Special thanks to his patience for allowing me the time to finish this thesis. I would like to thank my father, Dr. Donald D.-N. Chow for suggesting the pharmaceutical literature, which gave much background on compaction strengthening. I am also grateful to Professor Patrick J. Fox and Professor John S. McCartney, whose helpful discussions shed much light on the nature of clays and soils.

I would also like to thank my lab mates, assistants, and friends. Dr. Tzehan Chen, it was a pleasure being your colleague as part of this project. Prof. Weiyi Lu, Dr. Gang Wang, Dr. Cang Zhao, Yang Shi, Anh Le, Meng Wang, Daniel Noelle, and Ying Zhong, you were all enormously helpful. I hope I did not gossip too much. Lewis Fowler-Gerace and Rui Kou, I wish you both well on your future endeavors! Alex Finch, Ting-Hsiang Tseng, Juan Antonio Ramirez, and Cruz Galarza, thanks for all of your hard work. Handoko Hadisurya, you are a good friend.

Dr. Mojtaba Samiee, I owe you a lot for your generous help with lab equipment. Dr. Su-Wen Hsu, thank you for your help with the TEM characterization. Prof. Kenneth Vecchio and Cheng Zhang, I am grateful for your assistance with the X-ray diffraction. I also acknowledge Dr. Amanda Strom and Paige Roberts of the UC Santa Barbara TEMPO facility, who conducted the evolved gas analysis.

Chapter 4, in part, contains material that has been submitted for publication in 2016 with authors Brian J. Chow, Tzehan Chen, and Yu Qiao. The dissertation author was the experimental investigator and first author of this paper.

Chapter 5, in part, contains material that has been submitted for publication in 2016 with authors Brian J. Chow, Tzehan Chen, Ying Zhong, Cheng Zhang, Juan A. Ramirez, Cruz M. Galarza, and Yu Qiao. The dissertation author was the experimental investigator and first author of this paper.

Chapter 6, in part, contains material that has been submitted for publication in 2016 with authors Brian J. Chow, Tzehan Chen, Ying Zhong, Cheng Zhang, Juan A. Ramirez, Cruz M. Galarza, and Yu Qiao. The dissertation author was the experimental investigator and first author of this paper.

This research was supported by NASA under Grant. No. NNX12AI73G. The UC Santa Barbara TEMPO facility is supported by NSF-DMR#1121053.

VITA

2008	Bachelor of Science, University of California, San Diego
2010	Master of Science, University of California, San Diego
2011-2012	General Engineer, Stanford Mu Corporation
2013-*present*	Engineering Analysis Consultant, Stanford Mu Corporation
2016	Doctor of Philosophy, University of California, San Diego

PUBLICATIONS

Chen, T., Chow, B.J., Qiao, Y. Two-step gradation of particle size in an inorganic-organic hybrid. *Sci. Eng. Compos. Mater.* **22**, 643-647 (2015).

Chen, T., Chow, B.J., Wang, M., Shi, Y., Zhao, C., Qiao, Y. Inorganic-organic hybrid of lunar soil simulant and polyethylene. *ASCE J. Mater. Civil Eng*. **27**, 06015013.1-4 (2015).

Lu, W., Han, A., Kim, T., Chow, B.J., Qiao, Y. Endcapping treatment of inner surfaces of a hexagonal mesoporous silica. *J. Adhesion Sci. Tech*. DOI: 10.1163/ 156856111X599599 (2012).

Chow, B.J., Lu, W., Han, A., Lim, H., Qiao, Y. Ion repelling effect of nanopores in a hydrophobic zeolite. *J. Mater. Res*. **26**, 1164-1167 (2011).

FIELDS OF STUDY

Major Field: Structural Engineering (Focus in Aerospace Structures)

ABSTRACT OF THE DISSERTATION

Forming Infrastructural Materials by Mechanical Compaction of Lunar and Martian Regolith Simulants

by

Brian Justin Chow

Doctor of Philosophy in Structural Engineering

University of California, San Diego, 2016

Professor Yu Qiao, Chair

Sustainable habitat construction on the Moon and Mars focuses on *in situ* resource utilization (ISRU) to produce infrastructural materials while minimizing recurring supplies from Earth. The current study first explores uniaxial compaction of the soil simulants JSC-1A and JSC Mars-1a with binders. Solvents, monomer polymerization, and melt-compression are investigated for mixing binders with simulants. Results and challenges pertaining to each method are discussed. The second and main part of the current study investigates uniaxial compaction of Mars-1a and montmorillonite without binders. Experimental parameters include initial particle size, compression pressure, lateral boundary condition, and rate of loading. Mechanical strength of compacts is determined *via* three-point bending flexural strength. The applied compression pressure and lateral boundary condition strongly influence resultant strengths, while initial particle size and rate of loading exhibit more subtle effects. High compression pressures with reduced lateral boundaries generate ~30MPa flexural strength, stronger than a typical steel-reinforced concrete. A smaller initial particle size achieves higher strength. Impact loading of Mars-1a samples achieves marginally higher flexural strength compared to a given peak pressure in the quasi-static case, while montmorillonite shows no such difference. For the former, enhanced particle motion and phase transformation during impact may account for the higher strength. A given impact energy leads to similar flexural strengths regardless of variations in hammer mass or velocity. Characterization using thermogravimetric analysis, scanning electron microscopy, transmission electron microscopy, X-ray diffraction, CHNS/O elemental analysis, and evolved gas analysis corroborates the notion that a high specific surface develops secondary bonding responsible for strength. Characterization also rules out possible roles for trace water or organic matter on compaction strengthening. Compaction of analogue materials points toward nanoparticulate iron oxides as the agent of strengthening in Mars-1a. Measured nitrogen permeability suggests the solids are akin to dense rocks. Volumetric energy efficiency is estimated at 0.3-0.4GJ/m^3, or about one order of magnitude lower than thermal processes. The compaction process is expected to be scalable and portable to extant or emergent prototyping technologies.

1 Introduction

1.1 Space Habitats and Materials

The exploration and the eventual colonization of outer space remains persistent goal of humanity's efforts. The reasons are associated closely with the intrinsic needs and simple curiosity of humans, which have been repeatedly proven critical for the success of civilizations since ancient times. The survival aspect involves more diverse yet compelling reasons ranging from resource scarcity, economic expansion, political stability, climate change, or even stellar evolution.

Although the Earth is the only planet thus far known to support life, the technological possibilities for allowing for survival on extraterrestrial bodies exist, and have been investigated for a few decades. Key among such technologies are those concerning the research, development, and production of infrastructural materials. Widely used on Earth, these are most often connoted by, but not limited to construction of buildings, bridges, or highways. The scale of production reveals their importance: each year, 2-4 billion tons of Portland cement are produced. Ostensibly part of the very fabric of civilization itself, infrastructural materials are also critical in a space base. An extraterrestrial colony includes civil structures such as living quarters, transportation pavements, and launch pads in order to be habitable, functional, and reliable.

One of the most important governing criteria in the research and development of space infrastructural materials are *in-situ* resource utilization (ISRU) and energy efficiency [1][2]. A true ISRU material offers the clear advantage of not requiring supplies from earth, and in this way a colony can be self-sufficient with respect to its own infrastructure growth and expansion. Energy efficiency is important for the same tenets common throughout sustainability paradigms: using the same amount of energy, more material can be produced, or the same output can be maintained for a longer period of time.

The body of literature on space infrastructural materials development dates back several decades. In general, the oldest papers from the 1980s discuss cement-like concrete as a suitable material for lunar environments [3][4]. Thus, extraterrestrial infrastructural materials include masonry, as experience with the most popular construction material might suggest. The moon has supplies of feldspar-type minerals which may be processed into the lime required for cement manufacture [2][4]. Microwave separation of lime from the soil has also been proposed to serve as a source for cement [5].

Although ubiquitous on the earth, concrete or masonry materials require too much energy and resources in space environments. At present, large-scale industry is tailored around processing calcium carbonate raw material. This material is not found on the Moon [6], and is scarce on Mars [7]. Furthermore, high-temperature combustion up to 1550°C is required to process the silicate mineral into cement. Such processes are very energy-consuming. Lastly, water is required for conventional cement–usually 20-40wt% [8].

Direct fusing of lunar soil particles has also been proposed. The source of heating most often comes through a solar concentrator or by nuclear means. Some authors have addressed designs using cast molten rock [9]. Microwave sintering of lunar soil has been proposed as a twice-fold more efficient alternative over bulk heating, because only grain boundaries are involved [10]. This motif carries on as well to newer versions of sintering with rapid prototyping–or the so-called ‘3-D printing’ technique with ceramic particles.

The problems with direct melting via bulk heating are that it is costly and inefficient. The production of glass and molten rock is roughly an order of magnitude more energy-consuming than conventional concrete production, at 50GJ/m^3 [11]. Furthermore, fracture toughness of a material sintered to high temperatures does not always compare favorably to those sintered at lower temperatures [12][13]. Microwave sintering of soil particles is limited in its depth of penetration, and this is a non-trivial unsolved problem [10].

Therefore, it appears chiefly in light of the efficiency argument that cements are a preferable, but still difficult alternative. Research has sought to replace the cementing agent in concrete with other, more ISRU-oriented materials. Developing modified concretes remains an active area of research, with organic polymers and sulfur explored principally as cementing agents [14][15][16][17][18][19]. Sulfur has potential for ISRU because sulfides have been detected on both the Moon and Mars [2][19].

There may be challenges in using organic polymers. It is necessary to identify the polymers that are most radiation and temperature resistant for lunar application. Although polymers do not satisfy the ISRU criteria *per se*, one can minimize binder contents in accordance with what a space transportation budget allows for a mission. The strength may also be poor: polymers directly melted and mixed in 5wt% with lunar regolith simulant and glass fibers have reported a compressive strength of 2.7MPa [20]. Sulfur-based concretes compare more favorably, at around 22MPa compressive strength for 25wt% impregnated cement [19]. However, this weight fraction is rather large for a structural material used for civil purposes, and sulfur only occurs in trace sulfide minerals on the Moon and Mars [7] [19]. One assumes that free sulfur may occur as in elemental form in certain concentrated localities, however, as is the case near volcanoes on earth.

1.2 Geotechnical Stress and Water Content

Much of the extensive and voluminous works in geotechnical research focuses on the improvement of foundations for infrastructural purposes. The process of compaction is widely used for such improvements, and this is associated with an optimal amount of added water content. In order to better establish the scope of research, we seek to conduct a sample of geotechnical literature where, in each study, we extract the two parameters of stress and water content. Surveys which gather a number of studies and which extract a single point from each study are not unprecedented; see for example surveys in engineering (*e.g.* [21]) or other areas of science (*e.g.* [22]). In our survey, the cumulative body of data can be shown on a graph of stress and water content. We first give brief descriptions of particular studies in our survey.

The highest encountered stresses in geotechnical practice are when the soil particles themselves can no longer sustain the stress and breakage naturally occurs. Following the original observations of Terzhaghi and Peck [23], who first described the phenomenon of high-stress particle crushing, we shall extract the minor principal (compressive) stress or the principal effective stress for comparison. Terzhagi and Peck compressed sands up to 97MPa. De Souza [24] tested silica sand up to 138MPa. Lee and Farhoomand [25] tested various mineral particles to 20MPa. Hendron [26] conducted tests with 23MPa. Lade *et al.* [27] examined results on particle crushing to 70MPa. Hardin [28] plotted results from Lee and Farhoomand up to 14MPa, and noted that clays are not susceptible to breakage at these pressures. Nakata *et al.* [29] conducted tests to 100MPa and statistically described particle distribution curves. Murphy [30], Hagerty *et al.* [31] and Yamamuro *et al.* [32] considered pressures of 350MPa, 689MPa and 850MPa, respectively, which can be regarded as an extreme for most geotechnical applications, with the latter stating that such high pressure amounts more to scientific, geophysical study. An example of a geophysical study with clays is the work by Wang and Mao [33], having compressed clays to ~380MPa.

The stresses encountered in our survey fall into two groups: one which reflects typical stresses encountered in actual practice, and one which reflects the scientific probing of extreme limits. All of the stress values are included in our diagram, but it is worth to distinguish this difference.

Water is routinely used for soil compaction [34]. At the extreme end, a saturated clay (such as the type underlying Mexico City) easily exceeds ~400wt% when converting from void ratio [35], and such a slip is more conventionally described by the Atterberg limits [35][34]. Lawton, *et al.* examined the effect of volume changes of overburden clayey soil when wetted to 5-20wt% [36]. Daniel and Wu [37] studied the shrinkage properties of clay with water content 10-20wt%. Albrecht and Benson test several varieties of clayey soil, in order to assess their shrinkage properties after compaction with water contents ranging 10-34wt% [38]. Topp *et al.* used radio waves to measure soil water content from 2-8wt% [39]. Feng investigated water contents from 22-400wt% in a soil, correlating with fall-cone penetration distance [40]. Agus *et al.* studied suction in clay-sand mixtures for water content 8-52wt%. Zhang and Zhao developed a mathematical model simulated with discrete elements to describe anisotropy of soils ranging from 0-3wt% water content [41]. Kim and Hwang developed a model to describe a tensile strength—neglected in most geotechnical practice—for soils ranging from 0.5-4wt% water content [42]. Pepin *et al.*, using techniques like Topp *et al.*, described water contents from 0.2-1wt% in organic soils [43]. Sharma and Bora revisited the robustness of the classical Atterberg limits for soils with water content 13-400wt% [44]. Yu and Dmevich, also using techniques like Topp *et al.*, determined dry densities of soils compacted with water contents from 2-40wt% [45]. Tinjum *et al.* studied characteristic curves from 1.5-15wt% water [46]. Like Kim and Hwang, Pierrat and Caram studied the tensile strength of wet granular materials from dry to about 15wt% water content [47]. Barbour conducted a historical survey of the soil-water characteristic curve, and typified water contents in the range from ~4-25wt% [48]. Horpibulsuk *et al.* tested cement-reinforced soil at a controlled water content of 180wt% [49]. Cho and Santamarina related capillary action to deformations in a soil, with water contents from ~0-20wt% [50]. Daniel and Benson determined effects of water content on molding suitability for soil liners, from 12-25wt% [51]. Tripathy *et al.* investigated swelling and shrinking of soils compacted from 16-46wt% water content, and swelled and dried between 4-66wt% water content [52].

Figure 1-1 portrays the combined envelope, defined by two standard deviations for the stresses and water contents mentioned by the survey. The envelope for the same experimental parameters is also given for this work, for reference. The comparison of water contents is inexact, because the geotechnical works usually define water content as added water relative to samples air-dried at 110°C or less. This work, on the other hand, addresses total water contents of samples dried to 350°C to 600°C.

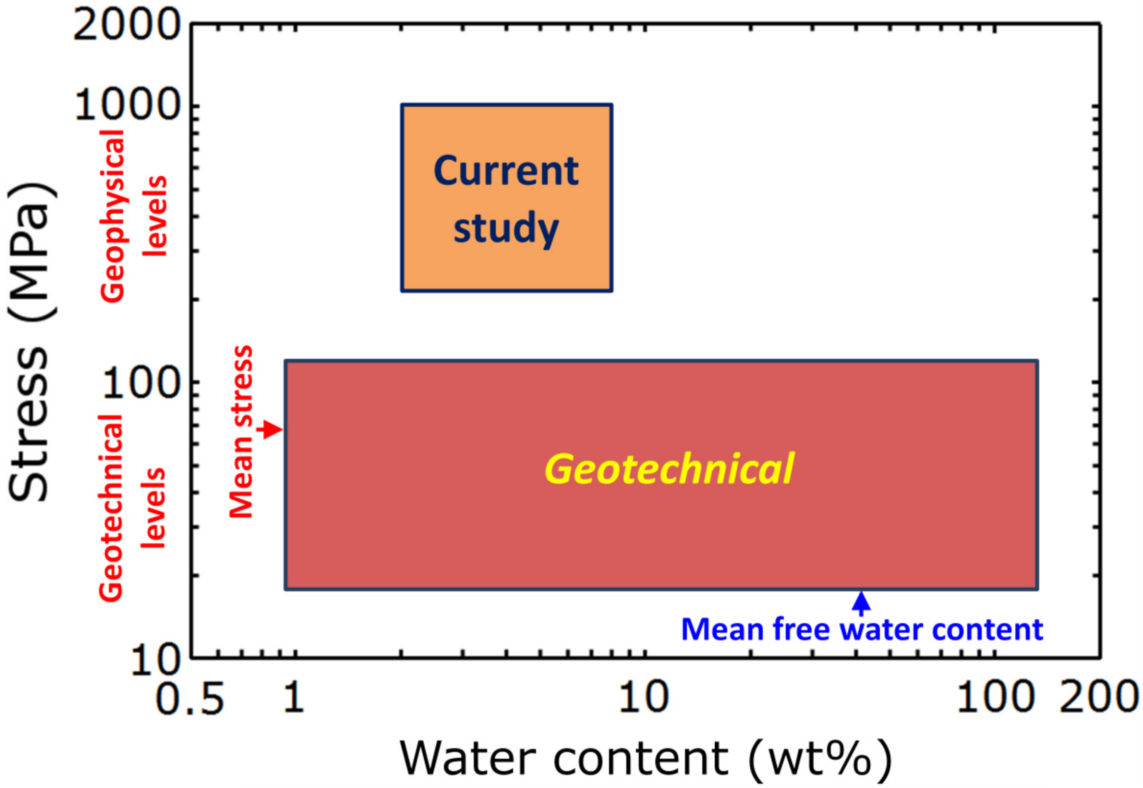

Figure 1-1 Research Stress and Water Content. Plots of the experimental parameters stress and water content usually encountered in geotechnical research and this work. Labels at upper-left near the ordinate axis are positioned at levels typical of geophysical research and geotechnical research. The latter, together with the water contents constitute the envelope for geotechnical research. The current study considers the total water content in the material, distinct from free (or added) water encountered in geotechnical research.

1.3 Compaction Strengthening in Industrial Tablets

Compressing or compacting particles to enhance shear strength is dominant in geotechnical practice for large-scale applications. The conventional tensile strength is assumed to be zero, or with zero flexural strength. In small-scale applications, however, much higher compression pressures are achieved and flexural strengths develop to be quite non-trivial. High-pressure compression of powder is done en masse in pharmaceutical technology, and has been developed as a method for drug delivery since 1843 when William Brockedon invented the first tableting machine [53]. Although tablets were once strongly rejected by academia in the early 20th century due to their once-poor design, they are now ubiquitously consumed [54].

Typical binders in drug tablets are solid powders, such as cellulose, starch, sucrose, complex alcohols, organic acids, *etc.*, compacted under a few hundred MPa [55][56][57][58][59][60][61]. The binder powder also takes on the role of a diluents or excipients and can be referred to by those names. A concise summary of mechanical descriptors for pharmaceutical tablets can be found in a review by Jain [62]. Another review, by Stanley, discussed experimental determination of tablet mechanical properties using flexural, Brazilian, and torsional tests [63]. Often times, these tests extended to cases involving more complex geometries [64][65]. Strength data was conventionally treated statistically most often with the Weibull distribution [63][64].

The description of tablet strength is not a unified science and remains under theoretical development. By some counts, at least 19 equations describe the densification of powder during compaction [66]. Generally, treatments of tablet strength as discussed in the literature ranged from stress analysis (*e.g.* [54][67]) to more abstract semi-empirical theory, utilizing explanations ranging from a simple uniaxial strength to detailed assessments of linear-elastic fracture mechanics (*e.g.* [68]).

A review by Hiestand listed some of the fundamental causes of particle-to-particle bonding in a compressed tablet and found strengths ranging from 2-3MPa [69]. Hiestand and Smith described some relevant performance metrics based on plastic flow at contact regions for a structurally intact tablet [70]. Li *et al.* investigated adhesive forces between particles in a dry tablet [61]. Hiestand also provided a theoretical basis for particle-to-particle bonding in a tablet, using fundamentals of constitutive behavior and fracture [71]. Ambrose *et al.* tested several tablets and found flexural strengths varied from 1-3MPa, with diametrical (Brazilian test) strength about one-third the flexural strength [72]. Newton *et al.* verified the tensile strength from diametrical compression as being the commonly assumed ratio of 1/10 of the uniaxial compressive strength [73]. Adolfsson *et al.* tested several powders including sodium chloride to compression pressures from 100MPa to 250MPa and found tensile strengths in the range of 0.2-6MPa [74]. In another set of tests, Adolfsson tested different sieve sizes in sodium chloride and found that smaller particles achieved a higher tensile strength for all compression pressures from 50-1200MPa, keeping porosity constant [75]. The overall description of particle crushing and cohesion can be divided into several qualitative ways, all of which utilize physical properties of the powder particles, behavior under pressure, and bulk properties of the powder [76][77][78]. Some have also successfully modeled the porosity of a certain granular solid as a function of applied load [68], or correlated the surface roughness of a compacted powder to mechanical properties [79]. Relations between Young’s modulus and strength were found to be more pronounced for relatively soft and rough particles than hard, smooth ones [80].

Tsukamoto and coworkers found that additions of water to most excipients corresponded to a decrease in mechanical properties [59]. Permeability measurements, besides measuring its namesake property, also determined the specific surface area and porosity in a powder compact using the Kozeny-Carman-Wasan theory based on viscous and slip flows [81][82]. Mixtures of different excipients were also tested by Wu *et al.*, and can be described by a linear rule of mixtures [83].

We note that the compaction pharmaceutical research achieved stresses comparable to this work. Key differences are that this work deals with geological materials instead of pharmaceutical ones, and that the technology is aimed towards large-scale production of civil-structural materials.

1.4 Overview of the Martian Surface

The main part of this research concerns compaction of two Martian soil simulants. To place this research into context more generally, we conduct a survey of what is found in Martian regolith.

Martian soils in general reflect the local bedrock composition. In general, the bedrock composition is mainly basaltic in mineralogical composition, although the surface has a reddish hue which is due to the presence of a ferric oxide compound which shows short-range order and evidence of poor crystallinity [7].

The composition of the crust of Mars is more homogenous than the earth, and similar to oceanic crust on Earth (*i.e.*, ultramafic basalt) [7]. Primary minerals, which were originally formed from an igneous environment, and many of which comprise the essentials of basalt, are listed in Table 1-1. Some secondary minerals, as those found in the altered or sedimentary rocks [7], are also listed in Table 1-1. Using broader categories, Martian soil can be divided as listed in Table 1-2.

Table 1-1 Minerals on the Martian Surface (adapted from Ehlmann and Edwards [7])

Classification	Mineral Name	Formula
Primary (Primordial, Igneous Rocks)	Olivines (forsterite, fayalite)	$(Mg, Fe)_2SiO_4$
	Orthopyroxenes	$(Mg, Fe, Ca)Si_2O_6$
	Clinopyroxenes	$(Ca, Mg, Fe)Si_2O_6$
	Plagioclase feldspars	$(Ca, Na)(Al, Si)_4O_8$
	Alkali feldspars	$(K, Na)(Al, Si)_4O_8$
	Pyrrhotite	$Fe_{1-x}S$
	Pyrite/marcasite	FeS_2
	Magnetite	$Fe_{3-x}Ti_xO4$
	Ilmenite	$FeTiO_3$
Secondary (Altered, Sedimentary Rocks)	Hematite	Fe2O3
	Goethite	FeO(OH)
	Fe/Mg smectites (e.g. nontronite)	$(Ca,Na)_{0.3-0.5}(Fe,Mg,Al)_{2-3}(Al, Si)_4O_{10}(OH)_2 \cdot nH_2O$
	Al smectite (e.g. montmorillonite)	$(Na,Ca)_{0.3-0.5}(Al,Mg)_2(Al, Si)_4O_{10}(OH)_2 \cdot nH_2O$
	Kaolin group (e.g. kaolinite)	$Al_2Si_2O_5(OH)_4$
	Chlorite	$(Mg,Fe^{2+})_5Al(Si_3Al)O_{10}(OH)_8$
	Al/K phyllosilicate (e.g. illite)	$(K,H_3O)(Al,Mg,Fe)_2Al_xSi_{4-x}O_{10}(OH)_2$
	Mg/Ca/Fe carbonates	$(Mg,Fe,Ca)CO_3$
	Hydrated sulfates	$(Fe,Mg)SO_4 \cdot nH_2O$
	Gypsum/bassanite/anhydrite	$CaSO_4 \cdot nH_2O$
	Jarosite	$KFe_3(OH)_6(SO_4)_2$
	Chlorides	*e.g.*, NaCl, $MgCl_2$
	Perchlorates	*e.g.*, $(Mg,Ca)(ClO_4)_2$

Table 1-2 Mineral Categories in Martian Soil (adapted from Christensen *et al.*[84]):

Component	Fraction (wt%)
Feldspars	50
Pyroxenes	25
Olivines	12
Phyllosilicates	13

The detailed chemical composition is included for reference in order to illustrate the predominance of some iron-bearing minerals, salts, and clay minerals. The other details contained in Tables 1-1 and 1-2 are for reference only and are not important for further discussion.

The Martian crust has undergone substantial compositional change ever since the formation of the planet. From earliest to latest, the order of Martian geologic history is divided into the epochs Noachian (greater than 3.7 billion years), Hesperian (3.7 to 3.1 billion years), and Amazonian (less than 3.1 billion years) [7][85]. The oldest time epochs, particularly the Noachian, have generally been found to produce the most evidence for water, including minerals which have been altered in an aqueous environment. Cross referencing maps of global water content variation revealed Arabia Terra and Terra Sabea, which straddle the equatorial plains, have a relatively high surface water content of 5-8wt% [85]. The lower water contents of the equatorial plains surrounding the north and south of Valles Marineris canyon, on the other hand, showed about 1-4wt% water content. Both aforementioned water contents were gathered *via* gamma ray spectroscopy on the Mars Odyssey spacecraft [85]. These would likely be indicative of the secondary minerals listed in Table 1-1. The average water content taken from the Viking samples was inferred to be 4-7wt% [85], consistent with the results from the Mars Odyssey [86].

Spectroscopic studies done with both thermal infrared and visible near-infrared wavelengths have determined some regional differences between the northern lowlands (*viz.*, Acidalia and Utopia Planitia) and the southern highlands of Mars [86]. In particular, the bedrock of the northern lowlands contain high-silica phases consistent with altered silica in the form of a fine-grained or amorphous coatings [7]. These coatings were brought about by a relatively light amount of aqueous alteration. In contrast, the southern highlands are richer in pyroxenes. However, overall, it is noted that iron content is higher in the northern lowlands, making the composition slightly more ultramafic than in the southern hemisphere of Mars [86].

In terms of elemental composition, the Mars GRS found 18-22wt% silicon, 10-20wt% iron, and 0.2-0.8wt% chlorine [86]. The chlorine composition assumes the form of halide minerals as listed in Table 1-1; a trace compound of chlorine is in the form of the perchlorate ion [86]. The chloride minerals are widespread across the highlands south of the equator.

Clay minerals, being water-altered forms of olivine or feldspars, are widespread on portions of the crust identified as having formed during the Noachian epoch [7][87]. Clay minerals are listed in Table 1-1. Widespread distribution is consistent with the distributions of the plagioclase and olivine mineral through thermal emission spectrometry of the Mars Global Surveyor spacecraft [88]. The regions on Mars showing high clay contents would be the Noachian terra regions around Valles Marineris, namely Terra Thaumasia, (northwest) Terra Noachis, and a concentration around Syrtis Major [7][87]. The highest concentration of clay minerals appears to be the highlands north of Hellas Planitia and Isidis, where carbonates and sulfates occur as well [7]. Smectites, such as montmorillonite, have also been verified on the surface [89][90].

Sulfur occurs mainly in the form of sulfide, sulfate, and sulfite ions, with an abundance of the former [7]. Sulfur-containing minerals are listed in Table 1-1. They are associated with sedimentary processes which were associated with water, and conditions on average were acidic. It is also noted that low pH values are also consistent with clay formation. The highest concentrations of sulfate-bearing minerals are from the Valles Marineris and a large concentration in the southwest of Arabia Terra. Sulfate occurrences largely overlap the clay mineral occurrences.

Martian soils at the location of the Mars Exploration rovers, Spirit and Opportunity, were cementitious and self-cohesive at the locations where they landed, namely Gusev crater and Meridiani Planum [91]. In fact, some knowledge about the mechanical properties of actual Martian soil are already inferred from photographs by Spirit and Opportunity. The bearing strength was estimated at 15-130kPa, with cohesive strength 1-7kPa, and an angle of internal friction of ~20°-25° [91]. A comparison to typical geologic sediments' properties suggests that the soil is clay [92]. The soil is formed from Martian fines and wind-driven deposits which form the first layers of the surface. Below the reddish surface underlay a darker-colored, finer grained self-cohesive soil [91]. The cohesion is thought to derive from the presence of sulfate and/or chloride minerals [91], but the fine quality of the molded impressions leaves open the possibility that a high clay mineral component is involved.

1.5 References

1. Bodiford, M. P., Burks, K. H., Perry, M. R., Cooper, R. W., Fiske, M. R. "Lunar In Situ Material-Based Habitat Technology Development Efforts at NASA/MSFC," *Earth and Space,*1-8 (2006).

2. Casanova, I., Aulesa, V. "Construction Materials from In-Situ Resources on the Moon and Mars," *Space 2000,* 638-644 (2000).

3. Lin, T. D., Senseney, J. A., Arp, L. D., Lindbergh, C. "Concrete lunar base investigation," *J. Aero. Eng.* **2**, *1*, 10-19 (1989).

4. Lin, T. D. "Concrete for Lunar Base Construction," *In: Lunar Bases and Space Activities of the 21st Century. Houston, TX, Lunar and Planetary Institute (Mendell, W. W., ed.)* (1985), pp. 381-390.

5. Lin, T. D., Bhattacharja, S. "Lunar and Martian resources utilization: cement," *Space 98,* 592-600 (1998).

6. Korotev, R. L. "How Do We Know That It's a Rock From the Moon?," Washington University in St. Louis, 5 October 2015. URL: http://meteorites.wustl.edu/lunar/howdoweknow.htm. [Accessed 2016].

7. Ehlmann, B. L., Edwards, C. S. "Mineralogy of the Martian Surface," *Annu. Rev. Earth Planet. Sci.* **42**, 291-315 (2014).

8. Mindess, S., Young, J. F., Darwin, D. Concrete. Prentice Hall (2003).

9. Happel, J., William, K., Shing, B., in *Center for Space Construction: Third Annual Symposium*.

10. Taylor, L. A., Meek, T. T. "Microwave Sintering of Lunar Soil: Properties, Theory, and Practice," *J. Aero. Eng.* **18**, *3*, 188-196 (2005).

11. Lin, T. D., in *Lunar Bases and Space Activities of the 21st Century* (1985).

12. Wang, W., Fu, Z., Wang, H., Yuan, R. "Influence of hot pressing sintering tempereature and time on microstructure and mechanical properties of TiB2 ceramics," *J. Euro. Ceram. Soc.* **22**, *7*, 1045-1049 (2002).

13. van Landuyt, P., Li, F., Keustermans, J. P., Streydio, J. M., Delannay, F., Munting, E. "The influence of high sintering temperatures on the mechanical properties of hydroxylapatite," *J. Mat. Sci. Mat. Med*. **6**, 8-13 (1995).

14. Toutanji, H., Fiske, M. R., Bodiford, M. P. "Development and Application of Lunar 'Concrete' for Habitats," *Earth & Space* (2006).

15. Gracia, V., Casanova, I. "Sulfur Concrete: A Viable Alternative for Lunar Construction," *Space 98,* 585-591 (2006).

16. Meyers, C., Toutanji, H. "Analysis of Lunar-Habitat Structure Using Waterless Concrete and Tension Glass Fibers," *J. Aero. Eng.* **20**, *4*, 220-226 (2007).

17. Toutanji, H., Grugel, R. N. "Mechanical Properties and Durability of "Waterless Concrete"," in *Earth and Space Conference 2008: 11th International Conference on Engineering, Science, Construction, and Operations in Challenging Environments*, Long Beach, California (2008).

18. Koh, S. W., Yoo, J., Bernold, L. E., Lee, T. S. "Experimental Study of Waterless Concrete for Lunar Construction," in *Earth and Space 2010: Engineering, Science, Construction, and Operations in Challenging Environments* (2010).

19. Toutanji, H., Glenn-Loper, B., Schrayshuen, B. "Strength and Durability Performance of Waterless Lunar Concrete," in *43rd AIAA Aerospace Sciences Meeting and Exhibit*, Reno, Nevada (2005).

20. Lee, J., Chang, B. C., Lee, S., Lee, T. S. "Feasibility Study on Lunar Concrete Landing Pad," *Earth and Space 2012*, 128-134 (2012).

21. Ashby, M. F. "Overview No. 80: On the Engineering Properties of Materials," *Acta Metall.* **37**, *5*, 1273-1293 (1989).

22. Oreskes, N. "The Scientific Consensus on Climate Change," *Science* **306**, *5702*, 1686 (2004).

23. Peck, R. B., Terzaghi, K. Soil mechanics in engineering practice. Wiley (1948).

24. De Souza, J. M. *Compressibility of sand at high presure, MS Thesis,* Massachusetts Institute of Technology (1958).

25. Lee, K. L., Farhoomand, I. "Compressibility and crushing of granular soil in anisotropic triaxial compression," *Can. Geotech. J.* **IV**, *1*, 68-86 (1967).

26. Hendron, A. J. *The behavior of sand in one-dimensional compression, PhD thesis,* University of Illinois (1963).

27. Lade, P. V., Yamamuro, J. A., Bopp, P. A. "Significance of Particle Crushing in Granular Materials," *J. Geotech. Eng.* **122**, *4*, 309-316 (1996).

28. Hardin, B. O. "Crushing of Soil Particles," *J. Geotech. Eng.* **111**, *10*, 1177-1192 (1985).

29. Nakata, Y., Hyodo, M., Hyde, A. F., Kato Y., Murata, H. "Microscopic Particle Crushing of Sand Subjected to High Pressure One-Dimensional Compression," *Soils and Foundations. Jap. Geotech. Soc.* **41**, *1*, 69-82 (2001).

30. Murphy, D. J. "Stress, degradation, and shear strength of granular material," in *Geotechnical modeling and applications (Sayed, S.M., ed.)*, Gulf Publishing (1987), pp. 181-211.

31. Hagerty, M. M., Hite, D. R., Ullrich, C. R., Hagerty, D. J. "One-Dimensional High Pressure Compression of Granular Media," *J. Geotech. Eng.* **119**, *1*, 1-18 (1993).

32. Yamamuro, J. A., Bopp, P. A., Lade, P. V. "One-Dimensional Compression of Sands at High Pressures," *J. Geotech. Eng.* **122**, *2*, 147-154 (1996).

33. Wang, C.-Y., Mao, N-H. "Mechanical Properties of Clays at High Pressure," *J. Geophys. Res.* **85**, *B3*, 1462-1468 (1980).

34. Das, B. M. <u>Principles of Geotechnical Engineering</u> (7th ed.). Cengage Learning (2010).

35. Fox, P. J. *SE 181 Lecture Notes,* UC San Diego (2015).

36. Lawton, E. C., Fragaszy, R. J., Hardcastle, J. H. "Collapse of Compacted Clayey Sand," *J. Geotech. Eng.* **115**, *9*, 1252-1267 (1989).

37. Daniel, D. E., Wu, Y.-K. "Compacted Clay Liners and Covers for Arid Sites," *J. Geotech. Eng.* **119**, *2*, 223 - 237 (1993).

38. Albrecht, B. A., Benson, C. H. "Effect of Dessication on Compacted Natural Clays," *J. Geotech. Geoenviron. Eng.* **127**, *1*, 67-75 (2001).

39. Topp, G. C., Davis, J. L, Annan, A. P. "Electromagnetic Determination of Soil Water Content: Measurements in Coaxial Transmission Lines," *Water Resources Res.* **16**, *3*, 574-582 (1980).

40. Feng, T.-W. "Fall-cone penetration and water content relationship of clays," *Geotechnique* **50**, *2*, 181-187 (2000).

41. Zhang, W., Zhao, C. "Micromechanics Analysis for Unsaturated Granular Soils," *Acta Mechanica Solida Sinica* **24**, *3*, 273-281 (2011).

42. Kim, T.-H., Hwang, C. "Modeling of tensile strength on moist granular earth material at low water content," *Eng. Geology* **69**, 233-244 (2003).

43. Pepin, S., Plamondon, A. P., Stein, J. "Peat water content measurement using time domain reflectometry," *Canadian J. Forest Res.* **22**, *4*, 534-540 (1992).

44. Sharma, B., Bora, P. K. "Plastic Limit, Liquid Limit and Undrained Shear Strength of Soil - Reappraisal," *J. Geotech. and Geoenv. Eng.* **129**, *8*, 774-777 (2003).

45. Yu, X., Drnevich, V. P. "Soil Water Content and Dry Density by Time Domain Reflectometry," *J. Geotech. Geoenv. Eng.* **130**, *9*, 922-934 (2004).

46. Tinjum, J. M., Benson, C. H., Blotz, L. R. "Soil-Water Characteristic Curves for Compacted Clays," *J. Geotech. Geoenv. Eng.* **123**, *11*, 1060-1069 (1997).

47. Pierrat, P., Caram, H. S. "Tensile strength of wet granular materials," *Powder Tech.* **91**, 83-93 (1997).

48. Barbour, S. L. "Nineteenth Canadian Geotechnical Colloquium: The soil-water characteristic curve: a historical perspective," *Can. J. Geotech. J.* **35**, 873-894 (1998).

49. Horpibulsuk, S., Miura, N., Bergado, D. T. "Undrained Shear Behavior of Cement Admixed Clay at High Water Content," *J. Geotech. Geoenviron. Eng.* **130**, *10*, 1096-1105 (2004).

50. Cho, G.-G., Santamarina, J. C. "Unsaturated Particulate Materials - Particle-Level Studies," *J. Geotech. Geoenv. Eng.* **127**, *1*, 84-96 (2001).

51. Daniel, D. E., Benson, C. H. "Water Content-Density Criteria for Compacted Soil Liners," *J. Geotech. Eng.* **116**, *12*, 1811-1830 (1990).

52. Tripathy, S., Subba Rao, K. S., Fredlund, D. G. "Water content - void ratio swell-shrink paths of compacted expansive soils," *Can. Geotech. J.* **39**, 938-959 (2002).

53. Burlinson, H. "The evolution of the compressed tablet," in *Plenary Lecture at the British Pharmaceutical Conference* (1968).

54. Drake, K. E., Newton, J. M., Mokhtary-Saghafi, S., Davies, P. N. "Tensile stresses generated in pharmaceutical tablets by opposing compressive line loads," *Euro. J. Pharm. Sci.* **30**, 273-279 (2007).

55. Kachrimanis, K., Malamataris, S. "Compact size and mechanical strength of pharmaceutical diluents," *Euro. J. Pharm. Sci.* **24**, *2-3*, 169-177 (2005).

56. Kachrimanis, K., Malamataris, S. " ‘Apparent’ Young's elastic modulus and radial recovery for some tableted pharmaceutical excipients," *Euro. J. Pharma. Sci.* **21**, *2-3*, 197-207 (2004).

57. Doelker, E., Mordier, D., Iten, H., Humbert-Droz, P. "Comparative Tableting Properties of Sixteen Microcrystalline Celluloses," *Drug. Dev. Ind. Pharm.* **13**, *9-11*, 1847-1875 (1987).

58. Lee, J. "Drug nano- and microparticles processed into solid dosage forms: Physical properties," *J. Pharm. Sci.* **92**, *10*, 2057-2068 (2003).

59. Tsukamoto, T., Chen, C. Y, Okamoto, H., Danjo, K. "The Effects of Adsorbed Water on Tensile Strength and Young's Modulus of Moldings Determined by Means of a Three-Point Bending Method," *Chem. Pharm. Bull.* **48**, *6*, 769-773 (2000).

60. Kuentz, M., Leuenberger, H., Kolb, M. "Fracture in disoedered media and tensile strength of microcrystalline cellulose tablets at low relative densities," *Int. J. Pharm.* **182**, *2*, 243-255 (1999).

61. Qin, L., Rudolph, V., Weigl, B., Earl, A. "Interparticle van der Waals force in powder flowability and compactibility," *Int. J. Pharm.* **280**, *1-2*, 77-93 (2004).

62. Jain, S. "Mechanical properties of powders for compaction and tableting: and overview," *Pharm. Sci. Tech. Today* **2**, *1*, 20-31 (1999).

63. Stanley, P. "Mechanical strength testing of compacted powders," *Int. J. Pharm.* **227**, *1-2*, 27-38 (2001).

64. Podczeck, F. "Methods for the practical determination of the mechanical strength of tablets - From empiricism to science," *Int. J. Pharm.* **436**, *1-2*, 214-232 (2012).

65. Davies, P. N., Worthington, H. E., Podczeck, F., Newton, J. M. "The determination of the mechanical strength of tablets of different shapes," *Euro. J. Pharm. Biopharm.* **67**, *1*, 268-276 (2007).

66. Etzler, F. M., Bramante, T., Deanne, R., Sienkiewicz, S., Chen, F. J. "Tablet Tensile Strength: An Adhesion Science Perspective," *J. Adhesion Sci. Tech.* **25**, *4-5*, 501-519 (2011).

67. Bassam, F., York, P., Rowe, R. C, Roberts, R. J. "Young's modulus of powders used as pharmaceutical excipients," *Int. J. Pharm.* **64**, *1*, 55-60 (1990).

68. Klevan, I., Nordstrom, J., Bauer-Brandl, A., Alderborn, G. "On the physical interpretation of the initial bending of a Shapiro-Konopicky-Heckel compression profile," *Euro. J. Pharm. Biopharm.* **71**, *2*, 395-401 (2009).

69. Hiestand, E. N. "Principles, tenets and notions of tablet bonding and measurements of strength," *Euro. J. Pharm. Biopharm.* **44**, *3*, 229-242 (1997).

70. Hiestand, H. E. N., Smith, D. P. "Indices of tableting performance," *Powder Tech.* **38**, *2*, 145-159 (1984).

71. Hiestand, E. N. "Tablet bond. I. a theoretical model," *Int. J. Pharm.* **67**, *3*, 217-229 (1991).

72. Ambros, M. C., Podczeck, F., Podczeck, H., Newton, J. M. "The Characterization of the Mechanical Strength of Chewable Tablets," *Pharm. Dev. Tech.* **3**, *4*, 509-515 (1998).

73. Newton, J. M., Alderborn, G., Nyström, C., Stanley, P. "The compressive to tensile strength ratio of pharmaceutical compacts," *Int. J. Pharm.* **93**, *1-3*, 249-251 (1993).

74. Adolfsson, Å., Olsson, H., Nyström, C. "Effect of particle size and compaction load on interparticulate bonding structure for some pharmaceutical materials studied by compaction and strength characterisation in butanol," *Euro J. Pharm. Biopharm.* **44**, *3*, 243-251 (1997).

75. Adolfsson, Å., Nyström, C. "Tablet strength, porosity, elasticity and solid state structure of tablets compressed at high loads," *Int. J. Pharm.* **132**, *1-2*, 95-106 (1996).

76. Wray, P. E. "The Physics of Tablet Comapction Revisited," *Drug Dev. Ind. Pharm.* **18**, *6-7*, 627-658 (1992).

77. Train, D. *Ph.D Thesis*, University of London (1956).

78. Huffine, C. L., Bonilla, C. F. "Particle-size effects in the compression of powders," *Am. Inst. Chem. Engrs. J.* **8**, *4*, 490-493 (1962).

79. Narayan, P., Hancock, B. C. "The relationship between the particle properties, mechanical behavior, and surface roughness of some pharmaceutical excipient compacts," *Mat. Sci. Eng. A* **355**, *1-2*, 24-36 (2003).

80. Roberts, R. J., Rowe, R. C. "The Young's modulus of pharmaceutical materials," *Int. J. Pharm.* **37**, *1-2*, 15-18 (1987).

81. Wasan, D. T., Ranade, M. B., Sood, S. K, Davies, R., Jackson, M., Kaye, B. H., Wnek, W. "Analysis and evaluation of permeability techniques for characterizing fine particles Part II. Measurement of specific surface area," *Powder Tech.* **14**, *2*, 229-244 (1976).

82. Alderborn, G., Pasanen, K., Nyström, C. "Studies on direct compression of tablets. XL Characterization of particle fragmentation during compaction by permeametry measurements of tablets," *Int. J. Pharm.* **23**, *1*, 79-86 (1985).

83. Wu, C.-Y., Best, S. M., Bentham, A. C., Hancock, B. C., Bonfield, W. "Predicting the Tensile Strength of Compacted Multi-Component Mixtures of Pharmaceutical Powders," *Pharm. Res.* **23**, *8*, 1898-1905 (2006).

84. Christensen, P. R., Bandfield, J. L., Hamilton, V. E., Ruff, S. W., Kieffer, H. H., Titus, T. N., Malin, M. C., Morris, R. V., Lane, M. D., Clark, R. L., Jakosky, B. M., Mellong, M. T., Pearl, J. C., Conrath, B. J., Smith, M. D., Clancy, R. T., Kuzmin, R. O., Roush, T., Mehall, G. L., Gorelick, N., Bender, K., Murray, K., Dason, S., Greene, E., Silverman, S., Greenfield, M. "Mars Global Surveyor Thermal Emission Spectrometer experiment: Investigation description and surface science results," *J. Geophys. Res.* **106**, *E10*, 23,823-23,871 (2001).

85. Morris, R. V., Klingelhöfer, G. "Iron mineralogy and aqueous alteration on Mars from the MER Mossbauer spectrometers," in *The Martian Surface: Composition, Mineralogy, and Physical Properties (Bell III, J. F., ed.)*, Cambridge University Press (2008), pp. 339-365.

86. Boynton, W. V., Taylor, G. J., Karunatillake, S., Reedy, R. C., Keller, J. M. "Elemental abundances determined via the Mars Odyssey GRS," in *The Martian Surface: Composition, Mineralogy, and Physical Properties (Bell III, J. F., ed.)*, Cambridge University Press (2008), pp. 105-124.

87. Ehlmann, B. L., Mustard, J. F., Murchie, S. L., Bibring, J.-P., Meunier, A., Fraeman, A. A., Langevin, Y. "Subsurface water and clay mineral formation during the early history of Mars," *Nature* **479**, 53-60 (2011).

88. Christensen, P. R., Bandfield, J. L., Rogers, A. D., Glotch, T. D., Hamilton, V. E., Ruff, S. W., Wyatt, M. B. "Global mineralogy mapped from the Mars Global Surveyor Thermal Emission Spectrometer," in *The Martian Surface: Composition, Mineralogy, and Physical Properties (Bell III, J. F., ed.)*, Cambridge University Press (2008) p. 195.

89. Poulet, F., Bibring, J.-P., Mustard, J. F., Gendrin, A., Mangold, N., Langevin, Y., Arvidson, R. E., Gondet, B., Gomez, C., the Omega Team, "Phyllosilicates on Mars and implications for early martian climate," *Nature* **438**, 623-627 (2005).

90. Clark III, B. C., Arvidson, R. E., Gellert, R., Morris, R. V., Ming, D. W., Richter, L., Ruff, S. W., Michalski, J. R., Farrand, W. H., Yen, A., Herkenhoff, K. E., Li, R., Squyres, S. W., Schröder, C., Klingelhöfer, G., Bell III, J. F. "Evidence for montmorillonite or its compositional equivalent in Columbia Hills, Mars," *J. Geophys. Res.* **112**, *E06S01* (2007).

91. Herkenhoff, K. E., Golombek, M. P., Guinness, E. A., Johnson, J. B., Kusack, A., Richter, L., Sullivan, R. J., Gorevan, S. "In situ observations of the physical properties of the Martian surface," in *The Martian Surface: Composition, Mineralogy, and Physical Properties (Bell III, J. F., ed.)*, Cambridge University Press (2008), p. 451.

92. Zhu, T. "Some Useful Numbers on the Engineering Properties of Materials (Geologic and Otherwise)," URL: http://www.stanford.edu/~tyzhu/Documents/Some%20Useful%20Numbers.pdf. [Accessed 2014].

2 Scope of this Research

2.1 First Part: Lunar and Martian Soils Compacted with Binders

Currently the main targets for manned space exploration are the Moon and Mars. Most research that has been overviewed focuses on lunar habitats. The scope of our research is to investigate what, if possible, any techniques may have to reduce or eliminate the need for binder contents in lunar or Martian regolith. The bulk of our efforts will be focused on martian soils for the reason that *indigenous* martian materials development is largely absent from the current literature.

Of the techniques for producing lunar bricks, we investigate low binder content inorganic-organic hybrids (IOHs) which have the capability to minimize the amount of required organic material shipments from the earth. We address several approaches, all of which involve mechanical compression:

1. Dissolving polymers and combining with soil particles;
2. Forming the polymer from a monomer mixture with soil particles;
3. Partially dissolving soil particles directly for bonding.

Techniques for producing Martian bricks are fundamentally different. As usual, we investigate low binder content applications. Since Mars is more distant from the earth, there is greater motivation to drastically reduce or even eliminate shipments from the earth. We address the following techniques, mechanical compression again being indispensable:

1. Forming the polymer from monomer mixture with soil particles;

2. Thermally aided mixing of polymer melt with soil particles;
3. Relying only on intrinsic soil cohesion without additives;

The above three approaches for processing Martian soils differ from those for lunar soils in an a chronologically *a posteriori* manner, with adjustments made in response to observations from the results of experiments ongoing.

2.2 Second and Main Part: Martian Soils Compacted without Binders

After some experimentation, we find relying only on intrinsic soil cohesion without additives is most promising, because it is able to best satisfy the ISRU requirement. We explore different types of soils which may be compressed into a strong solid, such as JSC Mars-1a, montmorillonite clay, and several salts, with focus on the first two. Key parameters affecting flexural strength were investigated, including compression pressure, initial sieved particle size, and, for mixtures, the constitution percentages.

Most of the mechanical properties of the solid are predominantly tested in three-point bending. We choose the measure of flexural strength (modulus of rupture) because it is generally indicative of the most important mechanical properties. For a brittle solid, increasing the flexural strength is generally well correlated with the other types of strength [1][2], elastic moduli [3], density [4], and permeability (*via* porosity [4]). For reference purposes, compression strength was occasionally measured.

Most experiments are performed in a closed steel die. We then modify the experimental setup during the compression forming process to investigate the dependence of strength on compression pressure. The lateral boundary condition of loading then reduces from a rigid die wall to a flexible wall or no wall at all restraining the sample circumference; these are referred to as the flexible and free lateral boundary conditions, respectively, and together they are collectively called the reduced lateral boundary conditions. Again, the resultant compact strengths are explored.

Two different rates of loading compacts the sample. Quasi-static loading is performed at about 3-6mm/min on a uniaxial load-displacement machine, whereas impact loading is performed at ~2-4m/s, representing about 5 orders of magnitude of difference. Differences in resultant compact strengths are examined between quasi-static forming and impact forming cases.

Characterization helps determine more performance-related attributes in martian infrastructural materials. Thermogravimetric analysis (TGA) helps determine the appropriate and suitable drying temperature for each simulant, when cross-referenced with literature-based water contents in actual Martian soils. Scanning electron microscopy (SEM) reveals the particle sizes, shapes, orientation, and other visual characteristics. CHNS/O analysis tests for organic matter in Mars-1a and, when combined with mechanical testing, reinforces an inorganic basis for the source of binding of the solid under compression. X-ray diffraction (XRD) can determine important information at molecular scales, suggesting sources of imperfection between particles of clay. An evolved gas analysis (EGA) helps to determine the identity of certain gases released from the soil upon heating, all of which can detect the presence of minerals or organic matter.

Finally, we test gas permeability because it is relevant to the ability of habitats to contain an atmospheric chamber. Another related practical consideration involves the calculation of volumetric energy efficiency for the compacted products in relation to other extant technologies for habitat construction.

2.3 References

1. Balendran, R. V., Martin-Buades, W. H. "The influence of high temperature curing on the compressive, tensile and flexural strength of pulverized fuel ash concrete," *Building and Environment* **35**, *5*, 415-423 (2000).

2. Adam, J. W., Ruh, R., Mazdiyasni, K. S. "Young's Modulus, Flexural Strength, and Fracture of Yttria-Stabilized Zirconia versus Temperature," *J. Am. Ceram. Soc.* **80**, *4*, 903-908 (1997).

3. Albakry, M., Guazzato, M., Swain, M. V. "Biaxial flexural strength, elastic moduli, and x-ray diffraction characterization of three pressable all-ceramic materials," *J. Prosth. Dent.* **89**, *4*, 374-380 (2003).

4. Duxson, P., Provis, J. L., Lukey, G. C., Mallicoat, S. W., Kriven, W. M., van Deventer, J. S. "Understanding the relationship between geopolymer composition, microstructure and mechanical properties," *Coll. Surf. A: Physiochem. Eng. Asp.* **269**, 47-58 (2005).

3 Simulant-Based Structural Materials with Binders

3.1 Lunar Simulant Selection

The lunar regolith is mainly comprised of basaltic minerals not unlike those found on the earth. A common simulant that represents the maria regions of the Moon is JSC-1A. The composition of JSC-1A approximates the samples gathered from at least two Apollo missions [1]. The bulk of the research involved JSC-1A, but ordinary silicate-feldspar sand was occasionally substituted.

3.2 Martian Simulant Selection

One of the more widely-used simulants for Martian soil is JSC Mars-1a, which can be described as a close mechanical analogue. The simulant is characterized as having a similar visible and near-infrared reflectance spectrum as the Olympus-Amazonis region on Mars and similar proportions of several oxides including SiO_2, Fe_2O_3, and CaO [2]. The orogenic environment from which Mars-1a is derived is essentially that of weathered basaltic rocks, which is descriptive of the Martian surface. Mars-1a contains anorthite feldspar and titanium magnetite as the significant minerals [2]. Over half of the iron present in Mars-1a is in the form of nanophase iron (III) oxide, with a particle size of less than 20nm [2]. A variety of poorly crystalline or amorphous iron (III) oxides have been reported across the Martian surface [3]. Thus, there exists a substantial nanoparticulate, poorly crystalline, and/or near-amorphous iron (III) oxide in both Mars-1a and Martian regolith soils. The iron oxides act as an aggregating agent, as is commonly assumed [4], and contributes to the cementation processes reported for fluvial Martian sedimentary formations [5][6]. Gypsum and clay are other widely reported cementing agents; the clay is appears mostly to be of an iron-rich smectite, montmorillonite, and/or nontronite. These mineral species are largely absent from Mars-1a, but are easily formulated in alternatives due to their terrestrial abundance. The mechanical properties between Mars-1a and real Martian soil are comparable, with coefficients of internal friction between 30 and 40° and cohesion values on the order of 1 N/cm^2 [7][8].

Appendix B presents an elementary analysis of Mars-1a simulant.

3.3 Lunar Simulant Processing

3.3.1 Direct Mixing

The simplest possible approach to combine a binder material with lunar simulant particles is through the application of mechanical mixing. The resulting material is known as an inorganic-organic hybrid (IOH). In the small-scale laboratory environment, hand mixing suffices for this purpose. Thermoplastic polymers are required to melt in order to form bonds between particles, whereas thermosets require no elevated temperatures. The Moon's peak daytime temperature is ~150°C, which decreases the amount of energy required to heat thermoplastics into a workable form. However, limits with this approach may include the wettability of the thermoplastic to substrates (Appendix A). Success with low binder contents can be made, however, under application of high compression pressure [9]. Rather than repeating the work of Chen in detail, we verify a small aspect of his work to illustrate the potential of other methods to distribute the binding phase.

Five-gram samples of JSC-1A soil were mixed with up to 4wt% epoxy by first compressing in a 19.05mm inner diameter steel cell at a pressure of 360MPa on a load-displacement machine (Instron 5582). The loading rate was specified as 0.3mm/min. Crushing of the particles was observed, and the resulting disc was ground into fine powder by means of a mortar and pestle. The powder was re-entered into the same load cell and compressed a second time with identical parameters. The resulting discs were cured in an oven preheated at 80°C for 1h. The discs were converted into beam specimens by making cuts in a secant-type fashion, and water lubricant was driven off by heating at 150°C for 30min.

In a separate investigation, silica-feldspar sand (La Jolla, CA) was compressed twice at various pressures inside of a confined cylinder dye, with matching pistons on both ends. The double compression produces higher strengths than a single compression for mixing the added binding phase. Both compressions prescribed identical pressures. The results of the beam flexure tests are shown in Table 3-1 and Figure 3-1. Results for compressed sand are tabulated in Table 3-2.

Table 3-1 Flexural Strengths of JSC-1A and Epoxy

Sample.	Binder Fraction (wt%)	Width (mm)	Thickness (mm)	Length (mm)	Flexural Strength (MPa)
160	4	7.48	3.07	12.9	21.44
161	4	7.52	3.46	12.9	26.48
162	4	7.49	3.31	12.9	29.76

Table 3-2 Double-Compressed Sand Strengths with 4wt% Epoxy

Sample	Pressure (MPa)	Width (mm)	Depth (mm)	Flexural Strength (MPa)
504	360	4.94	3.70	24.64
505		4.93	4.26	24.50
506		3.60	4.37	25.24
507		3.62	4.23	25.73
519	90	5.25	4.79	28.05
520		5.24	4.40	29.26
521	180	5.04	4.02	31.11
522		5.05	3.74	35.55
523	270	6.00	3.72	31.90
524		6.01	3.85	36.14
525	90	4.33	3.60	23.19
526		4.33	3.66	22.44
527		4.14	3.96	22.15
528		4.12	3.84	25.68
529		5.52	3.78	23.16
530		5.55	3.95	22.94
531		4.56	3.71	24.37
532		4.57	3.67	25.22
533	180	2.82	3.86	28.25
534		2.82	3.70	23.06
535		4.71	3.99	25.58
536		4.73	3.91	23.99
537		4.51	3.77	18.88
538		4.51	4.02	26.31
539		4.08	3.80	24.41
540		4.09	3.89	26.56
541	270	3.28	3.61	28.31
542		3.28	3.39	26.65
543		6.20	4.48	20.92
544		6.20	4.29	19.61
545		5.36	3.62	20.80
546		5.36	4.25	27.59
547		4.75	3.82	22.07
548		4.75	3.48	21.83
549	~0.3	4.95	4.40	8.58
550		4.95	3.86	6.81
551	10	4.30	3.85	10.75

Table 3-2 Double-Compressed Sand Strengths with 4wt% Epoxy (continued)

552	10	4.28	4.12	7.54
553	30	7.04	3.83	13.26
554		7.01	4.63	14.28
555	60	6.18	4.11	22.53
556		6.19	4.99	22.07
557	0.3	5.91	4.30	6.27
558		5.93	3.94	6.70
559	10	7.17	3.89	8.63
560		7.17	3.69	8.42
561	30	4.53	4.21	13.08
562		4.53	3.88	15.06
563	60	3.80	4.13	20.78
564		3.80	4.00	20.65
565	~0.3	5.22	3.95	6.73
566		5.22	4.06	5.31
567	10	5.77	3.74	8.20
568		6.06	3.55	9.27
569	30	5.59	3.82	13.99
570		5.59	3.23	13.31
571	60	5.38	4.69	19.48
572		5.38	4.12	18.75

Cure temperature was 100°C maintained for 1h.
Length between beam supports was 15.22mm.

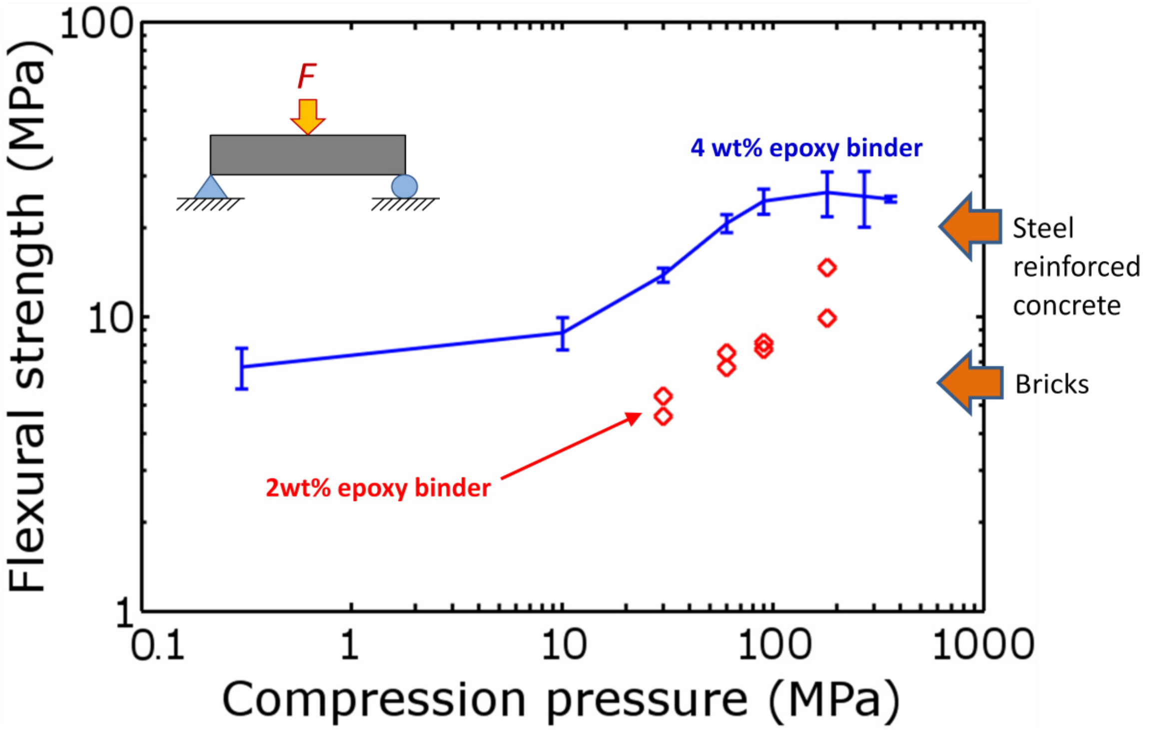

Figure 3-1 Flexural Strength 4wt% Epoxy Sand IOH. Samples are compressed to different pressures. Three-point bending schema shown at upper-left; reference materials shown at right.

The IOH made from 4wt% epoxy shows a three-fold higher flexural strength over that made from 2wt% epoxy. In order for the latter to reach the same strength as the former, it requires about one order of magnitude's worth of an increase in compression pressure. This shows that higher pressures may assist in driving down the binder content, up to a certain limit. For the compression pressures available by the equipment, the 4wt% epoxy samples showed a maximum flexural strength of ~30MPa, greater than a typical steel-reinforced concrete (see Appendix C).

3.3.2 Organic Solvents

The polymers PEI and PES were chosen specifically to have higher melting point and high viscosity. One method to mix the polymer with inorganic particles is to melt the polymer and mix it with inorganic particles by stirring. Difficulties arise in attempting to mix them evenly, and polymer tends to be oxidized under atmospheric conditions unless all operation is carried out under vacuum or inert environments. An alternative is to use a solvent-aided processing technique whereby mixing of the polymer and inorganic particles occurs thoroughly and homogenously. The PES polymer was chosen for its high thermal stability and radiation resistance.

Toluene, acetone, ethanol, and dimethyl acetamide (DMAc) were investigated separately for suitability in dissolving PES. Of these, only DMAc was found capable of dissolving the PES completely in less than a few hours. Thus, DMAc was chosen for processing PES.

IOH lunar cements of differing PES contents were prepared by changing the ratio of PES to lunar stimulant (JSC-1A) by weight, and the processing is shown in Figure 3-2.

For a 50wt% PES sample, 4g of PES was mixed with 20ml DMAc in a 50ml beaker and the mixture was stirred with a magnetic mot at a high temperature (~80^{o}C) to dissolve the polymer. After the polymer was dissolved completely, we added 4g lunar simulant grains of 100µm (JSC-1A) to the solution slowly. The mixture was stirred continuously until almost all the DMAc evaporated and the mixture become a viscous paste. The paste was then transferred to the steel mold which was preheated by heating and compressed with a 3kg weight overnight in an oven at 200^{o}C. The as-prepared sample was denoted as JSC-PES50. 33wt% and 20wt% samples were also prepared following the same procedure; these samples were denoted JSC-PES33 and JSC-PES20, respectively. Vacuum processing was also investigated on a sample of 20wt% PES, labeled JSC-PES20-V. Most of the PES was squeezed out of mold during the processing before the sample was solidified completely, making the labeled PES content only nominal. TGA tests were performed to detect the actual PES content in the product. Flexural tests using a 3-point bending configuration determined the resulting strength.

Further investigation introduced other methods of casting the solvent-IOH mixtures. The portion of the procedure with the dissolution and addition of lunar cements to form the paste were, in all cases, identical.

The first alternate method was the application of a high magnitude of load, using a C-clamp. The simulant in this case consisted of 100µm mixed with 20µm particles in a 765:235 ratio, respectively, and polymer contents were 5wt%, 10wt%, 20wt%, and 50wt%. Disc-shaped spacers allowed the fabrication of multiple disc-shaped samples within the same load cell. The torque applied was hand-tight to a minimum of 50Nm. The 5wt%, 10wt%, 20wt%, and 50wt% samples were named 007, 008, 009, and 010. These samples, after confinement, were heated to 50°C for a period of 12h, followed by release of the sample from the mold, and finally an unconfined drying at 200°C for 48h.

The second alternate method was to process the mixture as a thin film, whereby the procedure is simplified without the use of the more complicated molds. There are generally two subdivisions of this method.

In the first thin-film technique, the mixture spreads on top of a polytetrafluoroethylene sheet and dries under normal atmospheric conditions, before heating. The simulant in this case consisted of 100µm mixed with 20µm particles in a 765:235 weight ratio, respectively, and polymer contents were 5wt%, 10wt%, 20wt%, and 50wt%.

In the second thin-film technique, the mixture was pressed between two flat plates, as shown in Figure 3-4, and progressively heated to higher temperatures. A layer of Teflon sheets served as a quick release in between the plates. Strips of Nylon 6-6 0.51mm thick served as spacers between the flat plates, imposing a displacement-controlled condition. The simulant in this case consisted of 20µm particles only, and polymer contents were 5wt%, 10wt%, 20wt%, and 50wt%.

The temperature profile for both thin-film techniques were as follows:

1. Heat on hot plate at 50°C for 24h.
2. Heat on hot plate at 120°C for 24h.
    - *Released from mold.*
3. Heat in oven at 80°C.for 12h.
4. Heat in oven at 200°C for 12h.

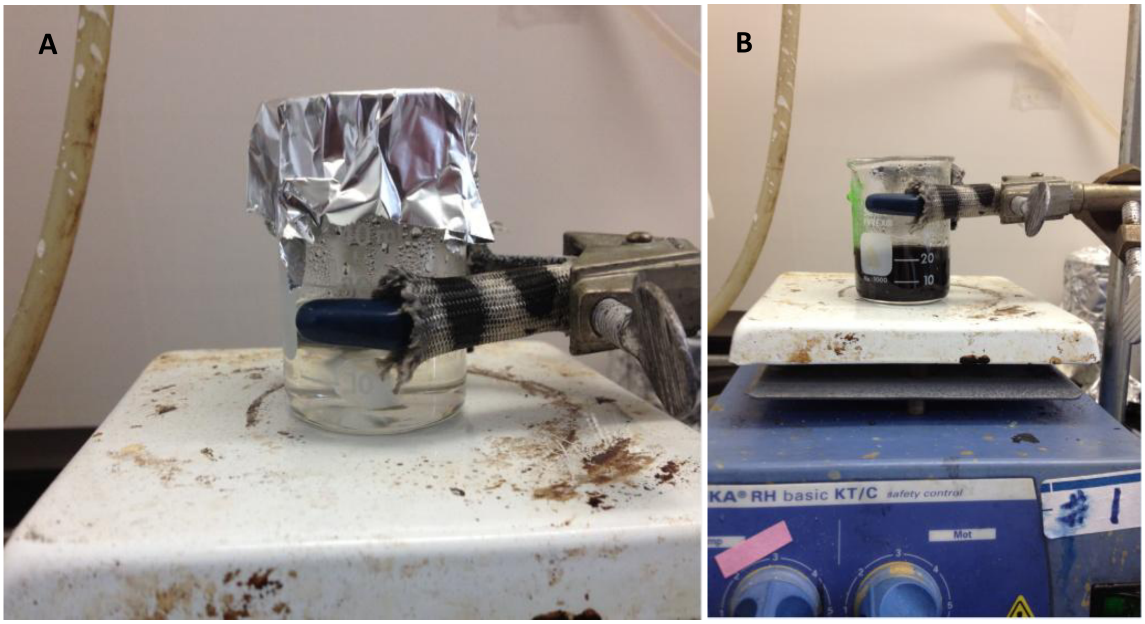

Figure 3-2 Solvent Processing JSC-1A. Dissolving of PES in DMAc (A) and mixing (B) with JSC-1A. Photographs courtesy of Gang Wang.

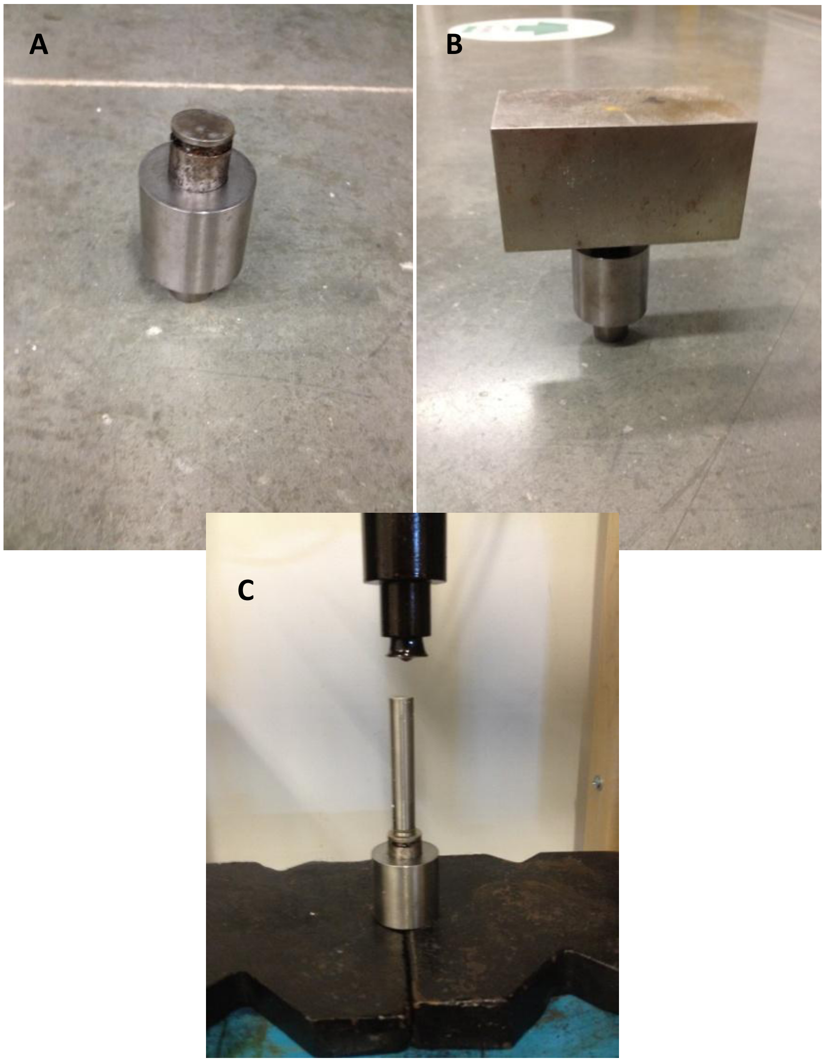

Figure 3-3 Deadweight Compression of IOH. Transfer of mixture to cylindrical mold (A), compressing of the mold (B), and removal of the sample after solidification (C). Photographs courtesy of Gang Wang.

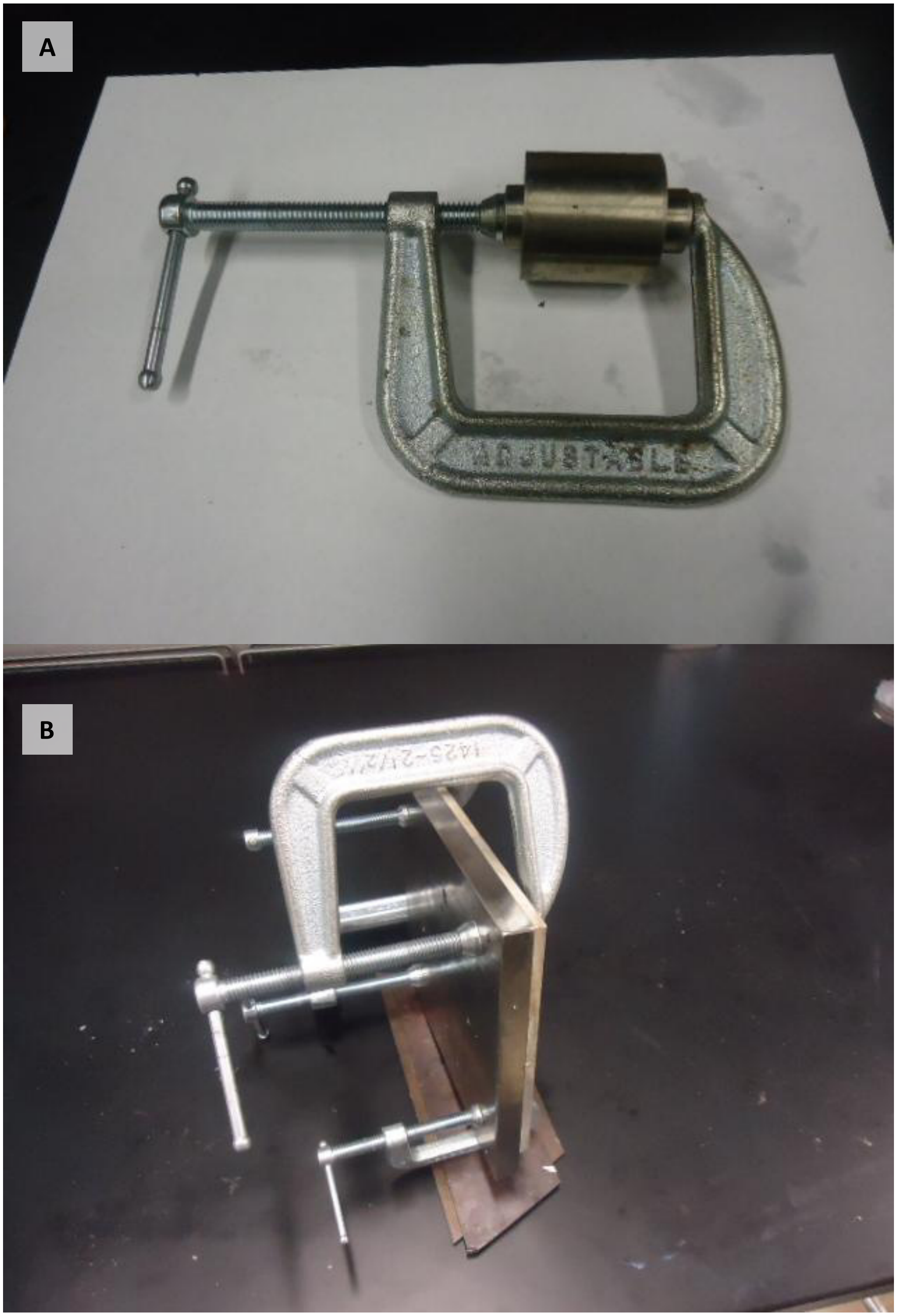

Figure 3-4 C-Clamp Compression of IOH. The clamp applies load to the mold (A) and plates secured to form the solvent-IOH mixture (B).

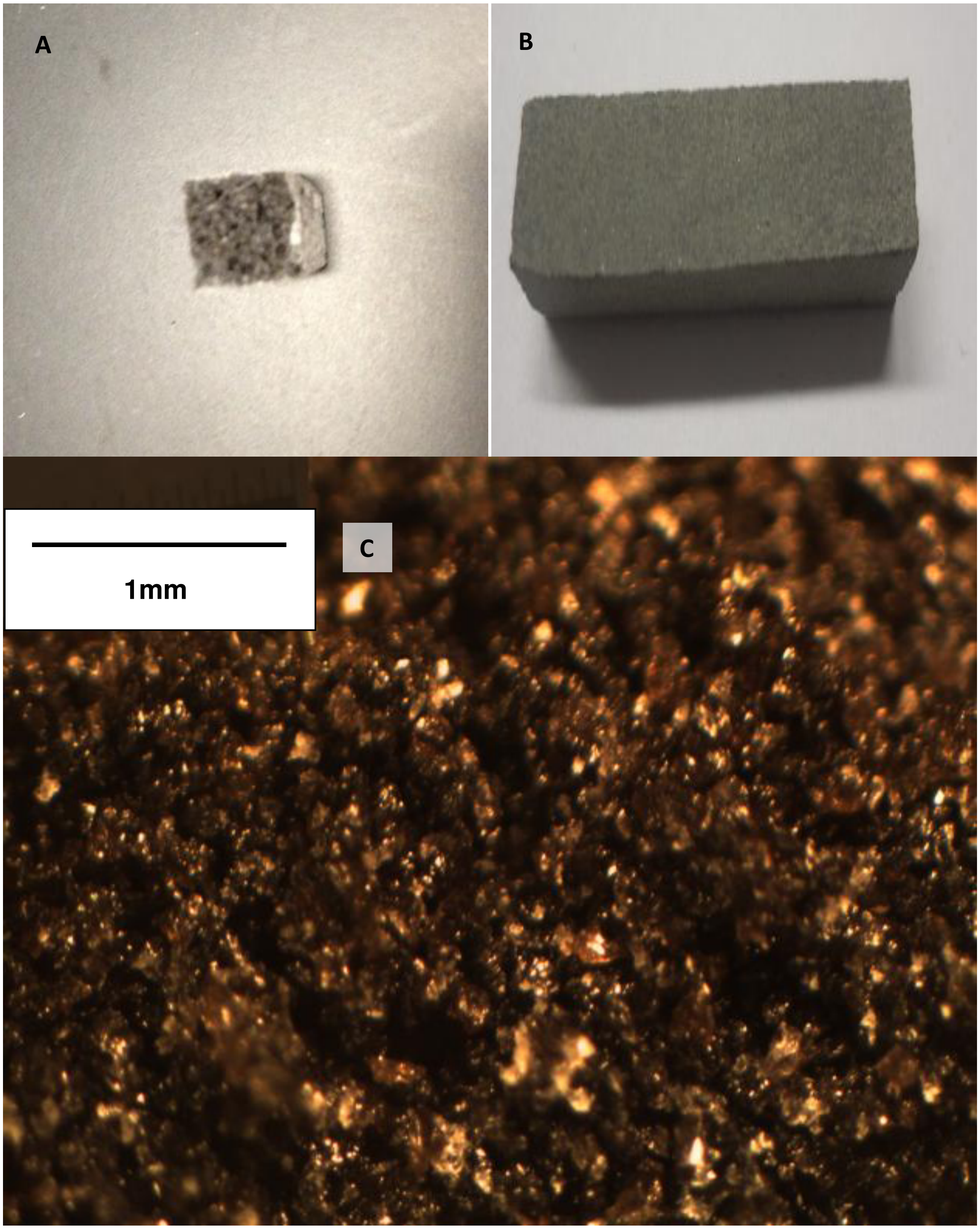

Figure 3-5 Photographs of PES IOH. A section of JSC-PES20 (A), JSC-PES20-V (B), and optical microscopy of surface of sample JSC-PES20-V (C). Pictures courtesy of Gang Wang.

Table 3-3 Effect of Vacuum Processing on Flexural Strength

Sample		Width (mm)	Depth (mm)	Flexural Strength (MPa)	Average Strength (MPa)
JSC-PES20	1	7.5	6.5	4.9	5.4
	2	7.5	5.8	6.2	
	3	7.5	6.6	4.8	
	4	7.5	6.1	5.6	
JSC-PES20-V	1	8.0	7.0	11.3	9.2
	2	7.0	6.7	9.4	
	3	6.4	6.1	7.0	

Table 3-4 Effect of C-Clamp Processing on Flexural Strength

Sample	PES Content (wt%)	Width (mm)	Depth (mm)	Flexural Strength (MPa)	Average Strength (MPa)
007-1	5	6.3	4.0	1.2	1.5
007-2		5.5	3.8	1.0	
007-3		6.5	4.4	2.8	
007-4		5.9	3.0	1.0	
008-1	10	6.8	2.6	2.2	3.8
008-2		5.9	3.0	4.6	
008-3		8.2	4.2	4.6	
009-1	20	3.9	2.0	24.5	20.4
009-2		4.2	4.4	16.3	
010	50	3.1	3.7	18.0	18.0

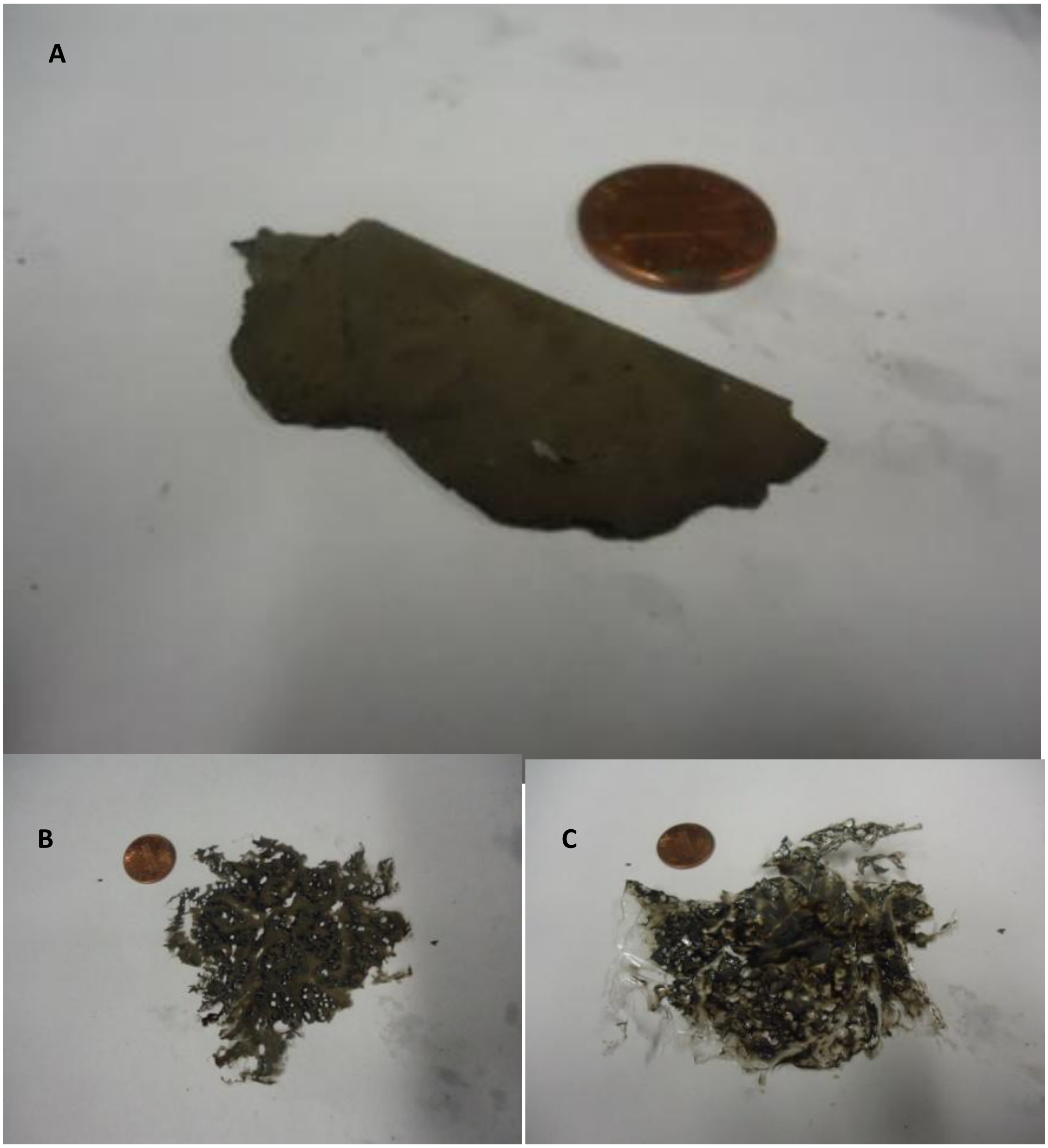

Figure 3-6 Thin Film PES IOH. A well-cast film of 10wt% PES IOH bearing the highest strength of any configuration in the solvent techniques (A), compared with poorly formed 20wt% (B) and 50wt% (C) PES IOH samples.

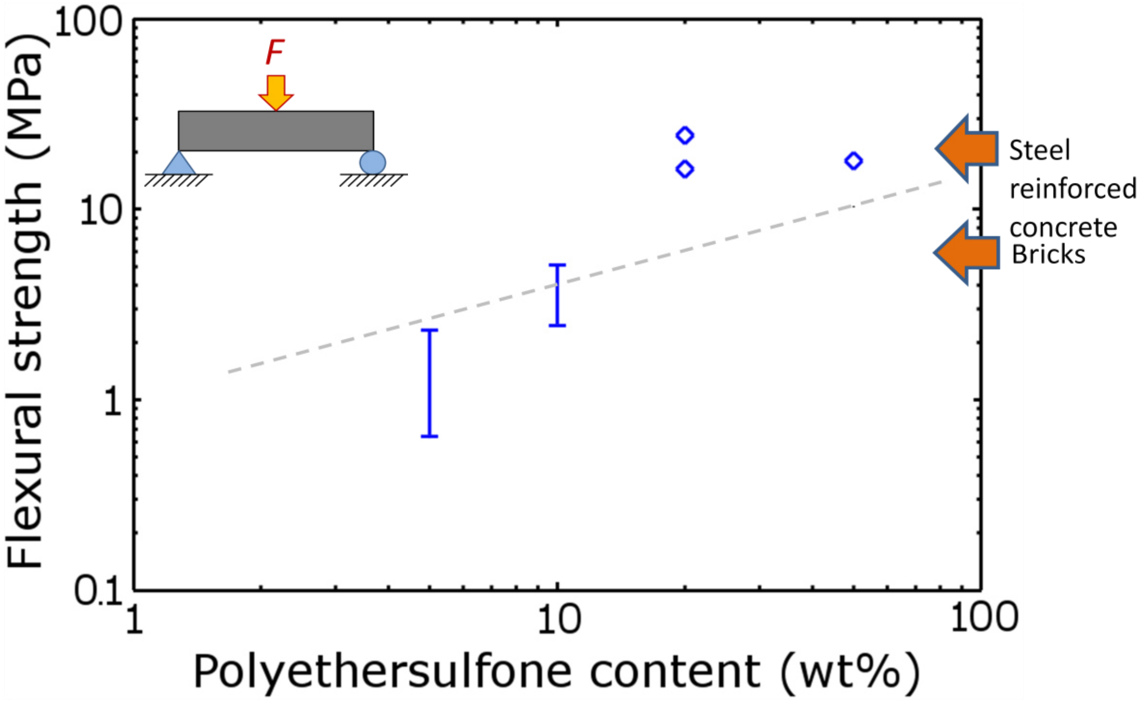

Figure 3-7 Flexural Strength of C-Clamped JSC-1A/PES IOH. Plots are a function of PES content. Three-point bending schema shown at upper-left; reference materials shown at right.

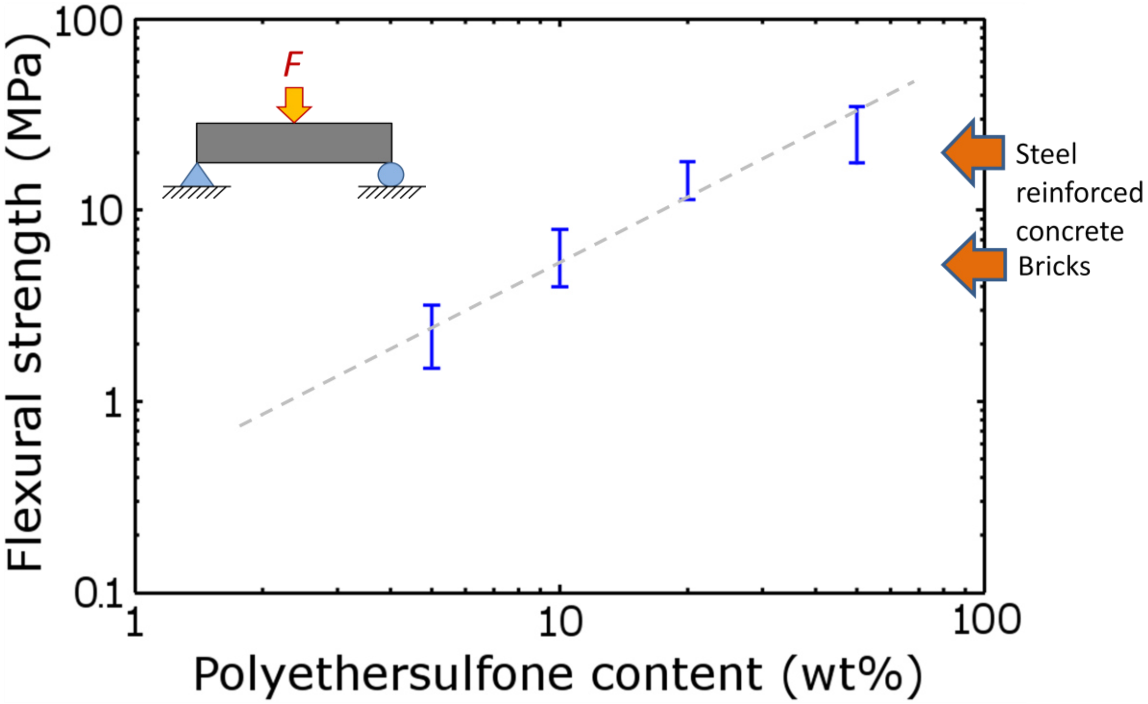

Figure 3-8 Flexural Strength of Thin-Film JSC-1A/PES IOH. Plots are a function of PES content. Three-point bending schema shown at upper-left; reference materials shown at right.

Flexural strengths were roughly doubled with vacuum processing, because the continuous pressing action of the block (Figure 3-3B) aided the vacuum to facilitate mobility of voids during solvent evaporation.

The strengths resulting from the C-clamp (Figure 3-4) were only comparable with those obtained by using a heavy block weight. This is presumably due to the load being relieved as the sample progressively dries, even if the initial magnitude of compression is higher.

With the thin-film plate method, a polymer content of 10wt% was found to have the highest strength in flexure tests: 4.5MPa. However, due to the large amounts of viscous polymers in higher polymer contents (viz., 20wt% and 50wt%), these produced poor quality samples with pervasive voids. The 5wt% samples disintegrated upon release of the mold, presumably from lack of sufficient compression.

One notices that at the 5wt% and 10wt% PES content samples, there is a precipitous drop in strength. Our own testing of the neat polymer of PES, in both direct tension and three-point flexure tests, indicate that PES has a strength of between 50-60MPa. The fact that higher polymer contents do not perform up to the magnitude of the neat polymer strength serves as a reminder of the importance of the issues pertaining to surface tension and wettability discussed in Appendix A.

3.3.2.1 Further Work: State of Evaporation

Further investigation probed the effects of evaporation state of the solvent mixture when it is cast on the strength, as well as the sample thickness. Sixteen samples were made, where the first eight corresponded to four samples extracted during an early evaporation state and four samples extracted during an intermediate evaporation state. The last eight were all made during a late evaporation state. The evaporation states were variable for each sample, due to unequal temperatures between hot plates and the size of the foil aperture for allowing evaporation.

The samples' evaporation states are calculated based upon the weight of the sample compared to the original weight with all the solvent initially present. A suffix for the usual nomenclature denotes “evb” for the early stage, “evl” for the intermediate stage, and “evl2” for the late stage. For the surviving samples we calculate:

- 022evb (10wt% PES) : 4.01g evaporated out of 9.35g total = 43wt% evaporated
- 024evb (50wt% PES) : 5.35g evaporated out of 9.35g total = 57wt% evaporated
- 022evl (10wt% PES) : 5.11g evaporated out of 8.19g total = 62wt% evaporated
- 024evl (50wt% PES) : 6.71g evaporated out of 9.00g total = 75wt% evaporated
- 021evl2 (5wt% PES) : 5.88g evaporated out of 9.35g total = 63wt% evaporated
- 025evl2 (10wt% PES) : 3.40g evaporated out of 6.95g total = 49wt% evaporated
- 023evl2 (20wt% PES) : 5.83g evaporated out of 9.35g total = 62wt% evaporated
- 026evl2 (50wt% PES) : 4.73g evaporated out of 8.84g total = 54wt% evaporated

Note that for each of the cases listed above, two thicknesses were made. In the early-evaporated samples, two out of four samples were lost due to extreme fragility: clearly the early evaporation stage represents the most difficulty for fabrication due to the excessive intumescence which develops under pressure in the oven. In the intermediate evaporation stage, one sample was lost for similar reasons. In the late evaporation state, one sample was lost during extraction of the sample from the oven.

The additional suffices “thn” and “thck” correspond to the the thin and thicker samples made from each polymer concentration, respectively.

Samples 35-52 were made with 5wt% PES. The evaporation states for those are as follows:

- 035 and 039: 2.83g evaporated out of 7.00g total = 40wt% evaporated
- 036 and 040: 3.36g evaporated out of 7.00g total = 48wt% evaporated
- 037 and 041: 3.70g evaporated out of 7.00g total = 53wt% evaporated
- 038 and 042: 3.89g evaporated out of 7.00g total = 56wt% evaporated
- 043 and 044: 2.48g evaporated out of ~5.3g total = 47wt% evaporated
- 045 through 048: 3.10g evaporated out of ~6.0g total = 52wt% evaporated
- 049 through 052: ~3.50g evaporated out of 7.00g total = 50wt% evaporated

Table 3-5 Flexural Strength of 5wt% PES IOH

Sample	Width (mm)	Depth (mm)	Strength (MPa)
021evl2-thn	10.76	1.58	2.25
021evl2-thck	9.28	3.95	4.18
029	11.08	1.26	1.11
030	11.72	2.07	1.01
031	10.82	2.00	2.70
032	12.35	2.03	1.53
035	10.67	0.91	4.70
036	13.02	1.33	8.11
037	12.46	1.10	5.51
038	7.76	0.96	1.45
039	14.02	2.18	3.12
041	11.28	1.27	8.56
042	12.97	2.62	1.87
043	7.21	3.15	7.82
045	9.62	2.23	3.60
046	10.64	2.40	2.46
047	11.41	2.73	4.56
048	12.35	2.24	3.82
049	11.73	2.19	1.91
050	11.11	1.85	3.87
051	11.58	2.63	3.53
052	11.55	3.10	3.10

The data indicate that certain processing variations other than the state of evaporation determine the strength, because there is no clear indication that a reduction in thickness or an increase in viscosity (a relatively retarded evaporation state) can produce reliably stronger samples. The dominant factor appears to be systematic uncertainty in the porosity of the produced sample and the uncertainty in flaw creation during the cutting process with respect the fragility of the sample. For example, a possible increase in strength or equivalent strength in low-PES content cements may be masked by the flaws created during sawing because sometimes the cut is not always clean in appearance.

In earlier samples, for a drying temperature fixed at 200°C and PES content fixed at 5wt%, there exists a trend where the thin sample strengths are generally higher than the thick sample strengths; for these, the statistical flaws govern the strength. Currently, the late evaporation states show a reverse trend, because pre-cracks in the binding matrix through the IOH composite are not recovered during the evaporation process. Further tests controlling evaporation temperature, for which thicknesses were random but still measured, were subject to the same fabrication procedures but showed an opposite trend, perhaps due to the sensitivity of flaws during the cutting process. Overall, the thickness appears to show a weak influence on the flexural strength.

A drying time of 168h is sufficient to evaporate the DMAc in a 120°C environment. However, even after 12h of additional drying after being liberated from their load cells, the samples were found to be insufficient in strength and only four samples survived: 029, 031, 033, and 034. These samples exhibited strengths of 1.11MPa, 1.01MPa, 2.70MPa, and 1.53MPa, respectively. Other samples were made to compare the states between the boiling temperature of 165°C and 200°C, due to the hypothesis that a lower temperature may inhibit void formation.

Table 3-6 summarizes the influence of drying temperature, within practical durations of drying time, on the flexural strength.

Table 3-6 Flexural Strength of PES IOH at Different Drying Temperatures

Sample	Drying Temperature (°C)	Drying Schedule confined + free (h)	Width (mm)	Depth (mm)	Flexural Strength (MPa)	Average Strength (MPa)
029	120	168 + 24	11.08	1.26	1.11	1.59
031			11.72	2.07	2.60	
033			10.82	2.00	2.70	
034			12.35	2.03	1.53	
053	157	12 + 12	9.97	4.23	3.63	1.74
054			10.15	2.82	1.60	
055			10.2	1.57	1.72	
056			10.1	1.81	0.65	
057			10.9	3.65	2.38	
058			6.71	1.59	0.64	
059			9.65	3.35	1.59	
060	200		10.72	1.85	3.53	3.95
061			11.69	2.25	2.73	
062			11.81	3.33	5.93	
063			12.35	3.62	4.26	
064			11.68	1.91	3.54	
065			9.99	1.59	3.42	
066			10.2	3.00	4.23	
067			12.08	4.26	3.94	

Inorganic phase is JSC-1A.
Polymer content is 5wt%.

It is noticed that the samples with the highest flexural strengths are found to have been made with a combination of a half-evaporated state (by weight) and a heavy deadweight rather than a C-clamp. This is due to the fact that a continuous load applied to a partially wet sample can still aid in the reconfiguration of the grains as gas bubbles attempt to nucleate in random fashion. Thus, the heavy block method of manufacture is superior.

The second polymer chosen as a candidate binder was polysulfone (PSU), based on the wettability tests performed. The polymer was found to adequately dissolve in the same solvent (DMAc), although the time required for dissolution of PSU is greater than that for PES. The procedure using load cells for the PES was kept the same for fabrication of the PSU-bound cements. Data for cement strengths as a function of binder content are shown in Table 3-7.

Table 3-7 Flexural Strength of JSC-1A/PSU IOH at Different Binder Content

Sample	PSU Content (wt%)	Particle Size (μm)	Width (mm)	Depth (mm)	Flexural Strength (MPa)	Average Strength (MPa)
105	1	Random	10.19	1.78	0.63	0.55
106			12.76	2.85	0.30	
108			10.47	2.34	0.71	
109	2		10.75	2.49	1.53	1.32
110			11.59	4.26	1.16	
111			10.31	1.75	1.29	
112			11.00	2.67	1.30	
120		500+100	8.61	2.62	0.66	0.53
121			9.28	2.33	0.39	
122			9.60	5.46	0.55	
116	3.5	Random	7.83	2.35	4.54	5.09
117			9.53	2.90	5.39	
118			6.96	2.28	4.34	
119			8.44	2.10	6.07	
123		500+100	7.85	2.23	1.01	1.24
124			9.84	2.89	1.91	
125			10.15	2.07	0.45	
126			9.19	5.54	1.60	
131		100	4.90	2.56	2.35	2.16
132			5.62	2.94	2.33	
133			5.30	3.37	2.20	
134			5.62	4.15	1.76	
135		100+20	6.41	2.32	5.20	3.93
136			6.29	2.50	4.08	
137			6.52	2.77	7.74	
138			5.70	3.71	4.81	
147			4.58	2.26	1.60	
148			4.62	2.87	1.23	
149			6.07	1.79	2.89	
150			4.46	3.46	3.87	
127	5	500+100	9.12	2.93	1.25	2.23
128			9.40	2.42	2.14	
130			8.33	6.20	3.19	
101		Random	10.03	2.72	6.02	4.80
102			9.08	3.08	4.96	
103			9.36	2.06	7.82	
104			9.12	3.53	5.47	
068			9.45	2.39	4.53	

Table 3-7 Flexural Strength of JSC-1A/PSU IOH at Different Binder Content (continued)

069	5	Random	11.59	2.51	8.28	4.80
070			11.69	2.83	5.23	
071			9.24	2.50	2.82	
093			6.06	3.06	5.01	
094			6.73	2.89	3.71	
095			7.87	2.30	0.91	
096			8.84	1.94	2.85	
139		100	6.00	2.11	3.89	3.05
140			6.45	4.10	3.22	
141			7.21	2.74	2.79	
142			7.32	4.09	2.31	
143		100+20	5.91	2.09	5.12	5.16
144			6.21	3.17	5.45	
145			5.99	2.87	4.21	
146			7.46	3.19	4.73	
151			5.47	1.61	5.29	
152			5.14	4.11	4.32	
153			5.07	1.68	7.21	
154			5.27	3.46	4.91	
076	10	Random	9.98	5.62	4.40	7.16
077			9.09	3.21	3.05	
078			8.83	2.80	5.89	
085			5.48	2.39	8.96	
086			3.77	1.70	9.19	
087			7.94	2.11	10.76	
088			8.01	2.03	7.89	
079	20		8.91	4.31	5.91	7.96
080			6.70	5.14	11.75	
081			8.71	2.72	5.38	
089			8.06	1.88	2.81	
090			7.39	1.40	15.21	
091			7.14	3.01	7.12	
092			3.14	2.76	7.53	
082	50		8.53	1.02	50.53	19.43
083			4.17	1.65	16.16	
084			8.37	1.89	19.09	
097			7.64	4.24	11.72	
098			5.09	3.94	14.39	
099			4.77	3.38	8.34	
100			4.4	3.69	15.81	

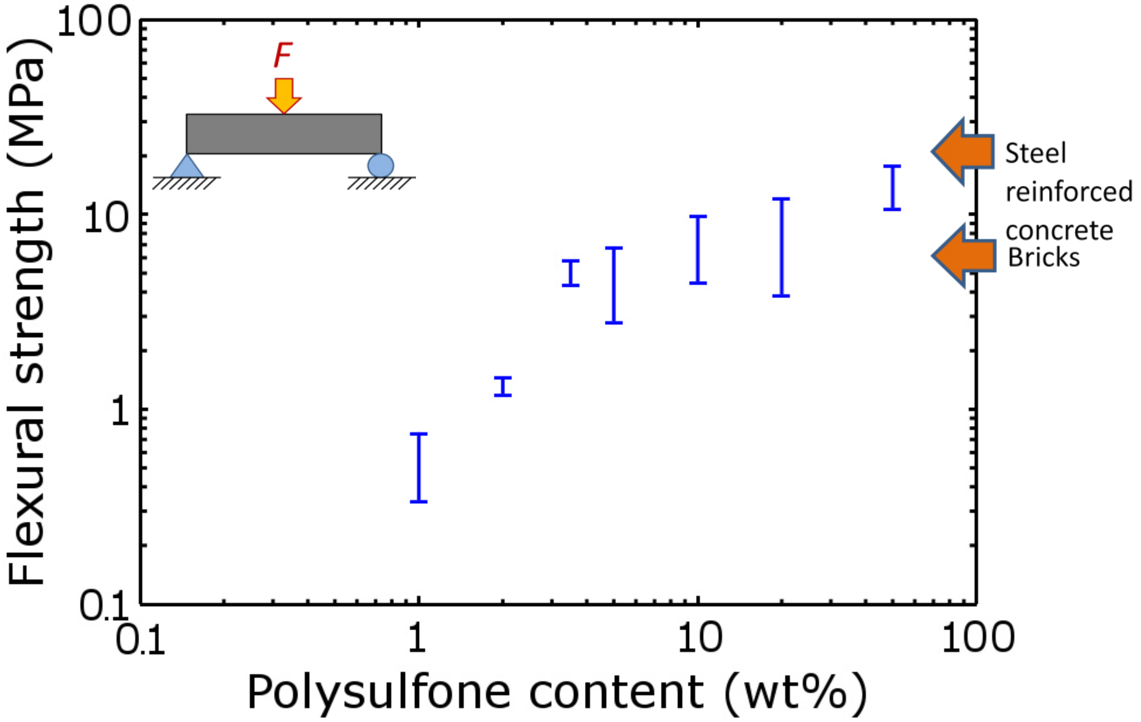

Figure 3-9 Flexural Strength of JSC-1A/PSU IOH. Plot of polysulfone IOH flexural strengths as a function of binder content, for random particle size distribution. Three-point bending schema shown at upper-left; reference materials shown at right.

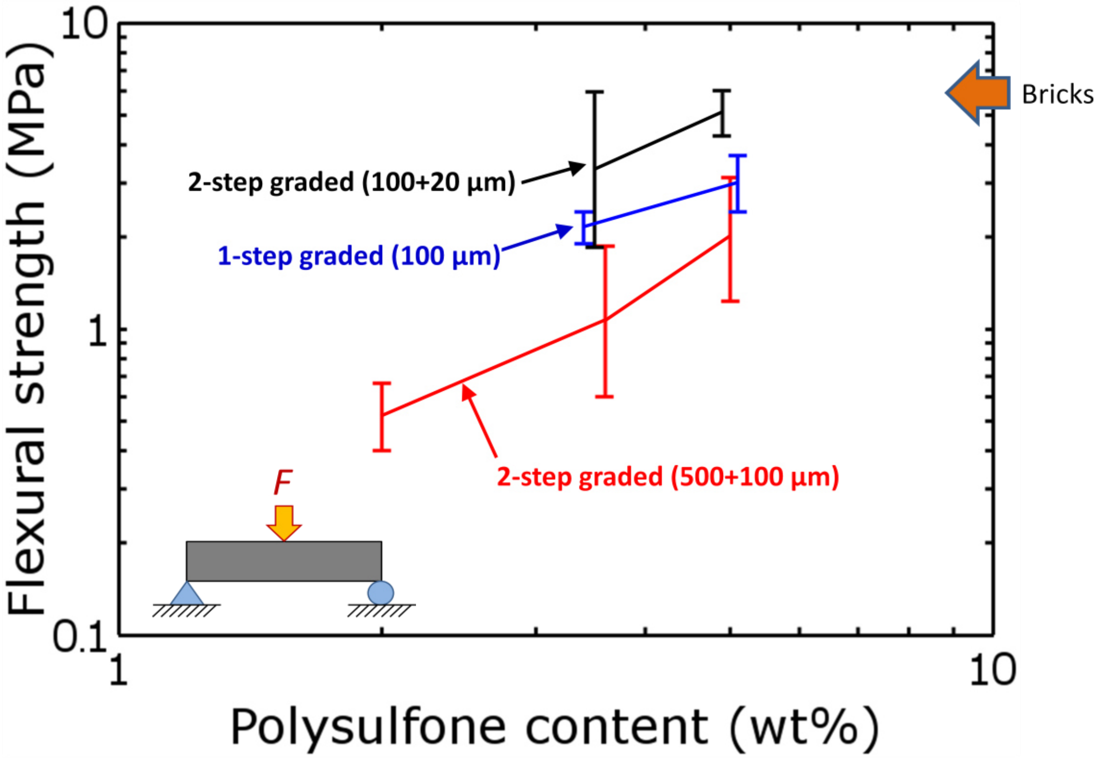

Figure 3-10 Flexural Strength of Graded JSC-1A/PSU IOH. Plot of polysulfone IOH flexural strengths as a function of binder content, for graded size distributions. Three-point bending schema shown at lower-left; reference materials shown at right.

3.3.3 Acids and Bases

The literature in archaeology and biology generally indicate that organic acids – in particular, oxalic, citric, and formic acids – may be capable of dissolving silica from certain minerals present in lunar minerals [10][11][12][13]. However, none of these organic acids can reach volatility as in the case of hydrochloric acid, thus precluding the ultimate possibility of a closed-loop process cycle. Hydrochloric (HCl) acid and sodium hydroxide (NaOH) are both common industrial solvents with low cost and were chosen as processing agents.

The etchants first used for this investigation included 20wt% sodium hydroxide and 20wt% hydrochloric acid, to represent base and acid, respectively. Hydrochloric acid very slightly attacks glass *via* cation interaction, whereas sodium hydroxide directly attacks silica. The HCl method was divided into two research approaches: one using hydrogen chloride vapor, and the other using the acid solution thereof.

Six grams of JSC-1A simulant remained the weighed sample size, as consistent with the organic solvent method using DMAc. The preliminary investigation added 6g of simulant into 10mL of NaOH, and six grams of simulant into 20mL HCl. A portion of the resulting mixture is added into acrylic load cells; the HCl sample was compressed by deadweight, while the NaOH was compressed via a hand-tightened C-clamp. Subsequent exposure to 120°C for 12h was performed with the intent to no damage the acrylic cells or their transparency.

For the HCl vapor processing, an acrylic tube was fitted with several pieces as shown in the photograph in Figure 3-11.

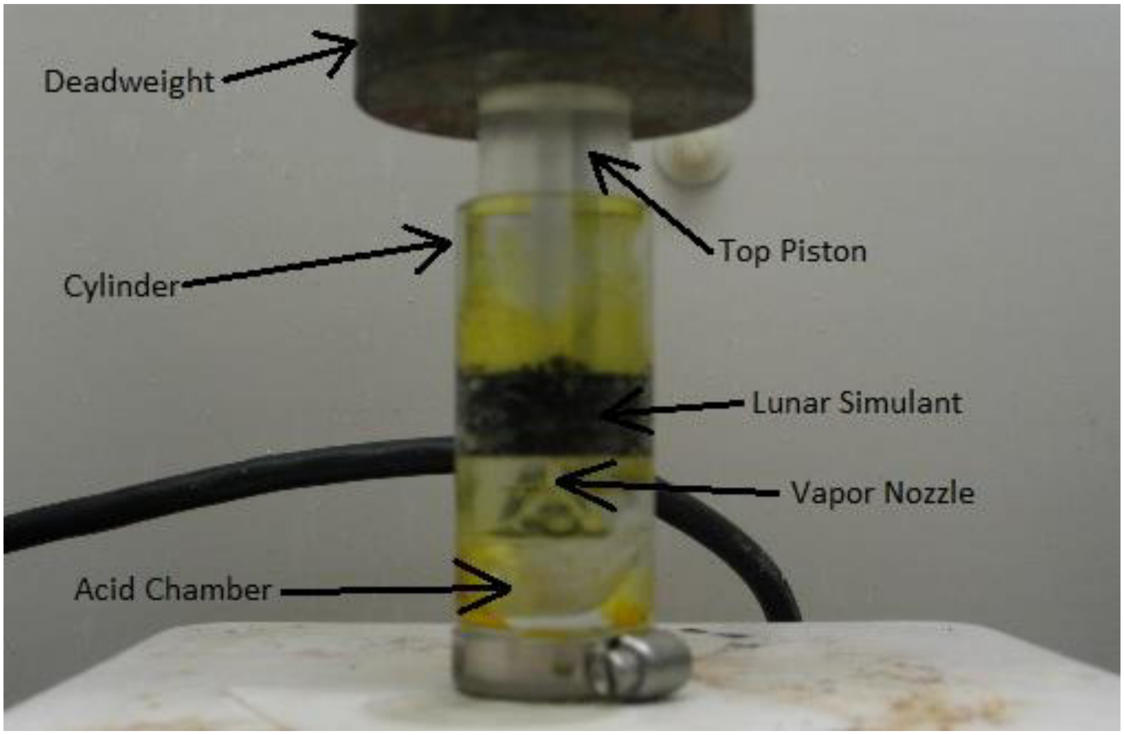

Figure 3-11 Acid Vapor Processing Apparatus.

As seen in Figure 3-11, the acid is pooled in a separate acrylic reservoir below the sample. The vapor intrudes through the central nozzle, and then is forced to migrate towards the outer circumference where chamfers are machined to facilitate escape of the gas.

Four samples were produced, with varying procedures due to the highly uncertain nature of the strengths:

- The first, numbered A1, was the HCl vapor-processed sample described on page 9 with the freshly extracted sample (after 12h) immersed in water to dissolve the water-soluble components. The sample then was dried in an oven at 200°C for 12h.
- The second sample, numbered A2, was a 5wt% HCl solution-processed sample which was confined and in a load cell using a C-clamp, with torsion applied during tightening.
- The third sample, a 10wt% HCl solution-processed sample, was loosely pressed with a deadweight in an oven set at 120°C for 12h, followed by a more thorough drying at 200°C for 12h.
- The fourth sample, a 5wt% NaOH solution-processed sample, was confined in a load cell with a C-clamp, with torsion applied during tightening.

Table 3-8 Splitting Tensile Strengths of JSC-1A Lye-Processed Silica Cylinders

Specimen	Lye Concentration (wt%)	Diameter (mm)	Height (mm)	Splitting Tensile Strength (MPa)
A5	5	19.04	16.41	4.08
A6	10	19.21	21.02	3.15
A7	10	19.14	15.84	6.93

At room temperature, the 20wt% hydrochloric acid mixture immediately develops a light yellow-green hue, and that after 12h, with only the presence of a ceramic spoon and the sample container (made from polypropylene), there is a gel-like consistency to the yellow-green solution although the particle grains settle on the bottom. The ceramic spoon sustained no damage upon removal from the solution.

The sample processed from NaOH produced a dry sample upon reheating for 12h at 200°C; the sample processed from HCl did not dry for 36h at 200°C. It is noticed for the latter that a hard component does develop in the sample, but it is still readily disintegrated upon rough contacts and especially upon exposure to water. The former, despite producing a dry sample, also disintegrated upon contact with water.

All samples showed negligible strengths (0.005MPa, 0.009MPa, 0.013MPa, and 0.106MPa, respectively) when tested with a cylinder splitting tensile test. The test choice reflects concern that the samples were not expected to survive into intact beam forms when sanding or cutting.

The weak strengths exhibited by samples A1 through A4 solicits the question of whether it is possible to work with silica from the NaOH or HCl systems first. A literature review indicates that sodium silicates are used for consolidation of silica materials, *viz.*, as a binder. Because basic lye (NaOH) can be used to produce sodium silicate by the action of sodium ions directly on the silica, we test pure samples of silica in the form of powdered quartz and determine strengths.

The quartz (Fluka Analytical) is of maximum mesh size of 230 (66μm). Two beakers are filled to 10mL of 5wt% and 10wt% NaOH, respectively. Ten grams of the quartz were then stirred in to each beaker, thickening the solution, and the mixtures were stirred for an additional 15min. These steps were performed at room temperature.

The slurry was transferred to load cells with deadweights placed on top of them, and dried at 170°C for 12h. Upon liberation from load cells, the cylindrical samples were further dried at 170°C for 12h. Due to solubility issues with wet cutting, split cylinder tests were carried out on these samples.

It has been observed qualitatively, through manual manipulation of the excess extrusions of the slurry, that the strength degrades quickly upon exposure to ambient room environments due to the presence of water vapor. However, it has also been noticed that the aqueous solution used to processed sample A4, when excess solution was decanted onto a glass plate and left to dry at room temperature, the resulting crystallized solid adhered strongly to the glass and a significant strength was attained such that small asperities could not be broken off with the action of fingers.

3.3.4 *in situ* Polymerization

Borrowing from the established niche industry of polymer-impregnated concretes, the goal of this study is to determine whether appreciable strengths can arise from *in situ* polymerization of the binding phase between lunar soil grains.

The binding phase was a methyl methacrylate (MMA) monomer liquid (Sigma-Aldrich), with the free radical initiator benzoyl peroxide (Sigma-Aldrich Luperox) constituting 2wt% of the solution. The particles were generally compressed to minimize voids, and the curing temperature was either 72h at 70°C or 36h at 80°C. A preliminary investigation has revealed that 2wt% and 4wt% *in situ* polymerization appears insufficient at producing a structurally intact specimen when the sample is C-clamped and not sealed via o-rings, as had been done for the solvent-aided processing of thermoplastics PES, PSU, PEI, and PEKK.

A 20wt% (nominal) composition was then tried, with the monomer and initiator prepared fresh, with a procedure adopted from the epoxy crush-mix-crush procedure. The MMA is highly volatile during all phases prior to curing, and a certain amount squeezed out during the first compression. Upon recombination, the sample was sealed with pistons containing butyl o-rings. A second set of samples was crushed only once, using the stock solution which was previously used for the preliminary investigation with the failed samples. Such a stock solution was inevitably enriched in the weight fraction of benzoyl peroxide because some of the MMA evaporated even when the container was sealed with a polyvinylidene chloride (PVDC) membrane.

A single aperture is enough for the MMA liquid to evaporate at 70°C. Samples 184, 187, and 188 were more representative of the composite strength due to the visibility of the binding phase upon cutting.

Table 3-9 Flexural Strengths of JSC-1A *in situ* Polymerized Samples

Sample	Binder	Binder (wt%)	TGA Binder (wt%)	Stress (MPa)	Width (mm)	Thickness (mm)	Length (mm)	Flexural Strength (MPa)
164	PMMA	<20	4.9	360 x2	4.38	3.05	13.02	23.97
165			-		6.48	4.68		17.89
166			-		6.43	3.17		22.67
167		20	-	360	7.01	3.46		41.42
168			-		7.94	2.94		33.86
169			-		8.19	3.43		45.00
173		10	7.92		7.16	3.47	15.22	39.99
174			-		7.14	3.20		35.28
175		15	9.88		5.98	3.57		46.13
176			-		6.22	3.52		42.95
177		10	7.79		6.85	3.61		42.71
178			-		6.83	3.16		47.87
179		15	-		6.82	2.96		34.77
180		4	-		11.08	6.74		0.68
181			-		10.11	8.64		2.24
182		6	-		10.33	6.93		3.31
185*		2	1.19		6.70	7.37		2.13
186*		6	1.22		8.05	2.14		2.48
187			2.56		4.69	4.17		26.59
188			5.17		4.26	3.78		28.88
189		4	2.24	180	7.84	4.25		7.25
190			2.94		7.84	3.62		6.22
191			2.32	270	7.54	3.9		8.56
192			-		7.61	3.76		6.15
193			-		7.71	4.09		4.78
194			2.42	360	7.2	4.33		12.35
195			2.59		7.17	3.48		13.41
196			2.79	270	7.33	4.01		5.56
197			2.67		7.30	3.61		4.61
198			3.29		7.76	5.29		4.80
199			3.48		11.92	2.97	12.51	5.71
200			2.96		12.32	2.81		7.23

Table 3-9 Flexural Strengths of JSC-1A *in situ* Polymerized Samples (continued)

214	PS	8	-	270	6.86	4.28	15.22	21.79
215			-		6.87	4.51		17.82
216			-		7.27	5.64		36.94
217			-		7.31	5.05		30.00
218	PMMA	4	-		7.27	5.22		8.55
219			-		7.23	5.53		10.00
220			-		7.20	5.56		8.90
221			-		7.18	5.15		8.60
222			-	360	12.49	3.36		3.12
223			-		12.47	3.36		3.24
226		6	-	270	7.11	4.25		26.84
227			-		7.26	4.06		32.81
228			-		7.24	3.72		30.99
229			-		7.26	4.14		28.25
230		8	-		7.36	3.75		37.28
231			-		7.36	3.71		38.54
232			-		7.22	3.94		27.50
233			-		7.24	3.76		34.13
234	PS	6	-		7.47	3.47		23.86
235			-		7.52	4.08		29.54
236			-		6.81	4.49		23.61
237			-		6.82	4.80		25.86
238	PMMA		-	360	12.64	3.86		20.24
239		4	-		7.27	4.48		23.00
240			-		7.29	4.23		20.30
241			-		7.07	4.19		20.23
242			-		7.18	4.35		22.35
243			-		8.54	5.15		25.60

*Samples 185 and 186 were not fully sealed because of o-ring defects.

3.4 Martian Simulant Processing

3.4.1 *in situ* Polymerization

The procedure from §3.3.4 used JSC-1A as the simulant. Here we shall use Mars-1a simulant; PMMA and PS are again the investigated binders. We note the choice of PMMA and PS are suitable in high-radiation environments as long as the inorganic phase acts as a shield to prevent ionization and polymer scission, which degrades mechanical properties. Being farther from the sun, the Mars experiences lower levels of ionizing radiation at the surface and the choice of these polymers is more justifiable on Mars than it is on the Moon. The lower temperatures encountered on Mars is especially beneficial in the case of PS, because its glass transition temperature is ~100°C.

In the first steps, we conduct a brief and independent verification of the elemental constituents of the soil simulant Mars-1a. Then, we proceed to the heat-melting procedure using the same procedure as that performed for JSC-1A *in situ* polymerization.

Table 3-10 Flexural Strengths of Mars-1a *in situ* Polymerized Samples

Sample	Binder	Binder (wt%)	TGA Binder (wt%)	Compression Pressure (MPa)	Width (mm)	Thickness (mm)	Length (mm)	Flexural Strength (MPa)
170	PMMA	10	1.87	360	7.99	3.64	15.22	19.84
171			-		8.02	3.26		16.34
172			-		8.03	2.44		16.71
184			3.10		7.61	3.56		25.25
203	PS		-	270	6.24	5.06		10.90
204			-		6.26	5.31		6.04
205			-		6.75	5.29		13.02
206			-		6.74	3.98		9.92
207			-		6.77	4.63		10.41
208			-		6.86	4.90		10.81
209			-		9.50	3.64	12.01	11.81
315	PMMA	4	-	360	9.27	4.48	15.22	6.01
316			-		9.19	5.12		7.01
317		6	-		9.49	4.72		7.02
318			-		9.39	5.17		5.91
319		8	-		8.7	5.44		8.96
320			-		8.48	4.86		8.78
321		10	-		8.62	5.01		9.07
322			-		8.63	4.52		9.19
357*		4	-	270	5.07	2.43		2.29
358*			-		4.34	4.50		2.60
359*			-		4.84	2.61		5.54
360*			-		4.50	2.91		4.19

*Sample was found to have imperfect sealing due to o-ring defect.

3.4.2 Melt-Compression

Volcanoes, such as the shield volcanoes found on Mars, can be a source of elemental sulfur. This mineral also occurs around igneous sources on Earth. A possible drawback involves the scarcity of elemental sulfur, but as discussed previously, the elemental forms can be isolated from sulfates or other sulfur-bearing compounds. We choose sulfur because it melts readily, and will not oxidize in a carbon dioxide atmosphere like that found on Mars.

Another potential salt of interest is the inorganic perchlorate salt, which has been detected in Martian soils [14]. We choose sodium perchlorate (NaPC). If this salt can be isolated and concentrated, one can assess it as a binder for structural applications through melt compression.

We begin our investigation by conducting a melt compression on sulfur and NaPC in varying concentrations with respect to the simulant Mars-1a. SEM micrographs are taken of select fracture areas for both sodium perchlorate salt and sulfur hybrids in Chapter 6.

Sulfur was added to the Martian soil simulant in prescribed amounts and mixed in a container. When the visible heterogeneity was no longer visible, the mixture was added into an aluminum load cell of bore diameter 19.05mm and the exterior of the aluminum on one side was heated *via* contact with an electrical resistance heater to 150ºC for 15min. The modal weight of the sample was 5g. After the 15min elapsed the heating band was turned off and the load cell rapidly repositioned below a mechanical compressor. The compression means in this investigation commenced with a hydraulic press with a pressure of 270MPa. Once the peak pressure was reached the load was maintained for 12h as the sample was allowed to cool. The load after 12h was 49kN from the original 80kN peak value corresponding to 270MPa.

The cutting procedure was essentially identical to the IOH samples. The results are given in Table 3-11. Between 201 and 202 the difference in flexural strengths is due to the varying degree of decay in the original binding magnitude due to water absorption during the cutting process, as the left side of the disk was exposed to aqueous cutting fluid well before the right side. These are the specimens 201 and 202, respectively.

A likewise procedure is developed for NaPC. The soak temperature for this salt, all else being normal, is 160°C.

Samples 288-307 were tested with an additional stirring procedure while heating the dry powder (inorganic and binder species) inside of the steel dye. Samples 288-298 are shaded due to inadvertent exposure to ambient air for 48h before a flexural test, as sodium perchlorate is hygroscopic and the hybrid cement would decrease in strength as atmospheric moisture is progressively absorbed into the samples.

Table 3-11 Flexural Strengths of Mars-1a Compacted with Sulfur and NaPC

Sample	Binder	Binder Content (wt%)	Compression Pressure (MPa)	Width (mm)	Thickness (mm)	Flexural Strength (MPa)
210	Sulfur	10	270	9.35	4.97	2.78
211				9.33	5.59	4.04
212		8	500	8.77	3.09	6.50
213				10.33	2.54	5.05
224		20	270	8.12	5.05	18.64
225				8.07	5.32	10.61
244		30		7.76	4.07	14.21
245				6.45	4.23	15.43
246		40		6.77	3.63	14.84
247				6.84	4.00	17.73
266		10	360	7.96	4.53	12.21
267				7.94	4.10	10.60
268		20		4.58	2.18	15.70
269				4.02	2.22	9.22
270				4.17	2.41	11.31
271				4.62	1.94	13.13
272				4.04	2.25	13.39
273		30		7.47	4.90	23.80
274				7.52	5.06	23.24
275		40		5.75	3.90	18.79
276				5.82	4.20	26.91
282	NaPC	6	270	8.97	4.89	6.17
283				8.96	3.93	5.44
284		8		7.68	4.02	6.62
285		10		7.21	4.36	11.83
286		15		4.38	3.70	11.80
287				5.42	3.27	9.45
288		6		5.97	5.66	0.36
289				5.33	4.42	0.88
290		8		6.28	5.04	1.00
291		10		9.20	5.53	1.14
292				9.25	4.96	1.20
293		15		5.79	5.76	1.43
294				5.79	4.72	2.12
295		30		8.93	4.43	5.86
296				9.00	4.47	6.09
297		40		8.29	4.69	9.39
298				8.27	5.32	11.02

Table 3-11 Flexural Strengths of Mars-1a Compacted with Sulfur and NaPC (continued)

299	NaPC	6	270	9.30	4.69	3.31
301				9.30	4.62	1.73
302		10		9.33	4.35	4.14
303				9.35	4.71	4.29
304		20		8.49	4.90	4.48
305				8.38	4.56	2.62
306		40		8.21	4.67	10.58
307				8.19	4.52	11.19

Length between beam supports was 15.22mm.
Shaded rows (Samples 288-298) were exposed to ambient air for 48h.

Adopting the heating band used from the sulfur-melt processing of the lunar and Martian IOH samples, a new focus has been to melt polymer powder that has been mixed with the soil grains beforehand. Heating was approximately 20°C per minute to a maximum which is approximately 30°C higher than the melting point of the binding phase at the load cell cylindrical boundary. Listed, these temperatures are:

- Ethylene Vinyl Acetate (EVA): 100°C (T_m = *70°C*)
- Polyvinyl Chloride (PVC): 200°C (T_m = *175°C*)
- Polymethylmethacrylate thermoset (TS-PMMA): 200°C (T_m = *170°C for TP-PMMA*)

Maximum temperature was kept for 15min if the thermocouple was placed directly on the powders for controlled measurements, or 30min (soak) if the sample was capped prior to heating for concerns of gas evolution in certain polymers.

The sample was left to cool for another 30min, and cut into beam sections. Table 3-12 shows the results of the flexural strengths in these specimens, and they are also plotted in Figure 3-12 and 3-13.

Table 3-12 Flexural Strengths of Mars-1a Polymer-Melt IOH

Sample	Binder	Binder Content (wt%)	Temp. (°C)	Stress (MPa)	Width (mm)	Thickness (mm)	Flexural Strength (MPa)
248	EVA	10	100	270	10.25	4.49	8.40
249					10.10	3.84	6.44
250	PVC		200		8.77	4.43	17.24
251					8.94	4.88	15.23
252		6			9.01	5.17	9.76
253					8.99	5.65	9.55
254		8			8.70	5.63	8.86
255					8.82	5.01	8.77
256		15			8.60	5.35	9.83
257					8.64	4.74	10.35
258		6		360	9.05	5.21	6.78
259					9.09	4.63	7.03
260		8			9.18	4.91	4.75
261					9.15	4.61	5.99
262		10			8.84	5.06	21.89
263					8.79	4.92	20.49
264		15			9.64	4.78	8.50
265					9.45	4.34	7.82
277	TS-PMMA	8		270	7.74	5.23	15.31
278					8.65	3.83	13.61
279		10			4.36	2.16	10.10
280					4.35	2.80	8.70
281		15			6.45	3.92	14.51
282		75			4.54	4.96	5.58
283					4.47	4.91	5.78
284		50			5.46	4.55	11.62
285					5.22	4.56	8.48
286		25			5.71	4.24	0.85
287					5.11	4.23	3.27
313	PVC	4			9.71	5.03	3.35
314					9.72	4.55	3.52
323				360	9.91	5.97	0.90
324					9.88	5.34	1.05
325		6			8.83	5.40	11.88
326					8.79	4.92	12.55
327		10			8.69	5.25	21.35
328					8.58	4.68	21.99
329		15			8.58	4.63	14.77

Table 3-12 Flexural Strengths of Mars-1a Polymer-Melt IOH (continued)

330	PVC	15	200	360	8.64	5.00	17.22
331		4			9.25	4.00	7.56
332					9.23	5.34	7.20
333		6			9.22	5.02	6.91
334					9.23	5.07	8.63
335		8			9.62	4.50	6.13
336					9.66	5.91	7.36
337		10			9.94	4.95	7.59
338					9.86	4.95	7.09
339		15			9.78	4.54	8.37
340					9.68	5.30	8.23
341		4	225		9.25	4.47	7.41
342					9.27	5.69	8.75
343			250		7.76	4.83	5.55
344					7.71	4.96	5.42
345			275		9.52	5.16	5.49
346					9.47	4.66	4.33
347			300		9.22	5.11	4.08
348					9.21	4.65	4.36
349			225		9.68	4.25	6.01
350					9.68	4.21	6.52
351		2			9.65	4.81	5.11
352					9.66	4.91	3.33
353		0			9.72	4.86	7.66
354					9.66	4.54	9.17
355		15			10.18	5.19	5.25
356					10.14	4.84	6.63
361	PMMA*	4			9.87	4.64	7.63
362					10.01	5.35	6.85
363		8			10.19	4.44	5.82
364					10.19	4.92	6.66
365		15			10.92	4.46	3.26
366					10.8	5.27	4.72

Shaded rows denote samples which were compressed first as dry powder, then heated in a quartz tube furnace instead of the heating band.

Length between beam supports was 15.22mm.

*These are coarse (600-micron) PMMA particles.

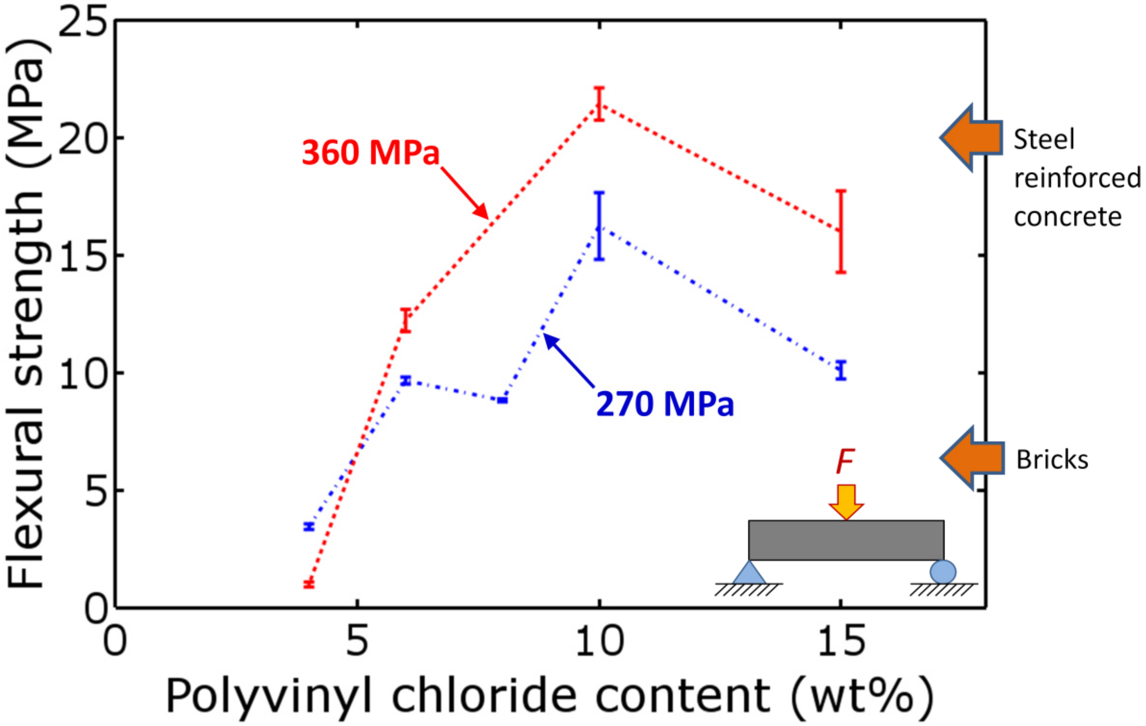

Figure 3-12 Flexural Strength of Mars-1a/PVC IOH. Flexural strength of JSC Mars-1a as a function of PVC weight fraction for heating and compression to two different pressures. Three-point bending schema shown at lower-right; reference materials shown at right.

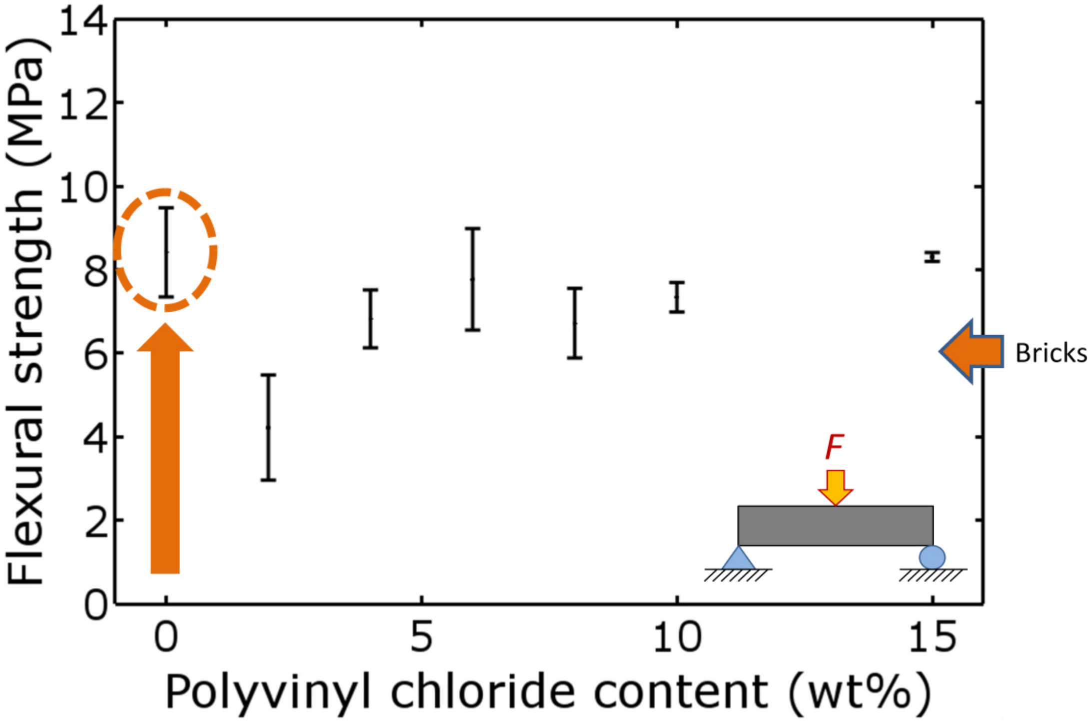

Figure 3-13 Flexural Strength of Cured Mars-1a/PVC IOH. Flexural strength of JSC Mars-1a as a function of PVC weight fraction for initial dry compression followed by heating in a protection environment. A significant result is indicated by the dashed circle at null binder content. Three-point bending schema shown at lower-right; reference materials shown at right.

The results from the melt-compression shows that, in the complete absence of binder, Mars-1a is intrinsically capable of forming a strong, compacted solid. The result is somewhat unexpected because small amounts of binder content above zero tend to decrease the flexural strength, and keeping in mind the experiential observations with JSC-1A, flexural strengths should rapidly tend toward zero as the binder content is eliminated.

However, as pointed out in Figure 3-13, a very significant and non-trivial flexural strength shows up in Mars-1a compressed without any binder. The strength is comparable with those made with relatively large fractions of PVC binder. It therefore is feasible to eliminate binders altogether from the process. This opens a new door to direct compaction-forming of strong parts made of Mars-1a simulant, which shall be the focus of Chapter 4.

3.5 References

1. Pinheiro, A. S., da Costa, Z. M., Bell, M. J. V., Anjos, V., Reis, S. T., Ray, C. S. “Thermal characterization of glasses prepared from simulated compositions of lunar soil JSC-1A,” *J. Non-Crystalline Solids* **359**, 56-59 (2013).

2. Allen, C. C., Jager, K. M., Morris, R. V., Lindstrom, D. J., Lindstrom, M. M., Lockwood, J. P. “Martian Soil Simulant Available for Scientific, Educational Study,” *Eos* **79**, *34*, 405-412 (1998).

3. Morris, R. V., Klingelhofer, G. "Iron mineralogy and aqueous alteration on Mars from the MER Mossbauer spectrometers," in *The Martian Surface: Composition, Mineralogy, and Physical Properties (Bell III. J. F., ed.)*, Cambridge University Press (2008), pp. 339-365.

4. Schwertmann, U. "Iron Oxides," in *Encyclopedia of Soil Science (Chesworth, W., ed.)*, Springer (2008), pp. 363-369.

5. Arvidson, R. E., Squyres, S. W., Bell III, J. F., Catalano, J. G., Clark, B. C., Crumpler, L. S., de Souza Jr., P. A., Fairén, A. G., Farrand, W. H., Fox, V. K., Gellert, R., Ghosh, A., Golombek, M. P., Grotzinger, J. P., Guinness, E. A., Kerkenhoff, K. E., Jolliff, B. L., Knoll, A. H., Li, R., McLennan, S. M., Ming, D. W., Mittlefehldt, D. W., Moore, J. M., Morris, R. V., Murchie, S. L., Parker, T. J., Paulsen, G., Rice, J. W., Ruff, S. W., Smith, M. D., Wolff, M. J. “Ancient Aqueous Environments at Endeavor Crater, Mars,” *Science* **343** (2014).

6. Williams, R. M. E., Grotzinger, J. P., Dietrich, W. E., Gupta, S., Sumner, D. Y., Wiens, R. C., Mangold, N., Malin, M. C., Edgett, K. S., Maurice, S., Forni, O., Gasnault, O., Ollila, A., Newsom, H. E., Dromart, G., Palucis, M. C., Yingst, R. A., Anderson, R. B., Herkenhoff, K. E., Le Mouelic, S., Goetz, W., Madsen, M. B., Koefoed, A., Jensen, J. K., Bridges, J. C., Schwenzer, S. P., Lewis, K. W., Stack, K. M., Rubin, D., Kah, L. C., Bell III, J. F., Farmer, J. C., Sullivan, R., Van Beek, T., Blaney, D. L., Pariser, O., Deen, R. G., MSL Science Team, “Martian Fluvial Conglomerates at Gale Crater,” *Science* **340**, 1068-1072 (2013).

7. Moore, H. J., Jakosky, B. M. “Viking Landing Sites, Remote-Sensing Observations, and Physical Properties of Martian Surface Minerals,” *Icarus* **81**, 164-184 (1989).

8. Perko, H. A., Nelson, J. D., Green, J. R. “Mars Soil Mechanical Properties and Suitability of Mars Soil Simulants,” *J. Aero. Eng.* **19**, *3* (2006).

9. Chen, T., Chow, B. J., Qiao, Y. "Two-stepped size gradation of particle size in an organic-inorganic hybrid," *Sci. Eng. Compos. Mater.* **22**, 643-637 (2015).

10. Henderson, M. E. K., Duff, R. B. "The Release of Metallic and Silicate Ions from Minerals, Rocks, and Soils by Fungal Activity," *J. Soil Sci.* **14**, *2*, 236-246 (1963).

11. Eick, M. J., Grossl, P. R., Golden, D. C., Sparks, D. L., Ming, D. W. "Dissolution kinetics of a lunar glass simulant at 25°C: The effect of pH and organic acids," *Geochimica et Cosmochimica Acta* **60**, *1*, 157-170 (1996).

12. Davidovits, J., Al Iaga, F. "Fabrication of Stone Objects, by Geopolymeric Synthesis, in the Pre-Incan Huanka Civilisation (Peru)," in *21st International Symposium for Archaeometry*, Brookhaven National Laboratory, New York (1981), p.21.

13. Davidovits, J., Bonett, A., Mariotte, A. M. "The Disaggregation of Stone Materials with Organic Acids from Plant Extracts, an Ancient and Universal Technique," in *Proceedings of the 22nd Symposium on Archaeometry*, University of Bradford, Bradford, UK (1982), pp.205-212.

14. Leshin, L. A., Mahaffy, P. R., Webster, C. R., Cabane, M., Coll, P., Conrad, P. G., Archer Jr., P. D., Atreya, S. K., Brunner, A. E., Buch, A., Eigenbrode, J. L., Flesch, G. J., Franz, H. B., Freissinet, C., Glavin, D. P., McAdam, A. C., Miller, K. E., Ming, D. W., Morris, R. V., Navarro-González, R., Niles, P. B., Owen, T., Pepin, R. O., Squyres, S., Steele, A., Stern, J. C., Summons, R. E., Sumner, D. Y., Sutter, B., Szopa, C., Teinturier, S., Trainer, M. G., Wray, J. J., Grotzinger, J. P., MSL Science Team, "Volatile, Isotope, and Organic Analysis of Martian Fines with the Mars Curiosity Rover," *Science* **341** (2013).

4 Compaction Mars-1a Simulant without Binders

4.1 Motivation from Previous Work

The Martian soil simulant JSC Mars-1a was found to have cohesive properties at room temperature and pressure. The result obtained from Chapter 3 on Mars-1a with polymeric binders has found that at 0wt% polymer, the flexural strength of the compact was a very nontrivial ~8MPa. Originally, the zero datum was investigated for the purpose of a sanity check for the 'kink' observed in the trend. Namely, for intermediate binder content (~2-4wt%), the strength was low, but at zero binder content, the strength appeared to increase once again. One would then investigate whether the PVC binder played an interfering role with flexural strength at the intermediate concentrations, presumably from a sparse dispersion isolating particles from contact adhesive forces while at the same time not forming an internally coherent network of its own. When all binder was removed, the sample regained strength, showing that low concentrations of PVC binder—perhaps more generally, any melt-viscous binder—interfered with strength.

Thus, instead of attempting to minimize the binder content, we now ask how strong a material can be formed without binder. Indeed, compaction without binders is routinely used in industry, as noted by the sources from the literature review.

The next two chapters, starting with this one, concern the compression of soil simulants directly into structural materials. No binder is used. First we begin with a literature review compressed soil materials. Then, we describe the small-scale structure of montmorillonite clay, an important simulants. The description is relevant later for formulating a simple model upon observed results. We then investigate flexural strength performance of compacts uniaxially compressed from Martian soil simulants. Simulants were primarily Mars-1a and montmorillonite; other simulants were occasionally explored. The importance of Mars-1a and montmorillonite is due to their sedimentary abundance on Mars: the entire surface of the planet is covered with red dust [1]. Clay has also been detected in substantial amounts, including the smectite mineral montmorillonite [2][3]. All experiments used a steel die, representing a rigid lateral boundary (die wall).

4.2 Research Hypothesis and Objectives

The bonding capabilities in Mars-1a are unlike those experienced for the lunar simulant JSC-1A which has larger particles and did not develop intactness after compression; such samples crumbling when handled manually. On the other hand, JSC Mars-1a has a different particle size distribution and chemical makeup such that it is possible to compress an intact solid out of apparently dry powder. It is first hypothesized that atmospheric moisture facilitates the bonding process.

An alternate hypothesis for strength is also possible. For this discussion, we must distinguish between the two phases in Mars-1a. Note that when referring to a 'phase' in the context of discussing Mars-1a, we broadly invoke two families of substances and not an ordered microstructure. The first is a basaltic mineral phase, which is thought to be inactive towards binding of the simulant. These minerals can be pyroxenes, olivine, or a number of other minerals common to basalt rock [4], or the amorphous glasses thereof [5]. The second is the npOx phase, which is present on the surfaces of the Mars-1a particles and is thought to be responsible for strength under compression and shear.

The reason why the npOx phase is thought as being responsible for the binding of Mars-1a is due to its fine-particle character. This results in a high specific surface, promoting surface forces in the form of secondary bonding, or electrostatic interactions such as the well-known Van der Waals forces [6]. The basalt particles are expected to contribute a minor portion of the strength through mechanical interlocking [6].

Given that the npOx minerals may resemble the modulus of silicate materials in bulk, we expect the samples to harden upon compression until they behave as a linear-elastic material. The modulus of elasticity is expected to be comparable to the silicate materials which comprise the bulk of the specimen, approximately 40-80GPa.

Changing the lateral boundary condition of loading should influence the flexural strength of the compact. In particular, the presence allowing lateral motion entails greater probability of a particle increasing its coordination number and falling into a lower system free energy configuration. Translational, rotational, and shearing motions of particles are all expected to increase when the lateral boundary condition to account for the optimization of particle configuration. In addition to particle motion, extensive particle crushing is expected to occurs, as the bulk strength of basalt is much less than the peak compression pressure, assuming an isostress model [7].

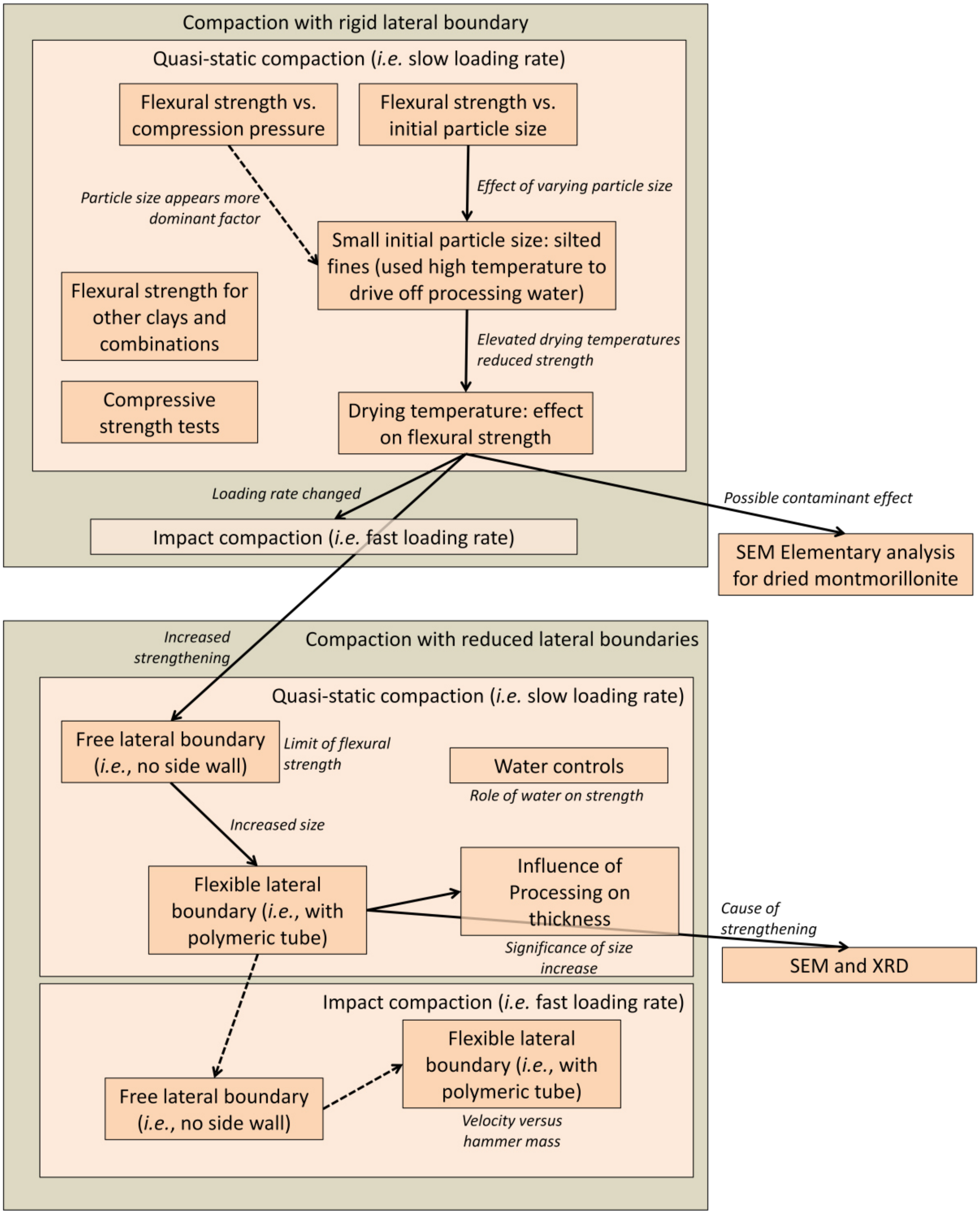

Figure 4-1 Direct Compaction of Mars-1a: Research Path.

4.3 Compaction with Rigid Lateral Boundary Condition

4.3.1 Quasi-Static Compaction

The procedure for quasi-static compaction is similar to that used in Chapter 3 involving polymeric binders. As-received Mars-1a simulant was pre-dried in a drying oven at 105°C for 24h. This pre-drying step is necessary to prevent particles from coalescing during sieving.

Sieving was performed with a mechanical sieve (W.S. Tyler Rotap RX-29) running at 350W for 30min. The sieve stack contained mesh sizes of 90µm, 53µm, 45µm, 25µm, and 20µm above the pan.

Particles were heated to a prescribed temperature using a quartz tube furnace (Carbolite CTF 12/75/700), determined by the TGA analyses in Chapter 6. This was done to rid the simulant of possible contaminants and to dry them to water contents comparable with water contents measured in actual Martian soil. The simulant is then added inside of a cylindrical steel die of outer diameter 38.1mm and inner bore diameter 19.05mm, and a bottom cylindrical steel piston. The top piston then caps the simulant, completing the die assembly. Both pistons were identical and squared at the ends. Dies generally exhibited hardness of R_c 55, and pistons R_c 60.

The die assembly was inserted between platens of a uniaxial load-displacement test machine (Instron 5582) and compressed to a prescribed pressure at a quasi-static rate of 6mm/min. An arbor press subsequently liberated the compacted simulant, in the shape of a disc, from the die assembly. Compacts were cut using a 0.4mm-wide abrasive wheel mounted on a rotary cutoff saw (MTI SYJ-40-LD). Two parallel cuts defined a beam; a single disc produced up to two test beams. Final reduction was performed with 26μm and 13μm sandpaper. The 13μm abrasive introduced a light chamfer in each lengthwise edge of the beams, as a countermeasure against edge defects. The beams were tested in 3-point bending, and flexural strength was calculated according to

$$R = \frac{3PL}{2bd^2}$$

where P is the midspan point load at failure, L the length between the fixture supports, b the width of the beam, and d the depth (or thickness) of the beam.

Figure 4-2 and 4-3 show schematics of the compression and test procedure. Figure 4-4 is a picture of a simulant pile, the Rotap sieve, and the Instron machine. A typical beam made of compacted Mars-1a is shown in Figure 4-5.

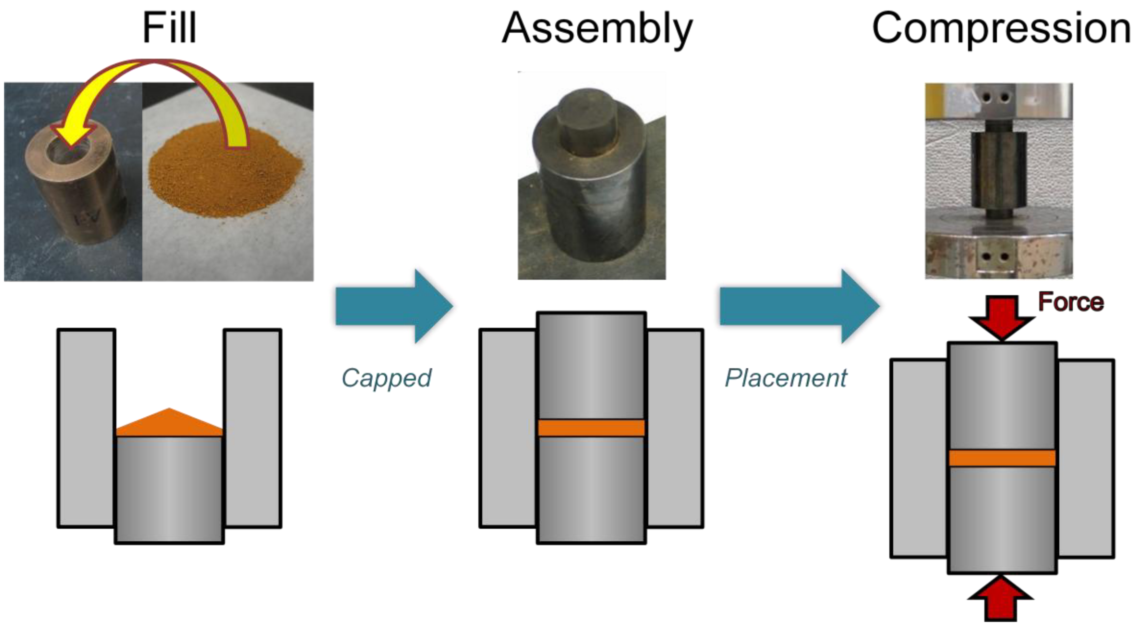

Figure 4-2 Mars-1a Rigid Lateral Boundary Compaction. Schematic of the compaction procedure.

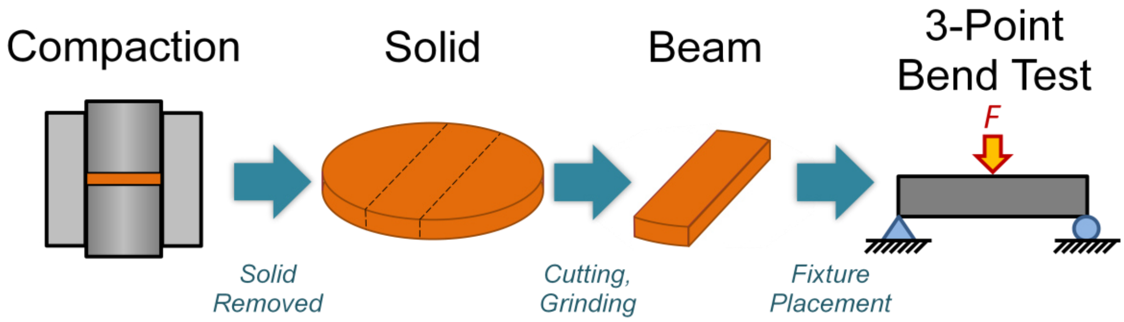

Figure 4-3 Mars-1a Shaping and Testing. Schematic of the compression, shaping, and testing processes.

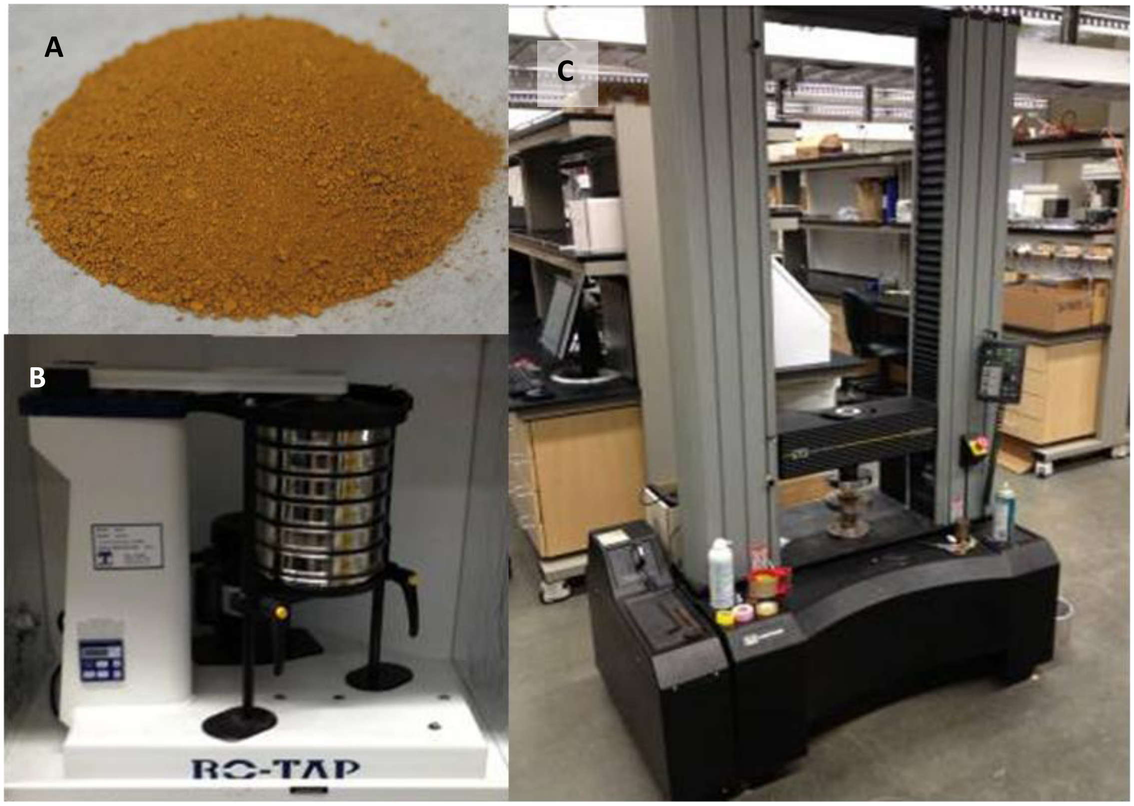

Figure 4-4 Photos of Mars-1a, Rotap, and Instron. A 5cm-wide pile of Mars-1a simulant (A), the Rotap sieve; machine base is 60cm wide, and the Instron 5582 uniaxial load-displacement machine (C).

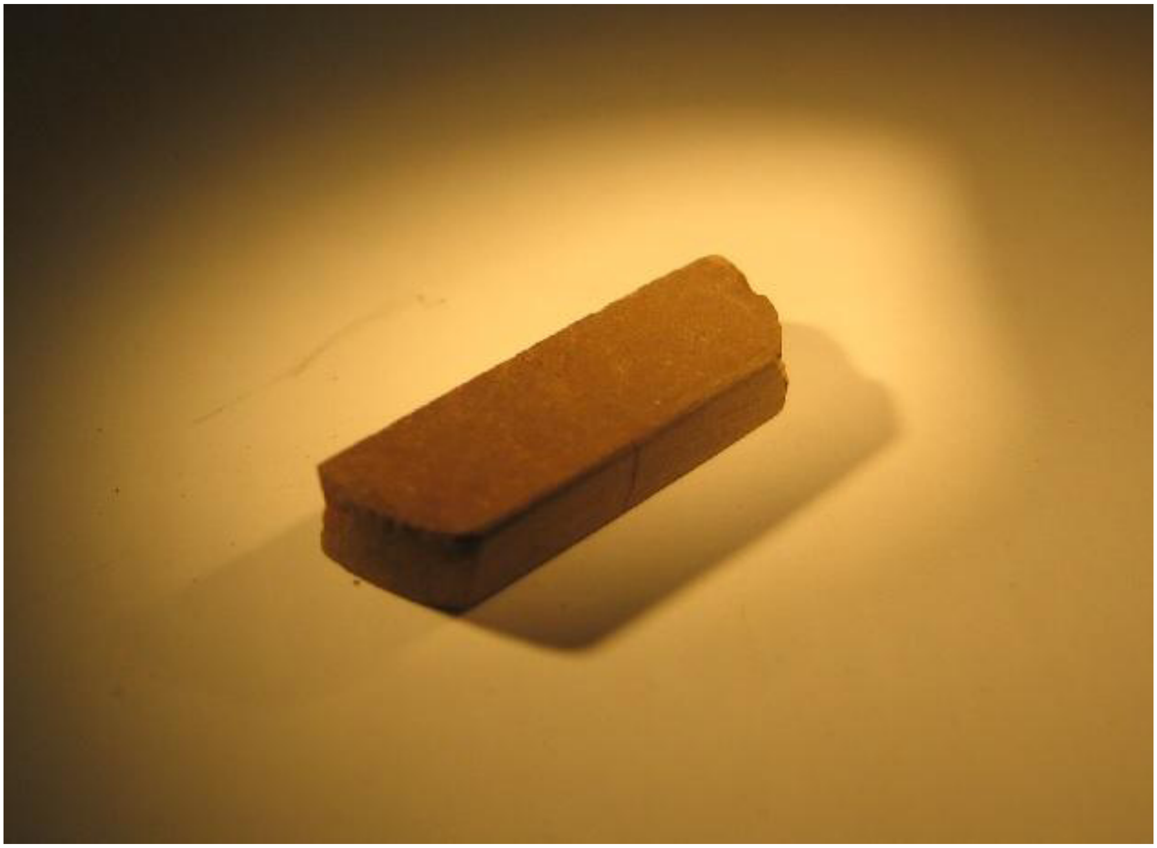

Figure 4-5 Photo of Mars-1a Beam. A photograph of a beam test coupon (Sample 661), produced under quasi-static compaction. The beam is ~2cm long; the curved edges follow the shape of the die.

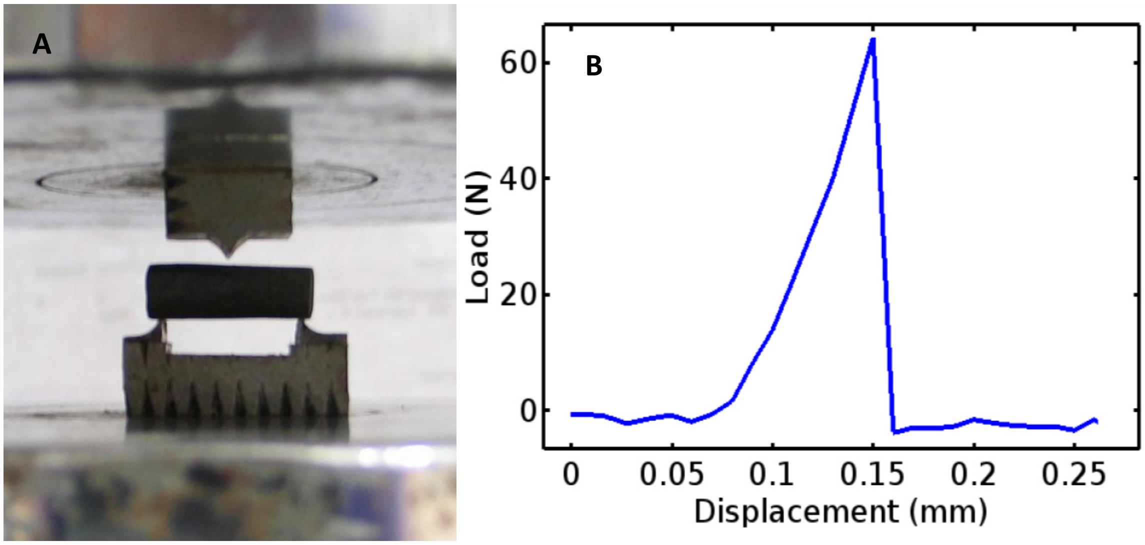

Figure 4-6 Beam Testing. A picture of the 3-point bending test using a test fixture (A); the gap between fixture bottom supports is 15.22mm. Right side is a typical load-displacement trace of 3-point bend test represented by Sample 661 (B).

A

4.3.1.1 Flexural Strength as a Function of Drying Temperature

This procedure is based from the polymer melt procedure in Chapter 3, which included the finding of the first intact 0wt% PVC Mars-1a (Samples 353 and 354 in Table 3-12). Originally, PVC particles were mixed inside a crucible with Mars-1a and stirred manually before quasi-static compression. The post-compressed mixture, still inside the steel die assembly, was heated inside the Lindberg-Blue quartz tube furnace with a protective environment consisting of either N_2 or CO_2, to a temperature of 225°C for 30min, before air cooling in the said inert environment.

The post-compression heating step—which we refer to as "curing"—procedurally continued for Martian soil simulant without any PVC binder particles. The initial investigation (post-353/354) focused on whether water was responsible for any portion of the strength in raw Mars-1a.

As-supplied simulant (*i.e.*, random particle size) was dried at 80°C, 110°C, or 350°C prior to compression. Post-compression curing was held at 225°C. Table 4-1 records samples made using alternate experimental procedures. Figure 4-7 shows three curves corresponding to the three temperatures, and Figure 4-8 shows the full abscissa of pressures for the samples made from particles dried at 350°C before compression.

Table 4-1 Flexural Strengths of Compacted Mars-1a with Several Variables

Sample	Compression Pressure (MPa)	Drying Temperature (°C)	Curing Temperature (°C)	Width (mm)	Depth (mm)	Length (mm)	Flexural Strength (MPa)
367	360	80	25	9.53	5.27	15.22	2.59
368				9.56	4.79		2.60
369				9.32	5.05		4.32
370				9.28	4.46		3.96
371	270			9.75	5.97		4.40
372				9.74	4.74		3.34
373				9.61	5.56		4.38
374				9.61	4.65		3.63
375 *	360	110	225	10.01	4.93		4.13
376 *			25	10.56	4.70		2.84
377 *				10.49	4.32		2.92
378 *				10.60	5.27		2.09
379 *				10.58	4.56		1.56
380		80	225	8.61	5.01		7.71
381				8.54	4.36		6.19
382				9.33	5.16		6.98
383				9.35	5.08		7.00
384				9.02	5.56		7.20
385				9.02	4.66		7.46
386				9.41	5.27		6.23
387				9.40	4.96		6.41
392 [1]				8.86	4.51		3.42
393 [1]				8.87	5.23		5.08
394 [2]				9.32	4.91		6.10
395 [2]				9.32	5.20		6.07
400	90			11.93	4.87		0.81
401				11.99	4.87		0.88
402	180			10.65	5.18		2.48
403				10.61	4.99		2.59
404	270			10.15	5.49		3.81
405				10.17	4.97		4.00
406	360			9.84	5.10		5.00
407				9.86	4.98		5.04
408 **	90	110		12.72	5.48		1.20
409 **				12.67	4.55		1.04
410 **	180			6.22	5.48		3.42
411 **				5.61	4.57		2.53
412 **	270			4.64	5.55		6.40
413 **				5.05	4.61		4.25
414 **				10.82	4.59		3.71
415 **	360			10.38	1.90		8.89
416 **				10.37	4.03		7.18
417	90	350		12.44	5.27		1.78
418				12.41	5.05		1.66
419	180			5.40	5.23		4.48

Table 4-1 Flexural Strengths of Compacted Mars-1a with Several Variables (continued)

420	180	350	225	11.13	4.53	15.22	3.30
421	270			10.81	4.93		4.95
422				10.81	4.22		6.64
423	360			4.00	4.32		7.65
424				7.59	5.15		6.92
441				8.23	4.71		4.25
442				7.81	4.86		3.59
449				4.96	4.10	9.78	12.49
450	450			5.28	4.26		12.71
451	540			6.39	4.07		14.55
452	360			4.13	4.36		8.90
453				3.97	2.93	15.22	9.38
454				5.19	3.21		9.82
457				3.94	3.97	9.78	10.16
458				8.75	4.20	15.22	8.43
461				4.39	1.90	9.78	10.18
462	450			4.92	2.00		14.16
463	540			4.89	1.92		10.57
464	630			5.46	3.80		8.93
465				4.90	3.96		11.84
466				5.40	3.93		9.50
467	720			4.93	3.82		11.62
469				5.32	3.84		10.66
470	360			4.25	4.20		13.70
471	450			5.36	4.12		10.16
472	540			3.78	3.98		12.01
473 [3]	360			4.21	4.30		5.28
474 [3]				4.85	4.19		8.96
475 [3]				4.74	3.68		8.68

Particle size is random.

*Samples were vacuum-dried overnight.

**Samples were vacuum-dried for 6h.

[1] Samples contained 14.3wt% water content during compression.

[2] Samples contained 9.1wt% water content during compression.

[3] Samples were compressed twice, with manual comminution in between.

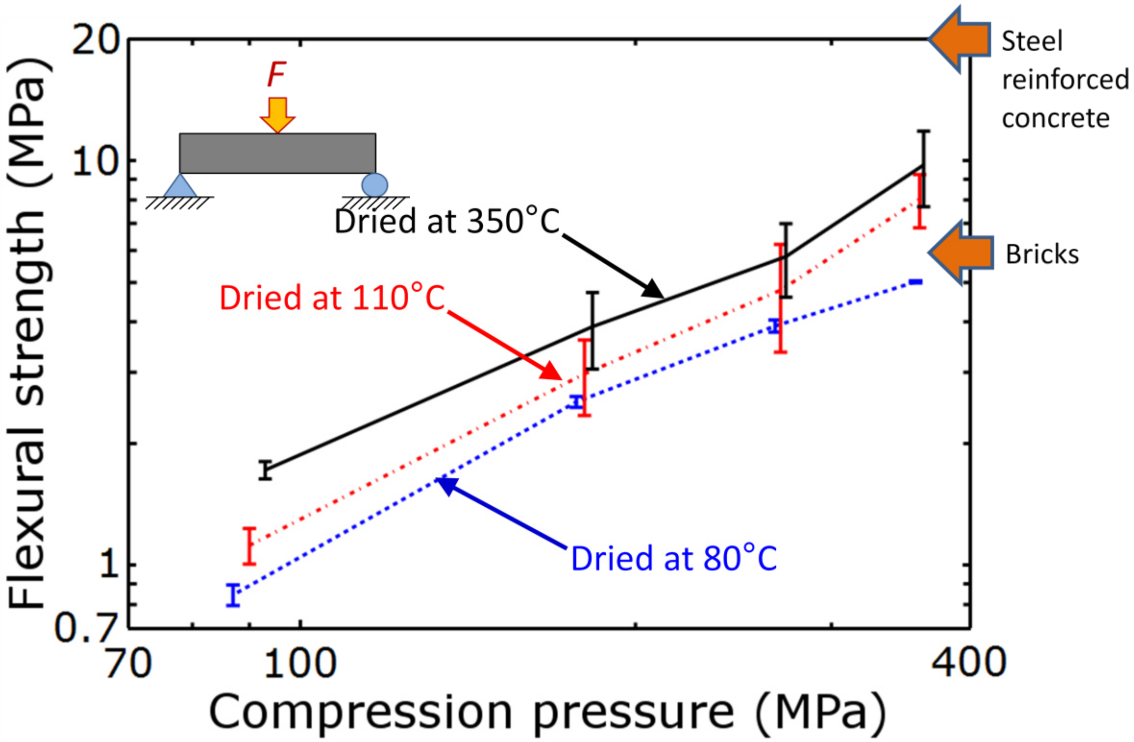

Figure 4-7 Mars-1a Flexural Strength *vs.* Compression. Flexural strengths for differently dried Mars-1a as a function of applied pressure. Error bars represent one standard deviation. Three-point bending schema shown at upper-left; reference materials shown at right.

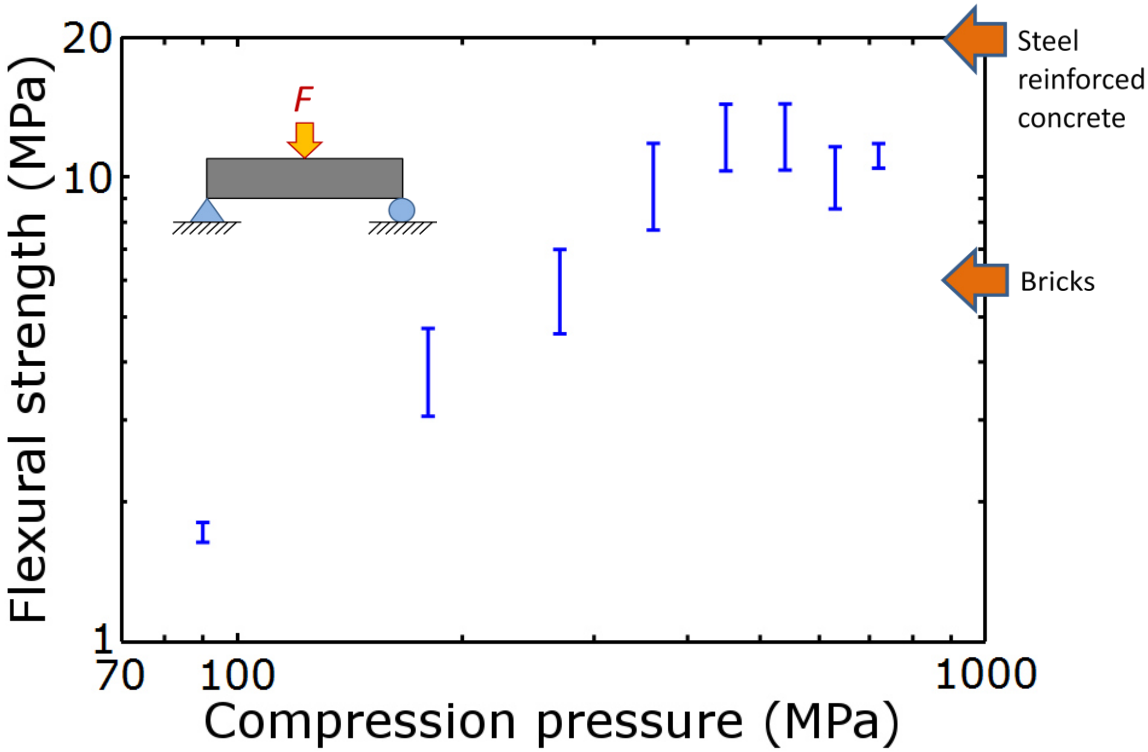

Figure 4-8 Mars-1a Flexural Strength *vs.* Compression, Extended. Flexural strengths Mars-1a dried at 350°C plotted as a function of compression pressure. Error bars represent one standard deviation. The four leftmost error bars appear in Figure 4-7. Three-point bending schema shown at upper-left; reference materials shown at right.

From these results, it is evident that a higher drying temperature leads to greater flexural strength. TGA analysis determined that Mars-1a contains high water contents, in the range from 25-30wt%. Because silicates do not adsorb much water actively, we deduce that the other phase, npOx, must hold the moisture. Above temperatures of 80°C, there appears a steep drop in the amount of water; this water corresponds to free water. In the context of Mars-1a, the adsorbed water on surfaces and pores of the npOx suffice to account for the definition of free water because the surface is more or less electrically neutral despite its hygroscopic tendency.

If water was the responsible binding agent, the easily liberated water from surfaces of the npOx should cause the greatest sensitivity in mechanical properties, but it did not. Instead, Figure 4-7 showed a slight increase in flexural strength when simulant particles were dried from 80°C to 350°C prior to compression, with remarkable uniformity across all peak compression pressures. The test therefore opposes the hypothesis that water or moisture is responsible for the strength in Mars-1a, and instead supports the notion that surface-dominated secondary bonding is.

Excess water slakes a compacted Mars-1a solid when applied directly on top. Capillary action forces a layer of water around each particle, resulting in complete disintegration.

A plateau exists towards higher compression pressure because the effective stress on the sample reaches an elastic limit of hardening, and also because the lateral wall friction inside the forming die increases. Both of these interact by means of the shear stress being transmitted from the die wall, through the solid, and into the piston face, increasingly so with further hardening and elasticity.

4.3.1.2 Flexural Strength as a Function of Curing Temperature

The strengths of samples made from Mars-1a soil simulant of the 53-90µm size range are probed as a function of curing temperature after compression. Pre-drying of the simulant was conducted after sieving, at 350°C for 12h prior to compression at 360MPa. Some results are listed in Table 4-2.

Table 4-2 Compacted Mars-1a Flexural Strengths *vs.* Cure Temperature

Sample	Curing Temperature (°C)	Width (mm)	Depth (mm)	Flexural Strength (MPa)
489	25	4.76	4.34	8.84
490		5.31	4.52	9.33
491		5.11	4.63	8.04
492	130	5.25	4.49	13.72
494		5.98	4.47	12.03
495	230	5.53	4.47	11.86
496		5.05	4.66	10.03
497		5.14	4.04	13.29
498	330	5.95	4.55	21.68
499		5.51	4.31	18.63
500		5.71	4.41	20.21
501	430	4.69	4.41	23.96
502		4.90	4.35	26.42
503		4.70	4.33	30.13
508	25	4.48	4.25	12.15
509	130	4.69	4.24	8.35
510	230	3.95	4.19	11.00
511	25	4.69	4.13	14.12
512		3.62	4.14	10.88
513		4.24	3.99	12.61
514	130	4.44	3.25	5.32
515		4.64	3.31	15.29
516	230	4.07	4.67	8.43
517		4.65	4.76	13.23
518		4.33	4.62	6.67

Compression pressure = 360MPa.
All beams had support length 9.78mm.
Particle size was 53-90μm.

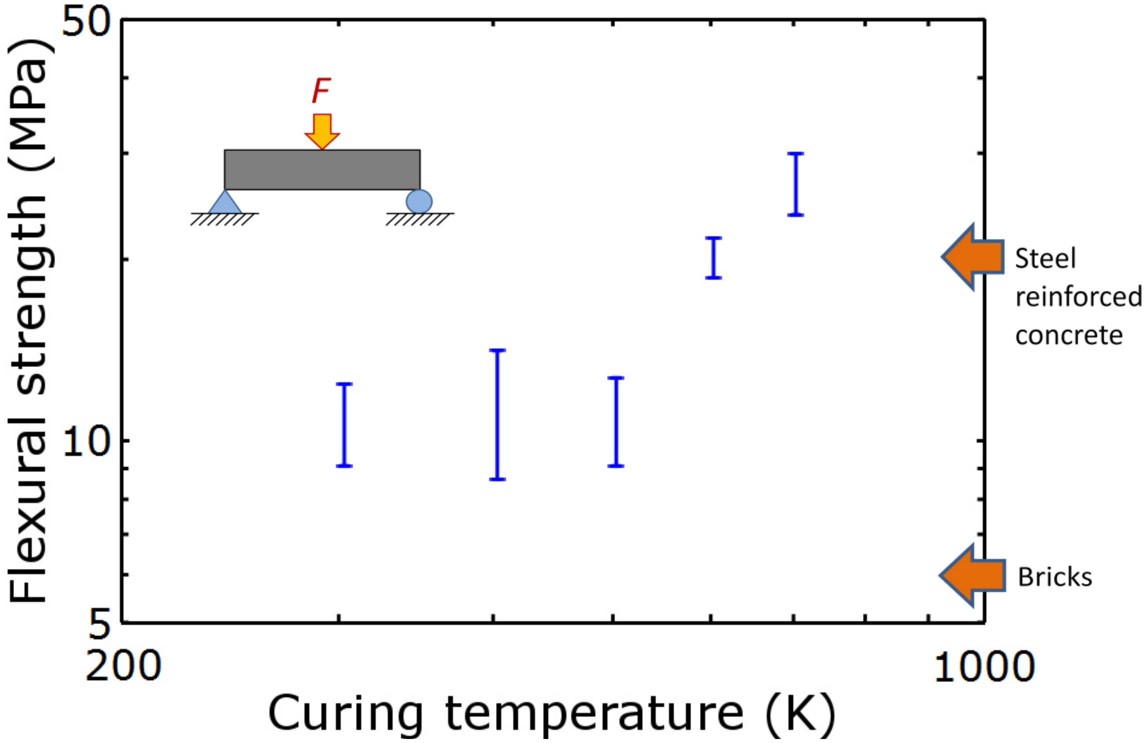

Figure 4-9 Mars-1a Flexural Strength *vs.* Curing. Flexural strength of Mars-1a samples as a function of curing temperature. Three-point bending schema shown at upper-left; reference materials shown at right.

The trend of curing temperature as indicated on Figure 4-9 shows increasing flexural strength for curing of post-compressed solids higher than 230°C. This temperature value represents the onset of the second steep drop observed in the TGA analysis, probably corresponding to slow dehydroxylation of FeOOH changes in the solid state.

The specific experimental procedure places particular emphasis on applicability: although increasing the pre-compression drying temperature also increased flexural strength in §4.3.1.1, the mechanism may be different. The post-compression curing here produced a unique trend at a different temperature domain, motivating an alternative physical scenario. Upon compression, the strength of solid Mars-1a is initially determined by secondary bonding between particles. Before curing begins, interfacial contacts between adjacent npOx particles are joined through the secondary bonding. At a certain elevated temperature, the hydroxyl release occurs simultaneously with bond formation with adjacent npOx particles. As hydroxyl water is driven off, they are replaced by stronger covalent bonds which account for the increase in strength. The bonding can occur across a defect vacancy within a solid, or at a neighboring particle surface in a true contact region.

4.3.1.3 Flexural Strength as Function of Compression Pressure

Mars-1a simulant from the 25-45μm size bin was dried at 350°C for 12h. The dried particles were placed into a cylindrical die and compressed at prescribed pressures of 90-720MPa. Compression pressures of 360MPa and less used dies with a 19.05-mm bore, and higher pressures used dies with a 12.7mm bore. One datum exists at 810MPa, where a 12.7-mm die was brought to the Instron's upper load limit, triggering the safety stop. The results are shown in Table 4-3 and Figure 4-10. We generated two series of data using the two (initial) particle size bins <20µm and 25-45µm.

Samples 417-475 from §4.3.1.1 used similar experimental parameters, except particle size was random (*i.e.*, unsieved) and samples were cured post-compression. However, inspection of Figure 4-7 and 4-9 suggests that the data is compatible, with merely slight differences in flexural strength. Together, the three data series help illustrate a statistical trend when combined using error propagation (*e.g.*, [8]).

Table 4-3 Compacted Mars-1a Flexural Strengths *vs.* Compression Pressure

Sample	Size Range (μm)	Peak Pressure (MPa)	Length (mm)	Width (mm)	Depth (mm)	Flexural Strength (MPa)	Average Flexural Strength (MPa)
1065	25 - 45	90	15.22	5.06	1.77	1.81	1.99
1066				4.29	1.78	1.91	
1067			9.78	5.02	1.95	1.83	
1068			15.22	3.78	1.97	2.41	
1069		180		5.09	1.96	2.73	3.05
1070				4.95	1.98	2.88	
1071				4.71	2.51	3.25	
1072				5.12	2.53	3.33	
1073		270		5.07	1.36	4.80	4.86
1074				5.16	1.37	5.19	
1075				5.34	1.49	4.72	
1076				5.42	1.47	4.72	
1077		360		5.86	1.35	5.75	6.99
1078				5.67	1.32	5.48	
1079				4.94	0.89	6.13	
1080				5.16	0.97	10.58	
1081 *		450	9.78	6.72	1.57	2.58 **	5.60
1082 *				4.98	1.04	1.26 **	
1083				7.48	1.68	5.39	
1084				6.24	1.95	5.61	
1085				5.70	1.47	5.80	
1086		540		6.76	2.07	8.06	6.37
1087				6.00	1.04	6.74	
1088				6.80	1.09	4.81	
1089				5.55	1.12	5.86	
1090		630		5.49	1.35	9.75	8.93
1091				5.72	1.55	8.49	
1092				6.11	1.06	6.26	
1093				4.64	1.29	11.21	
1094		720		6.37	1.38	10.61	11.24
1095				3.58	1.51	8.39	
1096				7.19	1.17	12.67	
1097				6.56	0.69	13.29	
1194	<20	90	9.78	6.05	1.21	1.72	1.71
1200				5.62	0.62	2.11	

Table 4-3 Compacted Mars-1a Flexural Strengths *vs.* Compression Pressure (continued)

1201 *	<20	90	9.78	5.25	1.02	0.43 *	1.71
1202				5.94	0.94	1.29	
1195		180		6.59	1.66	2.60	3.26
1203				4.71	0.72	3.12	
1204				5.39	0.97	3.53	
1205				4.65	1.05	3.78	
1196		270		6.81	1.18	5.46	5.28
1206				5.52	0.76	5.57	
1207				5.72	0.67	4.80	
1208		360		5.18	0.59	7.32	6.93
1209				5.64	0.38	6.84	
1210				4.71	0.48	6.62	
1197		450		7.27	0.84	9.67	8.43
1211				7.42	0.60	7.19	
1198		540		6.07	0.97	7.50	6.53
1212				5.05	0.44	5.55	
1199		630		4.99	0.39	16.82	16.16
1213				7.43	0.29	15.49	
1192		720		7.22	1.03	13.04	11.84
1193				6.61	2.01	10.64	
1214		810		7.77	0.48	15.41	15.41

Particles were dried at 350°C for 12h prior to compression.

* Specimen showed evidence of pre-cracking before testing.

** Specimen excluded from calculation of average.

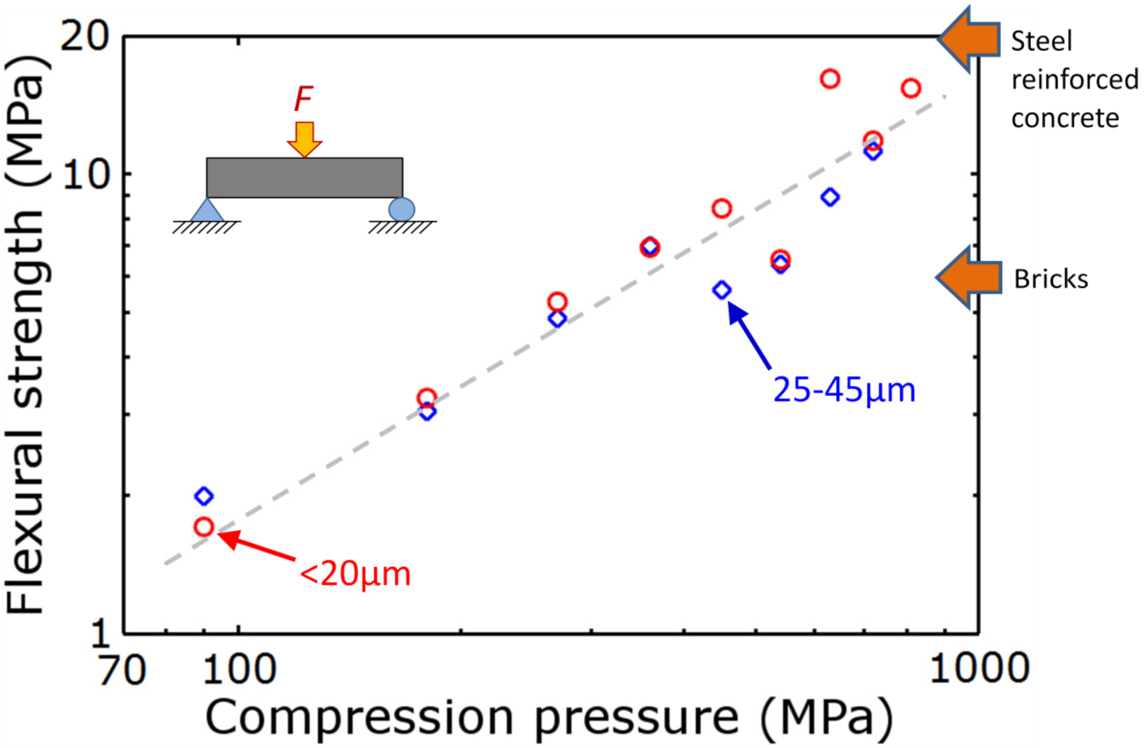

Figure 4-10 Mars-1a Flexural Strength *vs.* Compression, Averages. Flexural strength data plotted as function of peak compression pressure. Each point represents an average value from 2-5 tests. Mars-1a simulant initial particle size bins are indicated by arrows. Combined linear least-squares regression is shown by the dashed grey line. Three-point test schema shown at upper-left; reference materials are indicated at right.

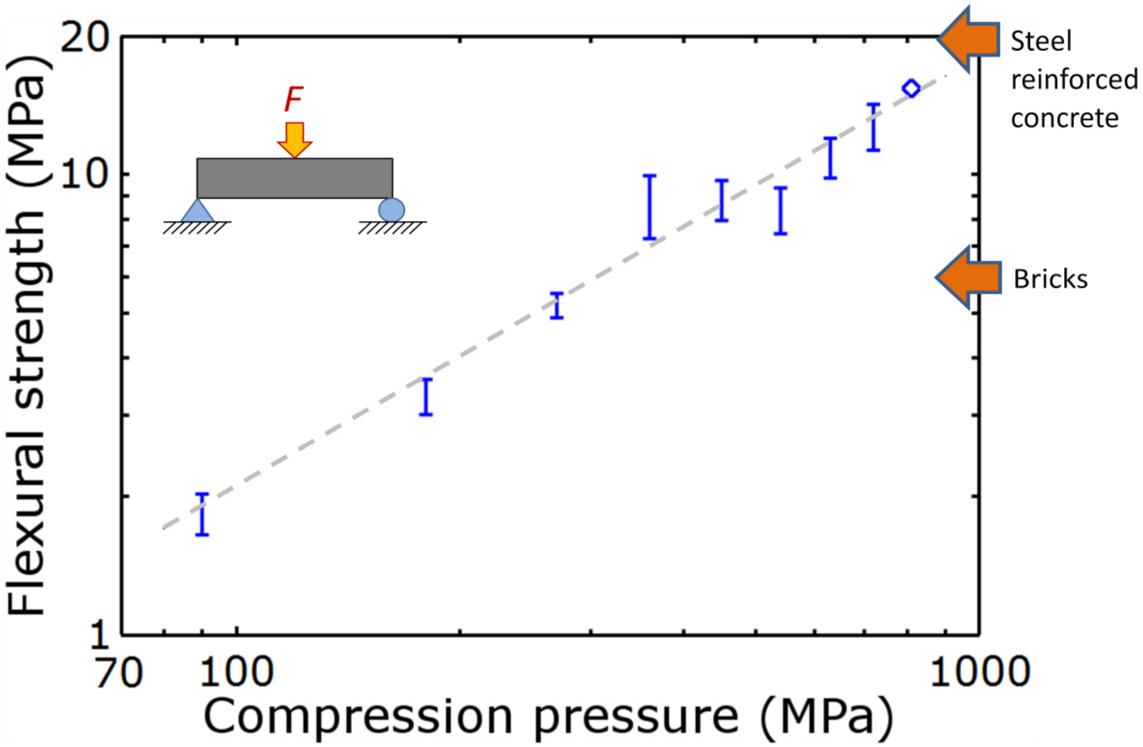

Figure 4-11 Mars-1a Flexural Strength vs. Compression, Combined. Flexural strength data plotted as function of peak compression pressure. Error bars denote one standard deviation; they combine data from Table 4-3 with Samples 417-475. The diamond point at upper-right is one test datum. Linear least-squares regression is shown by the dashed grey line. Three-point test schema shown at upper-left; reference materials are indicated at right.

The least-squares regression calculated from Figure 4-10 is

$R \approx 0.0163P + 0.117$

and from Figure 4-11 it is

$R \approx 0.0180P + 0.265$

where R is the flexural strength in MPa and P is the compression pressure on the sample inside the loading die, also in MPa. These pertain to the data without consideration of logarithms, and show that the flexural strength of the compact is directly proportional to compression pressure as noted for non-geologic materials in the literature [9].

4.3.1.4 Flexural Strength as Function of Initial Average Particle Size

The strengths of the samples are in accordance with motifs found across materials science, where a smaller grain or particle size permits higher strengths to be achieved (*e.g.*, [9][10]). The compression pressure on the pistons was set at 360MPa for one series of data (Samples 476-486/495-497 and 637-673), and 720MPa for another series (Samples 1182-1193). Table 4-4 and 4-5 lists these data respectively. The Carbolite furnace dried simulant particles to 350°C for Samples 476-486/495-497 and 637-673 prior to compaction; post-compaction curing at 230°C was performed for Samples 476-486, but no curing was performed for 637-673 or 1182-1193. Figure 4-12 shows the data for Samples 637-673 merged together with 1182-1193, while Figure 4-13 plots a scattergram of the data for Samples 476-486/495-497.

Table 4-4 Mars-1a Compacted to 360MPa

Sample	Size Range (µm)	Curing Temperature (°C)	Length (mm)	Width (mm)	Depth (mm)	Flexural Strength (MPa)
476	25–45	230	9.78	5.06	3.97	29.80
477				5.13	3.22	22.62
478	<20			4.80	3.27	31.44
479	20–25			4.97	1.86	18.77
480	45–53			4.13	3.86	14.54
481				4.28	4.47	17.15
495	53–90			5.53	4.47	11.86
496				5.05	4.66	10.03
497				5.14	4.04	13.29
482	90–112			4.78	4.28	11.73
483	112–500			4.70	4.18	6.61
484				4.22	5.16	7.57
485	500–560			4.34	4.24	7.52
486				4.53	4.20	7.71
637	<20	None (25)		6.14	1.23	12.63
638				5.55	1.48	6.03
639			15.22	5.70	2.18	9.27
640				6.10	2.23	9.78
641	20–25			6.71	2.66	8.66
642				6.52	2.67	8.84
643				6.62	3.04	8.96
644				6.36	3.05	7.33
645	25–45			6.58	6.48	16.28
646				6.18	6.50	12.94
647	<20			4.92	1.29	13.94
648	25–45			7.12	6.51	11.95
649				6.80	6.56	11.89
650	45–53			6.04	5.32	8.81
651				6.69	5.29	6.83
652				7.01	5.54	5.52
653				6.83	5.52	10.09
654	53–90			4.71	3.48	2.80
655				4.10	5.31	N/A
656				7.34	6.92	8.18
657				7.20	7.02	9.01
658	<20			6.64	3.56	9.50
659				8.93	3.55	11.91

Table 4-4 Mars-1a Compacted to 360MPa (continued)

660	<20	None (25)	15.22	7.70	3.70	16.18
661				6.04	3.67	17.68
666	90–112			6.22	3.07	5.84
667				6.14	2.33	4.79
668				6.63	6.43	7.33
669				6.90	6.39	8.02
670	20–25			5.71	3.50	7.83
671				6.33	3.51	9.37
672				5.85	3.83	9.05
673				6.56	3.79	7.27

Particles were dried at 350°C prior to compression.

Table 4-5 Mars-1a Compacted to 720MPa

Sample	Size Range (µm)	Length (mm)	Width (mm)	Depth (mm)	Flexural Strength (MPa)
1182	25–45	9.78	5.06	3.97	29.80
1183			5.13	3.22	22.62
1184	<20		4.80	3.27	31.44
1185	20–25		4.97	1.86	18.77
1186	45–53		4.13	3.86	14.54
1187			4.28	4.47	17.15
1188	53–90		5.53	4.47	11.86
1189			5.05	4.66	10.03
1190			5.14	4.04	13.29
1191	90–112		4.78	4.28	11.73
1192	112–500		4.70	4.18	6.61
1193			4.22	5.16	7.57

Particles were dried at 350°C prior to compression.

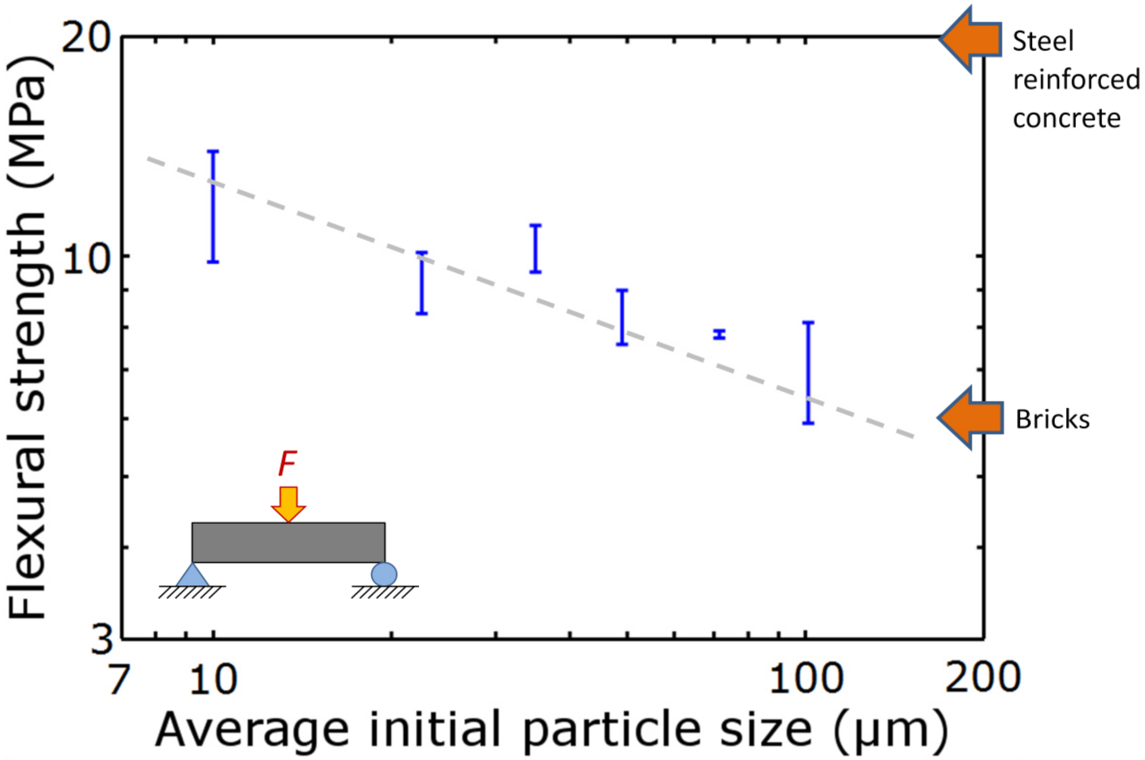

Figure 4-12 Mars-1a Flexural Strength *vs.* Initial Particle Size. Flexural strength of uncured Mars-1a samples as a function of particle size. The data merges the series generated from two different compression pressures, 360MPa and 720MPa. Error bars denote one standard deviation. Dashed gray line represents the linear least-squares regression. Three-point test schema shown at upper-left; reference materials are indicated at right.

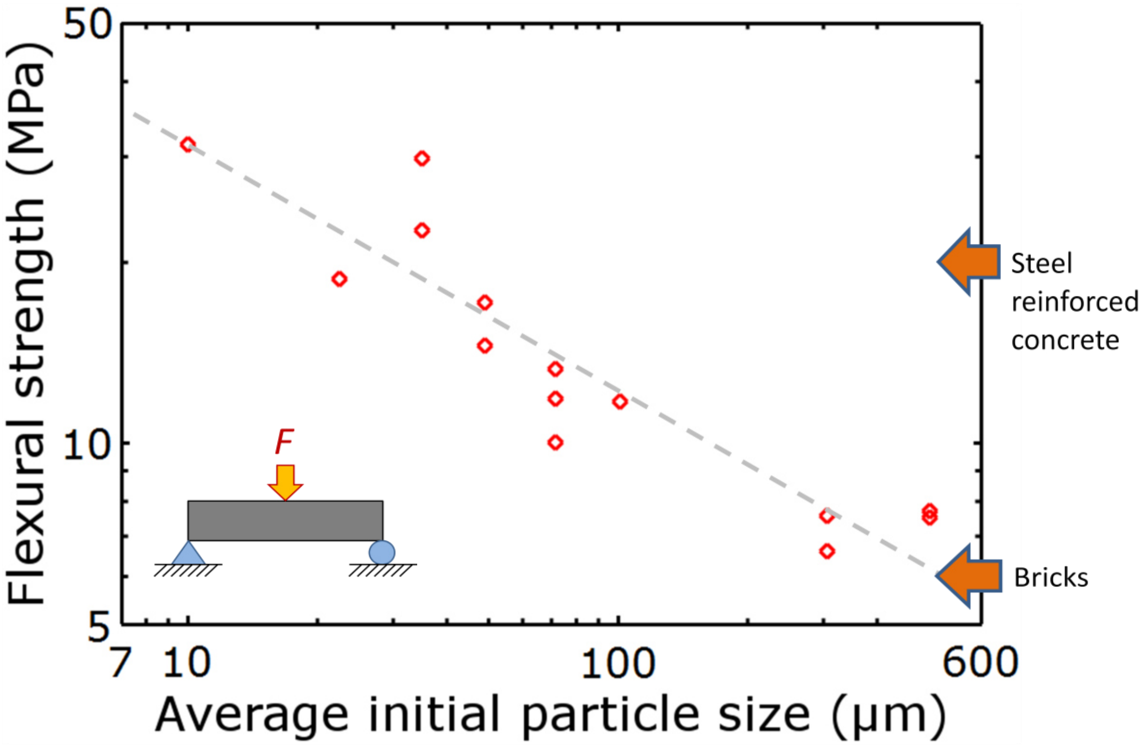

Figure 4-13 Mars-1a Flexural Strength *vs.* Initial Particle Size, Cured. Scatter plot of flexural strength Mars-1a as function of particle size, for samples 476-486/495-497. Each point represents a sample datum. Samples were cured at 230°C after compression forming. Dashed gray line represents the linear least-squares regression. Three-point test schema shown at upper-left; reference materials are indicated at right.

Samples 476-486/495-497 are plotted separately from the other data because compression pressure predicts flexural strength better than the effect of curing temperature (compare Figure 4-11 with Figure 4-9). Thus, the two trends generated with different compression pressures are more reliable combined as a merged data set.

With the observed inverse relation, a least-squares regression incorporates the base-10 logarithms of the data. Both trends corroborate the empirical relationship first posited by Orowan and Knudsen [9], where the flexural strength, R, relates to the initial average particle size, d, *via*

$$R = kd^{-\beta}$$

For Figure 4-12 the constants are $k \approx 25.13$ and $\beta \approx 0.299$, and for Figure 4-13 they are $k \approx 80.61$ and $\beta \approx 0.409$. The equation is empirical because dimensional units are not equivalent between the right and left-hand sides but commonly describes mechanical strength in compacted powders.

4.3.1.5 Peak Pressure and Initial Particle Size Map for Mars-1a

Having investigated Mars-1a as a function of size and compression pressure, we may reveal a map of the effective surface that portrays both of these variables in a single scatter plot. Data from Table 4-3 was used for plotting the flexural strength as a function of compression pressure, while data from Table 4-4 (*viz.*, Samples 637-673) and 4-5 were used for plotting that as a function of initial average particle size. We will briefly summarize the two experimental procedures.

In Table 4-3, sieved Mars-1a simulant belonging to the <20 and 25-45μm bins were dried at 350°C for 12h. The dried particles were placed into a cylindrical die and compressed at prescribed pressures of 90-810MPa.

In Table 4-4 and 4-5, sieved Mars-1a simulant belonging to the <20, 20-25, 25-45, 45-53, 53-90, and 90-112μm bins were dried at 350°C for 12h. The dried particles were placed into a cylindrical die and compressed at prescribed pressures of 360MPa and 720MPa.

A three-dimensional scatter plot is shown in Figure 4-14, and a least-squares plane is shown in Figure 4-15.

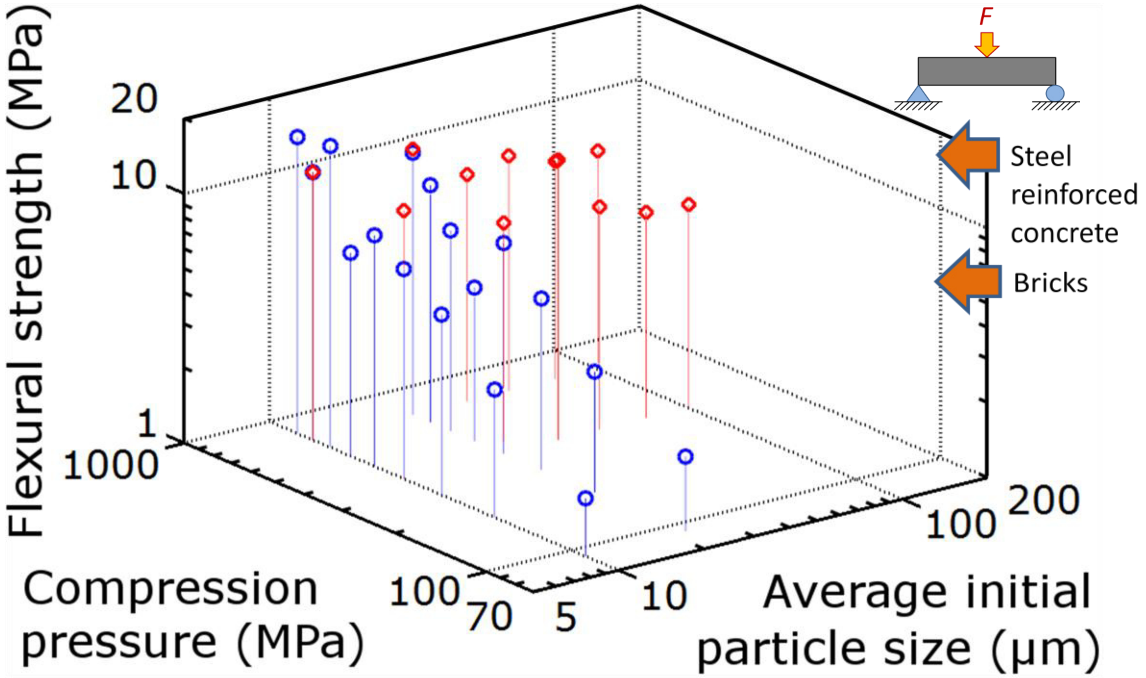

Figure 4-14 Flexural Strength Map of Mars-1a. Flexural strength is plotted as function of particle size and compression pressure, shown as 3-dimensional scattergram. Each point represents a mean value; lines are drawn to the 1MPa ordinate for visual perspective. Schema of 3-point bend test shown at upper-right; reference materials shown at right.

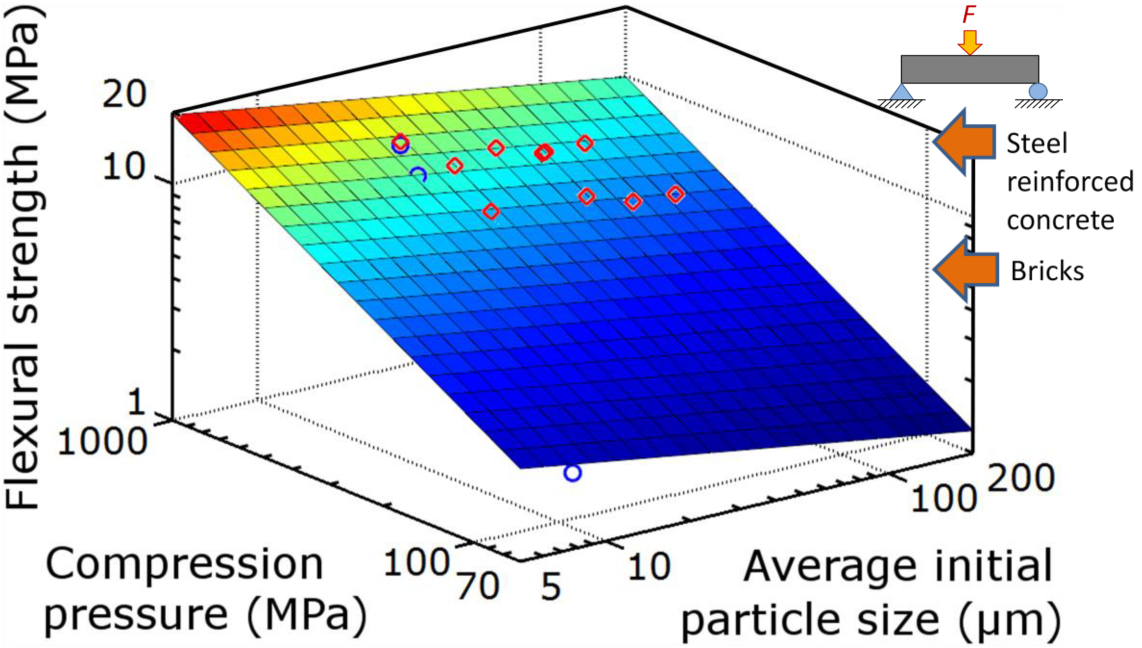

Figure 4-15 Flexural Strength Fitted Map of Mars-1a. Least-squares plane fitted to the data used for calculating the means (shown as points) of flexural strength as a function of compression pressure and the average initial particle size. Schema of 3-point bend test shown at upper-right; reference materials shown at right.

In the maps, the flexural strength data are handled by taking logarithms of the variables and performing multivariate linear regression with least squares (*e.g.*, [11]). We express R in terms of both P and d as

$$R = 10^{\beta_1} d^{\beta_2} P^{\beta_3}$$

where the multivariate regression determines $\beta_1 = -0.917$, $\beta_2 = -0.185$, and $\beta_3 = 0.779$ to give

$$R = 0.121\, d^{-0.185}\, P^{0.779}$$

The greater magnitude of the exponent β_3 associated with the compression pressure indicates it controls the strength more potently in a compacted Mars-1a simulant. A basalt particle's compressive strength is typically less than 10MPa [7], suggesting that the applied pressure, if isostress, significantly reduces particle size during compaction. In contrast, the initial particle size influences the end particle configuration less.

4.3.1.6 Flexural Strength of Mars-1a Diluted with Basalt

We investigate the scenario where Martian surface soils contain rock particles. Realistically, such a scenario may occur if a particular regolith location naturally contains unaltered particles, or if larger basalt particles were inadvertently comminuted into the rest of the soil. Recall that most of the martian bedrock is basaltic, of mineralogical composition similar to terrestrial basalt [12]. We can therefore modally represent the presence of rock particles in simulant as basalt particles.

Some authors have also proposed mechanical interlocking as a possible mode of strengthening compacted solid powders [6]. For this purpose, recall that a typical Mars-1a particle consists of two phases: a basaltic core and an alteration rind [5]. Besides practical interest in field conditions, one may also determine whether the basaltic phase of Mars-1a is responsible for part of the flexural strength *via* interlocking, because one simply reintroduces more basalt content into the simulant. The underlying assumption is that the mechanical characteristics of the basalt found in Mars-1a are identical to the added basalt, which is approximate but sufficient for the purposes of this investigation. In regards to chemical identity, magmatic mixing in the interior of the earth homogenizes basalt mineral compositions worldwide to within a well-defined ensemble of minerals [13], further justifying this assumption.

To ensure the absence of long-term weathering or short-term process contamination, we produced basalt rock from macroscopic samples. A mortar and pestle comminuted cleaned basalt rock (Washougal Quarry, WA) into fine flour. The mechanical sieve (Rotap RX-29) fractionated sizes, and the furnace (Carbolite CTF)dried at 600°C for 12h. Identically processed Mars-1a manually mixed with the flour in prescribed fractions using a spatula. The resulting blend was compacted, machined, and tested as described by §4.3.1. Basalt particles mixed with the Mars-1a in prescribed proportions of 10wt%, 25wt%, 50wt%, and 75wt%. Results are summarized in Table 4-6.

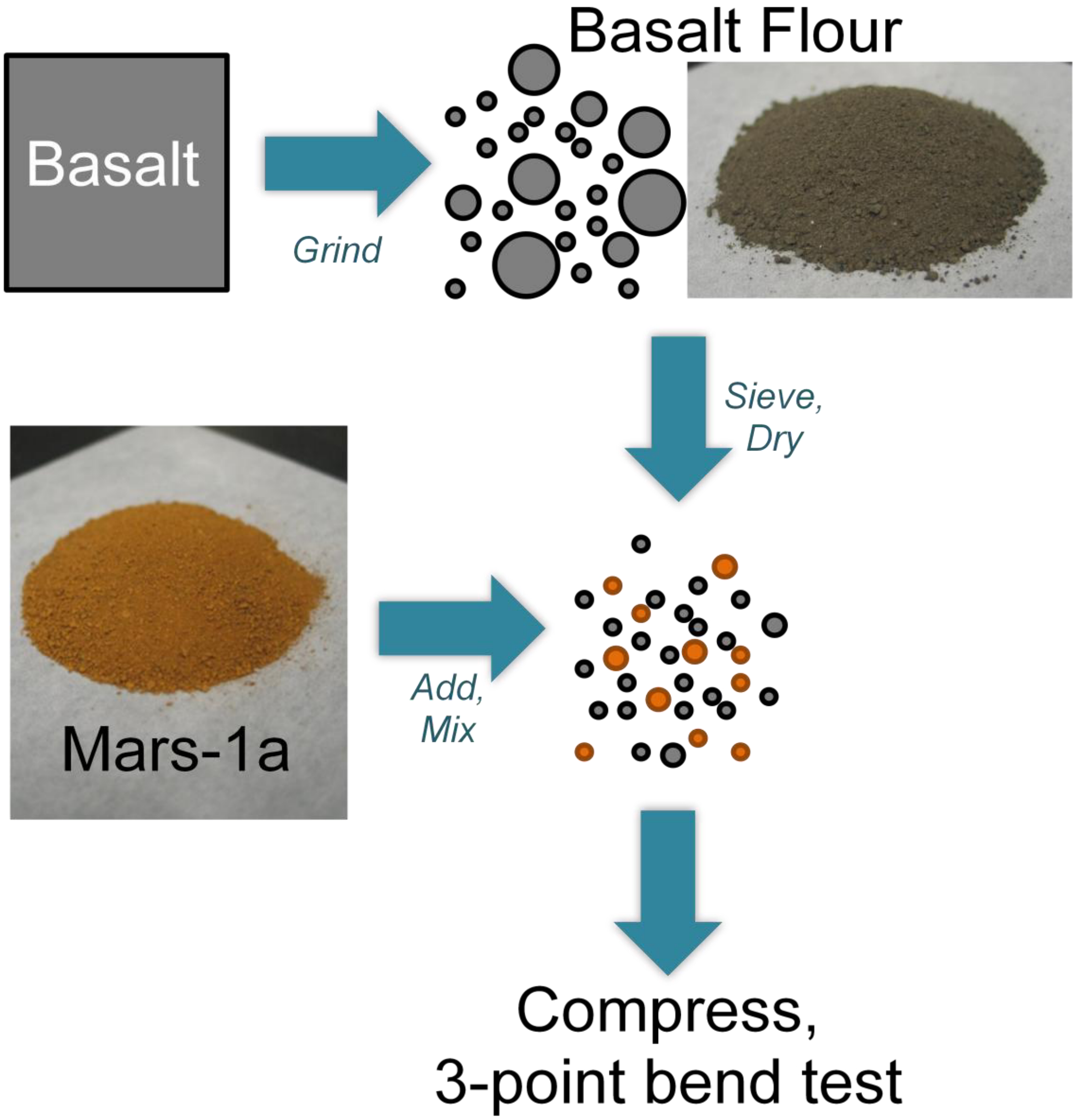

Figure 4-16 Mixing Basalt with Mars-1a. Schematic of the process of mixing basalt particles with Mars-1a. In the both photographic insets, the piles are 5cm wide.

Table 4-6 Mars-1a Mixed with Basalt. Flexural Strengths of Mars-1a Mixtures with Basalt Particles in Various Proportions.

Sample	Basalt Content (wt%)	Flexural Strength (MPa)
458 (reference)	0	8.43
714	10	6.25
715		6.45
686	25	8.94
687		6.51
684	50	2.38
685		3.06
706	75	2.33
707		1.32
N/A *	100	0

* Note: samples were serialized only if it could be sliced and ground into a beam.

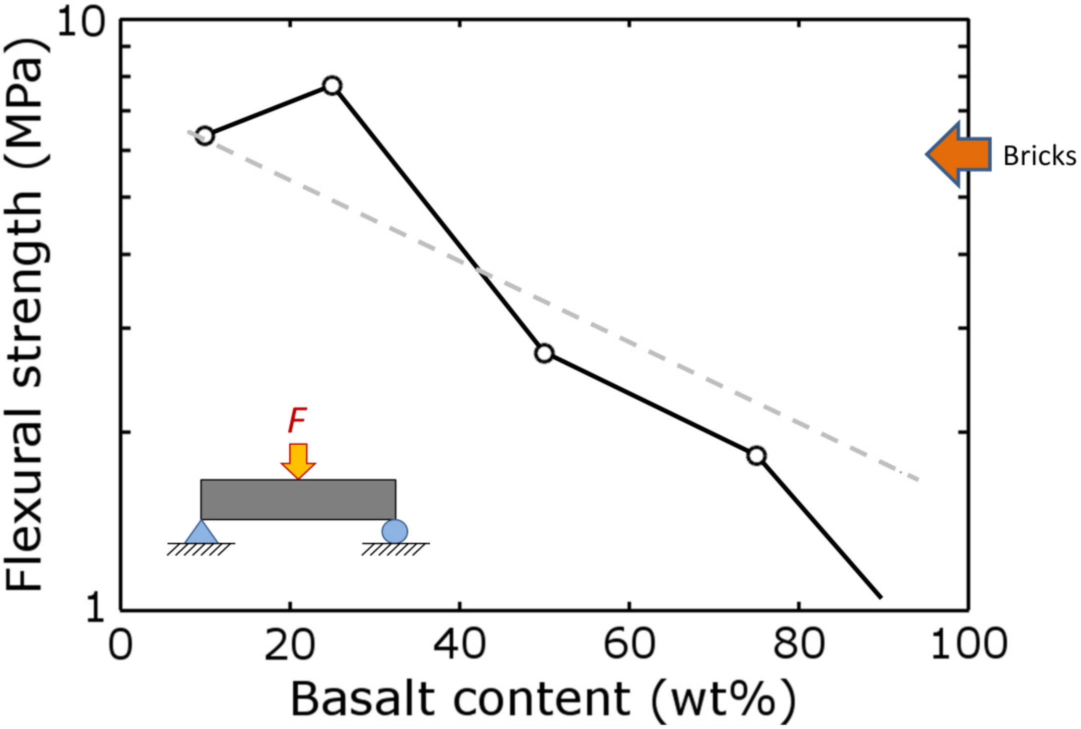

Figure 4-17 Mars-1a Flexural Strength *vs.* Basalt Content. Flexural strength of basalt-Mars-1a mixtures compacted to 360MPa, plotted as a function of basalt content. Points represent means, connected together by the solid black line. The trail-off at lower-right signifies the zero datum. Dashed line represents the least-squares regression. Three-point bending schema is shown at lower-left. Reference strength for brick material appears at right.

Table 4-6 gives strong evidence for a loss in strength upon added basalt particles. The basalt flour acts as an inert filler which does not contribute to the strength of Mars-1a. A beam made completely of basalt flour was too fragile to handle manually. This datum was procedurally assigned zero strength. The functional absence of mechanical strength for compressed basalt flour suggests that mechanical interlocking plays no role in compaction-strengthening of basalt or Mars-1a. Assuming that the particles remain self-similar and convex upon crushing into smaller sizes, such an outcome can be expected.

The trend of the strengths from Figure 4-17 follows a modified rule of mixtures. For a particulate composite, the strength can be described by the volumetric proportions of the active binding component to the inert filler. The log-scale linear relationship between basalt content, C (in wt%), and flexural strength, R, is calculated as

$$R = 10^{-0.0068C+0.8645}$$

with a corresponding correlation coefficient of $\rho = -0.904$ and a Pearson product moment correlation coefficient of $p = 0.002$. Both statistical measures exceed those computed for the linear-in-y hypothesis, motivating an explanation. Consider first the behavior on the right-hand side end of Figure 4-17. The number of connecting adhesive grains is sparse and can be rudimentarily described as a circular junction (a “spot weld”) between two infinite planes in linear fracture mechanics. Assume an isostress condition. The boundary of the circle represents the crack tip, propagating towards catastrophic failure towards the interior of the junction. If a is the radius of the junction, and P is the far-field load, the dominant stress intensity K_I is [14]

$$K_I = \frac{P}{2\pi\sqrt{\pi a}}$$

In the sparse condition, only the far-field stress increases, lending credence to the linearity in flexural strength with small and intermediate amounts of Mars-1a. Now consider the left-hand side of Figure 4-17. With abundance of adhesive Mars-1a, some of the junctions coalesce into larger ones and this condition on the other extreme starts to resemble a circular defect in an infinite solid. Its dominant stress intensity is [14]

$$K_I = \frac{2\sigma}{\pi}\sqrt{\pi a}$$

where P is the applied far-field load perpendicular to the plane of the defect. Unlike the sparse condition, the far-field stress and P on the particle is nearly constant. As a decreases, K_I rapidly decays to zero, accounting for the behavior on the left end of the linear regression in Figure 4-17.

4.3.1.7 Flexural Strength of npOx Analogues

Ruling out mechanical interlocking as a contributor to strength, attention now turns towards the agent of strengthening. As discussed previously, we hypothesize npOx to be responsible for the strength *via* large available specific surface during compaction. The possibility remains, however unlikely, that a synergistic effect between npOx and the basaltic substrate in Mars-1a could cause strengthening. In order to provide confidence that npOx is the strengthening agent, one should demonstrate that it can strengthen by itself.

Difficulties arise when attempting to isolate the npOx found in Mars-1a. It is extremely fine and partially amorphous [5]. Furthermore, it is mixed together with rock-forming silica on the molecular level, as evidenced by its lack of transformation to hematite at 600°C (described in Chapter 6). This highly heterogenous state precludes isolation by means of selective dissolution using solvents. Chemical methods are further encumbered by npOx's own inherent hereogeneity, because the term describes a broad class of iron oxides which have similar stability regions for a given environment [15]. Iron cations in solution may precipitate as different phases, altering the composition of this npOx. Such challenges motivate the focus towards analogues of npOx. Goethite and fresh orange-yellow rust are two materials similar in composition to npOx; although approximate, rust represents a collection of nanoparticulates included in npOx, and goethite is the modal component of rust.

We generated rust fines from carbon steel. A 0.2M acetic acid solution exposed approximately 100g of machined shavings (swarf) and a rectangular carbon steel bar for 168h, overturning every 24h to maximize air exposure. About half of the shavings sat above the waterline. Manual agitation of the corroded shavings separated the rust fines inside a 200-ml beaker filled with ethanol. The shavings were manually removed, and debris silted for 60s from the suspension. A second beaker received the remaining (supernatant) suspension from the first, followed by another silting for 24h. After the second silting, the supernatant ethanol decants out of the beaker slowly, revealing the rust fines. After a final rinsing with distilled water and acetone, the fines were oven-dried at 80°C, 350°C, or 500°C for 12h. The particles were not mechanically sieved, because freshly generated rust is known to have particle sizes of ~30nm [16].

We used goethite (Sigma-Aldrich 71063-100G) as-supplied without processing. It was not dried, because unlike the npOx found in Mars-1a, pure goethite exhibits low-temperature transformation sensitivity [17]. As the main component of rust, goethite particles generated by conventional synthesis are also quite small [17] and were not amenable to mechanical sieving.

Both rust fines and goethite were compacted and tested according to the rest of the normal procedure described in §4.3.1. Figure 4-18 shows the schematic for producing rust fines, and Table 4-7 lists the results for flexural strength.

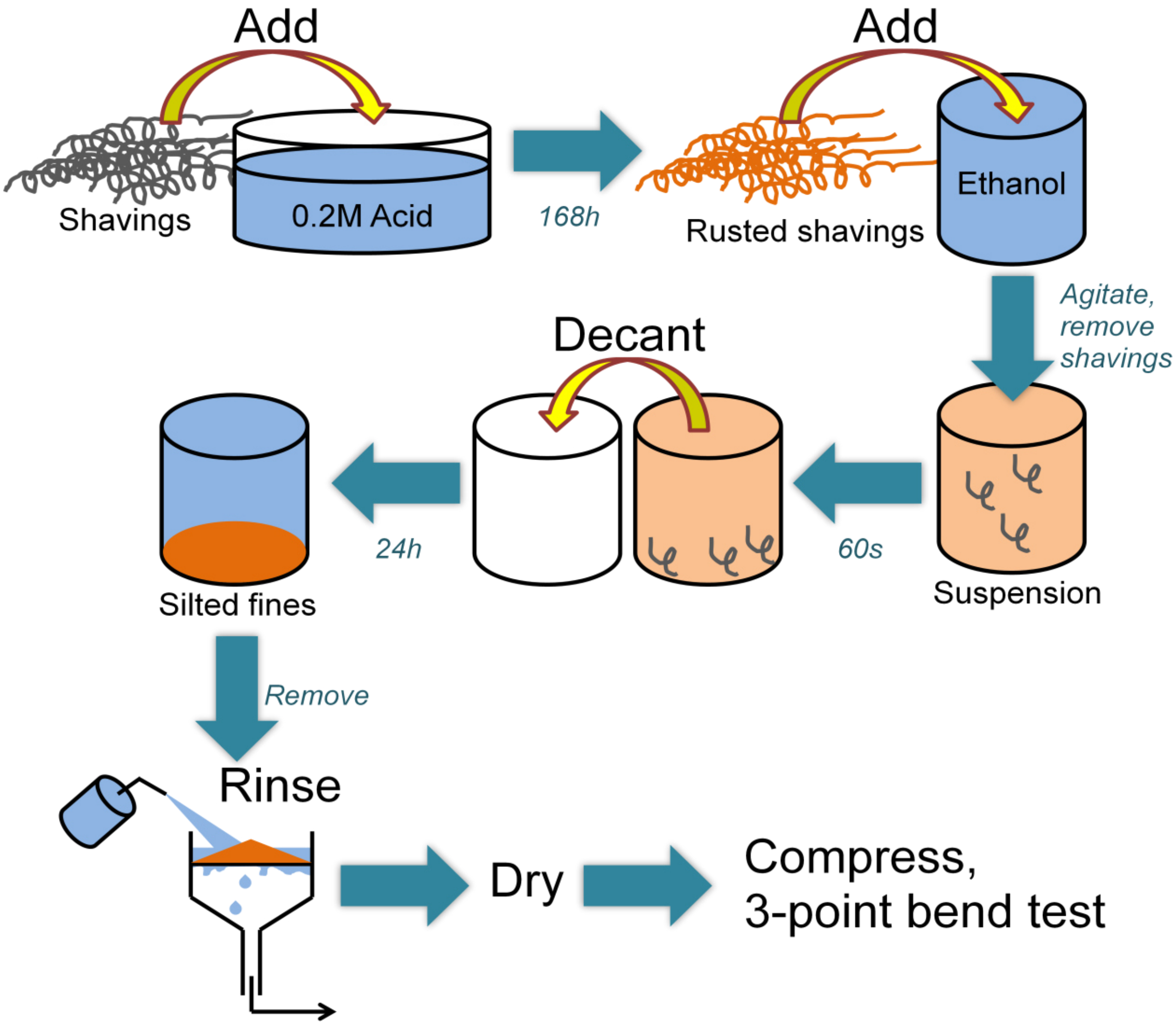

Figure 4-18 Generation of Rust. Schematic of the generation of rust fines.

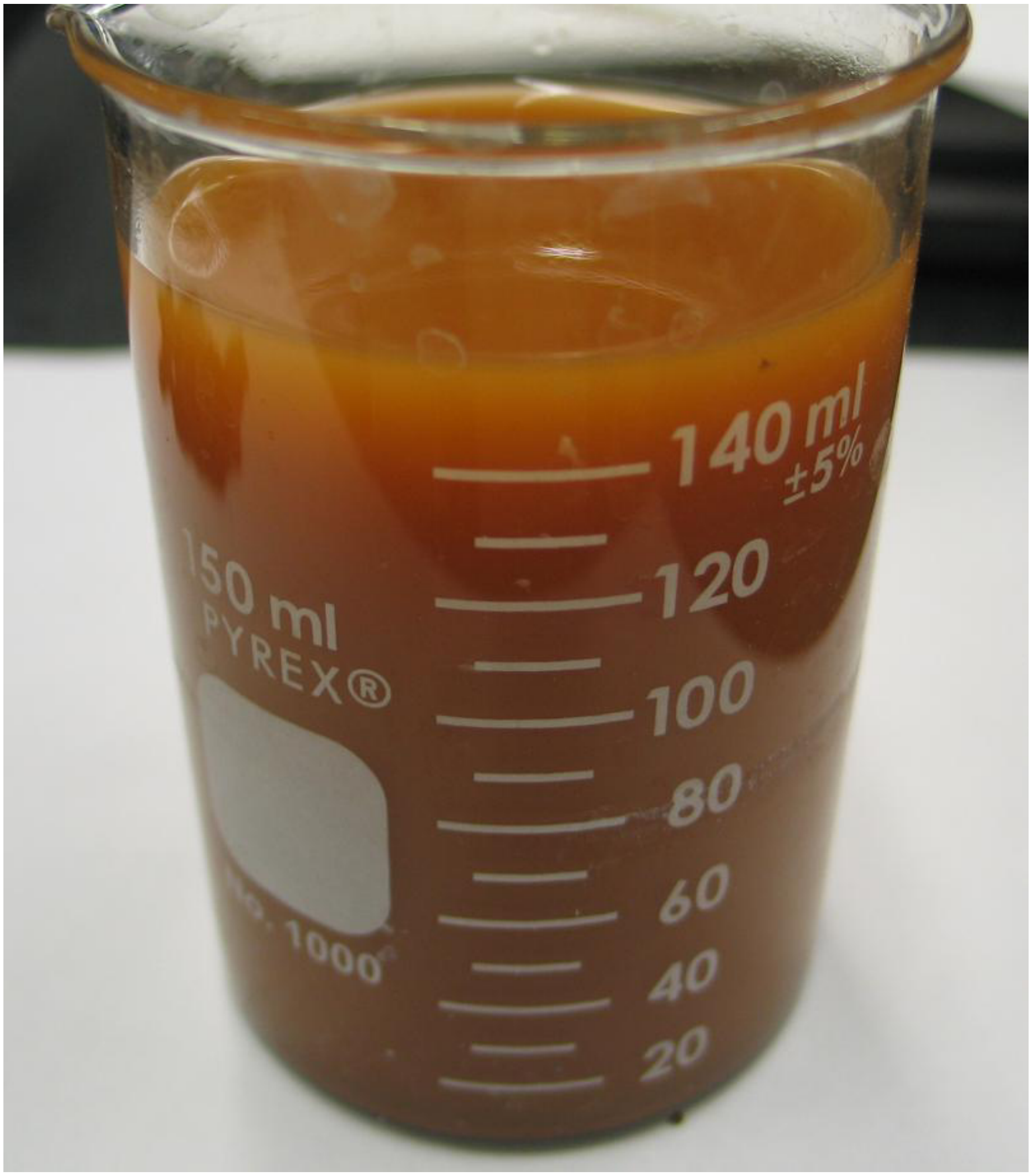

Figure 4-19 Photo of Silting Rust. Photograph of the second silting showing the color of the suspension of rust fines dispersed in ethanol inside a beaker; beaker is ~5cm wide.

Figure 4-20 Photo of Dried Rust. Color of rust fines in crucible after drying at 350°C for 12h. The rim of the crucible is ~3.5cm wide.

Table 4-7 Flexural Strengths of Compacted npOx Analogues

Sample	Material	Compression Pressure (MPa)	Drying Temperature (°C)	Width (mm)	Depth (mm)	Flexural Strength (MPa)
932	Rust Fines	360	80	5.11	0.67	7.46
933				4.86	0.65	8.78
993				4.88	0.28	7.29
994				5.89	0.26	9.85
995				6.26	0.24	7.32
919			350*	4.73	0.89	5.44
958			500*	5.70	0.75	6.27
959				5.45	0.75	5.06
960				6.05	0.67	4.96
961				6.33	0.71	4.87
1012			350*	5.97	0.94	6.06
1013				6.16	0.85	6.41
973	Goethite		None (25)	5.42	0.58	12.40
1060		720		7.17	0.30	13.41
1350**	Rust Fines	1000		4.09	0.20	18.30
1351**				4.96	0.18	22.82
1352**				3.63	0.24	15.75

* Visible evidence of particle transformation to hematite.
** Compacted with the free lateral boundary condition in §4.4.1.1.
Length between beam supports = 15.22mm (except Samples 1350-1352 = 4.99mm)

The results suggest that materials belonging to the family of substances considered to be npOx described in the literature [18][12][19][20][21][22][23][24][25] develop mechanical strength when compacted under high pressures. It is remarkable that the rust fines, despite being silica-free, also develop strength despite transforming into hematite at higher pre-compression drying temperatures. In contrast, separate tests have shown that neat hematite does not strengthen upon compaction. The subjected drying temperature of 500°C is lower than sintering temperature, but promotes phase transformation in the so-called "inherited" microstructure of the precursor FeOOH[17]. Retention of inherited phases of FeOOH ensures a high specific surface remains for available bond contacts to form when compressed. The lower strength at higher pre-compression drying temperatures may be due to higher intrinsic strength of the hematite phase, or the depletion of hydrogen bonds from the liberated hydroxyl groups.

4.3.1.8 Carbon Contaminants on the Attribution of Strength

The evidence presented for npOx may otherwise be causal for strength in Mars-1a, but rigorously speaking, organic contaminants may also be a confounding factor. With the CHNS/O elemental analysis in Chapter 6, we provide evidence that carbon contamination is not responsible for development in strength. Previous work with polymeric binders (Chapter 3; [26][27]) shows that, should the presence of carbon be granted, they would not be capable of producing structural strength beyond in small proportions; indeed the investigation with PVC has shown that small proportions of organic material interfere with strengthening.

4.3.2 Impact Formation

Mars-1a particles were sieved and dried at 600°C according to the procedure described in §4.3.1. The 25-45μm bin size was used. Approximately 0.2g filled the bore of a 12.7-mm steel die, capped on both ends with matching pistons. A hammer weighing 7.64kg in the shape of a cylindrical tube was dropped from a height of 1.52m, impacting the die assembly. Samples were removed manually and tested according to the procedure described in §4.3.1.

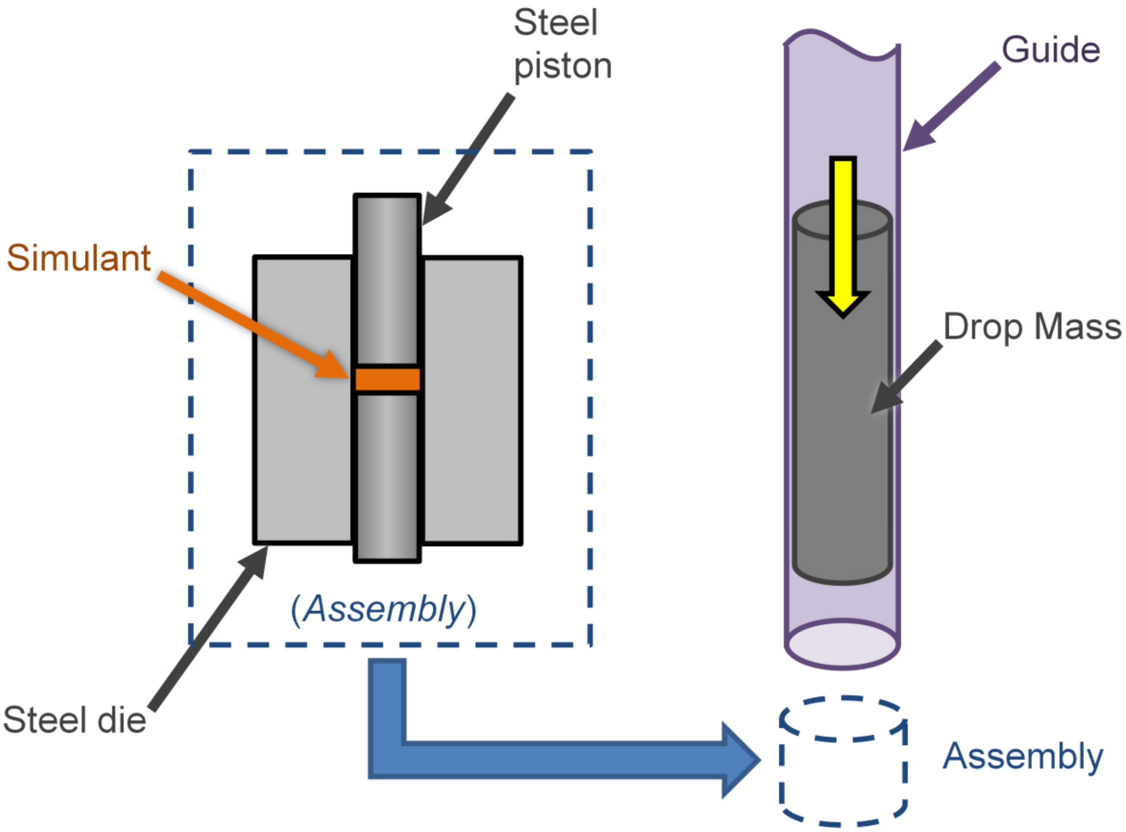

Figure 4-21 Mars-1a Rigid Lateral Boundary Impact Compaction. Schematic of the impact compaction process of forming.

Table 4-8 Impact-Formed Mars-1a with Rigid Lateral Boundary.

Sample	Length (mm)	Width (mm)	Depth (mm)	Flexural Strength (MPa)
1391	9.78	6.52	0.68	5.79
1392	4.99	6.05	1.13	11.95
1393	9.78	5.84	1.26	18.50
1394	9.78	4.87	1.57	15.01

Initial particle size range was 25-45μm.
Pre-compression drying temperature = 600°C.

Satisfactory strength was achieved by means of the compaction process, and the strengths are somewhat higher than those originating from quasi-static compaction for a similar amount of energy (both ~100J). We attribute the increased strength to effectively reduced friction between the sample and the die wall, possibly from a high-energy component of the shock wave upon impact. There also exists the possibility that a phase transformation in the npOx occurs, but this hypothesis is challenged by the observed resistance to phase transformation at high drying temperature prior to compaction.

During these tests it was also found that the attrition rate is nontrivial, with some samples cracking from an elastic rebound of the hammer mass upon the die assembly. Methods were developed to increase the reliability of the impact formation procedure.

4.3.3 Summary of Findings with Rigid Boundary

We now present the findings with a rigid lateral boundary condition, from the experiments with a lateral rigid boundary (that is, using a steel die). All strengths refer to flexural strengths from bricks compressed under 360MPa pressure. For combinations, the lower strength represents between 0wt% and 25wt% of the binder and the higher strength represents between 75wt% and 100wt% binder.

Table 4-9 Basaltic, Iron Oxide, and Salt Minerals Tested

Neat Particles			
Abbreviation	Simulants Tested	Description	Remarks
M1A	Mars-1a	Weathered basalt. Over 80wt% of the dry mass is silica, alumina, and iron oxide minerals. Volatile composition 20-25wt%.	Typical flexural strength 10-15 MPa; extreme range 3-30 MPa only when 230°C cured. Uncured strength is 5-10 MPa. Compressive strength ~20 MPa (see Appendix F). Long-term strength is unaffected at ambient conditions (see Appendix H).
CMS	CMS-1	Proprietary blend (Ceralink); likely contains hematite.	Strengthens with water (Appendix G)
BAS	Basalt	Dark volcanic rock. Dry mass is mainly silica, alumina, and iron oxide minerals.	Fines do not form bricks.
RS	Rust fines	Inherently a mixture of FeOOH phases.	Strength is 5-10 MPa.
RS2	Rust scale, aged.	Greater magnetite composition than fresh rust.	Weaker than fresh rust, about 3-5 MPa.
HM	Hematite	Deep red, hard iron oxide Fe_2O_3.	Fines do not form bricks. Hematite converted from rust or goethite have strength 4-7 MPa.
GT	Goethite	Yellow, soft nanoparticulate α-FeOOH.	Strength 3-12 MPa. 350°C-cured strength 7-13 MPa.
CAL	Calcium carbonate	Calcite ($CaCO_3$), white powder.	Strength 1 MPa (Appendix I).
GYP	Calcium sulfate dihydrate	Gypsum ($CaSO_4$), white powder	Strength 6-9 MPa (Appendix I).
MGC	Magnesium carbonate	$MgCO_3$, white powder.	Strength 19-37 MPa (Appendix I).
MGS	Magnesium sulfate	$MgSO_4$, white powder.	Strength 26-39 MPa (Appendix I).

Table 4-9 Basaltic, Iron Oxide, and Salt Minerals Tested (continued)

Combinations of Particles		
Combination Tested	Description	Remarks
M1A + BAS	Dark brown color.	Strength 1-9 MPa.
GT + BAS	Grey-yellow color.	Strength 1-3 MPa (Appendix I).
MGC + BAS	Grey color.	Strength 5-17 MPa (Appendix I).
MGS + BAS	Grey color. Brick of 50-50wt% composition.	Strength 3-20 MPa (Appendix I). Shape warps days after testing when left at ambient.

4.4 Compaction with Reduced Lateral Boundary Conditions

The compaction thus far performed in this work has relied on a steel die. We may regard the steel die as an approximately rigid lateral boundary surrounding the circumference of the sample. Simultaneous work on montmorillonite clay (Chapter 5) has found that altering the lateral boundary results in significant increases in flexural strength. We pursue the same process and proceed in parallel fashion with the research on montmorillonite clay.

We did not resort to altering the die wall friction for a number of reasons. First, the very thin aspect ratio of the compacted solids precluded necessity for lubricants. Second, investigators applying pressures to ~100MPa note deleterious effects on resulting mechanical properties when applying lubricants to the compression system [28][29]. Third, friction is subject to very high variability and cannot be precisely controlled.

4.4.1 Quasistatic Compaction

As-supplied Mars-1a simulant was dried at 105°C for 24h prior to sieving. The Rotap sieve (W.S. Tyler RX-29, 350W) separated the different size bins for 30 minutes. The sieve stack contained mesh sizes of 90μm, 53μm, 45μm, 25μm, and 20μm above the pan. Particles were heated to a prescribed temperature using a quartz tube furnace (Carbolite CTF 12/75/700), again for drying purposes.

A uniaxial load-displacement test machine compressed the simulant (Instron 5582 or SATEC M600XWHVL) at a quasi-static rate of 6mm/min. Most samples used the Instron machine, while larger samples requiring >360MPa compaction with a

19.05mm-diameter sized sample exceeded the 100kN load limit on the Instron and required the SATEC machine.

The compacted simulant was removed manually, in the shape of a disc, from the die assembly. Compacts were ground into beam specimens with 26μm and 13μm sandpaper. The 13μm abrasive introduced a light chamfer in each lengthwise edge of the beams to counter edge defects. Fixtures machined to set length supported each beam during three-point bending tests, and flexural strength was evaluated as

$$R = \frac{3PL}{2bd^2}$$

Where P is the midspan point load at failure, L the length between the fixture supports, b the width of the beam, and d the depth (or thickness) of the beam.

4.4.1.1 Free Lateral Boundary Condition

It remains unknown whether there an upper limit to strength exists, in any process configuration. First, we form an 8.71mm diameter pellet under a manual compression pressure of ~150MPa using a 10kN arbor press. This pellet is inserted into a much larger, oversized 19.05mm-diameter piston-die assembly, such that the pellet is essentially compressed between the flats of the pistons without contact with the lateral inner die wall. This configuration—the absence of a retaining wall around the circumference of the sample—is referred to as the “free lateral boundary” condition.

A schematic of this method is depicted in Figure 4-22. There were two pre-compaction drying temperatures prescribed for the simulant prior to compression forming: 350°C and 500°C. Table 4-10 tabulates the flexural strength results. The highest pressure so far achieved was 1.5GPa on an 8.71mm diameter disc.

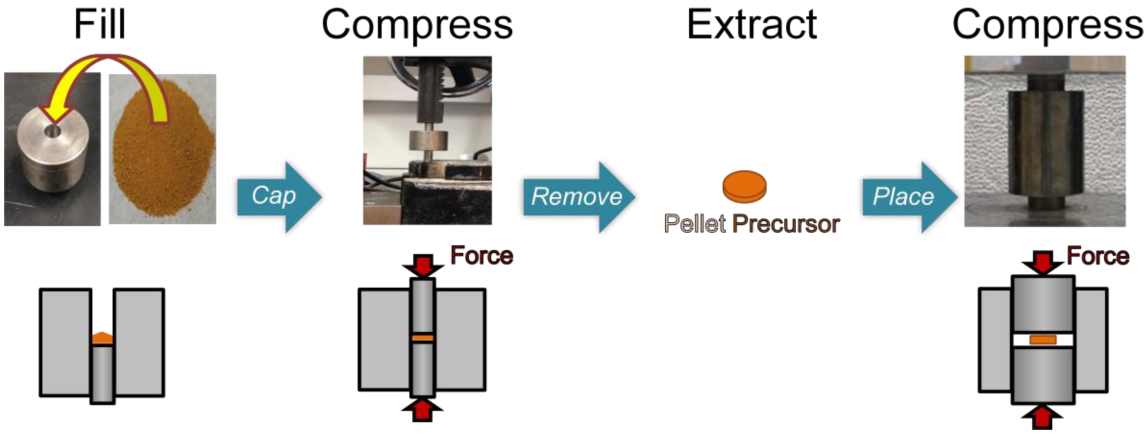

Figure 4-22 Mars-1a Free Lateral Boundary Compaction. Schematic of the process for the free lateral boundary condition.

Figure 4-23 Photo of SATEC Machine. Photograph taken of the SATEC M600XWHVL machine used to compress 19.05mm-diameter precursors to 800MPa with the free lateral boundary condition. The width of the square loading platens is ~30cm.

Table 4-10 Mars-1a Compacted with Free Lateral Boundary

Sample	Drying Temperature (°C)	Particle Size (μm)	Peak Pressure (MPa)	Width (mm)	Depth (mm)	Flexural Strength (MPa)	Average Strength (MPa)
1311	350	25-45	1500	3.57	0.29	14.21	23.50
1312				3.74	0.29	17.13	
1313				4.31	0.38	31.71	
1314				4.03	0.30	30.96	
1357			1000	4.44	0.30	13.49	12.47
1358				2.89	0.24	11.24	
1359				4.14	0.29	12.90	
1360				4.21	0.25	12.23	
1361			360	3.69	0.29	8.92	8.73
1362				4.39	0.25	7.64	
1363				3.09	0.19	10.74	
1364				3.94	0.32	7.61	
1431	600	<20	1000	2.58	0.19	37.77	36.78
1432				3.13	0.19	48.36	
1433				3.61	0.14	42.31	
1434				3.71	0.17	44.68	
1435				3.76	0.12	16.59	
1436				3.16	0.10	45.00	
1437				3.52	0.17	47.83	
1438				3.31	0.16	36.22	
1439				3.56	0.16	32.85	
1440				3.51	0.18	38.83	
1441				3.52	0.12	32.49	
1442				3.70	0.20	36.92	
1443				2.75	0.10	38.11	
1444				5.42	0.67	24.43	
1445				4.23	0.98	29.33	

Length between fixture supports was 4.99mm.

Table 4-11 Mars-1a Compacted with Free Lateral Boundary (Large)

Sample	Particle Size (μm)	Width (mm)	Depth (mm)	Flexural Strength (MPa)	Average Strength (MPa)
1812	<20	5.51	1.54	21.45	17.60
1813 *		4.44	1.57	9.25	
1814		5.04	1.71	23.07	
1815 *		5.65	1.71	9.88	
1816		6.83	1.78	24.36	
1817	25-45	10.88	1.00	20.85	18.60
1818		10.09	1.10	17.96	
1819		9.90	0.99	12.72	
1820		10.93	1.22	22.86	
1821	53-90	5.69	1.16	17.93	17.96
1822		6.18	1.21	18.92	
1823		6.63	1.21	23.83	
1824		5.32	1.19	24.20	
1825		10.48	1.31	11.51	
1826		11.73	1.39	11.35	

* Samples showed visible precracks prior to testing.
Length between fixture supports = 9.78mm.
Pre-compression drying temperature = 600°C.
Compression pressure on the pistons = 800MPa.

Most of the data presented in Table 4-10 and 4-11 are combined with the data for the flexible boundary condition in the following section for plotting, to offer a comparative perspective between two different lateral boundary conditions.

Consider Samples 1361-1364. The flexural strengths of these compacts formed under 360MPa are comparable with those produced using the rigid lateral boundary; compare to Figure 4-12. The observed similarity suggests that particle crushing is sufficient to distribute npOx throughout newly fractured basalt surfaces, which contain no npOx rind. For higher pressures, consider Samples 1311-1314. Comparing to the same figure for the rigid lateral boundary, we find that the flexural strength is marginally higher than that predicted by the linear regression. At higher pressures, the lateral motion is necessary to prevent seizure of particles because the compaction arrangement is not completely self-similar, with particles marginally increasing their average coordination number under further compression. A rigid boundary promotes the seizure, representing a more hydrostatic stress condition on the sample. A free boundary condition promotes further particle motion, so that npOx can be optimally distributed across each particle at the crushed, small-size extreme.

4.4.1.2 Flexible Lateral Boundary Condition

The free lateral boundary condition achieved high flexural strengths, but pressed compacts down to wafer-thin dimensions of ~0.2mm thickness. The thin geometry poses a constraint for practical scaling and application. There exists, therefore, a practical motivation to develop an alternative method to produce thicker specimens with the same diameter of piston.

The parallel investigation on montmorillonite (Chapter 5) successfully devised a method of using a clear PVC tube to increase compact thickness, while still being able to attain relatively high strengths comparable with the free boundary condition. The flexible lateral boundary condition refers to this method. It was selected from several different trial procedures. A brief description of the method now follows.

A 30mm segment of transparent elastomeric PVC tube (Finger Lakes Extrusion Clearflex 70-1 8170-2590, Durometer hardness 70A) with outer diameter 25.4mm and wall thickness 3.2mm was fitted around the end of a hardened steel piston of diameter 19.05mm and height 25.4mm, forming a barrel cavity. The tube fits snugly around the piston, with interference produced by 3-4mm overlap. Approximately 3g of sieved and dried simulant was added to this cavity; simulant was dried at 600°C for 12h. A matching piston sealed the top of the tube before compressing the assembly. The load divided by the piston face area determined the compression pressure. The tube's exterior was exposed to ambient, and not hydrostatically controlled. In general, peak compression pressure was 360 MPa, representing the load limit of the Instron on the 19.05mm-diameter piston. About 5-10 seconds of elapsed time maintained peak pressure, after which it was relieved. A 10-kN arbor press liberated the sample manually from the surrounding flash material, consisting of unhardened, loose powder. The sample is cut using a 0.4-mm abrasive cutoff saw at low speed (MTI SYJ-40-JD, ~400 RPM setting); grinding to the final beam coupon and testing followed the rest of the procedure described in §4.3.1. Results are listed in Table 4-12 and shown in Figure 4-26.

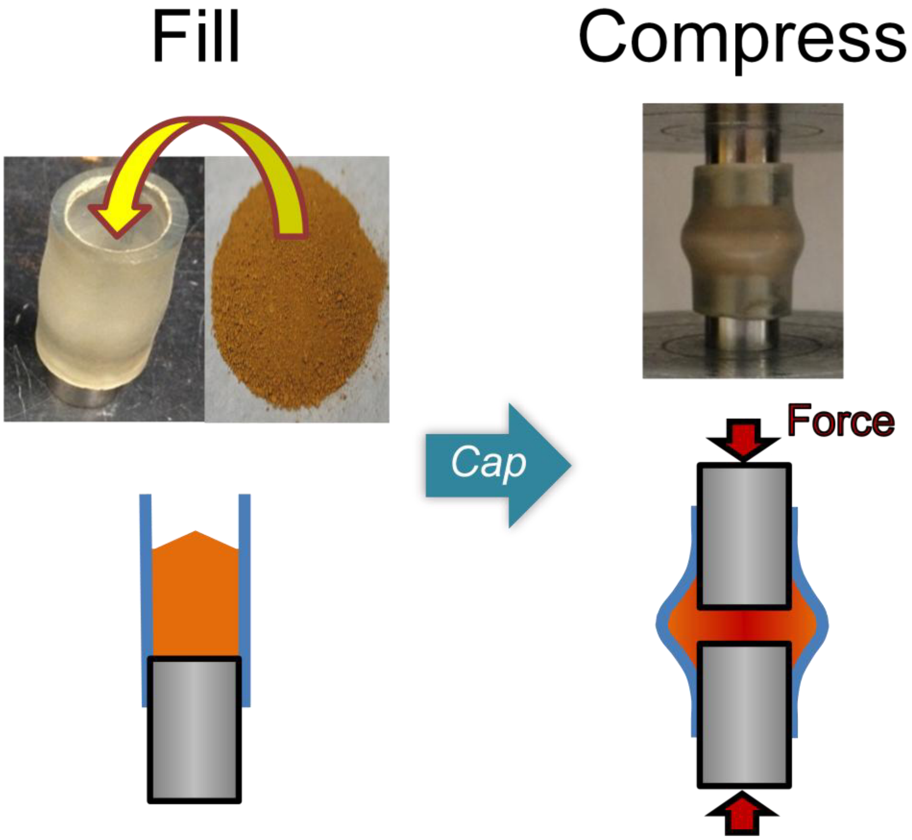

Figure 4-24 Mars-1a Flexible Lateral Boundary Compaction. Schematic described for the flexible lateral boundary condition, where compression is performed using a flexible tube. The undeformed outer diameter of the tube is 25.4mm. The upper-left shows a Mars-1a simulant pile that is 5cm wide.

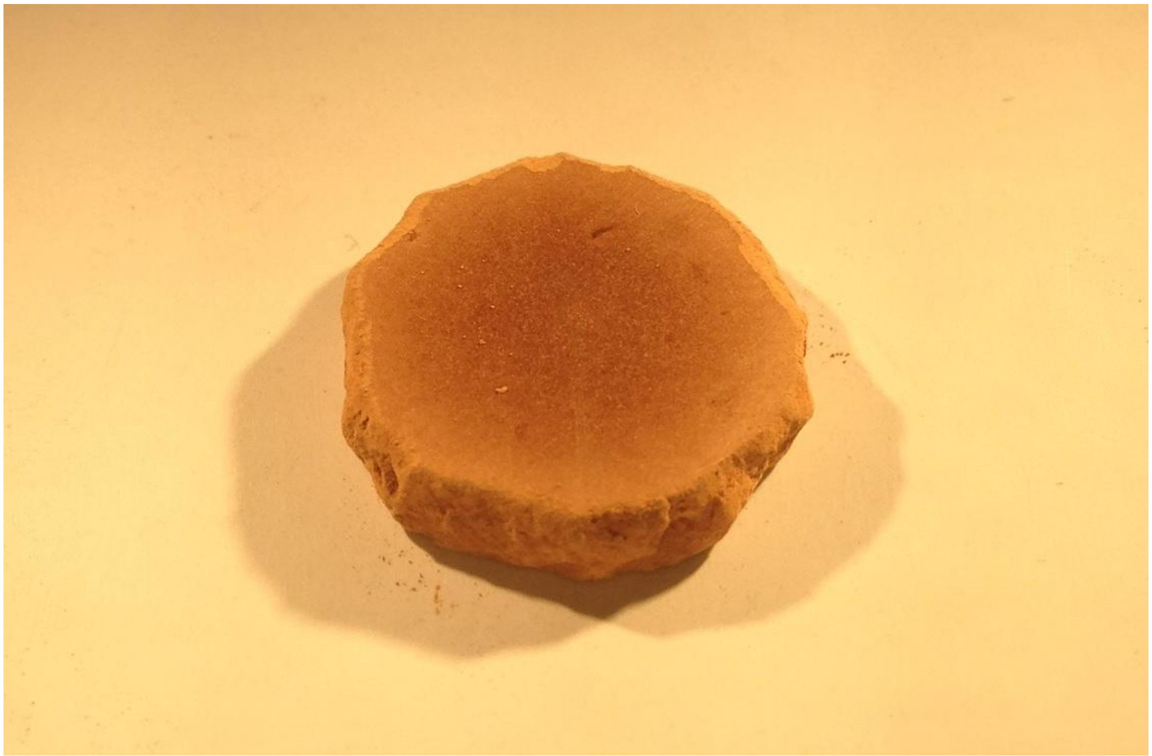

Figure 4-25 Photo of Mars-1a Compact. Compacted Mars-1a simulant with flexible boundary, before the cutting and grinding process. Compression pressure was 360 MPa and initial particle size range was 25-45μm. Particles were dried at 600°C for 12h prior to compression. The lighter areas around the periphery represent more friable areas that are removed along with the rest of the flash. Compact is ~15mm in diameter.

Table 4-12 Mars-1a Compacted with Flexible Lateral Boundary

Sample	Particle Size (μm)	Width (mm)	Depth (mm)	Flexural Strength (MPa)	Average Strength (MPa)
1894	<20	4.58	2.64	26.24	25.55
1895		6.77	3.09	32.09	
1896		7.19	2.86	23.02	
1897		6.63	3.12	20.86	
1870	25-45	7.27	3.41	22.87	24.77
1871		7.58	3.39	27.78	
1872		7.51	3.36	26.92	
1873		8.59	3.43	21.50	
1866	53-90	6.53	3.33	24.21	21.17
1867		6.95	3.37	24.01	
1868		7.41	3.05	21.56	
1869		7.58	3.61	14.89	
1902	>560	6.80	3.55	8.22	9.62
1903		6.46	3.47	11.01	

Length between fixture supports = 9.78mm.
Pre-compression drying temperature = 600°C.
Compression pressure on the pistons = 360MPa.
Tube was 19.05mm outer diameter, 3.18mm wall thickness, and durometer hardness 70A.

In Table 4-12 we notice the presence of >560μm initial particle size ranges to represent an extreme case. The lower strength is expected, based on the trends observed from compaction with a rigid lateral boundary.

The initial particle size range of interest is 0-90μm. Using data from Table 4-12 along with Table 4-11 and Table 4-5 for the free and rigid lateral boundary conditions, respectively, we can generate a comparison plot for the flexural strength as a function of particle size.

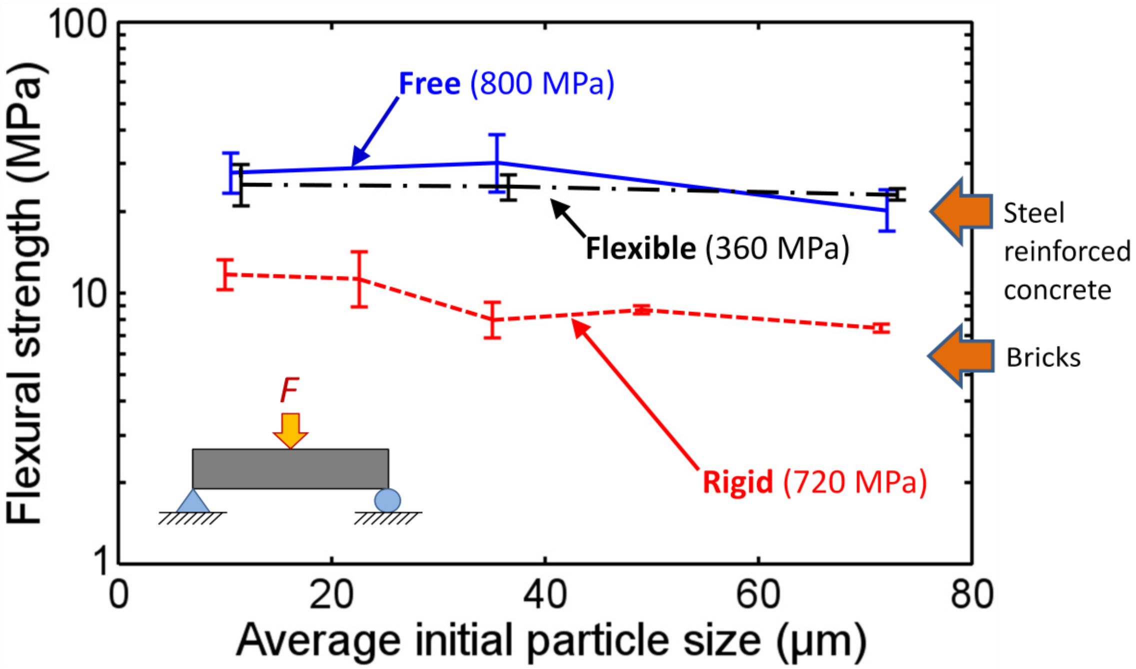

Figure 4-26 Mars-1a Flexural Strength *vs.* Lateral Boundary Condition. Flexural strength is plotted as a function of particle size for different lateral boundary conditions, labeled in bold for each series. The peak compression pressure is indicated in parentheses. Schema of 3-point bending test shown at lower-left; reference material flexural strengths shown at right.

4.4.2 Impact Compaction

The rate of loading is as of yet an unexplored parameter in addition to the boundary condition. We may investigate the effects that a high rate of loading may have on the flexural strength of the compact, as opposed to a quasi-static loading of 6mm/min setting for the Instron and SATEC machines. Towards this end, we construct drop towers to introduce a very high, shock-like rate of loading to form compacted Mars-1a samples.

4.4.2.1 Free Lateral Boundary Condition

Mars-1a simulant was sieved and dried in a furnace at 600°C for 12h. We then formed an 8.71mm diameter pellet precursor under manual compression to 150MPa using an arbor press. The precursor was inserted concentrically between pistons belonging to an oversized 19.1mm-diameter piston and die assembly, such that the pellet is essentially compressed between the flats of the pistons without contact with the die wall. Again, this configuration is referred to as the free lateral boundary condition.

Before insertion of the precursor, the die was inserted inside a polyurethane jacket (Pleiger Plastics MCTB9595145B, Durometer hardness 90A) to protect the sample against rebound strikes. The jacket had dimensions 76.3mm in outer diameter, and ~38mm inner diameter which matches the outside diameter of the steel die and introduces interference. Insertion required about 2-3kN of force with an arbor press. The steel mold’s top annular face depressed 1mm beneath that of the jacket when their bottom annular faces coincided.

Disc cushions pressed from 1g of corrugated aluminum foil protected the pistons on the top and bottom. The top cushion was situated on top of the top piston, and another was positioned beneath the bottom piston. They were pressed using the identical 19.1-mm molds at a pressure of 5kN, to 1-2mm thickness.

The jacketed assembly aligns with the drop hammer direction by a bolted fixture. The fixture is a U-shaped semicircular parapet that secures the horizontal position of the assembly using some a semi-circular acrylic piece and U-clamps. The top of the parapet connects to an acrylic guide tube 76.3mm outer diameter, with 4.8mm wall thickness. Three different lengths of guide tube corresponded to different drop heights for the hammer mass. The longest guide tube, measuring 1.52m in length, was additionally fastened at its upper end (in this particular implementation, *viz.*, secured to the ceiling) to provide stability. Mass of the hammer kept constant at 7.64kg.

Upon impact, the simulant was generally confined inside the assembly without leakage. The impact energy was determined using the equation $V = mgh$, with V being the impact energy as the potential energy of a mass under constant gravitational field. m being the mass of the drop hammer, g the constant of standard gravity, and h the height from which the drop hammer was released.

The drop weight and height remained the same. These results are shown in Table 4-13 and plotted in Figure 4-30.

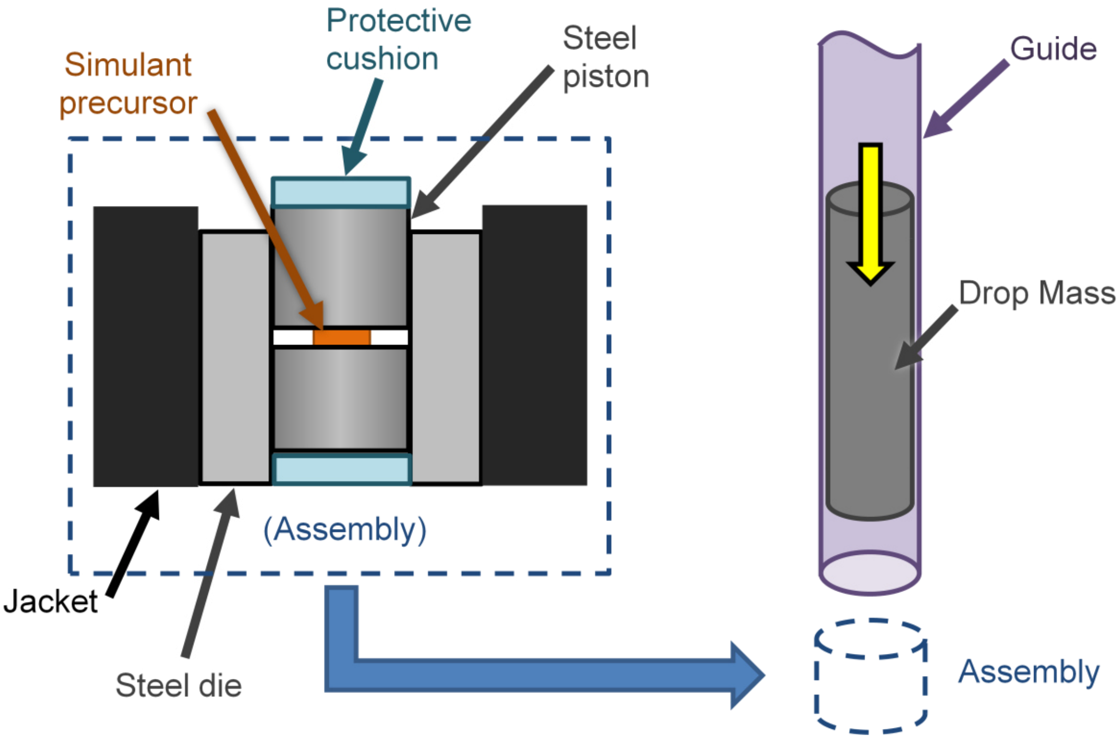

Figure 4-27 Mars-1a Free Lateral Boundary Impact Compaction. Schematic for the impact compaction process applied to the free lateral boundary condition. Both outer diameter of the jacket and guide are 76.3mm.

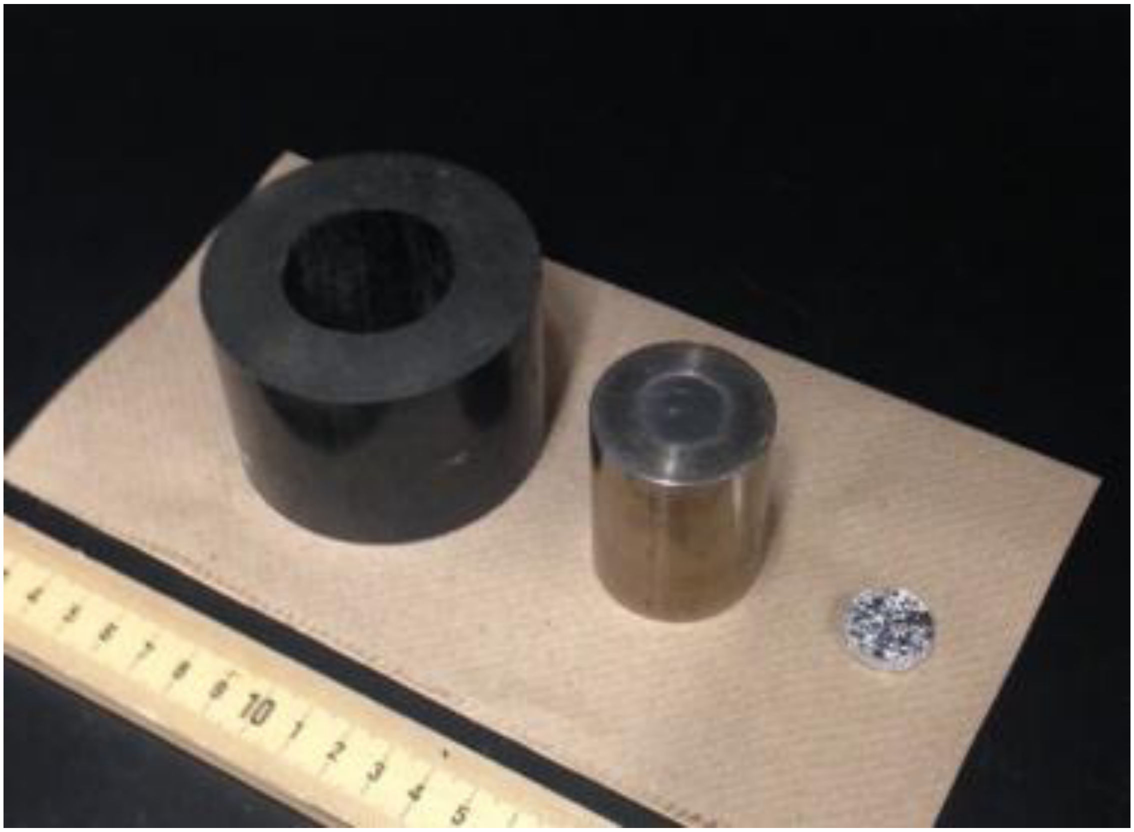

Figure 4-28 Photo of Jacket, Die, and Cushion. Photograph taken of the elastomeric jacket (left), steel die (center), and protective cushion (right). Note the free lateral boundary condition uses a relatively undersized precursor pellets positioned concentrically between pistons in the steel die. Ruler is shown for scale; the jacket, die, and cushion outer diameters are 76.3mm, 38.1mm, and 19.05mm, respectively.

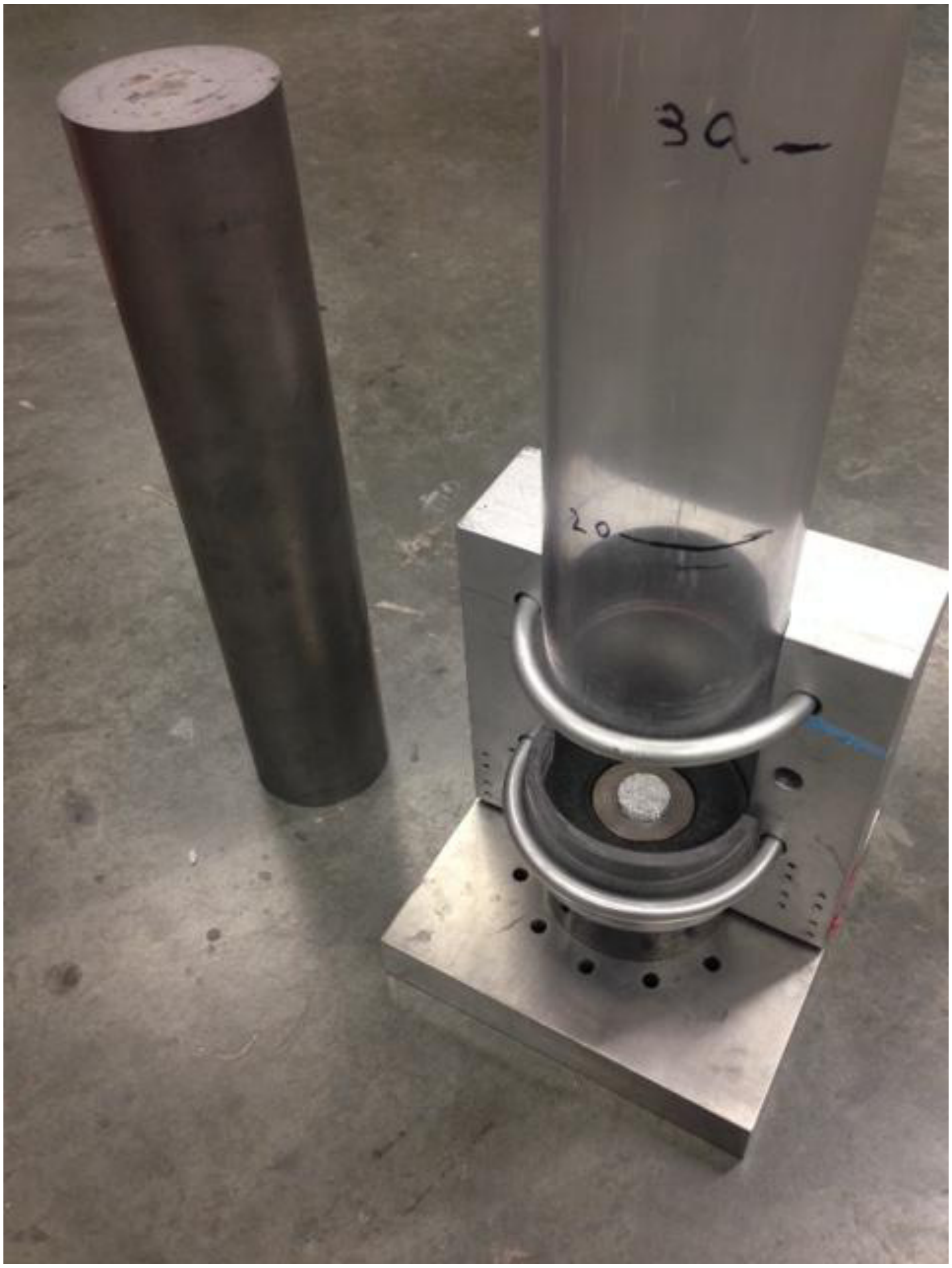

Figure 4-29 Photo of Drop Weight and Fixture Assembly. Photograph of the fixture (lower-right) used to secure the die (shown secured in place) assembly collinear with the direction of the drop weight (left) as guided by an acrylic tube (upper-right).

Table 4-13 Mars-1a Impact-Formed with Free Lateral Boundary

Sample	Drop Height (m)	Particle Size (μm)	Width (mm)	Depth (mm)	Flexural Strength (MPa)	Average Strength (MPa)
1500	1.52	53-90	4.73	0.87	32.99	28.61
1501			4.88	0.71	32.31	
1502			3.73	0.82	20.03	
1503			4.89	0.79	29.09	
1504		25-45	2.93	0.65	72.74	42.01
1505			2.94	0.67	45.37	
1506			5.21	0.90	26.82	
1507			2.85	0.85	50.57	
1508			2.55	0.85	21.92	
1509			3.02	0.82	32.66	
1510		<20	4.13	0.67	46.19	52.37
1512			3.26	0.85	34.51	
1513			3.84	0.42	53.59	
1514			3.75	0.51	75.20	
1515	0.91	53-90	4.79	0.73	30.79	21.86
1516			4.03	0.82	13.44	
1517			4.06	0.72	21.34	
1518		25-45	4.47	0.64	38.59	41.02
1519			4.21	0.79	52.36	
1520			4.54	0.75	35.82	
1521			4.47	0.85	37.31	
1522		<20	5.25	0.53	22.59	33.42
1523			5.45	0.48	43.04	
1524			4.94	0.56	30.78	
1525			4.02	0.47	37.26	
1538	0.30	53-90	4.00	0.95	29.34	19.96
1539			4.52	0.79	20.48	
1540			3.59	0.68	10.82	
1541			4.09	0.72	19.20	
1542		25-45	3.74	0.70	15.68	24.41
1543			3.74	0.63	11.35	
1544			3.96	0.67	11.79	
1545			3.68	0.67	58.80	
1546		<20	3.79	0.63	22.39	32.32
1547			3.78	0.72	41.41	
1548			3.52	0.65	32.61	
1549			3.83	0.70	32.86	

Drying temperature of particles prior to compression was 600°C.
Length between fixture supports was 4.99mm.
Hammer mass was 7.64kg.

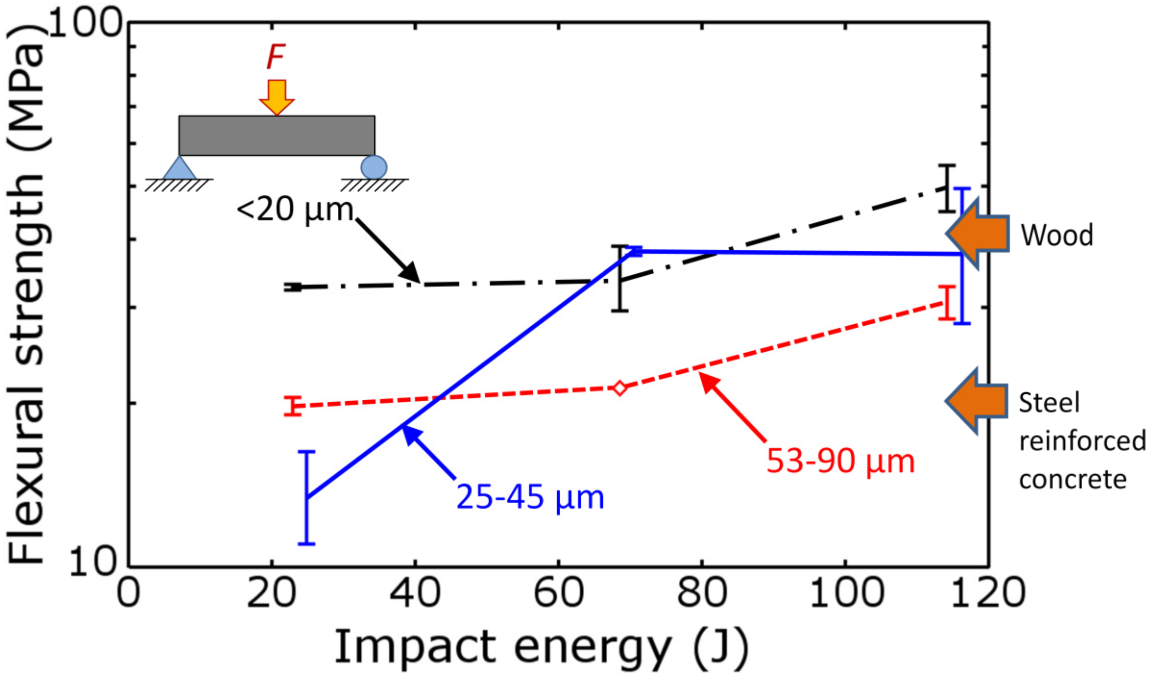

Figure 4-30 Mars-1a Flexural Strength *vs.* Impact Energy. Flexural strength of impact-formed Mars-1a compacts as function of impact energy. Three series are displayed, each corresponding to a different initial particle size bin. Error bars denote one standard deviation; diamond point denotes single datum. The drop hammer had a constant mass of 7.64kg. Three-point bending schema shown at upper-left; reference materials shown at right.

4.4.2.2 Flexible Lateral Boundary Condition

A 25mm segment of transparent elastomeric tubing (Saint Gobain Tygon R-3603 AAC00037, Durometer hardness 60A) with outer diameter 12mm and wall thickness 2.4mm was fitted around the end of a hardened steel piston of diameter 12.7mm and height 25.4mm, forming a barrel cavity. The tube fitted snugly around the piston, with some interference produced by a 5mm overlap. This interference did not allow pistons to slip freely under gravity, nor to allow particles to escape when compressed.

Approximately 2g of sieved and dried simulant was added to this cavity; simulant was dried at 600°C for 12h. A matching piston sealed the top of the tube. The load divided by the piston face area determined compression pressure. The tube's exterior was exposed to ambient, and not hydrostatically controlled. This configuration surrounding the sample, again, is referred to as the flexible lateral boundary condition. A light compression <1kN introduced a visible circumferential bulge at the midspan of this subassembly and reduced its standing height to ~6 cm.

A rubber jacket (Thomas Scientific 9544T65, Durometer hardness 50A) encapsulated the above-mentioned subassembly, as a means for protecting it against multiple rebounds. The jacket measured 38mm outer diameter, 19mm inner diameter, and 74mm height. The bottom piston became flush with the bottom of the jacket, with interference between the Tygon tube and jacket being the result of the bulge introduced to the former. In this condition, the top piston was situated ~1cm beneath the top surface of the jacket.

The jacketed assembly was manually inserted on the bottom of a cup-shaped steel base. The base measures 25.4mm in height, and contained a concentric, 38mm-diameter bore to a depth of 10.4mm. As an option, to introduce additional interference between the base and jacket, a rubber band can be stretched around the jacket. The bottom of the bore was squared and was in direct contact with the bottom piston and bottom jacket face. Cushions of diameter 12.7mm and thickness 2-3mm formed under an arbor press at 2-3kN protected the upper piston from excessive damage introduced by impact, completing installation of the assembly. The entire assembly is shown inside the dashed box in Figure 4-31.

The assembly was loaded inside the bay of an automated drop tower (Instron CEAST 9350). Development testing ensured the peak pressures was roughly characteristic of those generated by quasi-static procedures, while the energy was characteristic of the drop tower in §4.4.2.1. Hammer mass generally varied from 2.8kg to 5.8kg, defined as the total drop weight of the frame (tup), added weights, transducer, and hammer head. Compacted samples were isolated from the surrounding loose material. Figure 4-34 shows a typical impact pulse.

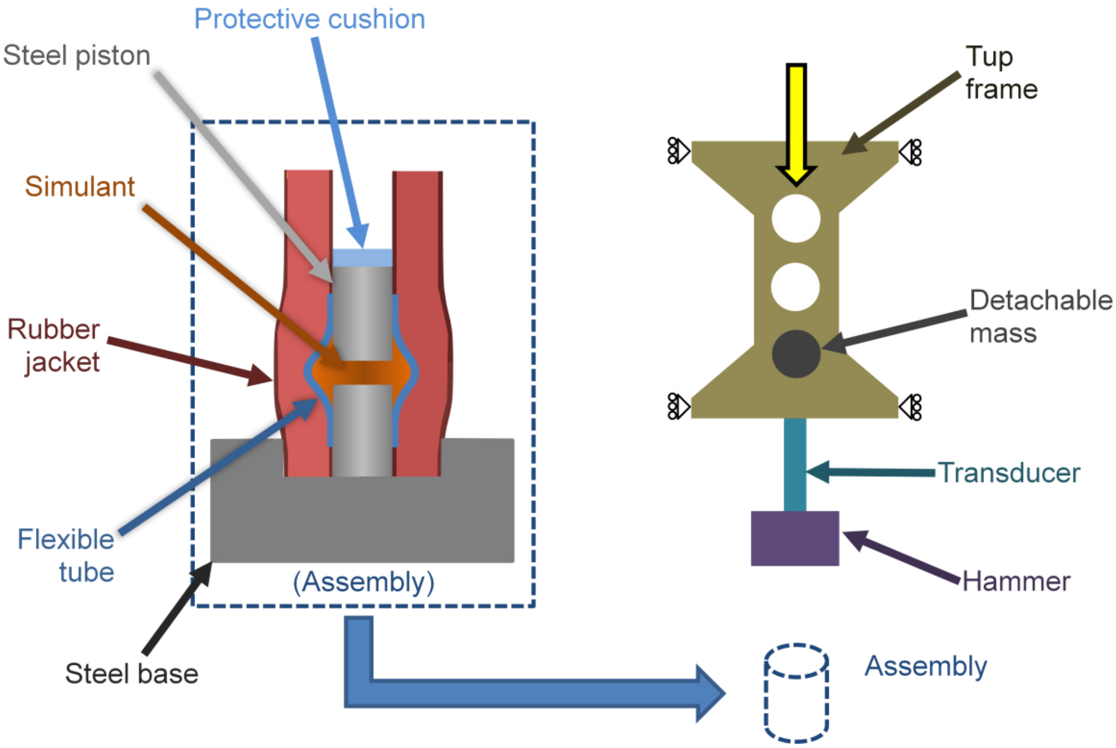

Figure 4-31 Mars-1a Flexible Lateral Boundary Impact Compaction. A schematic showing the cross-sectional configuration of all assembly components (left) as it is installed into the drop tower. The drop mass components are labeled at right.

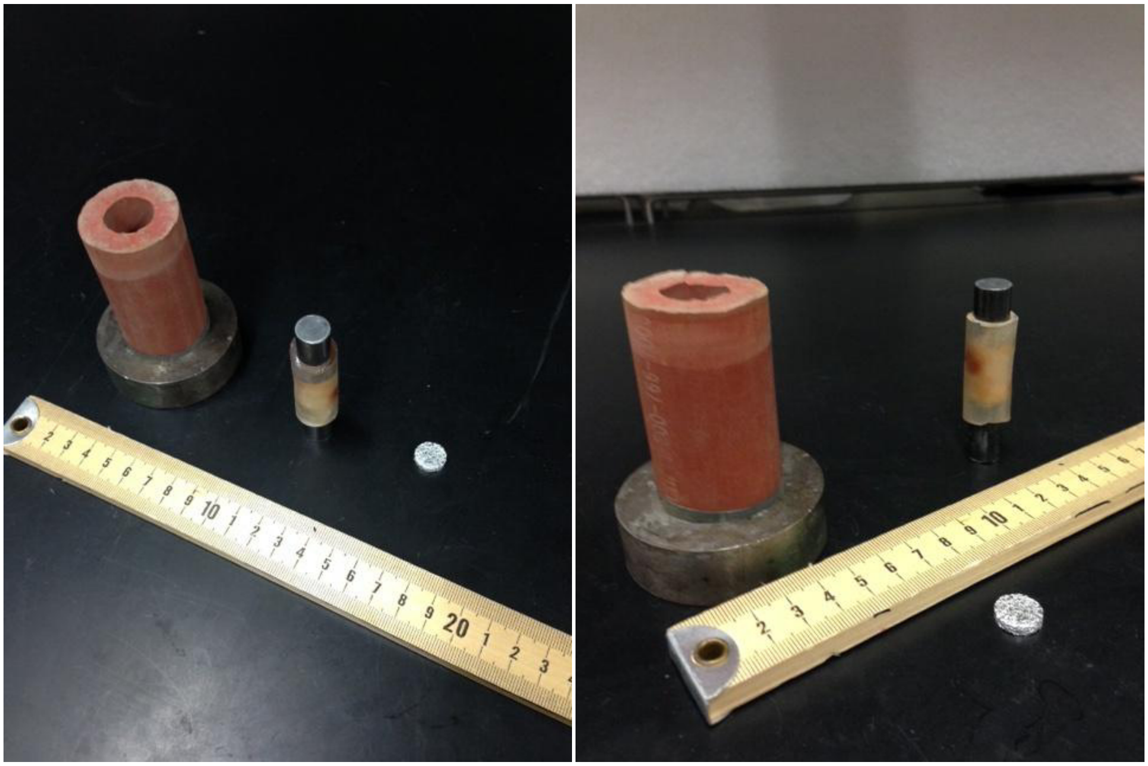

Figure 4-32 Photos of Jacket, Subassembly, and Cushion. Photographs of assembly components, with ruler provided for scale. The jacket is attached to the steel base (left in both photos). The flexible lateral boundary containing the sample is shown before the pre-compression bulge. The shock cushion (right in both photos) is loose from all other components.

Figure 4-33 Photo of Drop Tower. Photograph taken of the CEAST 9350 drop tower. The width of the drop chamber is ~60cm.

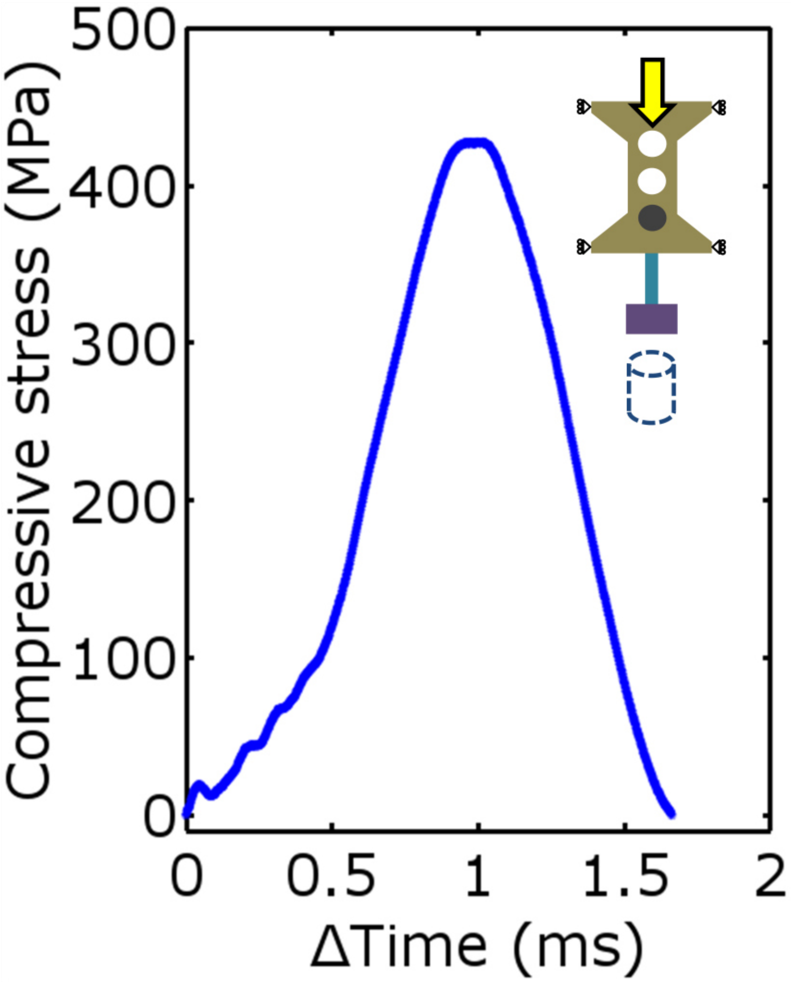

Figure 4-34 Mars-1a Impact Time History. Time history of a 120J impact pulse. Load was converted to stress by dividing by the cross-sectional circular area of the piston. The time abscissa is arbitrary elapsed (Δ) time. A schema of the drop test is shown at upper-right.

Table 4-14 Mars-1a Impact-Formed with Flexible Lateral Boundary

Sample	Drop Height (m)	Hammer Mass (kg)	Peak Pressure (MPa)	Width (mm)	Depth (mm)	Flexural Strength (MPa)
1932 *	2.6	3.77	428	5.31	2.28	5.19
1933 *			310	3.28	2.43	10.59
1934			415	4.92	2.11	42.86
1935			282	4.48	1.87	38.06
1936 *			295	4.50	2.10	30.21
1937			320	4.68	2.11	35.25
1938 *			382	3.35	2.36	51.71
1939 *			382	2.08	1.99	58.05
1940 *			311	3.11	2.38	49.18
1941 *		2.77	154	4.24	2.63	24.52
1942			141	4.76	2.36	22.87
1943			145	4.23	1.99	26.64
1944			158	4.38	2.29	24.02
1945 *			113	3.66	1.31	59.62
1946 *			133	3.95	2.24	25.66
1947			164	4.08	2.51	23.04
1948			157	3.45	3.03	17.45
1949		4.77	320	4.74	2.35	52.42
1950			322	5.07	2.47	43.87
1951			460	5.93	2.11	39.52
1952			332	4.92	1.78	49.86
1953			356	4.75	2.35	52.37
1954 *			460	5.63	2.36	55.82
1955			353	4.92	2.31	53.34
1956 *			305	4.36	1.97	52.37
1957		5.77	395	4.93	2.01	28.90
1958 *			349	5.11	2.20	53.63
1959			414	5.07	2.12	49.89
1960			386	4.88	2.39	41.94
1961			375	5.12	2.27	51.20
1962			409	4.43	1.91	63.93
1963			416	5.36	2.18	48.11
1964 *			415	5.11	2.27	87.10
1965	2.2	4.77	256	4.92	2.19	35.81
1966			346	4.61	1.83	46.72

Table 4-14 Mars-1a Impact-Formed with Flexible Lateral Boundary (continued)

1967	2.2	4.77	314	3.11	1.28	67.00
1968			298	4.60	2.63	48.48
1969			296	4.31	2.20	49.71
1970			349	4.31	2.20	60.25
1971			303	4.27	2.36	49.63
1972			250	4.12	2.57	49.85
1973	3.0		338	4.71	2.40	50.25
1974			421	4.73	1.90	52.76
1975			325	5.07	1.87	53.64
1976 *			293	4.57	1.54	46.57
1977 *			334	4.84	2.08	45.62
1978			279	4.51	1.71	35.56
1979 *			317	4.35	2.16	48.87
1980 *			280	4.32	2.46	78.30
1981 *	1.8		172	4.03	1.65	9.24
1982 *			172	4.52	1.14	7.72
1983			215	3.79	1.38	50.11
1984			235	4.34	2.31	31.15
1985			269	4.28	2.10	41.04
1986 *			185	3.82	1.20	15.16
1987 *			185	3.56	1.59	16.20
1988 *			211	3.92	1.56	12.31
1989 *			211	3.97	1.29	15.59
1990			245	4.47	2.18	43.23
1991			199	4.50	1.97	21.33

* Failure did not occur at midspan, or visible defects were spotted before test.
Pre-compaction drying temperature was 600°C.
Length between fixture supports was 4.99mm.
Particle size was 25-45μm.
Flexible tube is 12.7mm inner diameter.

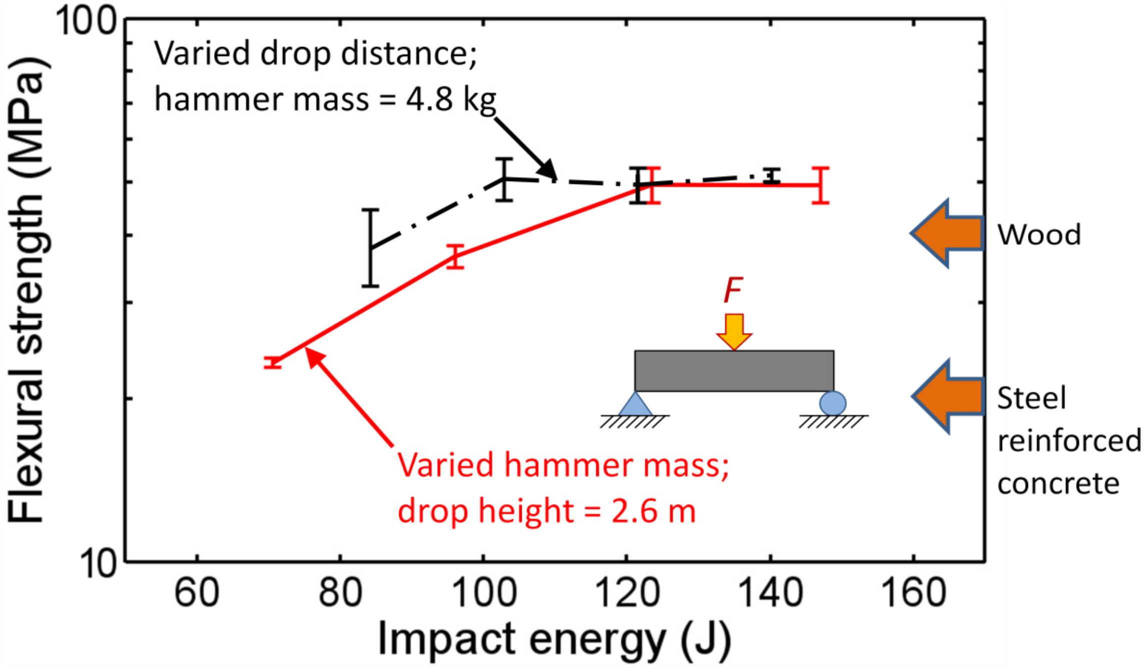

Figure 4-35 Mars-1a Flexural Strength *vs.* Impact Energy, Flexible Boundary. Impact-compacted Mars-1a flexural strength vs. impact energy for two series. One series holds the drop (hammer) mass constant while varying the drop distance, and the other series vice-versa. Schema of three-point bending is shown at lower-right; reference materials shown at right.

The trends from Figure 4-35 credibly establishes that similar impact energies will lead to similar flexural strengths of the resulting compact. In classical kinematics, the difference in squares of velocity for a given stop distance is proportional to acceleration. With Newton's second law, the acceleration is proportional to the compressive force (or stress). Thus, the magnitude of the compressive force should increase as the square of velocity and linearly with mass. Experimentally, the adjusted parameter dictating the velocity was the drop height, and linearly increasing drop height augments the square root of velocity. More simply considered is the potential energy of the drop, which varies linearly with both bass and height.

One hypothesis may be that high strain rates are essential to concentrate forces on molecular defects, because the fracture of ceramics is also determined by dislocations [30]. Sufficient time allows the transient stresses to dissipate as phonons. Compare this to the phenomenon of an adiabatic modulus for metals [31]. However, the presence of internal waves may be difficult to verify on a particle-level scale. Globally, the entire sample undergoes a uniform compression because the characteristic speed of sound requires very little time to traverse the sample. With a sample thickness of ~1mm and a speed of sound on the order of 1km/s, this required time can be estimated as $T = \sim 10^{-3}\ m \div \sim 10^{3}\ m/s = \sim 1\ \mu s$. This is much less than the characteristic period of the impact pulse determined from the time history graph (Figure 4-34). Thus, mechanical compression occurs uniformly throughout the sample and higher modes of vibration do not seem to be distinguished from it, especially in comparison with the quasi-static method.

Comparing the flexural strengths at the 100-120J impact energies (~400MPa peak pressure) with the quasi-static flexural strengths for samples compacted to 360MPa peak pressure shows that the flexural strength produced by impact significantly exceeds that of the quasi-static case, for a given peak pressure or energy of compaction. This difference may be attributed to the ability of minute amounts of npOx to phase-transform under sustained pressure. It is known that FeOOH transforms under mechanical load [17]. The characteristic time difference between quasi-static and impact compaction is on the order of $10^2 \div 10^{-3} \approx 10^5 s$, which is comparable to findings of near-complete mechanical transformation of goethite to hematite in literature [32]. The stronger phase is hematite, which would resist further crushing and exhibit lower specific surface contact.

4.4.3 Effect of Compaction with Water Content

Compacted Mars-1a is known to slake upon added water, indicating a significant interaction. It is not yet known whether introducing water into Mars-1a will promote strength development, because part of the functional groups attached to FeOOH is the hydroxyl groups, promoting hydrogen bonding in npOx. Supposing that Mars-1a is hygroscopic, we hypothesize that introducing water during compaction promotes mechanical properties (indicated by flexural strength) from remnant water molecules, and the possibility for water to dissolve and reprecipitate a small amount of npOx, which is one of the key processes behind natural sedimentary concretions [17][33].

We dried Mars-1a simulant to 600°C overnight in the furnace (Carbolite CTF 12/75/700), to establish the same baseline set of material from which strong solids were produced with the reduced lateral boundary condition. Disc-shaped pellets (precursors) were then made by pressing the dried powder inside of an 8.71mm die (that is, with the rigid lateral boundary).

The precursors, once extracted from the die, were rehydrated with various amounts of water in two steps. First, one drop of water (~0.030g) was added directly on the face of a pellet using a pipette, while concentrically positioned on the face of an oversized 19.05mm-diameter piston. This ‘floods’ the precursor sample beyond its plastic limit and represents the maximum added water content. Second, the pistons along with the wetted precursors were brought to air-dry at 80°C for between 8min to ~1.5h in order to attain water contents ranging from 2wt% to 8wt%; the water content is checked intermittently every 5min using a balance with sensitivity 0.1mg. Nominal water contents were 2.3, 7.8, and 16.8wt% besides the furnace-dry state. At 16.8wt% water content, no drying was performed at all.

All compaction work was carried out in the ambient environment. The time lapse between furnace drying and compaction was anywhere between 15min to several hours, during which atmospheric water could have adsorbed onto the Mars-1a simulant surfaces and served as an inadvertent agent of lubrication and bonding.

Rehydrated (or dry) pellets were compressed on the same oversized piston inside the 19.05mm die to 800MPa using a load-displacement testing machine (Instron 5582) with a loading rate of 3mm/min. The lower loading rate is to account for thin dimension of the sample. We applied a gentle torsion to liberate one piston from the compacted montmorillonite, which adheres to the other piston. A few dabs with tissue remove the small amounts of water around the periphery of the compact, still adhering to one piston. This piston with the attached sample is then dried for a final time at 100°C in an oven for 2h. After this final drying, the compact is ground into a beam specimen and tested in three-point bending setup.

The entire procedure was repeated for three initial particle size bins: <20µm, 25-45µm, and 53-90µm. A plot of the overall results is shown in Figure 4-36, while the individual data points from Table 4-14 can be seen in Figure 4-37.

Table 4-15 Mars-1a Compacted with Various Water Contents

Sample	Measured Water Content (wt%)	Target Water Content (wt%)	Initial Particle Size (µm)	Width (mm)	Depth (mm)	Flexural Strength (MPa)
1629	(dry)	0	<20	3.59	0.61	27.46
1630				2.90	0.46	29.15
1631				3.72	0.57	34.19
1632				3.73	0.68	42.14
1633				3.98	0.75	52.06
1634				4.12	0.54	34.83
1635				4.74	0.61	33.78
1636				4.16	0.66	49.03
1637			25-45	4.23	0.64	49.42
1638				4.33	0.58	34.38
1639				3.79	0.42	25.08
1640				3.78	0.77	40.58
1641				4.03	0.59	46.42
1642				4.05	0.74	52.31
1643				3.97	0.60	49.75
1607			53-90	4.44	0.66	29.10
1608				4.59	0.50	14.55
1609				4.59	0.64	21.54
1610				4.54	0.63	24.55
1611				4.18	0.75	22.47
1612				4.27	0.75	19.26
1613				3.25	0.80	21.95
1614				4.42	0.68	21.53
1718	2.14	2	<20	4.00	0.67	38.43
1719	2.45			2.97	0.56	27.73
1720	2.10		25-45	3.22	0.66	54.59
1722	2.40		53-90	3.10	0.55	20.75
1723	2.90			3.88	0.54	18.92
1678	6.70	8	<20	3.59	0.82	40.84
1679	5.40			3.22	0.64	18.05
1680	5.80			3.84	0.65	33.68
1681	7.70			3.80	0.62	15.12
1682	8.10			4.00	0.62	36.07
1683	9.52			3.33	0.65	39.90
1684	6.63			3.95	0.70	16.90
1685	6.83			3.18	0.60	34.26
1686	9.80		25-45	4.24	0.55	33.21
1687	10.31			4.26	0.56	10.70
1688	10.60			3.45	0.70	61.28

Table 4-15 Mars-1a Compacted with Various Water Contents (continued)

1689	8.31	8	25-45	4.60	0.67	46.90
1690	6.12			3.37	0.77	42.71
1691	8.80			3.87	0.67	32.49
1692	7.20			3.30	0.74	44.15
1693	~8			3.91	0.62	35.11
1694	~10		53-90	3.61	0.71	35.78
1695	6.63			3.75	0.75	17.99
1696	~15			4.13	0.75	17.27
1697	9.4			3.43	0.69	27.87
1698	10.1			3.87	0.73	17.02
1699	~15			2.52	0.70	15.21
1700	9.5			4.06	0.73	20.03
1701	~5			2.97	0.72	19.73
1656	17.15	16	25-45	4.04	0.81	23.80
1657	16.72			4.12	0.89	45.99
1658	16.80			3.93	0.83	53.94
1659	17.28			4.15	1.00	53.56
1660	16.67			3.39	0.74	32.86
1661	16.10			3.59	0.71	43.06
1662	13.99			3.63	0.79	43.98
1663	16.78			3.58	0.78	21.89
1664	16.54			4.13	0.78	28.00
1665	13.73			3.89	0.73	22.57
1666	15.81			3.54	0.80	24.75
1667	16.14			3.75	0.79	20.79

Compression pressure = 800MPa.
Drying temperature prior to compression = 600°C.
Compression performed with free lateral boundary condition.

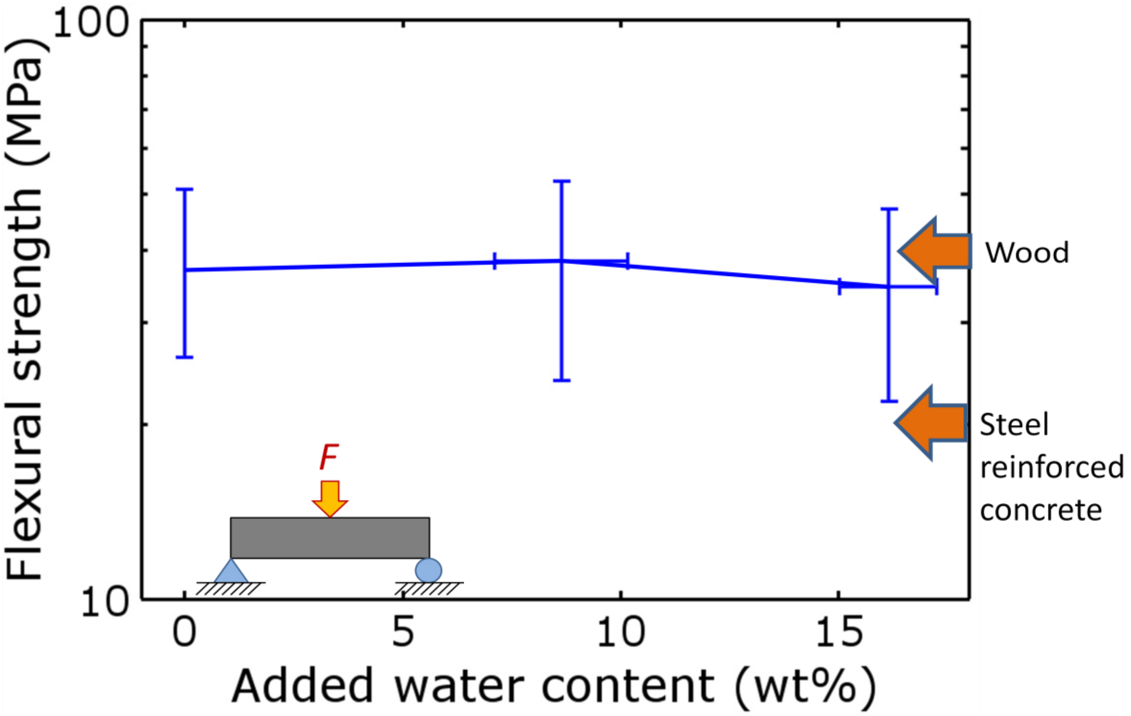

Figure 4-36 Mars-1a Flexural Strength *vs.* Added Water. Flexural strength of rehydrated Mars-1a simulant compacted to 800MPa followed by subsequent air-drying, plotted as a function of the added water during rehydration. The horizontal error bars show the standard deviations of the actual water contents with respect to the nominal (target) water content. Comparison references are shown at right; test schema at lower-left.

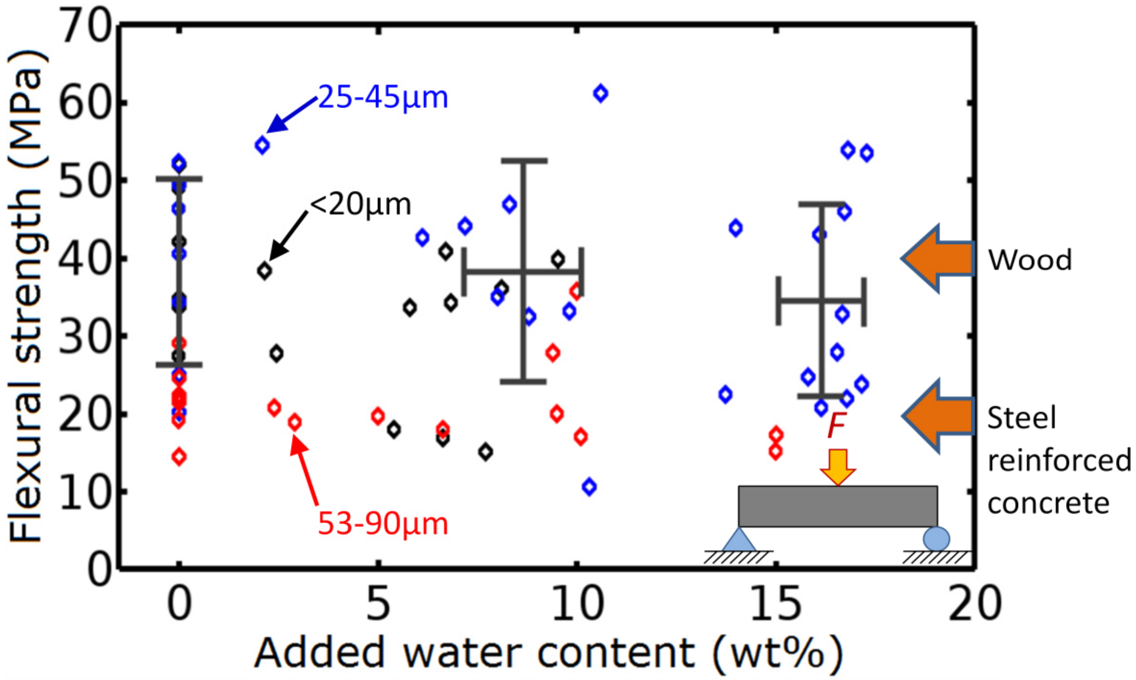

Figure 4-37 Mars-1a Flexural Strength vs. Added Water Scattergram. Linear plot of flexural strength of rehydrated montmorillonite compacted to 800MPa followed by subsequent air-drying, plotted as a function of the added water during rehydration. The horizontal error bars show the standard deviations of the actual water contents with respect to the nominal (target) water content. Individual data points are included, with the color corresponding to the initial particle size bin. Comparison references are shown at right; test schema at lower-right.

The results in Figure 4-36 indicate that for relatively high compression pressures of 800MPa, the strength of the resulting compacts is, within variation, the same for all levels of added water. Adding water, although fully wetted to the npOx, does not serve to functionally increase the mechanical properties of the compact during compaction. Convex particles are expected to harden predominantly by crushing, rotation, and shearing during compression to very high-pressures independently of the presence of water.

With hardening of the solid to ultra-high pressures like 800MPa, density increases. The density increase associates with a rise in elastic modulus, such that the contribution of water to the overall sample stiffness progressively minimizes with further loading. The effective stress (i.e., the stress acting only on the skeletal particle network) is therefore approximately the same as the applied stress during peak loading. Water also consolidates out through a relatively efficient interstitial pore network. Contrast this result to findings for montmorillonite clay (Chapter 5), which does not have the same interstitial geometry.

4.5 Sample Size Effects of Compacted Mars-1a Flexural Strengths

The tables of flexural strength in the preceding sections show that process conditions can considerably influence the size of compacts for both rigid and reduced lateral boundary conditions. The flexible boundary condition increased the characteristic thickness of the compact over that of the free lateral boundary condition. Likewise, the SATEC machine increased the volume of compacts with identical lateral boundary condition by virtue of its higher load capacity.

Very often, however, strengths are subject to inherent statistical variation due to defect populations in solids. Larger samples would tend to exhibit less strength because of the largest flaw size permissible is larger as well. The two-parameter Weibull analysis is a standard tool for describing the failure distribution of brittle solids[30] [34].

For a simple assessment of strengths with respect to size of compacted Mars-1a, we examined the largest groups of samples fabricated under identical process conditions. We select the following:

- 367-370, 375-387, 392-395, 406-407, 415-416, 423-424, 441-442, 449, 452-454, 457-458, 461, 473-475, 645-646, 648-649, 1077-1080 (rigid boundary quasi-static, 25-45μm, 360MPa)
- 1431-1445 (free boundary quasi-static, <20μm, 1000MPa)
- 1866-1873, 1894-1897 (flexible boundary quasi-static, <20μm + 25-45μm + 53-90μm, 360MPa)
- 1504-1509, 1510-1514, 1518-1521, 1522-1525 (free boundary impact, <20μm and 25-45μm, >68J impact energy)
- 1949-1953, 1955, 1957, 1959-1963, 1973-1975, 1978 (flexible boundary impact, 25-45μm, >120J impact energy)

We seek to generate a scattergram of these data by plotting the logarithm of flexural strength, $\log R$, as a function of the logarithm of beam volume, $\log V$. The scatter is shown in Figure 4-38.

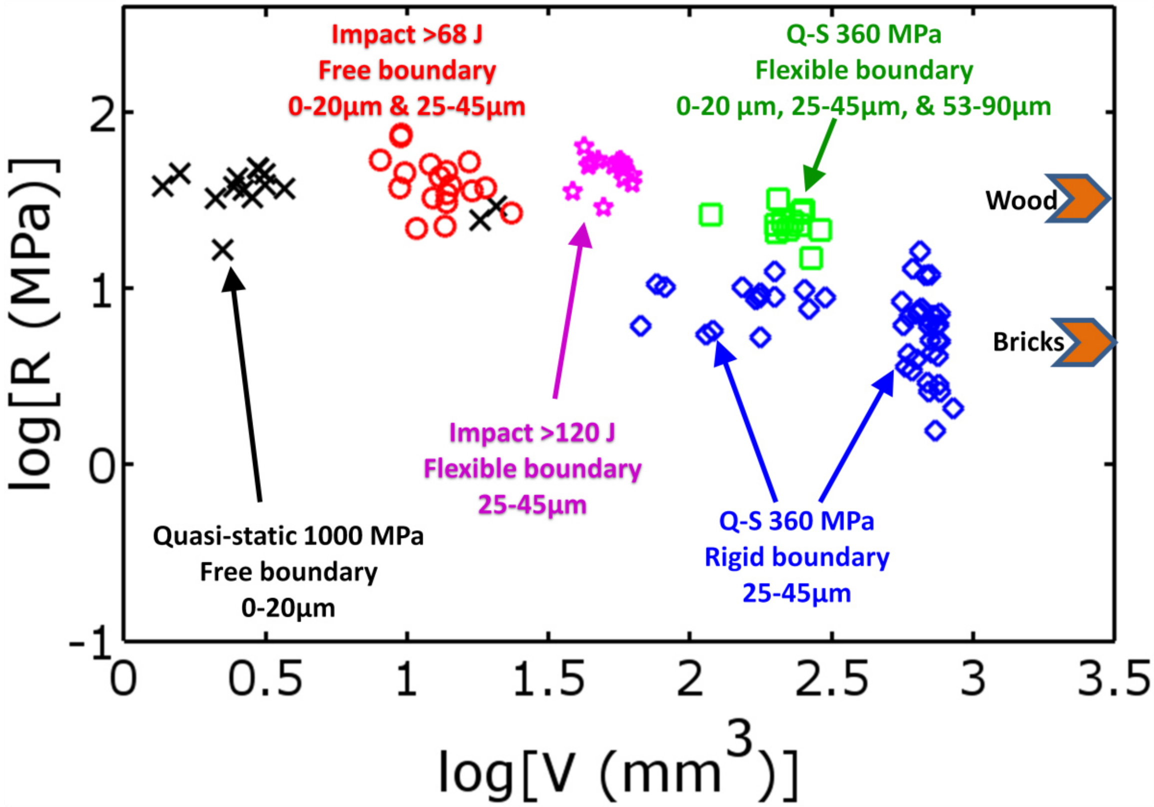

Figure 4-38 Mars-1a Flexural Strength *vs.* Sample Volume. Empirical scatter plot of experimental flexural strengths versus the sample volume, taken from configurations containing at least 12 samples. Reference flexural strengths are shown on the right. The vertical axis bottom ordinate is chosen as the lower limit of fragility anticipated by manual handling.

In Figure 4-38, flexural strengths closely associate with the processing configuration and not the volume of the sample. That is, for each group representing a process configuration, no obvious linear trends are apparent. The most obvious example is the difference between the rigid and flexible boundary conditions for beams of volume 100-300mm^3. We can verify the absence of significant trends within each process configuration using correlation coefficients and Pearson's product moment correlation *p*-values. The former ranges from -0.019 to -0.437, and the latter ranges from 0.219 to 0.945.

Although Weibull analysis can be used to extrapolate strengths, we caution that the process configuration defining each group exerts significant impact on the resultant flexural strengths and may affect a global trend analysis significantly. A possible exception is as follows: the black x's and green squares in Figure 4-38 represent very close process configurations, each belonging to one of the reduced lateral boundary conditions, but with different pressures and initial particle sizes. If one were to regard these as a single data set, the line drawn would appear to be nearly horizontal, having only a slight negative trend. Thus, the reduced boundary condition is robust against size effects to at least two orders of magnitude and offers confidence that processing with a reduced boundary can be scaled up without detriment to mechanical strength.

4.6 Model of Mars-1a

4.6.1 Simple Description of Particle Crushing

The main particle motions responsible for the onset of tensile strengthening are crushing, shearing, rotation, and translation. Here we give a relatively simple description the crushing of particles. Our goal is to capture the behavior of the particle size distribution in the sample with applied compressive stress. The rest of the motions are thought of as agents assisting in the flow of material, away from regions of high stress. We proceed directly from first principles with a basic set of assumptions, specifically:

1. The distribution of particle size follows a two-parameter Weibull distribution probability density function (PDF), as demonstrated by Tenchov and Yanev [35].
2. A particle fractures perfectly into two particles, each having an effective diameter that is a constant factor, G, of the original particle.
3. The strength increase due to the comminution of particles is due to a combination of increased particle coordination number and intrinsic strength governed by defect population, but does not distinguish between the two.
4. When crushed, the cumulative density function (CDF) of failure is controlled by the same statistical parameters that produced the original distribution in the first place; statistical parameters remain constant.
5. A uniaxial, isostress condition exists for all particles.

Writing x as the particle diameter, the initial PDF of the particle size S_0 before the onset of crushing is

$$S_0(x) = \frac{x^{\alpha-1}}{x_o^{\alpha}} e^{-\left(\frac{x}{x_0}\right)^{\alpha}}$$

with x_0 a characteristic size constant and α a graph constant. The CDF of particle failure F_0, under applied stress σ, describes crushing throughout the sample:

$$F_0(x) = 1 - e^{\left(\frac{x}{x_0}\right)^{\alpha}\left(\frac{\sigma}{\sigma_0}\right)^{\beta}}$$

with σ_0 a characteristic strength constant. Resembling canonical Weibull form, this function is more robust than other possible expressions. Nakata and coworkers empirically determined the constant $\beta = 3$ [36]. We treat the variable σ as a constant, although multivariate formulation is certainly possible for other scopes.

Call the breakage curve with respect to the original size distribution B_0

$$B_0(x) = S_0\, F_0$$

Recall the constant G is the ratio of daughter-to-original effective diameter. We can express the production curve P of newly-crushed daughter particles as

$$P_0(x) = \frac{2B_0(Gx)}{G} \equiv \frac{2B_0^{(G)}}{G}$$

using the parenthetical superscript as shorthand for a scaled argument in a function. A factor of 2 appears on top because two daughter particles form for each fracture. The factor G appears again in the denominator because the production curve is shrunk along the abscissa in $B^{(G)}$, yet should be the area of the B_0 curve were it not for the fact daughter particles are produced.

Overall, during a single, crushing step at pressure σ, B subtracts from S_0, producing P:

$$S = S_0 - B_0 + P_0 = S_0 - S_0F_0 + \frac{2B_0^{(G)}}{G}$$

giving rise to the current, instantaneous distribution S. An alternate expression is the sum of the original distribution and the change in the distribution, respectively:

$$S = S_0 + \Delta S_0$$

$$\Delta S_0 = \frac{2B_0^{(G)}}{G} - B_0$$

The above expression applies to an arbitrary, discrete step. Within this step, an infinitesimal increment is

$$d(\Delta S_0) = \frac{2dB_0^{(G)}}{G} - dB_0$$

Substituting, there follows

$$(1 + F_0)dS + SdF_0 = dS_0 + \frac{2}{G}\left(F_0^{(G)}dS^{(G)} + S^{(G)}dF_0^{(G)}\right)$$

which is an implicit differential equation that is not readily evaluated. However, in a single-crush event, we can integrate the change in the distribution ΔS_0. Although this introduces some error, being wholly taken with respect to the original particle size distribution, it is sufficient qualitatively. The single-crush approximation is written as

$$\Delta S_0 = \frac{2}{G}\int dB_0^{(G)} - \int dB_0$$

To keep this analysis as simple as possible, we only choose a univariate form with respect to separation distance x. The distribution works out to

$$S = \left(\frac{\alpha x^{\alpha-1}}{x_0^{\alpha}}\right)\left\{e^{-\left(\frac{x}{x_0}\right)^{\alpha}} + \frac{\left(\frac{\sigma}{\sigma_0}\right)^{\beta}}{1 + \left(\frac{\sigma}{\sigma_0}\right)^{\beta}}\left[\left(\frac{2e^{-\left(\frac{x}{Gx_0}\right)^{\alpha}}}{G^{\alpha+1}} + e^{-\left(\frac{x}{x_0}\right)^{\alpha}}\right)\left(1 - e^{\left(\frac{\sigma}{\sigma_0}\right)^{\beta}}\right)\right]\right\}$$

but is not normalized. The normalized version reads

$$\bar{S} = \frac{S}{\int_0^{\infty} S\ dx}$$

with the denominator simply a constant factor of how much S is too large. In realistic situations, G may take on values from 0.5-0.8. The expression for S is able to qualitatively capture the shifting of the distribution, where the PDF peak moves towards zero with greater height. Of interest is the typical or mean size, which we calculate as the expected value μ of the distribution [11]

$$\mu = \int_0^\infty x\bar{S}\ dx$$

Evaluating this [37], one arrives at

$$\mu = -\frac{x_0}{\alpha\int_0^\infty S\ dx}\Gamma\left(\frac{1}{\alpha}\right)\left\{\frac{3\left(\frac{\sigma}{\sigma_0}\right)^\beta - \left[1+4\left(\frac{\sigma}{\sigma_0}\right)^\beta\right]\left[1+\left(\frac{\sigma}{\sigma_0}\right)^\beta\right]^{1+\frac{1}{\alpha}}}{\left[1+\left(\frac{\sigma}{\sigma_0}\right)^\beta\right]^{2+\frac{1}{\alpha}}}\right\}$$

and this obeys the necessary condition that $\mu \to 0$ as $\sigma \to \infty$. The takeaway is that this expression for the crushed mean, albeit from a single-crush approximation, predicts that crushing will always occur with increased stress. For comparison, the original or uncrushed distribution mean is

$$\mu_0 = \frac{x_0}{\alpha}\Gamma\left(\frac{1}{\alpha}\right)$$

In summary, the stress increases without bound to drive the particle size to null. The stress increase physically manifests itself as strain energy in stressed particles. The SEM particle counting exercise in Chapter 6 verifies that crushing continues to occur with increased compressive stress, with the PDF peak shifting leftwards during the crushing of particles.

Elsewhere, surface energy is used by some authors in relationship to geotechnical shear strength [38]. Supposing that indefinite crushing occurs without friction, the applied stress increase then derives from the increase in specific area. Compaction occurs to the point where the infinitesimal work performed by the available loading is balanced by the rate of increase of surface energy, arresting at peak loading.

4.6.2 Size Dependence

One seeks to describe why smaller particle sizes achieve higher strength in compacted Mars-1a, using a simple and qualitative description with basic assumptions. With pressure known as the dominant factor in mechanical properties, our analysis assumes (but is not particular to) the post-compressed state of the solid. To proceed, assume the following:

1. A uniform particle diameter representing the expected value of the real distribution can model the behavior of the real particle system.
2.
    a. If the particles are spherical, the overall separation force depends on the number of connections between particles, with a certain unit force between particles.
    b. If the particles are plate-like, the overall separation force depends on the area of contact between particles.
    c. For particles in between, the results of the two above are interpolated.
3. The required shearing of small particles in the zone of true contact (*i.e.*, within a few nm) is the same as that in tension due to far-field interactions from a relatively greater displacement.
4. A uniaxial, isostress condition exists for all particles.

Consider a square array of particles of uniform particle diameter with a mechanical force exerted normal to that plane. The dimensions of the square are s x s, and the particle diameter is d. The number of particles N inside this square is

$$N(d) = \left(\frac{s}{d}\right)^2$$

Per the assumption list, first assume spherical packing. Each particle-particle connection has a unit force of separation ΔF_0, with the total force of separation F being

$$F = N(d)\,\Delta F_0$$

Two factors are left out of the above are purposely omitted for simplification. The first is geometric correction, that is, trigonometric scaling. The second is the coordination ratio, for close-packed lattice-like configurations of particles. If the force is applied consistently over the whole area s^2, the strength is

$$\sigma = \frac{F}{s^2} = \frac{N(d)\Delta F_0}{N(d)d^2} = \frac{\Delta F_0}{d^2}$$

So far there has been no discussion of the dependence of ΔF_0 on d. There is almost always some sort of dependence, but for non-spherical geometries there could be a near-constant value of the unit force.

Consider, for a first example, an acicular vertex of a polyhedron upon contact with a neighboring particle face. The actual cleavage surfaces of particles, as well as randomly oriented grains of a substance with at least one dimension much smaller than the other(s), motivate such a picture. Only the vertex, being a true geometric point, has a 'true' contact condition with a neighboring particle. Thus, no matter the size of the particle, the same point maintains true contact and the unit force required to pull particles apart scales invariantly with the radius of particles.

As a second example, we imagine two contacting spheres. Certain curved faces of solids in contact with each other motivate this picture. The amount of surface in contact, notwithstanding the Hertzian stress contact, would depend on the curvature of the sphere. For rigid bodies, surface contact within a small threshold is reciprocally proportional to the radius. It can be readily shown that, given a constant small-distance threshold, that the amount of contact interface (being the unit force) is proportional to the radius. There can be a more detailed exposition of this with Hertzian contact theory, and other contact theories including adhesion, but is considered beyond the scope of this rudimentary assessment. One also arrives at a linear dependence of unit force on particle radius if a straight edge of one particle contacts a planar face of another.

As a third example, suppose there are particles with one dimension much less than the other two, in an aligned configuration. Their flat faces would dictate the unit force, required to pull apart the particles, and thus the dependence is upon the square of the radius.

In light of the three examples above, the degree of the dependence of the unit force ΔF_0 on the particle diameter can then be stated as

$$\Delta F_0 \propto d^n \qquad n \in [0,2]$$

where n is a parameter with some possible integer values of 0, 1, or 2 as discussed above, but actually represents a continuous range due to the large number of particles of various geometries in any practical specimen. We have, consequently,

$$\sigma \propto d^{n'} \qquad n' \in [-2,0]$$

which describes the possible ranges of slope on a log-log plot of flexural strength versus actual particle size. With this model, linear trends in said plots cannot be steeper than slope -2, nor be positive. Although quite broad, these slope limits are in agreement with the experimental data. The equation form of this proportionality, putting a constant in front, also agrees with the model proposed by Orowan and Knudsen [9].

One of the most straightforward ways to compute a likely estimate of the parameter n is to proceed from the argument of proportionality of energy on a linear-elastic stress-strain diagram. This is applicable to highly compressed solids. Denoting the ultimate strength as σ_u and the strain energy as U,

$$U \propto \sigma_u^2$$

Since the total surface area A of most fracture surfaces shows dependence

$$A \propto d^{-1}$$

If the energy required for any form of adhesion per unit is constant, there follows

$$\sigma \propto d^{-\frac{1}{2}}$$

as consistent with the Hall-Petch expression for metallurgical grain size. As a consequence $n = 3/2$ is the expected modal value.

4.6.3 Theoretical Cohesive Strength of Mars-1a

We can estimate the theoretical cohesive strength of Mars-1a by its active component, npOx. Recalling that npOx can be a collection of iron oxides and oxyhydroxides, we choose to model the force potential for a fairly generic unit common to all compounds in npOx, namely the interaction between iron and oxygen. This complex nature of the force potential is expressed in many forms, such as the Mie or Lennard-Jones potential [39]. A study by Rustad and coworkers expresses the Fe-O force field with the following potential [40]:

$$E = Ae^{-Br} + \frac{C}{r^6} + \frac{D}{r^{12}}$$

where E is the Fe-O interaction energy, r is the separation distance, and the rest of the letters are constants, given as [40]

$$A = 1827.7\ e^2/\AA$$

$$B = 4.9255\ \AA^{-1}$$

$$C = -2.1362\ e^2\AA^5$$

$$D = -74.680\ e^2\AA^{11}$$

The units convert as $1\ e^2/Å = 2.3072 \times 10^{-18} J$. The derivative of energy with respect to separation distance gives the interaction force F:

$$F = \frac{dE}{dr} = -ABe^{-Br} - \frac{6C}{r^7} - \frac{12D}{r^{13}}$$

Another derivative, the rate of change of force with respect to distance, equals zero to correspond to the force maximum. Numerically, one finds the distance at maximum force to be

$$r = 1.63\ Å$$

The unit force ΔF_0 required to pull apart an iron atom from an oxygen atom is then

$$\Delta F_0 = F(1.63\ Å) = -2.2 \times 10^{-8}\ N$$

The lattice parameter between iron and oxygen is about 1nm. Thus, the cohesive strength can be calculated as

$$\sigma = \frac{\Delta F_0}{1\ nm^2} = \frac{2.2 \times 10^{-8}\ N}{10^{-18}\ m^2} = 22\ GPa$$

Assuming an elastic modulus of 220GPa for Fe-O bonds based on dense iron oxides[41], this result agrees rather well with one of the adjusted sinusoidal approximations popular in structural materials and fracture mechanics (*e.g.* [34][30]):

$$\sigma \approx \frac{E}{10} = \frac{220\ GPa}{10} = 22\ GPa$$

This strength value is, of course, much higher than that reported for the actual strengths of the compacted solids. We attribute the presence of defects, such as voids and inclusions, as responsible for the strength decrement. Notably, the experimental work has found that the basaltic component of Mars-1a act as inert fillers, and can be regarded as inclusions. Inspection with the data also shows the strength of real solids is about several orders of magnitude less than the calculated theoretical strength, which is typical.

The scope of this work does not necessarily warrant indefinite attempts of closing the gulf between real-world strengths and theoretical strengths. Rather, it is sufficient to demonstrate that the processing can significantly increase strength. Furthermore, the objective of this discourse is to provide a perspective on the fact that the limit of strength is much higher than obtainable by our methods. The motivation is loose, because a 30MPa flexural strength can be deemed satisfactory for most civil-structural applications.

This chapter, in part, contains material that has been submitted for publication in 2016 with authors Brian J. Chow, Tzehan Chen, and Yu Qiao. The dissertation author was the experimental investigator and first author of this paper.

4.7 References

1. Leshin, L. A., Mahaffy, P. R., Webster, C. R., Cabane, M., Coll, P., Conrad, P. G., Archer Jr., P. D., Atreya, S. K., Brunner, A. E., Buch, A., Eigenbrode, J. L., Flesch, G. J., Franz, H. B., Freissinet, C., Glavin, D. P., McAdam, A. C., Miller, K. E., Ming, D. W., Morris, R. V., Navarro-González, R., Niles, P. B., Owen, T., Pepin, R. O., Squyres, S., Steele, A., Stern, J. C., Summons, R. E., Sumner, D. Y., Sutter, B., Szopa, C., Teinturier, S., Trainer, M. G., Wray, J. J., Grotzinger, J. P., MSL Science Team, "Volatile, Isotope, and Organic Analysis of Martian Fines with the Mars Curiosity Rover," *Science* **341** (2013).

2. Ehlmann, B. L., Mustard, J. F., Murchie, S. L., Bibring, J.-P., Meunier, A., Fraeman, A. A., Langevin, Y. "Subsurface water and clay mineral formation during the early history of Mars," *Nature* **479**, 53-60 (2011).

3. Clark III, B. C., Arvidson, R. E., Gellert, R., Morris, R. V., Ming, D. W., Richter, L., Ruff, S. W., Michalski, J. R., Farrand, W. H., Yen, A., Herkenhoff, K. E., Li, R., Squyres, S. W., Schröder, C., Klingelhöfer, G., Bell III, J. F. "Evidence for montmorillonite or its compositional equivalent in Columbia Hills, Mars," *J. Geophys. Res.* **112**, *E06S01* (2007).

4. "Definition of basalt," Mindat.org, Hudson Institute of Mineralogy, 2016. URL: http://www.mindat.org/glossary/basalt. [Accessed 2016].

5. Allen, C. C., Jager, K. M., Morris, R. V., Lindstrom, D. J., Lindstrom, M. M., Lockwood, J. P. “Martian Soil Simulant Available for Scientific, Educational Study,” *Eos* **79**, *34*, 405-412 (1998).

6. Nyström, C., Alderborn, G., Duberg, M., Karehill, P.-G. "Bonding Surface Area and Bonding Mechanism- Two Important Factors for the Understanding of Powder Compactibility," *Drug Dev. Ind. Pharm.* **19**, *17-18*, 2143-2196 (1993).

7. Hardin, B. O. "Crushing of Soil Particles," *J. Geotech. Eng.* **111**, *10*, 1177-1192 (1985).

8. Taylor, J. R. An Introduction to Error Analysis: The Study of Uncertainties in Physical Measurements (2nd ed.). University Science Books (1997).

9. Shotton, E., Hersey, J. A. "Compaction and Compression," in *The Theory and Practice of Industrial Pharmacy (Lachman, L., Lieberman, H. A., Kanig, J. L., eds.)*, Lea & Febiger (1970), pp. 174 - 196.

10. Callister, W. D. J. Materials Science and Engineering: An Introduction Wiley (2003).

11. Ang, A. H.-S., Tang, W. H. Probability Concepts in Engineering. Wiley (2007).

12. Ehlmann, B. L., Edwards, C. S. "Mineralogy of the Martian Surface," *Annu. Rev. Earth Planet. Sci.* **42**, 291-315 (2014).

13. Yoder, H. S. <u>Generation of basaltic magma</u>. National Academies (1976).

14. Tada, H., Paris, P. C., Irwin, G. R. <u>The Stress Analysis of Cracks Handbook</u>. ASME (2000).

15. Navrotsky, A., Mazeina, L., Majzlan, J. "Size-Driven Structural and Thermodynamic Complexity in Iron Oxides," *Science* **319**, 1635-1638 (2008).

16. Nakayama, T., Ishikawa, T. "Analysis of Iron Rusts by X-ray Diffraction and X-ray Absorption Fine Structure Measurements," in *Characterization of Corrosion Products on Steel Surfaces (Waseda, Y., Suzuki, S., eds.)*, Springer (2006), pp. 223-244.

17. Cornell, R., Schwertmann, U. <u>The Iron Oxides: Structure, Properties, Reactions, Occurrences and Uses</u> (2nd ed.). Wiley-VCH Verlag (2003).

18. Morris, R. V., Klingelhöfer, G. "Iron mineralogy and aqueous alteration on Mars from the MER Mossbauer spectrometers," in *The Martian Surface: Composition, Mineralogy, and Physical Properties (Bell III, J. F., ed.)*, Cambridge University Press (2008), pp. 339-365.

19. Banin, A., Ben-Schlomo, T., Margulies, L., Blake, D. F., Mancinelli, R. L., Gehring, A. U. "The Nanophase Iron Mineral(s) in Mars Soil," *J. Geophys. Res.* **98**, *E11*, 20831-20853 (1993).

20. Ming, D. W., Mittlefehldt, D. W., Morris, R. V., Golden, D. C., Gellert, R., Yen, A., Clark, B. C., Squyres, S. W., Farrand, W. H., Ruff, S. W., Arvidson, R. E., Klingelhöfer, G., McSween, H. Y., Rodionov, D. S., Schröder, C., de Souza Jr., P. A., Wang, A. "Geochemical and mineralogical indicators for aqueous processes in the Columbia Hills of Gusev crater, Mars," *J. Geophys. Res.* **111**, *E02S12* (2006).

21. Bell III, J. F., McSween Jr., H. Y., Crisp, J. A., Morris, R. V., Murchie, S. L., Bridges, N. T., Johnson, J. R., Britt, D. T., Golombek, M. P., Moore, H. J., Ghosh, A., Bishop, J. L., Anderson, R. C., Bruckner, J., Economou, T., Greenwood, J. P., Gunnlaugsson, H. P., Hargraves, R. M., Hviid, S., Knudsen, J. M., Madsen, M. B., Reid, R., Rieder, R., Soderblom, L. "Mineralogic and compositional properties of Martian soil and dust: Results from Mars Pathfinder," *J. Geophys. Res.* **105**, *E1*, 1721-1755 (2000).

22. Morris, R. V., Klingelhöfer, G., Schröder, C., Rodionov, D. S., Yen, A., Ming, D. W., de Souza Jr., P. A., Fleischer, I., Wdowiak, T., Gellert, R., Bemhardt, B., Evlanov, E. N., Zubkov, B., Foh, J., Bonnes, U., Kankeleit, E., Gütlich, P., Renz, F., Squyres, S. W., Arvidson, R. E. "Mossbauer mineralogy of rock, soil, and dust at Gusev crater, Mars: Spirit's journey through weakly altered olivine basalt on

the plains and pervasively altered basalt in the Columbia Hills," *J. Geophys. Res.* **111**, *E02S13* (2006).

23. Blake, D. F., Morris, R. V., Kocurek, G., Morrison, S. M., Downs, R. T., Bish, D., Ming, D. W., Edgett, K. S., Rubin, D., Goetz, W., Madsen, M. B., Sullivan, R., Gellert, R., Campbell, I., Treiman, A. H., McLennan, S. M., Yen, A. S., Grotzinger, J., Vaniman, D. T., Chipera, S. J., Achilles, C. N., Rampe, E. B., Sumner, D., Meslin, P.-Y., Maurice, S., Forni, O., Gasnault, O., Fisk, M., Schmidt, M., Mahaffy, P., Leshin, L. A., Glavin, D., Steele, A., Freissinet, C., Navarro-Gonzalez, R., Yingst, R. A., Kah, L. C., Bridges, N., Lewis, K. W., Bristow, T. F., Farmer, J. D., Crisp, J. A., Stolper, E. M., Des Marais, D. J., Sarrazin, P., MSL Science Team. "Curiosity at Gale Crater, Mars: Characterization and Analysis of the Rocknest Sand Shadow," *Science* **341** (2013).

24. Bish, D. L., Blake, D. F., Vaniman, D. T., Chipera, S. J., Morris, R. V., Ming, D. W., Treiman, A. H., Sarrazin, P., Morrison, S. M., Downs, R. T., Achilles, C. N., Yen, A. S., Bristow, T. F., Crisp, J. A., Morookian, J. M., Farmer, J. D., Rampe, E. B., Stolper, E. M., Spanovich, N., MSL Science Team. "X-ray Diffraction Results from Mars Science Laboratory: Mineralogy of Rocknest at Gale Crater," *Science* **341** (2013).

25. Morris, R. V., Ming, D. W., Blake, D. F., Vaniman, D. T., Bish, D. L., Chipera, S. J., Downs, R. T., Gellert, R., Treiman, A. H., Yen, A. S., Achilles, C. N., Anderson, R. C., Bristow, T. F., Crisp, J. A., Des Marais, D. J., Farmer, J. D., Grotzinger, J. P., Leshin, L. A., McAdam, A. C., Morookian, J. M., Morrison, S. M., Rampe, E. B., Sarrazin, P. C., Spanovich, N., Stolper, E. M, MSL Science Team. "The Amorphous Component in Martian Basaltic Soil in Global Perspective from MSL and MER Missions," in *44th Lunar and Planetary Science Conference* (2013).

26. Chen, T., Chow, B. J., Shi, Y., Zhao, C., Qiao, Y. "An inorganic-organic hybrid of lunar soil simulant and polyethylene," *ASCE J. Mater. Civil Eng.* **27**, *06015013*, 1-4 (2015).

27. Chen, T., Chow, B. J., Qiao, Y. "Two-stepped size gradation of particle size in an organic-inorganic hybrid," *Sci. Eng. Compos. Mater.* **22**, 643-637 (2015).

28. Doelker, E., Mordier, D., Iten, H., Humbert-Droz, P. "Comparative Tableting Properties of Sixteen Microcrystalline Celluloses," *Drug. Dev. Ind. Pharm.* **13**, *9-11*, 1847-1875 (1987).

29. Jain, S. "Mechanical properties of powders for compaction and tableting: and overview," *Pharm. Sci. Tech. Today* **2**, *1*, 20-31 (1999).

30. Pelleg, J. Mechanical Properties of Ceramics. Springer (2014).

31. Timoshenko, S. P., Goodier, J. N. Theory of Elasticity. McGraw-Hill (1970).

32. Šubrt, J., Pérez-Maqueda, L. A., Criado, J. M., Real, C., Boháček, J., Večerníková, E. "Preparation of Nanosized Hematite Particles by Mechanical Activation of Goethite Samples," *J. Am. Ceram. Soc.* **83**, *3*, 294-298 (2000).

33. Arvidson, R. E., Squyres, S. W., Bell III, J. F., Catalano, J. G., Clark, B. C., Crumpler, L. S., de Souza Jr., P. A., Fairén, A. G., Farrand, W. H., Fox, V. K., Gellert, R., Ghosh, A., Golombek, M. P., Grotzinger, J. P., Guinness, E. A., Herkenhoff, K. E., Jolliff, B. L., Knoll, A. H., Li, R., McLennan, S. M., Ming, D. W., Mittlefehldt, D. W., Moore, J. M., Morris, R. V., Murchie, S. L., Parker, T. J., Paulsen, G., Rice, J. W., Ruff, S. W., Smith, M. D., Wolff, M. J. "Ancient Aqueous Environments at Endeavor Crater, Mars," *Science* **343** (2014).

34. Hertzberg, R. W. Deformation and Fracture Mechanics of Materials (2nd ed.). Wiley (2004).

35. Tenchov, B. G., Yanev, T. K. "Weibull Distribution of Particle Sizes Obtained by Uniform Random Fragmentation," *J. Colloid. Interface Sci.* **111**, *1*, 1-7 (1986).

36. Nakata, Y., Hyodo, M., Hyde, A. F. L., Kato, Y., Murata, H. "Microscopic Particle Crushing of Sand Subjected to High Pressure One-Dimensional Compression," *Soils and Found., Jap. Geotech. Soc.* **41**, *1*, 69-82 (2001).

37. Gradshteyn, I. S., Ryzhik, M. Table of Integrals, Series, and Products (8th ed.) (Zwillinger, D., Moll, V., eds.). Academic Press (2014).

38. Ueng, T.-S., Chen, T.-J. "Energy aspects of particle breakage in drained shear of sands," *Geotechnique* **50**, *1*, 65-72 (2000).

39. Israelachvili, J. Intermolecular and surface forces. Academic Press (1985).

40. Rustad, J. R., Felmy, A. R., Hay, B. P. "Molecular statics calculations for iron oxide and oxyhydroxide minerals: Toward a flexible model of the reactive mineral-water interface," *Geochimica et Cosmochimica Acta* **60**, *9*, 1553-1562 (1996).

41. Ouglova, A., Berthaud, Y., François, M., Foct, F. "Mechanical properties of an iron oxide formed by corrosion in reinforced concrete structures," *Corrosion Sci.* **48**, 3988-4000 (2006).

5 Direct Compaction of Montmorillonite Simulant

5.1 Introduction to Montmorillonite

5.1.1 Molecular Structure

An overview of the molecular structure is given in Appendix J. Generally, montmorillonite is a smectite-group mineral that exhibits extremely fine particle size [1]. The particles are in the form of plate-like particles consisting of two outer silica layers sandwiching an inner alumina layer. Each clay mineral layer, or lamella, is about 9.6Å [2][3]. Isomorphous substitution causes a net negative charge on the outer layers [1], with further consequence on interactions with water and cations on the exterior of each clay mineral layer.

5.1.2 Water in Montmorillonite

Fine clay minerals, such as montmorillonite, are easily wetted. Dropped water racing through thin, dry cracks on the order of 1m/s offers powerful common anecdote. Such cracks serve as capillary conduits and show the montmorillonite surface is strongly hydrophilic. A bulk sample of montmorillonite also swells noticeably when rehydrated, indicating aggressive water uptake.

The shell of water bound by clay particles is known as the diffuse double layer. The first few layers of water molecules, being bound more strongly, exhibit a greater viscosity than free water [4][5]. One of the mathematical models used to describe the charge density away from the clay surface is the Gouy-Chapman theory, whose solution is a exponential function [6]. The theory assumes that hydroxyl ions are present on the surface of the clay, balanced by protons in the aqueous medium [7], although it is not strictly necessary. The negative charge on the clay surface is balanced some distance out by cations, and the potential difference that is developed across this distance is sometimes termed the zeta potential [7]. A larger distance corresponds to a larger diffuse double layer and zeta potential. This is important for applications involving wet processing because the tendency to form aggregates (flocculation) is determined by the size of the double layer and zeta potential.

The detailed reasons for water uptake in montmorillonite remain an area of active research [8][9], but the basic framework explaining the geometry of the water's arrangement has been established by a number of researchers [1]. Grim's review [1] of the hypotheses of Terzhaghi, Hendricks-Jefferson, Macey, Barshad, and Mering approximate the phenomenon. Terzhagi thought of water molecules as two-dimensional dipoles, which form a strong order for the first few molecules close to the surface and breaking down away from the surface due to thermal motion [1][10]. Subsequent models rely upon the similarity of the hexagonally-arranged silica tetrahedral on the surfaces of montmorillonite to the dimensions of packed water molecules. The model by Hendricks and Jefferson builds three-dimensional detail, proposing that the water forms a hexagonal network tied to the clay surface by means of hydrogen bonding with every other water molecule that is oriented out-of-plane, under some molecular strain [1][11]. Macey proposed that the structure is similar to ice, and this concept has been adopted by many researchers in much subsequent work but is recognized to be a looser form, like a kind of two-dimensional fluid [1][12][4]. Barshad hypothesized a more dense tetrahedral geometry, but appears to be geometrically implausible [1]. Mering focused on adsorption around the cations, arguing that the water is packed octahedrally around them first [1][13].

Affinity between montmorillonite and water can be explained by the structural similarity of the clay lamellar surface to the dimensions of an ice-like structure, the electrical charge separation of the lamella itself, and the associated cations as a result thereof. These explanations are not mutually exclusive. Electrical imbalance appears to be dominant, being responsible for the last two explanations. For two parallel, closely-spaced lamellae, an extremely nonuniform electrical field must exist near the side. Nonuniform fields attract water directly by the mechanism of induced dipoles [14]. The water is further drawn inside the sandwich by osmotic pressure of cations—the cations' electrostatic pull combined with surface tension of water—and packed by thermal motion until settling upon the lowest system free energy configuration (*i.e.*, representing the 'ice-like' geometries elucidated above).

5.1.3 Clay-Based Structural Materials

Inherited technology from ancient times, as well as more recent research on clay-based structural materials, is reviewed in Appendix J. The motif from ancient and traditional processes center about a fundamental role for water in the process of fabricating structural materials; clay requires water to cast or deform, before subsequent drying and calcinations take place. Bricks generally have flexural strengths 6-14MPa [15]; for comparison purposes, 6MPa is used throughout as a reference datum on graphs for the performance of the material.

Direct compressing of earth or clay materials also finds application in waste sealing, but those formulations often require binders, or small amounts of moisture (Appendix J).

5.2 Research Hypothesis and Objectives

The research presented in this chapter is motivated not only by the confirmation of abundant clay minerals on Mars [16][17], including montmorillonite [18][19], but also the scarcity of water on the Martian surface [*e.g.*, [20]]. Although some regions of Mars have a relative abundance of water, others are extremely dry [21]. Conservative engineering judgment entails that scarce resources on Mars must be prioritized to support life; to conserve water one should avoid using water to construct habitats.

For making structural clay products, virtually all the processes mentioned above—both traditional and more recent— either require binders, water, or both. Martian clays, including montmorillonite, are generally very dry, with possibly less than 1wt% water content [*e.g.*[21], and other references in Chapter 1]. The limitation of binders was overcome by the finding that Mars-1a simulant compacts by itself, and we seek to investigate whether that is possible with montmorillonite as well. Although npOx binds the basaltic phase in Mars-1a and acts as mechanical cement, the underlying reasons for strength development may have something in common with montmorillonite.

Forming strong materials from dry clay without binder proceeds with the high pressure, uniaxial compaction used for Mars-1a. We propose that strength development should be possible due to electrostatic forces between clay lamellae. As two lamellar montmorillonite plates are squeezed together closely enough, they may bond together strongly through secondary molecular interactions, such as the Van der Waals forces [22][23] and tend to manifest at high specific surface areas, such as at the feet of a gecko[24]. The high surface area of montmorillonite—up to 800m^2/g [5]—should contribute significantly to a high strength by analogy. Large specific area would then be the underlying factor common to both npOx and montmorillonite. Thus, a strong solid may be possible, despite a near-total lack of water and hydrogen bonding.

Our process is distinguished (for example, from compressed earth blocks) by ultrahigh compression pressure, zero binder content, and zero added water. A summary of the research is shown in the flowchart in Figure 5-1.

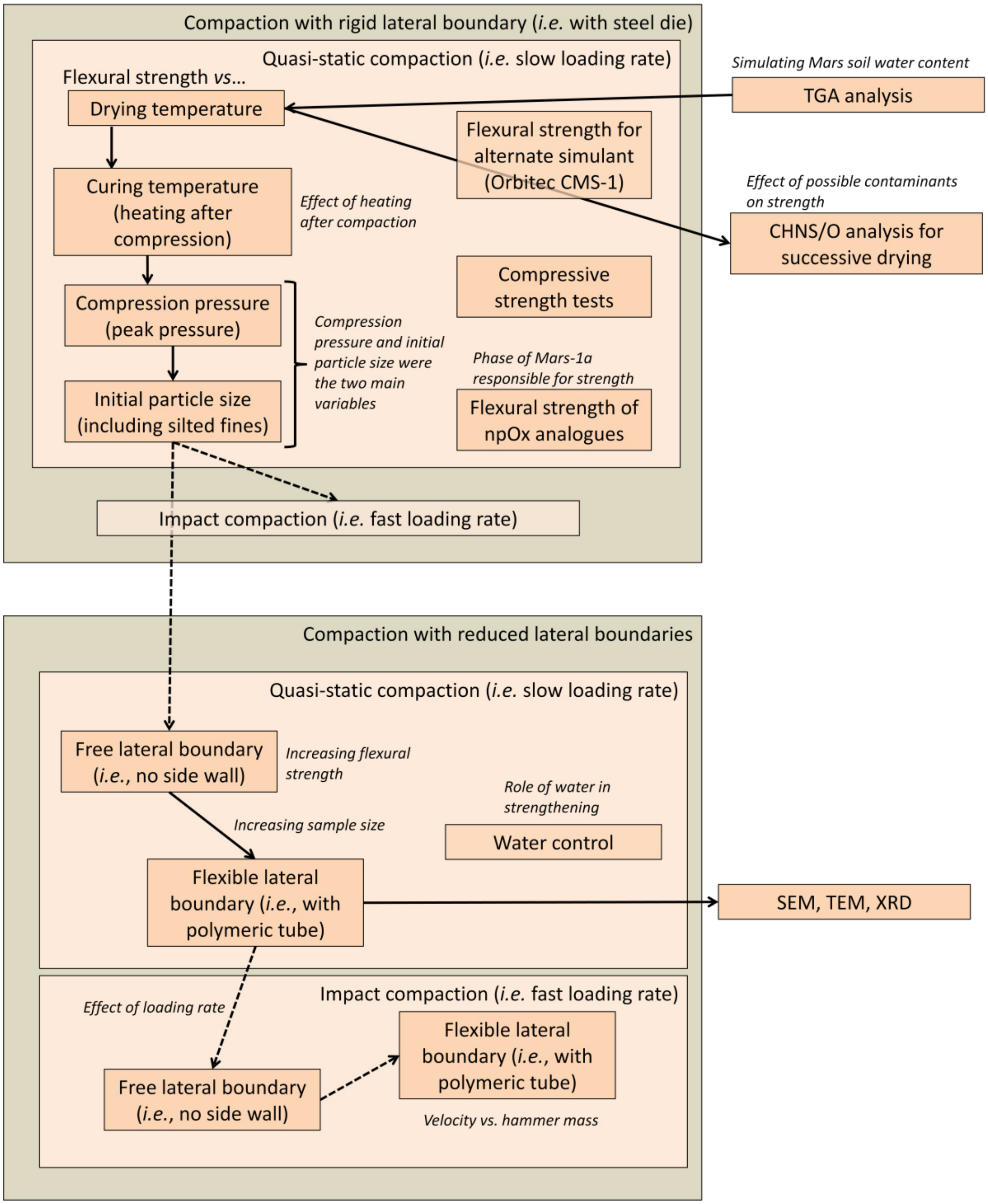

Figure 5-1 Direct Compaction of Montmorillonite: Research Path.

5.3 Compaction with Rigid Lateral Boundary Condition

5.3.1 Quasi-static Compaction

Quasi-static compaction was achieved with a uniaxial load-displacement test machine (Instron 5582) shown in Figure 4-4C. The rate of quasi-static compression was controlled at 6mm/min. A picture of a typical beam specimen is shown in Figure 5-4.

The same basic procedure as §4.3.1 was followed using montmorillonite simulant (Sigma-Aldrich K10 69866-1kg). Before compression, particles were dried to an appropriate temperature between ambient and 600°C; specific temperatures are indicated herein. A TGA of the montmorillonite is shown in Chapter 6. The drying temperatures were determined based on these TGA temperatures to best mimic the water content found in Martian soil, which is generally <6wt%. Conservatively, water content should be as close to zero as possible. With this consideration, the TGA curves determine that the range of 350°C-600°C represents adequately Martian surface water content, with the latter as more conservative. Other drying temperatures, however, also appear for self-comparison purposes.

A schematic showing the overall process is shown in Figure 5-2 and 5-3.

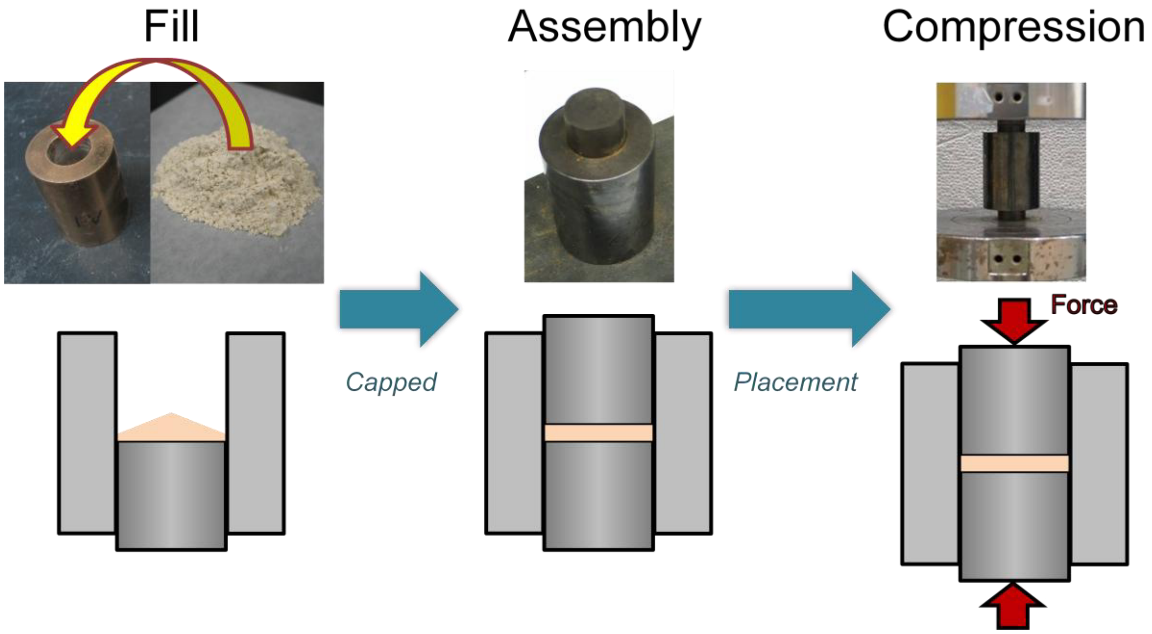

Figure 5-2 Montmorillonite Rigid Lateral Boundary Compaction. Schematic showing the overall experimental processes for montmorillonite. Variants of this process with additional or omitted steps are indicated where applicable. The die is of bore diameter 19.05mm and outer diameter 38.1mm.

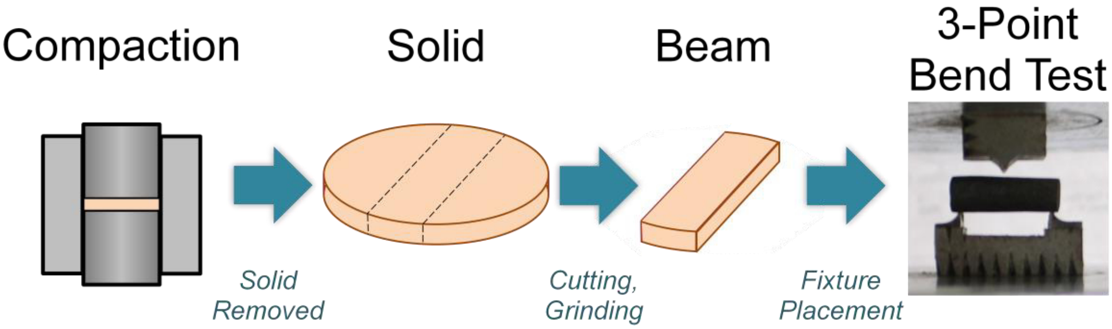

Figure 5-3 Montmorillonite Shaping and Testing. Schematic showing the overall experimental processes for montmorillonite. Variants of this process with additional or omitted steps are indicated where applicable. The bore diameter in the die (first step) is 19.05mm; support distance in the photograph (last step) is 15.22mm.

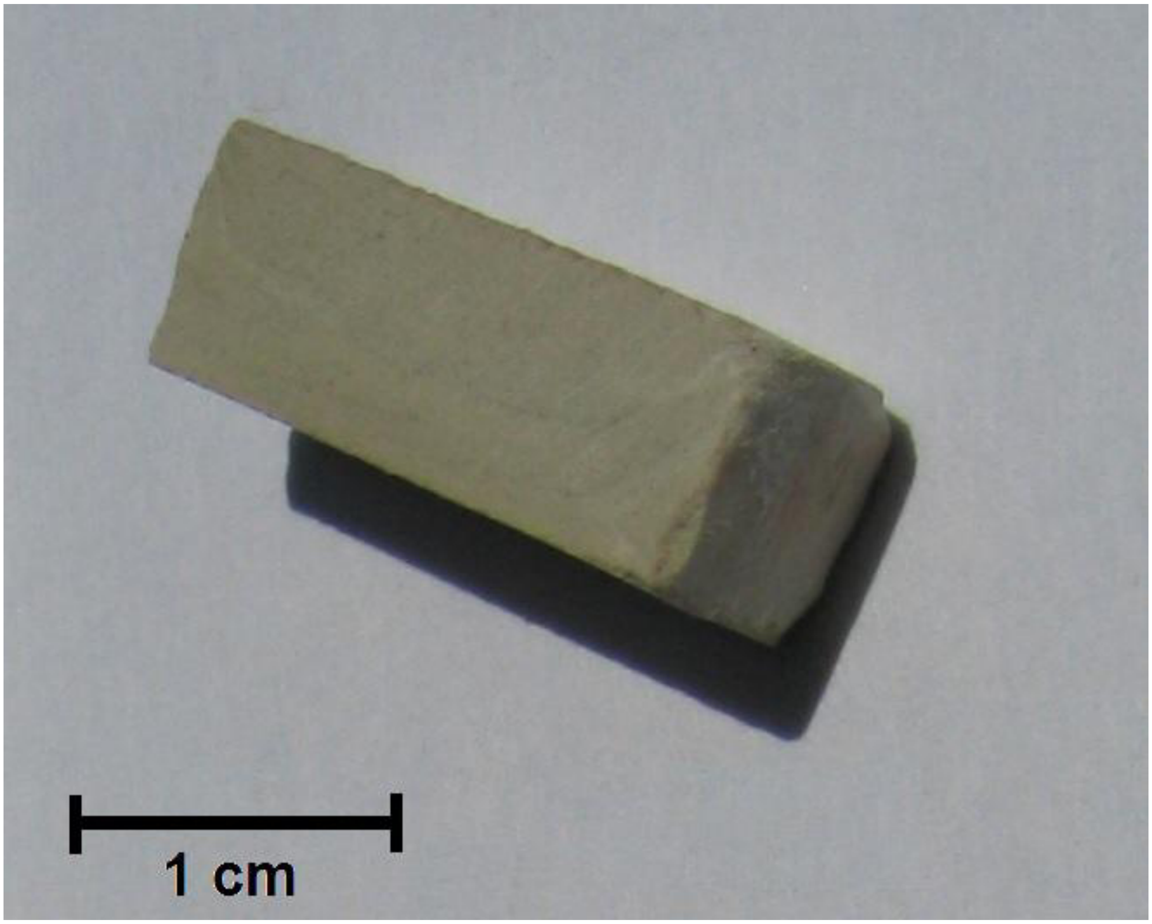

Figure 5-4 Photo of Montmorillonite Beam. Typical compacted montmorillonite, cut and ground into a beam specimen.

5.3.1.1 Flexural Strength as Function of Compression Pressure

Montmorillonite produced relatively fragile specimens when subjected to drying at elevated temperatures, and in response drying is initially precluded from flexural strength characterizations as a function of pressure. Particles are sieved into their size bins before compression. The <20µm size fraction was subjected to 360MPa and 720MPa compression pressures. In a separate series of tests, the 25-45µm size fraction was subject to 180MPa, 360MPa, 540MPa, and 720MPa compression pressures. Both <20µm and 25-45µm size fractions were investigated, but the 25-45µm size fraction experienced more pressure levels because it was more prevalent and representative of the as-supplied montmorillonite clay.

Testing was also performed on a closely related clay material, bentonite. No sieving was performed and the particle size is considered random. Prior to compression, the material was dried to 350°C overnight in an open atmosphere in order to simulate Martian soil water content; the temperature was selected based on the TGA analysis for montmorillonite. The dried powders were then compressed at 360MPa and the resultant solid discs were cured at 225°C for 30min afterwards. Curing was performed as an artifact of melt-processing of polymers. Note that for most other testing, we eliminated post-compression curing.

Table 5-1 Compacted Montmorillonite *vs.* Compression Pressure

Sample	Piston Pressure (MPa)	Width (mm)	Depth (mm)	Length (mm)	Flexural Strength (MPa)
1008	360	5.58	0.89	15.22	14.36
1009		5.84	0.89		13.62
1010		5.34	1.38		15.98
1011		5.52	1.37		15.89
1014	720	4.57	0.26	9.78	12.82
1015		7.47	0.57		15.53
1016		6.35	0.49		18.19
1017		5.52	0.60		14.76

All samples were compacted from particles that were not dried.
Initial particle size range was <20μm.

Table 5-2 Compacted Montmorillonite *vs.* Compression Pressure, Extended

Sample	Piston Pressure (MPa)	Width (mm)	Depth (mm)	Support Length (mm)	Flexural Strength (MPa)
692	90	4.64	1.91	15.22	7.42
693		4.58	1.91		6.83
694		6.57	2.45		9.84
695		6.79	2.43		8.54
696	180	5.83	2.80		14.49
697		6.35	2.78		14.89
698		6.20	2.60		12.53
699		5.62	2.63		16.44
700	270	7.08	1.93		19.91
701		6.49	1.92		22.90
702	360	4.53	2.30		15.24
703		4.30	2.28		16.34
704		4.46	1.73		11.12
705		4.52	1.74		12.51
2041	180	7.91	1.47	9.78	5.07
2042		7.40	1.52		3.90
2043		5.89	1.58		5.60
2044		6.44	1.93		6.09
2045		7.40	1.48		5.30
2046		7.03	1.53		5.00
2047	360	6.33	1.45		9.42
2048		6.21	1.27		10.03
2049		5.78	1.29		10.89
2050		6.44	1.39		10.92
2051		6.40	1.54		8.56
2052		5.80	1.37		12.45
2053	540	6.89	1.46		12.79
2054		5.93	1.29		12.70
2055		7.03	1.39		12.22
2056		6.22	1.46		12.74
2057		5.84	1.43		11.53
2058		6.94	1.27		12.95

Table 5-2 Compacted Montmorillonite *vs.* Compression Pressure, Extended (continued)

2059	720	7.39	1.33	9.78	14.22
2060		6.37	1.37		14.65
2061		5.61	1.37		15.40
2062		6.95	1.31		12.42
2063		5.97	1.27		13.82
2064		6.73	1.41		13.47

All samples were compacted from particles that were not dried.
Initial particle size range was 25-45μm.

Table 5-3 Compacted Bentonite *vs.* Compression Pressure

Sample	Piston Pressure (MPa)	Width (mm)	Depth (mm)	Flexural Strength (MPa)
433	90	6.57	4.37	3.28
434		5.72	5.83	0.59
435	180	8.07	4.62	0.40
436		8.09	4.46	6.24
437	270	4.77	4.84	2.66
438		4.78	4.49	3.79
439	360	6.02	4.90	6.95
440		6.03	4.93	3.12

All samples were compacted from particles dried at 350°C overnight and cured at 225°C for 30min.

Initial particle size was random.

Beams had support length of 15.22mm.

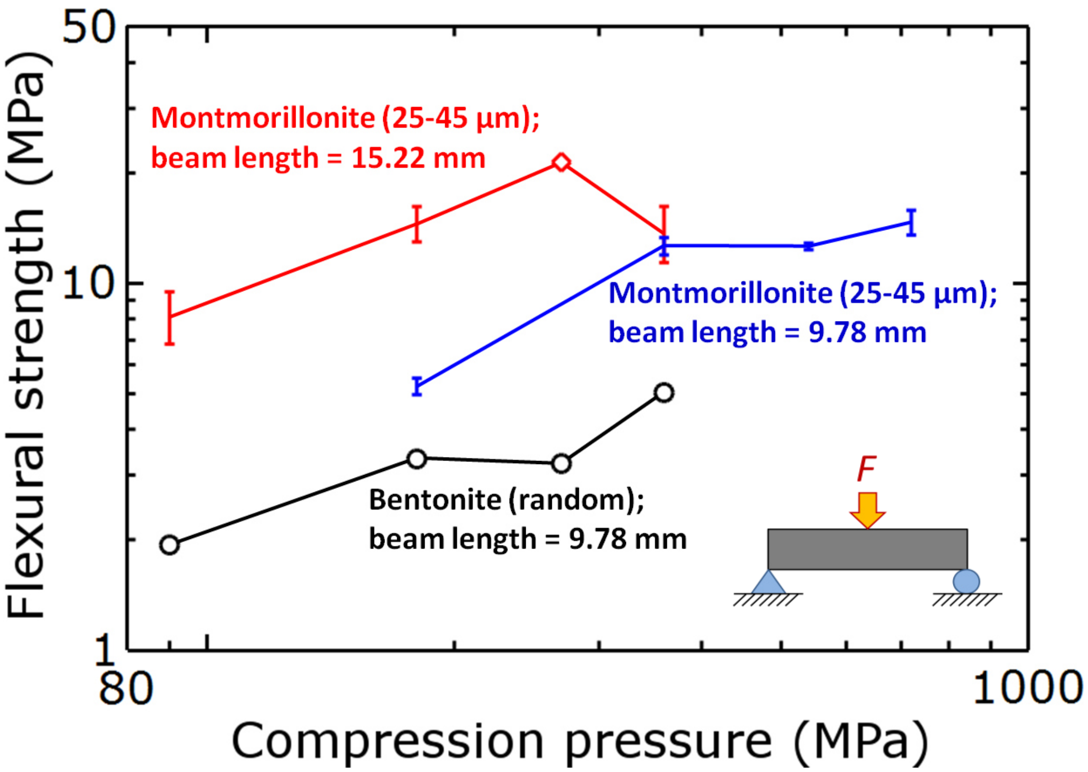

Figure 5-5 Montmorillonite Flexural Strength *vs.* Compression. Flexural strength as a function of the compression pressure for montmorillonite and bentonite. Piston diameter was 19.05mm for 15.22mm beam length and 12.7mm for 9.78mm beam length. The initial particle size range was 25-45μm for montmorillonite, and random for bentonite. Lower-left inset shows a 3-point bending test configuration.

5.3.1.2 Flexural Strength as Function of Initial Particle Size

For Mars-1a, we investigate the effect of the initial particle size. For the sake of convenience, The term ‘particle’ in the case of clay refers to a tactoid, or agglomeration of lamellae, bound by secondary molecular interactions [25]. Testing can reveal whether such an apparent ‘initial particle size’ exerts an effect on the overall flexural strength of the sample after compressed to high pressures.

Table 5-4 Compacted Montmorillonite *vs.* Initial Particle Size

Sample	Size Range (μm)	Length (mm)	Width (mm)	Depth (mm)	Flexural Strength (MPa)
573	20–25	15.22	3.95	2.09	14.55
574			4.17	2.08	17.71
575	25–45		4.32	1.66	13.42
576			4.10	1.66	12.12
577	45–53		4.39	1.84	7.68
578			3.87	1.83	8.81
579	53–90		4.71	1.80	4.49
580			4.52	1.80	4.68
581	25–45	9.78	5.26	2.08	21.27
582			5.55	2.22	11.26
583	45–53		4.96	1.93	12.70
584	53–90		5.09	1.98	7.35
585			6.11	2.42	1.64
586	25–45		7.19	1.18	8.79
587		15.22	4.07	2.33	12.40
588			3.72	2.49	11.88
589			4.63	1.57	8.00
590		9.78	4.96	1.44	7.13
591		15.22	3.70	1.57	12.52
592			2.77	2.05	11.77
593	45–53		4.16	2.42	6.56
594			4.49	2.45	5.08
595	53–90		4.43	1.73	3.44
596			4.02	1.77	3.63
597	90–112		7.98	1.53	4.89
598	112–500	9.78	9.29	1.16	3.52

All samples were not dried above ambient; *i.e.*, drying temperature was 25°C

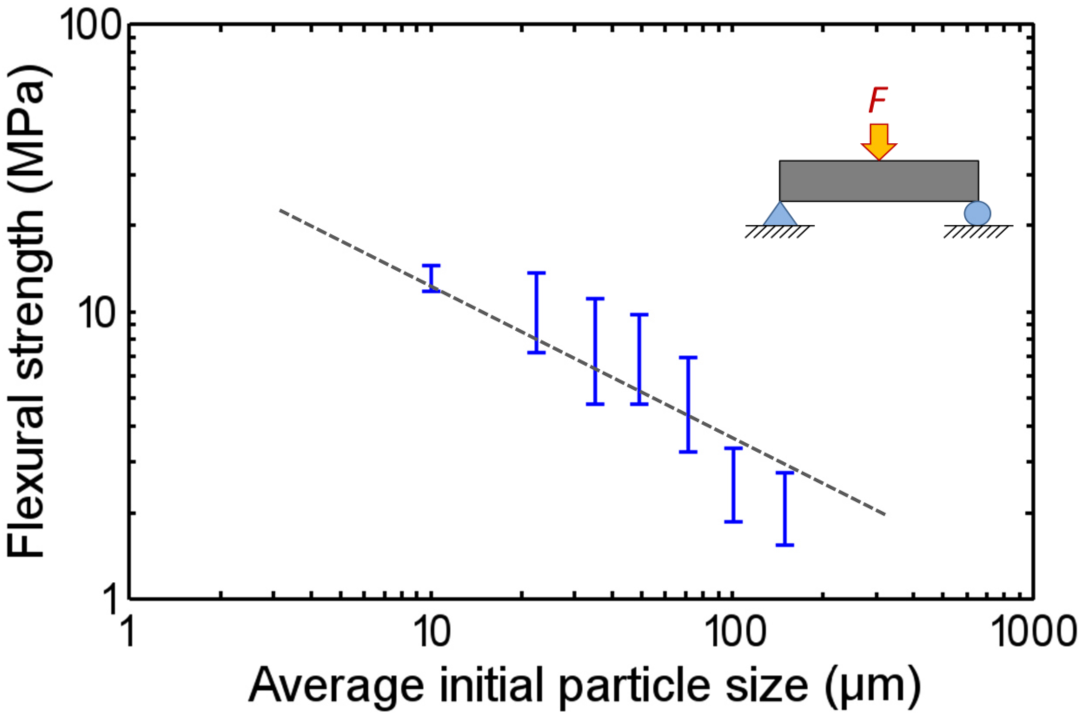

Figure 5-6 Montmorillonite Flexural Strength *vs.* Initial Particle Size. Flexural strength plotted against average initial particle size for compacted montmorillonite not dried to elevated temperatures. Compaction pressure was 360MPa inside a 19.05mm-diameter piston fitted to a steel die, representing a rigid lateral boundary condition. A linear regression is shown in dashed line.

The trend of flexural strengths as a function of initial average particle size can be expressed using a least-squares regression as in §4.3.1.4

$$R = kd^{-\beta}$$

where $k \approx 40.87$ and $\beta \approx 0.525$. The inverse relation between flexural strength and particle size is expected based on the reasoning developed by way of geometric arguments in §4.6.2. The unexpectedly steeper slope achieved with clay mineral layers presupposes that the particle size does not change as much as Mars-1a upon crushing. This supposition is corroborated by the relatively larger observed particle sizes in the SEM micrographs in Chapter 6.

5.3.1.3 Flexural Strength of Silted Fines

Testing data show that the strength increases with decreasing average initial particle size, in the particle size range of mechanical sieving. Silting uses a fluid can separate much smaller particles of <2μm size from a randomly distributed mixture [5]. We silted particles in 300ml of water, for which a bulk mixture of ~50g was agitated and left to settle for 30min at room temperature. The remaining supernatant fluid was decanted. The silted fraction was dried at 350°C for 3h. Before drying, some samples were rinsed with acetone and ethanol in case the water (deionized, *i.e.*, not pure) imparted trace organic species on the clay. Results are shown in Table 5-5.

Table 5-5 Montmorillonite Silted with Water

Sample	Length (mm)	Width (mm)	Depth (mm)	Flexural Strength (MPa)	Comments
662	15.22	6.04	3.76	2.41	No rinsing
663		6.24	3.1	3.43	
664		6.12	4.66	3.26	
665		6.49	3.32	3.19	
674		6.15	2.27	4.89	Rinsed
675		5.80	2.73	4.92	
676	9.78	7.26	2.55	5.71	
677		5.26	1.93	3.67	
678	15.22	6.16	2.16	2.99	
679		6.01	2.16	3.82	

The strength of the solid montmorillonite is relatively low, comparable to that of conventional fired bricks (~10MPa [15]). The finding runs against the hypothesis that further decreasing particle size should lead to a stronger sample. The average initial particle size again refers to the tactoids of montmorillonite lamellae. Such agglomerates are loosely bound by secondary bonds at pinpoint interfaces and easily destroyed by mechanical compression, as observed by shear hardening of randomly oriented plastic clays at low pressures [7]. The same phenomenon should hold at dry conditions, and conservatively so if the compression is done at high pressure. If the size of agglomerates is itself indicative of the plate size of montmorillonite, then one should have already tested the strength of that size (left error bar of Figure 5-6). In other words, the lowest bin size of mechanical separation (the pan) already contained the smallest sizes expected to be encountered in the as-supplied montmorillonite, and the finally compressed solid destroys the initial agglomerates regardless of initial state. We will corroborate this hypothesis with further inferences from the experiments performed with a reduced lateral boundary.

Another possible factor is that drying to high temperatures of 350°C can negate certain properties of the montmorillonite to lead to the observed lack of strength, or bonding between particles. If hydrogen bonding between clay particles promotes the mobility of clay particles during compression, then severely drying montmorillonite should lower the strength. This is explored in the following section.

5.3.1.4 Influence of Drying Temperature on Flexural Strength

We explore whether high drying temperatures can indeed cause a drop in flexural strength. This is best characterized by a continuum, so we chose to test compacted solids made from particles initially dried at a number of temperatures. The applied compression pressure was 360MPa. A photograph of the visual difference in montmorillonite is shown in Figure 5-7. Results, including cross-listed data from other parts of the current study, are listed in Table 5-6.

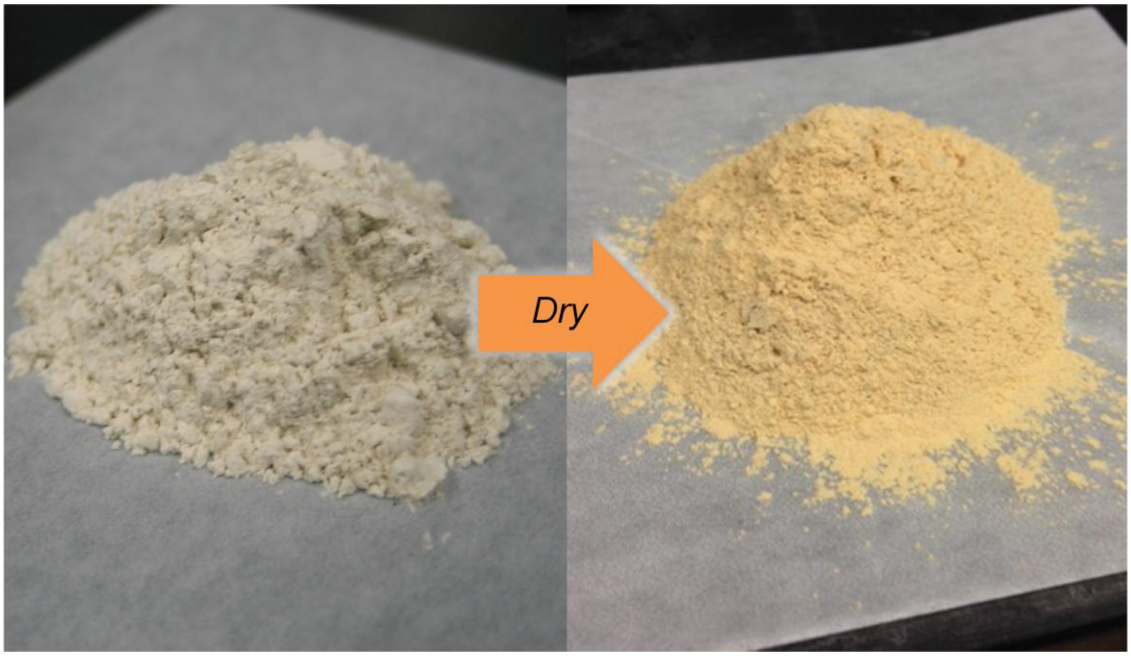

Figure 5-7 Photo of Drying Montmorillonite. Visual difference is observed for montmorillonite powders before (left) and after (right) drying at 600°C for 12h. Dried montmorillonite develops a light tan color after elevated temperature drying. The width of the pile is about 5cm.

Table 5-6 Compacted Montmorillonite *vs.* Drying Temperature

Sample	Drying Temperature (°C)	Width (mm)	Depth (mm)	Strength (MPa)	Average Flexural Strength (MPa)
1118	90	5.99	1.79	8.31	8.93
1119		6.08	1.82	8.25	
1120		5.90	1.98	10.05	
1121		5.71	2.00	9.10	
1141	110	5.81	1.95	7.62	7.81
1142		5.54	1.95	8.20	
1143		5.59	2.11	8.22	
1144		5.36	2.10	7.19	
1250	190	6.30	1.66	2.50	3.66
1251		5.04	1.66	3.67	
1252		5.78	1.47	3.82	
1253		4.75	1.46	2.93	
1254		5.91	2.21	3.73	
1255		5.07	2.21	3.98	
1256		5.34	2.14	4.00	
1257		6.14	2.12	4.64	
1258	270	6.74	1.40	3.01	4.48
1259		5.71	1.42	1.86	
1260		5.75	1.06	3.22	
1261		5.70	1.06	7.09	
1262		6.01	1.11	3.42	
1263		5.73	1.09	4.20	
1264		6.00	0.78	7.88	
1265		6.46	0.77	5.13	
1035	350	6.02	1.68	4.11	3.45
1036		5.88	1.67	5.23	
1165		5.66	1.08	2.94	
1166		4.73	1.08	3.60	
1167		5.66	1.91	2.19	
1168		6.23	1.89	2.63	
1274	400	6.00	1.58	2.94	3.63
1275		5.79	1.55	3.07	
1276		6.15	2.65	3.83	
1277		5.12	2.61	3.32	
1278		5.57	1.28	3.50	

Table 5-6 Compacted Montmorillonite *vs.* Drying Temperature (continued)

1279	400	5.51	1.26	4.33	3.63
1280		5.23	2.32	3.93	
1281		5.26	2.31	4.08	
1282	500	5.70	1.64	4.90	4.13
1283		5.35	1.67	4.94	
1284		5.54	1.53	5.70	
1285		5.35	1.49	5.34	
1286		6.05	1.97	3.26	
1287		4.83	1.96	3.05	
1288		5.83	2.49	3.31	
1289		5.68	2.49	2.55	
1229	600	5.39	2.01	2.07	2.29
1230		5.99	2.03	1.99	
1231		5.98	1.96	2.69	
1232		5.90	1.98	2.41	

Drying temperature is applied to loose montmorillonite powders prior to compaction.
Particle size range was 25-45μm.
Beam support length was 15.22mm.
Compression pressure was 360MPa.

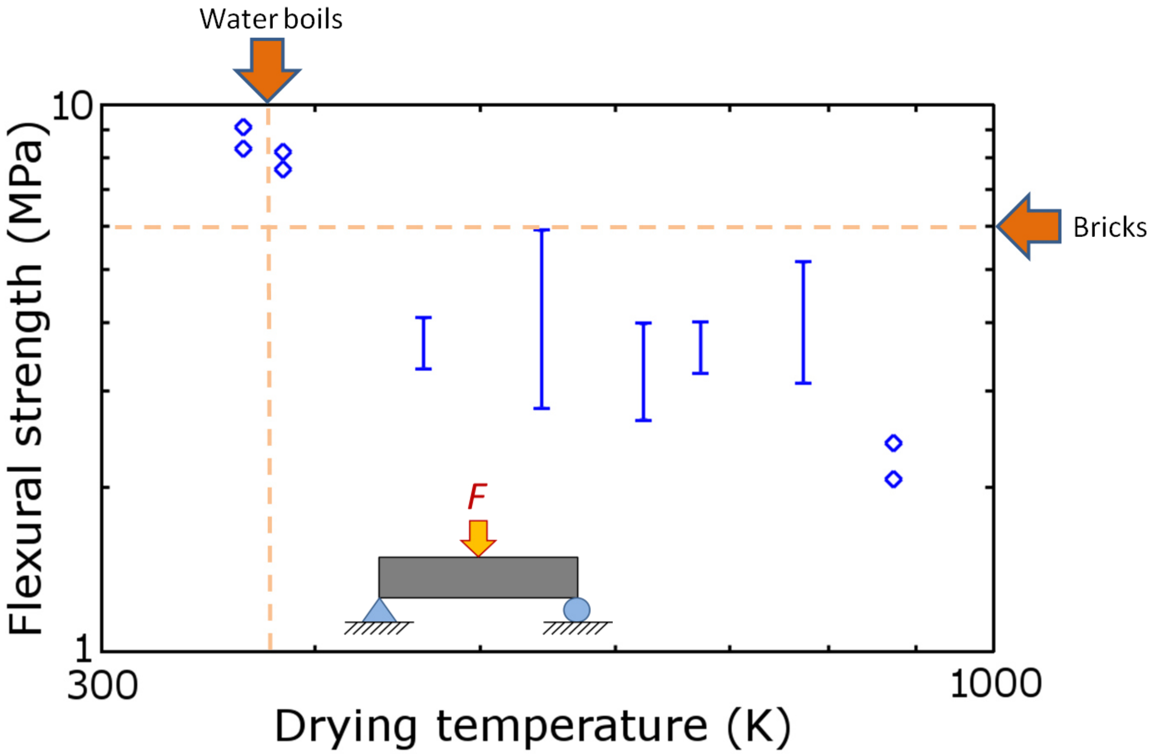

Figure 5-8 Montmorillonite Flexural Strength *vs.* Drying. Flexural strength of compacted montmorillonite as a function of drying temperature. Diamonds represent individual data points. Compression pressure was 360MPa; initial particle size range was 25-45μm. Diagram on the lower-left is a three-point bending test schematic.

From Table 5-6 and Figure 5-8, it is evident that with the rigid boundary condition of compression, heating montmorillonite particles causes them to lose strength. First, hydrogen bonding could be destroyed, as water is driven from the clay during the furnace-drying process prior to compaction. Second, interlamellar lubricity may be reduced from a reduced diffuse double layer, resulting in seizing of clay particles and prevention of their rearrangement into a more dense structure during compression. Third, foreign contaminants may be present in the surrounding environment during furnace-drying that coats the montmorillonite particles and prevents their bonding.

5.3.2 Impact Formation

Loose montmorillonite (Sigma-Aldrich K10 69866) was fractioned in a mechanical sieve (W.S. Tyler Rotap RX-29) and the 25-45μm size bin was dried at 600°C overnight. About 0.5g of the material was added into a 12.7mm diameter steel die as portrayed in Figure 5-9. Compression was performed by compressing the assembly inside of a shock jacket using a 7.64kg drop hammer dropped from a height of 1.52m.

The impact-hardened solids were removed from the die and ground into beam specimens. Three-point bending tests determine the flexural strengths of beams. Results are shown in Table 5-7.

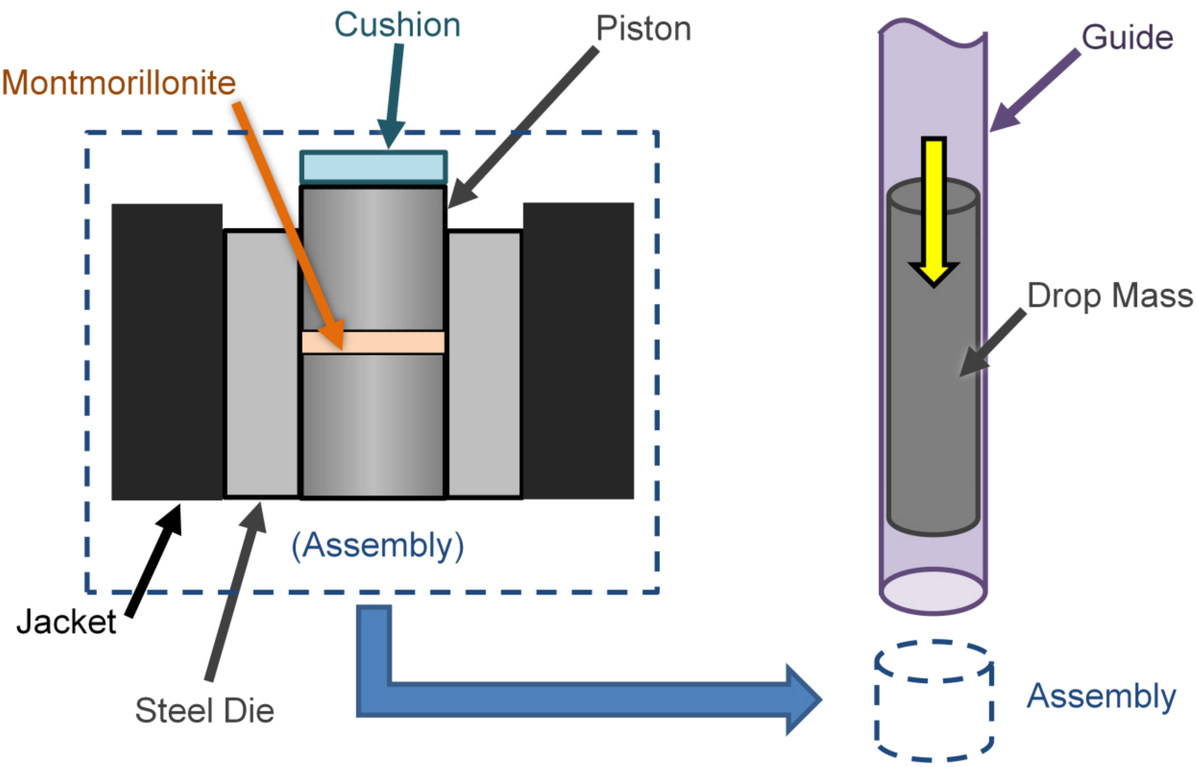

Figure 5-9 Montmorillonite Rigid Lateral Boundary Impact Compaction. Schematic of the impact formation process using the lateral rigid boundary. Both the outer diameter of the jacket and the guide tube is 76.3mm. The steel die has bore diameter 19.05mm and outer diameter 38.1mm.

Table 5-7 Impact-Formed Montmorillonite with Rigid Lateral Boundary

Sample	Width (mm)	Depth (mm)	Flexural Strength (MPa)
1387	6.12	1.14	4.81
1388	5.81	1.14	3.96
1389	5.89	1.24	2.88
1390	5.56	1.39	4.03

Particles were dried at 600°C prior to compression.
Initial particle size range was 25-45µm.
Length between supports was 9.78mm.

Recall elevated drying temperatures applied to the particles before compression lowered the strength of the resultant compact. It is evident that low strengths are still produced even with a transient compression force applied to ultra-dry particles. The application of impact forces to the dry particles does not raise the strength above the levels found in Figure 5-8. The reasons for this are in common with those enumerated for the loss in strength upon heating from §5.3.1.4. Namely, there is a loss of water from the montmorillonite diffuse double layer reducing hydrogen bonding in the compacted solid, an increase in friction among particles during compression, and/or contamination from the elevated drying temperature prior to compression.

5.3.3 Elementary Analysis of Heated Montmorillonite

We examine whether an unknown foreign substance, specific organic impurities that may influence the binding strength among particles, transmitted onto the montmorillonite. Heating in an oxidizing atmosphere at ambient should also preclude contamination.

SEM elementary analysis on the heated powder was conducted. The <20μm size fraction of montmorillonite was chosen, as it has the highest surface area. The particles were heated in a furnace (Carbolite CTF12/75/700) to 350°C for 12h. Particles were manually transported on carbon tape until the surface was thoroughly coated. Elementary analysis was performed with an SEM. Findings are summarized in Chapter 6. Based on these findings, we suggest the following:

1. Carbon is relatively more abundant in the experimental (*i.e.*, suspected contaminated) samples, but the positioning on maps as silhouettes around particles strongly suggests that it is an artifact from the carbon tape. The carbon

content is consistently low and below the level of difference or variation between the other elements.

2. Aluminum is relatively enriched in the contaminated samples, but there is no plausible explanation for a relative depletion in either oxygen or silicon upon heating. The homologue temperatures for typical clay (T_m = 1500K), silica (T_m = 2000K), and alumina (T_m = 2300K) far exceeds the drying temperature, and thus the transport of these elements between different phases in the clay is implausible. As the elemental differences are likely due to sample variation, the reported errors in elemental composition can be effectively ignored.
3. Particle size is significantly larger in the contaminated samples. Particle size is smaller in the uncontaminated samples. This may be related to the hypothesis that the clay loses hydrogen bonding and flocculates during heating in the absence of free liquid, and also due to the reduction of the diffuse double layer.

The elemental compositions of the clay are consistent with that found in its un-dried state. The absence of carbon on the montmorillonite particles precludes interference by a foreign-deposited substance to the binding of particles. The open literature reveals that the montmorillonite (Sigma Aldrich) contains a proportion of Fe_2O_3 [26], which is compelling for a color change upon heating due to precipitation of free hematite upon cooling [7].

Two hypotheses for the low strength of compressed dried clay remain. First, as discussed in #3 above, the size of the diffuse double layer shrinks during heating, causing flocculation of particles, basically equivalent to larger particle sizes prior to compression. A water loss is closely associated with loss of hydrogen bonding as proposed toward the end of §5.3.1. Larger particle sizes lead to lower strength. However, size growth seen after drying to elevated temperatures does not result in particles larger than ~50μm, with most particles 20-40μm. This should, on the other hand, lead to higher strength than current observations, were it not for drying of the particles.

The second hypothesis proposed towards the end of §5.3.1 is related to the first. Severely dried clay particles develop more friction and would resist motion towards energetically favorable orientations. Shear banding tends to happen sporadically when using the rigid boundary condition (*i.e.*, a steel die with piston) to compress particles. This may be indicative of hydrostatic seizing because the rigid boundary builds up the friction, which is not a major factor negatively impacting the strength of compacted samples because the flexural strength is measured from a failure that occurs at the center, where the lateral pressure is evenly distributed.

5.3.4 Other Clays

In total, six different clays were tested. The majority of the work focused on montmorillonite. Bentonite, closely related to montmorillonite, is tested as part of the compression pressure curve in Figure 5-5. Other clays include mixed illite-smectite, kaolinite, nontronite, and saponite clays, all of which have been detected on the Martian surface. Testing data for these clays are found in Appendix K. Also tested were mixtures of montmorillonite with basalt, nontronite with saponite, and montmorillonite with kaolinite; these are also found in Appendix K.

Table 5-8 List of Clay Minerals Tested

Neat Particles			
Simulants Tested		Description	Remarks
BEN	Bentonite	White clay, synthesized. Minor zeolite component [27].	Strength 3-7MPa.
M	Montmorillonite	White clay, synthesized. Turns slightly yellow upon heating.	Strength 3-18MPa; lower strengths upon heating. Compressive strength ~20MPa (Appendix F)
MIS	Mixed Illite-Smectite	White-grey clay, from field	Strength 1-4MPa (Appendix K).
K	Kaolinite	White clay, synthesized. Turns slightly pink upon heating.	Strength 4-11MPa (Appendix K).
N	Nontronite	Green smectite, from field.	Strength 1-8MPa (Appendix K).
S	Saponite	Brown smectite, from field.	Strength 0-2MPa (Appendix K).
Combinations of Particles			
Combination Tested		Description	Remarks
M + BAS*		Grey color.	Strength 1-6MPa (Appendix K).
N + S		Green-brown color. Nontronite more dominant binder.	Strength 3-8MPa (Appendix K). Higher strength is for high nontronite.
M + K		White color.	Strength 6-8MPa. Strength 9-20MPa when compressed ~1GPa (Appendix K).

‘Strength’ in this table refers to ‘flexural strength’ except where otherwise indicated.
Compression pressure is assumed to be 360MPa.
*BAS refers to basalt fines.

5.4 Compaction with Reduced Lateral Boundary Conditions

As montmorillonite is heated to increasing temperatures, resultant flexural strength decreases from 15MPa to ~2MPa. The latter value represents fragile material near zero strength. Heating is performed in order to simulate dry Martian clay. A near-zero flexural strength renders the material impractical for structural utility and questions the ability of the material to compaction-strengthen.

Engineering design and processing contain many variables that are open to investigation rather than the several parameters of compression pressure, initial particle size, and drying temperature. The lateral boundary condition of compaction is one such variable.

5.4.1 Quasi-static Compaction

Quasi-static compaction was achieved with a uniaxial load-displacement test machine (Instron 5582 or SATEC M600XWHVL), All samples were compressed using the Instron machine, while larger samples requiring >360MPa compaction with a 19.05mm-diameter sized sample exceeded the 100kN load limit on the Instron and required the SATEC machine. The rate of quasi-static compression was controlled at 6mm/min.

5.4.1.1 Free Lateral Boundary Condition

One explores here whether there is an upper limit to strength, in any process configuration. Two methods were developed.

- Method 1: First, we form an 8.71mm-diameter pellet under a manual compression pressure of ~150MPa using a 10kN arbor press. This precursor (pellet) is placed concentrically on the face an oversize 19.05mm-diameter piston, and compressed inside a 19.05mm-diameter die to a prescribed pressure, which acted as parallel plates. Compression pressure is calculated as force divided by original precursor area. The sample is ground into a beam and the flexural strength was measured.
- Method 2: Loose particles are placed inside of a 19.05mm-diameter bore, with a flat steel bottom. An impinging piston of 8.71mm in diameter is compressed against the loose particles directly at the prescribed forming pressure. Pressure is calculated as the force divided by the area of the piston.

Methods 1 and 2 are depicted in Figures 5-10. Montmorillonite particles were dried to elevated temperatures prior to compression forming. Table 5-9 lists the results for flexural strengths obtained under high compression pressure.

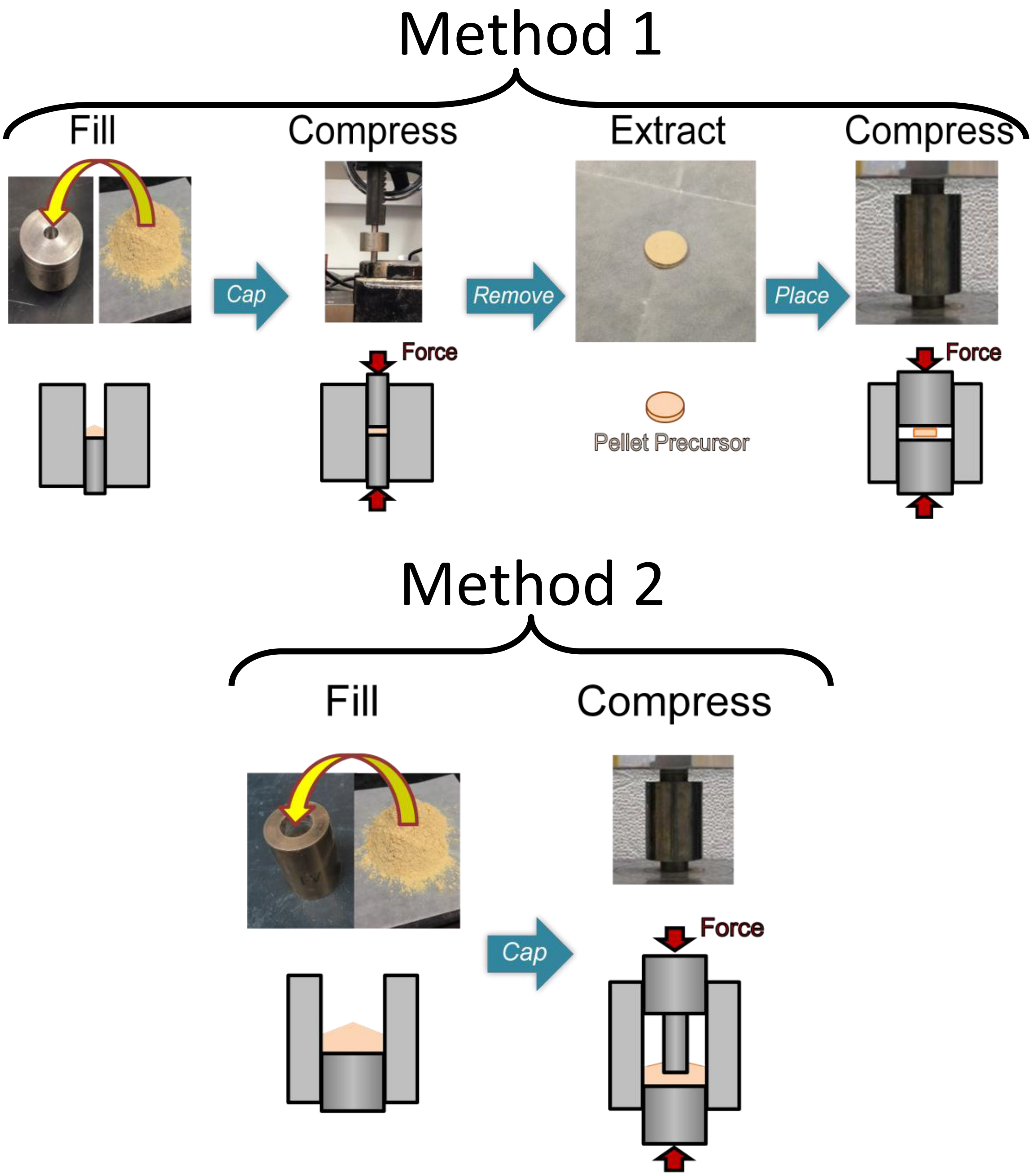

Figure 5-10 Montmorillonite Free Lateral Boundary Compaction. Schematic of processing described above as Method 1 (top) and Method 2 (bottom). The die shown in the first step of Method 1 has bore diameter 8.71mm and outer diameter 38.1mm. The pellet shown in the third step of Method 1 has diameter 8.71mm. The die in the last step of Method 1 has bore diameter 19.05mm and outer diameter 38.1mm. This die is also used in Method 2.

Table 5-9 Montmorillonite Compacted with Free Lateral Boundary

Sample	Method	Compression Pressure (MPa)	Initial Particle Size (µm)	Drying Temperature (°C)	Length (mm)	Width (mm)	Depth (mm)	Flexural Strength (MPa)	Average Strength (MPa)
1296	1	>800	25-45	500	9.78	4.38	0.48	12.21	18.15
1297						3.88	0.43	18.20	
1298						3.69	0.34	24.42	
1300						3.76	0.40	17.07	
1301					4.99	3.83	0.33	18.84	
1302	2	1500	<20	25 (none)		3.38	0.21	20.59	20.59
1303			25-45	500		4.32	0.56	22.98	14.69
1304						4.61	0.86	11.92	
1305						3.36	0.95	14.49	
1306						4.35	0.92	15.08	
1307						3.39	0.85	9.41	
1308						3.43	0.91	14.47	
1309						4.21	0.79	8.09	
1310						4.33	0.96	14.50	
1327		1000				2.57	0.24	12.14	20.13
1328						3.99	0.41	28.35	
1329						3.84	0.32	23.98	
1330						3.17	0.25	15.11	
1331						3.19	0.24	9.37	
1332						3.82	0.29	15.14	
1333						4.32	0.42	21.81	
1334						3.62	0.42	35.16	
1339		360				3.89	0.72	7.65	5.43
1340						3.77	0.33	5.65	
1341						3.61	0.33	3.62	
1342						1.86	0.20	7.04	
1343						4.13	0.31	4.15	
1344						3.15	0.20	5.94	
1345						3.12	0.21	4.35	
1346						4.05	0.27	5.07	
1415	2	1000	<20	600	4.99	4.73	0.16	34.00	37.17
1416						4.49	0.15	31.86	
1417						4.45	0.14	27.46	
1418						4.12	0.12	34.06	
1419						4.56	0.14	29.31	

Table 5-9 Montmorillonite Compacted with Free Lateral Boundary (continued)

1420	2	1000	<20	600	4.99	4.15	0.14	41.41	37.17
1421						4.73	0.16	40.80	
1422						3.06	0.10	31.80	
1423						3.53	0.09	34.03	
1424						3.86	0.21	58.48	
1425						4.08	0.12	39.49	
1426						4.68	0.12	31.10	
1427						4.28	0.14	32.12	
1428						4.04	0.17	48.08	
1429						3.47	0.12	34.45	
1430						4.39	0.15	46.22	

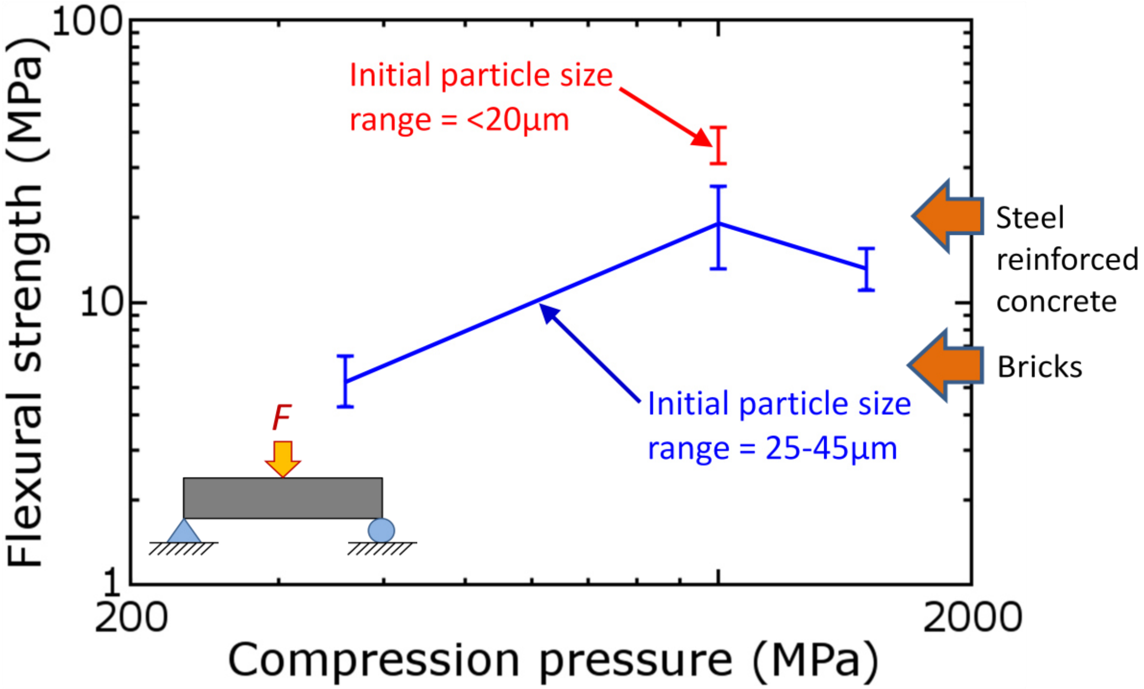

Figure 5-11 Montmorillonite Flexural Strength *vs.* Compression, Free. Quasi-statically compressed montmorillonite flexural strength versus compression pressure with free lateral boundary condition using Method 2. Three-point bending diagram is shown on lower-left.

5.4.1.2 Flexible Lateral Boundary Condition

Samples were less than one millimeter thin using a flat-faced 8.71mm-diameter piston pressing down on montmorillonite particles using the free lateral boundary condition. This imposes a practical limitation on size of compacts than may be produced on larger scales. In order to increase the thickness of the sample and to demonstrate scalability of the process, we attempt the formation of thicker samples using a flexible boundary condition. This boundary takes the form of a stout, polymeric tube that is roughly analogous to a triaxial test without hydrostatic control [5]. The free lateral boundary process is repeated as a control.

Some different techniques were investigated to probe the hardening of clay samples under compression. The first technique was to use a larger pellet size, such that it would fill the larger chamber that guides the pistons where the piston surface serves as parallel flats. The second technique is to squeeze pistons without the presence of a steel die; the die was replaced by a flexible membrane. Two such flexible membranes were investigated: Tygon tubing close to 19.05mm inner diameter, and rubber vacuum tubing close to 12.7mm inner diameter. Denote the following samples for the preliminary investigation:

- C0 is a 25-45μm montmorillonite pellet, 15mm in height, compressed at 100MPa, then compressed at between 360MPa to 800MPa inside the 19.05mm die.
- C1 is a 25-45μm montmorillonite pellet, 8mm in height, compressed at 100MPa, then compressed at between 360MPa to 800MPa inside the 19.05mm die.
- A is a 53-90μm montmorillonite pellet, 10mm in height, compressed at 100MPa, then compressed inside of a rubber vacuum tube to between 360MPa and 800MPa.

- B is a 25-45µm montmorillonite, loose powder, compressed inside of a flexible PVC tube (Finger Lakes Extrusion Clearflex 70-1 P/N 8170-2590) to 360MPa. The tube is 25.4mm round by 3.18mm wall thickness, with Durometer hardness 70A.

Resultant flexural strengths for compacts made using these different methods are shown in Table 5-10. Based on the relative success of procedure B, we continued compacting samples from the 25-45µm and 53-90µm bin sizes using this method. In the following discussion, Method “B” will be referred to as using a ‘flexible tube’, or compression with the ‘flexible lateral boundary condition.’ The flexural strengths are tabulated in Table 5-11 and shown together with the flexural strengths from the rigid boundary (Figure 5-6) and free boundary (‘Dry’ data in Table 5-14) in Figure 5-14.

A picture of a beam specimen produced using the flexible boundary is shown in Figure 5-13.

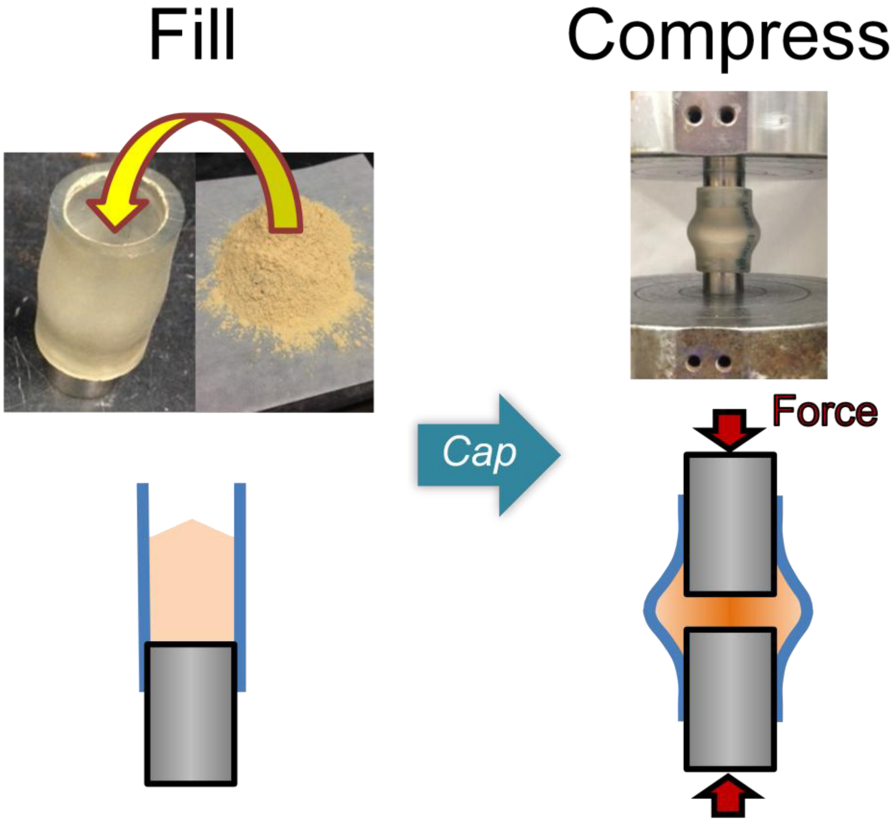

Figure 5-12 Montmorillonite Flexible Lateral Boundary Compaction. Schematic described for Method “B” where compression is performed using a flexible tube, or flexible lateral boundary. The undeformed outer diameter of the tube is 25.4mm. The upper-left shows a montmorillonite pile which is ~4cm wide.

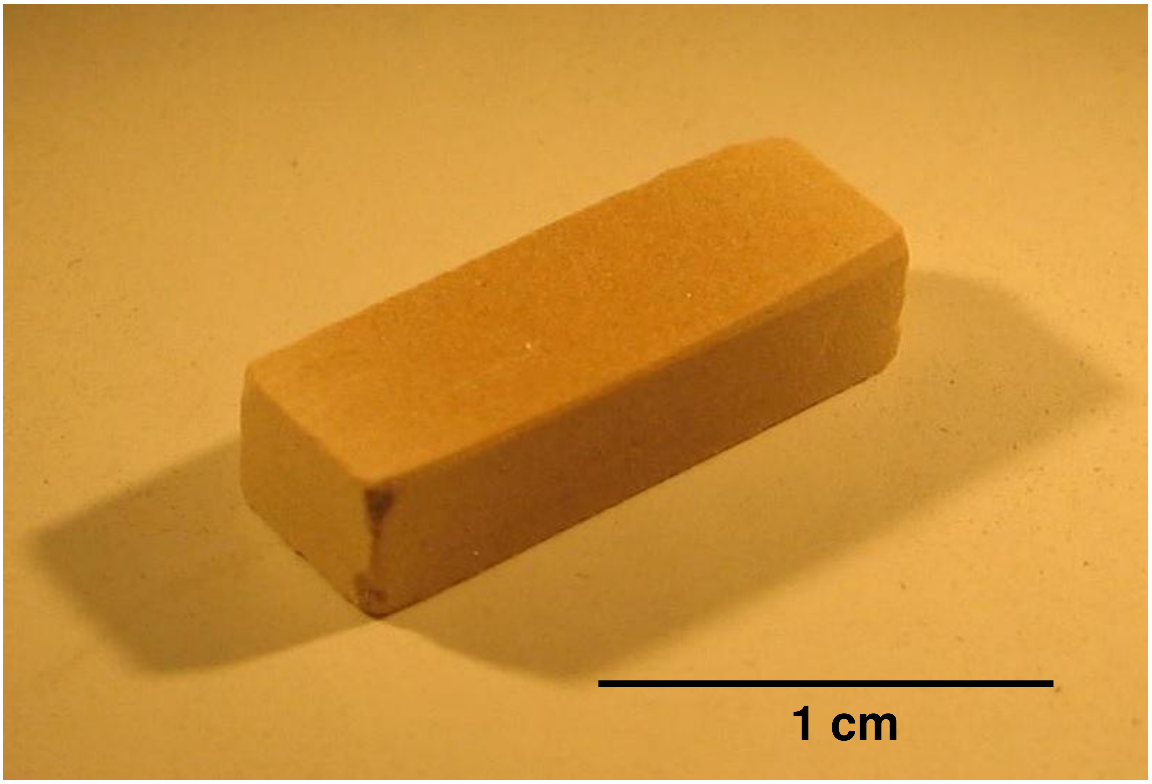

Figure 5-13 Photo of Strong Montmorillonite Beam. A beam of solid montmorillonite exhibiting flexural strength on par with, or greater than, steel-reinforced concrete. This particular specimen used 25-45μm powder dried to 600°C for 12h, and compressed to 360MPa inside a flexible tube. This specimen was not serialized.

Table 5-10 Quasi-static Formed Montmorillonite with Different Methods

Sample	Method	Length (mm)	Width (mm)	Depth (mm)	Flexural Strength (MPa)
1852	C0	9.78	6.68	1.67	2.54
1853		15.22	5.02	1.53	2.78
1854	C1	9.78	5.86	1.93	6.10
1855	A		6.60	3.31	5.31
1856	B	15.22	6.28	1.84	9.37
1857		9.78	7.01	2.73	15.95
1858			7.92	2.86	22.32

Piston diameter was 19.05mm.

Table 5-11 Montmorillonite Compacted with Flexible Lateral Boundary

Sample	Particle Size (µm)	Width (mm)	Depth (mm)	Flexural Strength (MPa)
1859	53-90	6.45	3.38	8.35
1860		7.12	3.41	8.54
1861		7.05	3.39	7.48
1862		6.30	4.51	3.40
1863	25-45	6.15	3.18	9.99
1864		6.37	3.22	18.74
1865		6.50	3.36	38.17
1874		3.48	3.05	9.96
1875		3.35	3.07	10.97
1876		4.05	3.40	27.71
1877		3.55	3.41	28.54
1878		6.30	1.84	16.96
1879		6.31	1.43	11.57
1880		3.87	3.47	18.84
1881		3.95	3.47	22.52
1882		3.91	3.57	30.57
1883		4.17	3.57	28.93
1884		3.94	3.57	28.58
1885		3.63	3.57	28.91
1886		4.55	3.77	15.87
1887		3.97	3.76	17.92
1888		4.16	3.51	20.88
1889		4.13	3.50	27.69
1890		4.03	3.16	32.60
1891		4.34	3.16	24.64
1892		4.33	3.24	26.98
1893		3.85	3.24	23.28
1912		5.32	3.54	25.82
1917		4.18	3.45	36.57
1904	<20	3.88	3.08	32.04
1905		3.43	3.08	30.88
1906		3.55	3.15	37.54
1907		3.58	3.13	40.53
1908		3.45	3.20	43.29
1909		3.55	3.19	40.99
1910		3.78	2.96	49.02
1911		2.93	2.96	39.53

Piston diameter was 19.05mm.
Compression pressure on piston was 360MPa.
Tube was 19.05mm outer diameter, 3.18 mm wall thickness, and durometer hardness 70A.
Beam support length was 9.78mm.

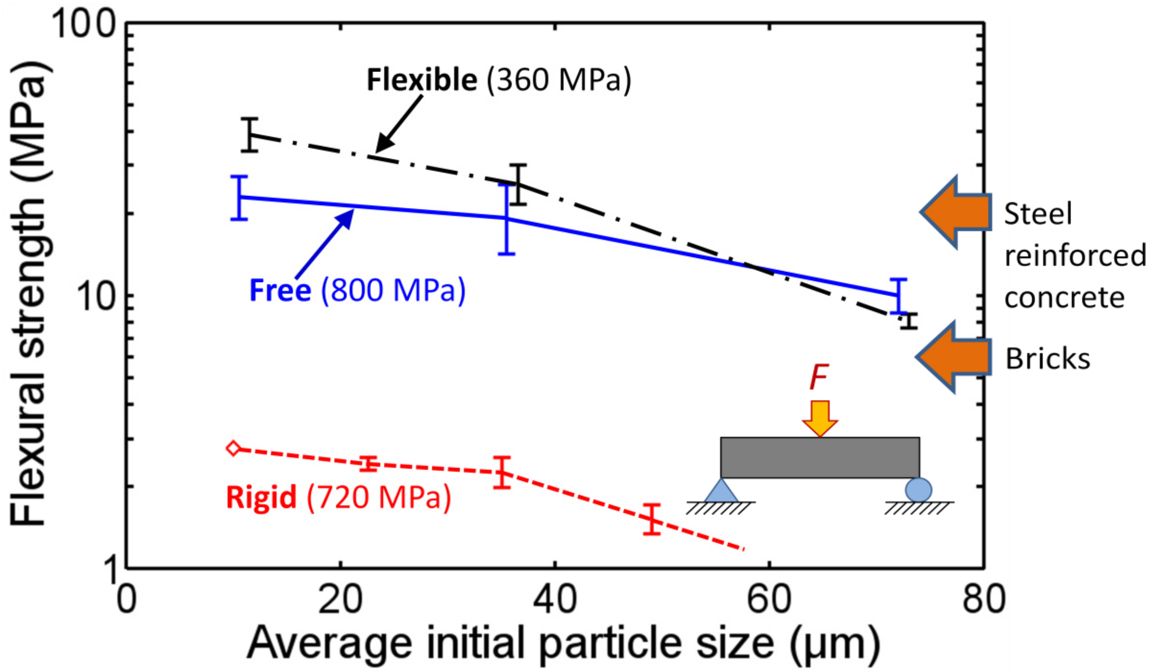

Figure 5-14 Montmorillonite Flexural Strength *vs.* Lateral Boundary Condition. Flexural strength plotted versus particle size for different lateral boundary conditions. Error bars denote one standard deviation; diamond represents single test point. Parentheses show the peak compression pressures. Schematic of three-point bending is shown on lower-right; comparison reference materials are shown at right.

These samples, compacted using the flexible boundary, are noticeably thicker than the ones produced from the free boundary condition. It is suspected that the flexible tube preempts hardening of the powder ensemble because it prevents excessive lateral motion of the particles. We can determine that the thickness gain, or aspect ratio change, of the samples is size-invariant by controls with similar sizes of the same piston.

By now, it is evident that different lateral boundary conditions significantly influence the geometry of the compact. Suppose that clay lamellae are like cards. Here, a card house serves as an analogy: pushing down without side support, the cards scatter on the supporting table with little thickness, but with some side support, the collapse occurs over a smaller area with increased thickness of the card pile. By extension, one can also explain the low strength of the rigid boundary: too much side support avoids a complete collapse, and full density cannot be achieved. The reason that a flexible boundary can build up more thickness is because it can moderate the lateral expansion of the collapsing lamellae enough to initiate local hardening in the interior of the sample.

5.4.1.3 Influence of Processing on Thickness

Without any lateral confinement during compaction, the sample thickness was only 0.4mm-1.2mm thick. The latter thicknesses were achieved by means of a 19.05mm diameter precursor pellet, compressed at 360MPa quasi-statically to a final pressure of 800MPa between parallel steel flats without any circumferential retainer. Regardless of the initial pellet thickness, the final wafer thickness was roughly the same. On the other hand, compressing a 8.71mm diameter precursor pellet to 800MPa in an identical fashion resulted in thicknesses of about 0.6mm, indicating that the aspect ratio was preserved in this method. The increase in thickness was achieved by inserting a 25.4mm diameter by 3.18mm wall thickness tube (flexible PVC, Shore A Durometer hardness 70) between aligned 19.05mm diameter steel pistons. The method uses only freestanding particles (*i.e.*, no pellet), such that the formation processing was restored to a one-step compression. The resulting thickness of the sample was ~3mm.

However, it has not yet specifically been demonstrated that compressing freestanding particles between 19.05mm pistons will not produce specimens of similar thicknesses. Previously, it was found that an 8.71mm piston compressing freestanding particles produces a 0.3mm-thick sample. Assuming proportionality in aspect ratio, we expect that 19.05mm pistons will produce a thickness close to 1 mm without using a flexible tube.

Montmorillonite with a particle size of 25-45μm was heat treated to 600°C for 12h. A 50.8mm-diameter bore with a flat bottom contained freestanding particles filled to a height of 2cm. A 19.05mm diameter (flat-faced) piston was quasi-statically compressed on top of this pile to a stress of 360MPa, producing the hardened product. The rate of quasi-static compression was 6mm/min.

The thickness of the resulting compact was 0.92mm, confirming the expectation. This control demonstrates that using a flexible tube decisively increases the thickness of the sample by 3-4 times, compared with the free boundary condition method.

5.4.2 Impact Compaction

5.4.2.1 Free Lateral Boundary Condition

A cylindrical drop weight of diameter 63.5mm weighing 7.64kg was dropped from a height of 1.52m. The impact area was upon the face of a 12.7mm piston in a matching die. A schematic of the test setup is shown in Figure 5-17. Results for the flexural strengths are shown in Table 5-12 and plotted in Figure 5-18.

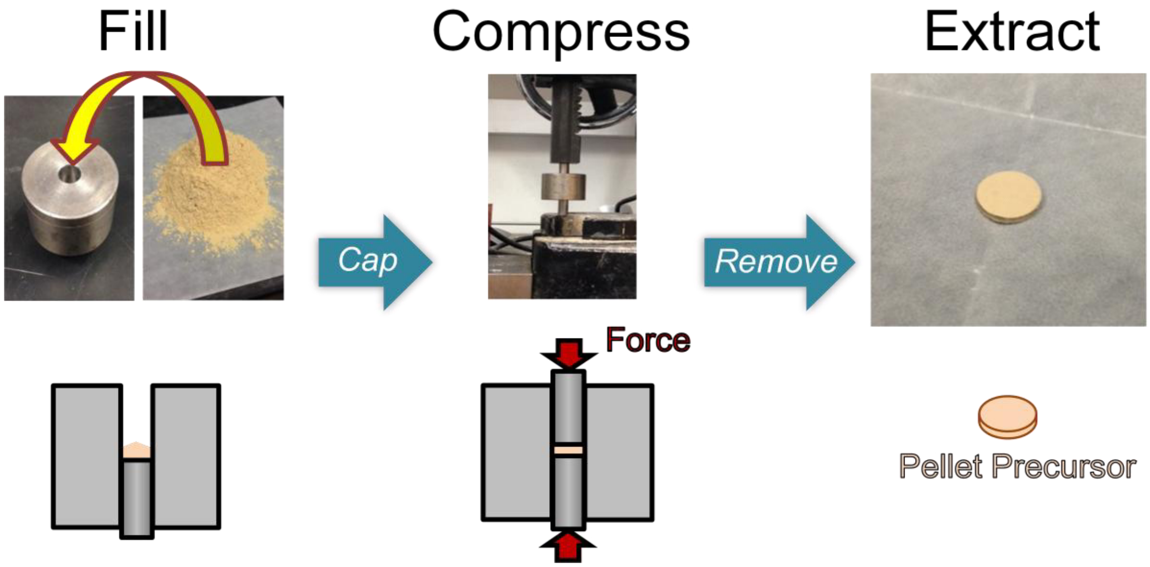

Figure 5-15 Precursor Fabrication. Schematic of the precursor-making process. The small die in the first step has bore diameter 8.71mm and outer diameter 38.1mm. The pellet shown in the last step has diameter 8.71mm.

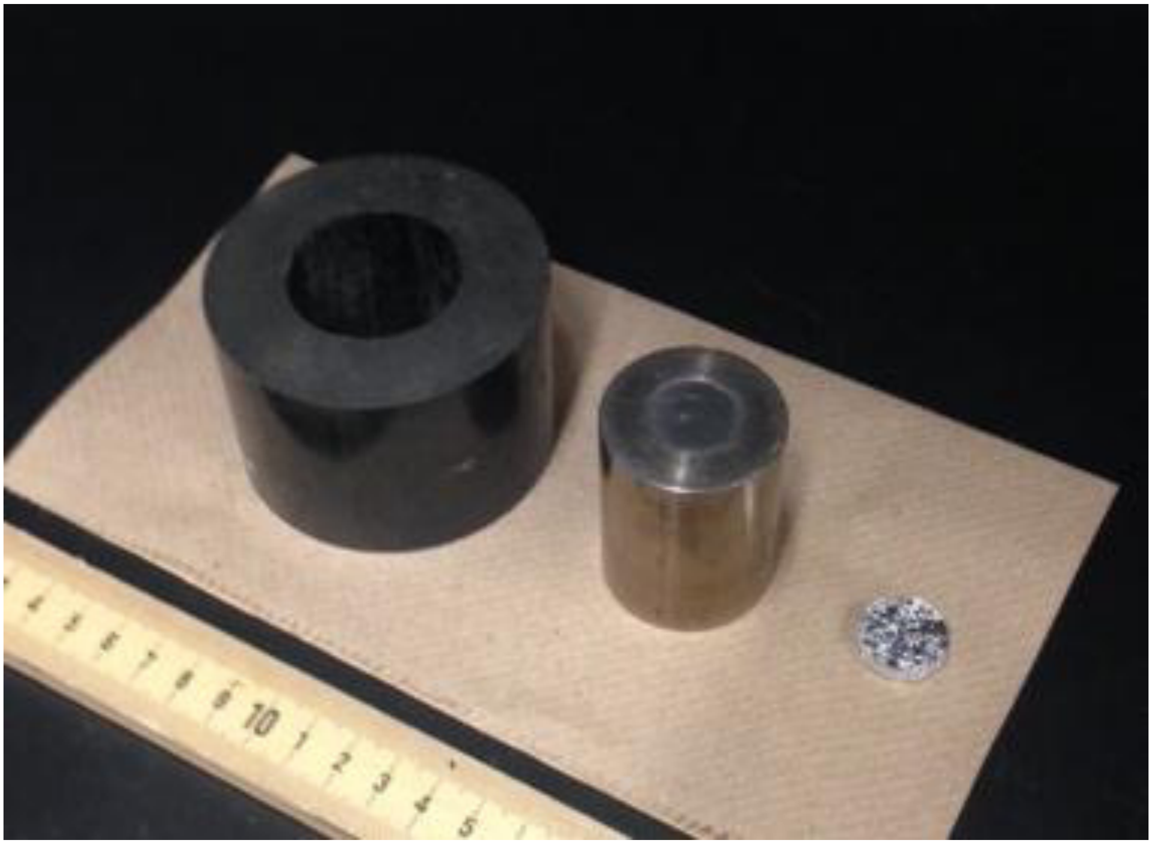

Figure 5-16 Photo of Jacket, Die, and Cushion. Photograph taken of the elastomeric jacket (left), steel die (center), and protective cushion (right). Note the free lateral boundary condition uses a relatively undersized precursor pellets positioned concentrically between pistons in the steel die. Ruler is shown for scale; the jacket, die, and cushion outer diameters are 76.3mm, 38.1mm, and 19.05mm, respectively.

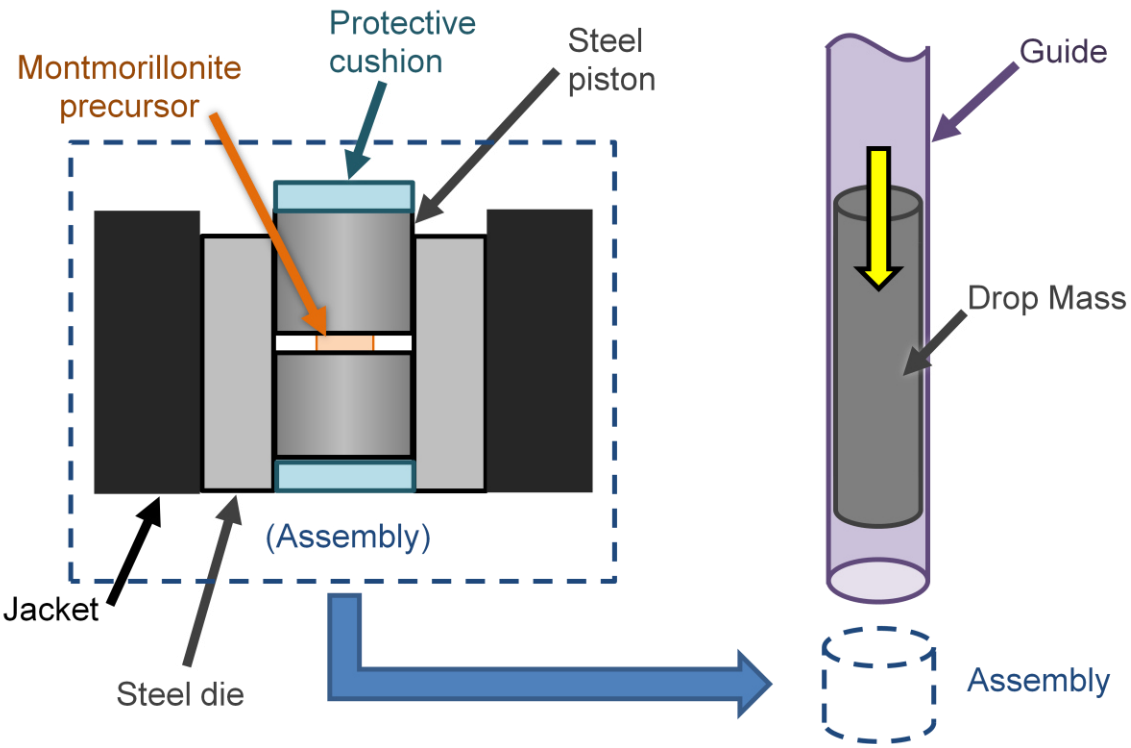

Figure 5-17 Montmorillonite Free Lateral Boundary Impact Compaction. Schematic showing the impact formation configuration with a drop tower. Both outer diameter of the jacket and guide are 76.3mm.

Table 5-12 Montmorillonite Impact-Formed with Free Lateral Boundary

Sample	Drop Height (m)	Particle Size (µm)	Width (mm)	Depth (mm)	Flexural Strength (MPa)	Average Strength (MPa)
1496	1.52	53-90	3.89	0.92	11.03	12.91
1497			3.93	0.84	12.88	
1498			4.39	1.00	15.52	
1499			3.40	1.03	12.20	
1474		25-45	4.09	0.81	93.53	56.60
1475			4.86	0.89	122.81	
1476			4.64	0.78	74.39	
1477			4.17	0.71	59.43	
1478			3.22	0.57	47.22	
1479			4.28	0.64	23.70	
1480			4.30	0.72	53.29	
1481			4.53	0.77	15.27	
1482			4.52	0.71	54.37	
1483			3.94	0.76	47.07	
1484			3.93	0.84	68.07	
1485			4.03	0.65	28.53	
1486			3.93	0.82	19.71	
1487			4.05	0.76	84.98	
1488		<20	4.50	0.76	152.08	59.31
1489			3.73	0.93	55.73	
1490			4.20	0.92	29.48	
1491			3.87	0.99	34.71	
1492 *			4.56	0.91	15.78	
1493			4.03	0.73	56.81	
1494			3.53	0.77	50.60	
1495			3.73	0.82	35.78	
1526	0.91	53-90	3.7	0.6	5.56	6.45
1527			3.73	0.5	7.95	
1528			4.04	0.83	5.19	
1529			4.21	0.7	7.08	
1530		25-45	4.17	0.72	37.19	29.65

Table 5-12 Montmorillonite Impact-Formed with Free Lateral Boundary (continued)

1531	0.91	25-45	4.45	0.64	20.78	29.65
1532			4.19	0.82	38.92	
1533			3.3	0.58	21.71	
1534		<20	4.36	0.46	17.28	28.28
1535			3.8	0.65	59.45	
1536			4.09	0.75	19.59	
1537			4.08	0.41	16.81	
1550	0.30	53-90	3.51	0.76	17.57	11.82
1551			3.43	0.81	7.65	
1552			3.02	0.8	6.2	
1553			3.92	0.78	15.85	
1554		25-45	3.96	0.72	39.6	30.68
1555			4.48	0.89	36.22	
1556			3.74	0.74	23.65	
1557			4.21	0.67	33.59	
1558			3.49	0.8	20.34	
1559		<20	3.68	0.51	30.18	18.77
1560			3.46	0.74	17.54	
1561			3.51	0.5	10.92	
1562			3.36	0.29	16.42	

Particles were dried at 600°C prior to compression.
Length between supports was 4.99mm.
Drop mass was 7.64kg.
* Pre-cracks observed near mid-span.

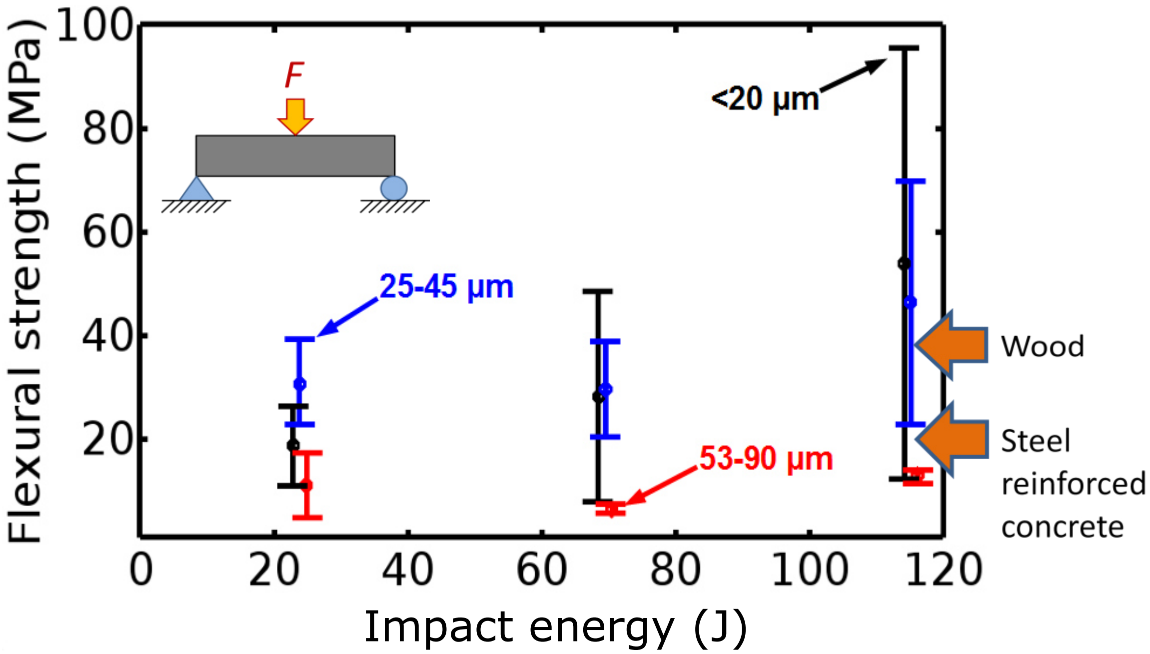

Figure 5-18 Montmorillonite Flexural Strength *vs.* Impact Energy. Impact-formed solid montmorillonite flexural strength plotted as a function of drop varying the drop height. Mass of the drop hammer was 7.64kg. Schematic of three-point bend test is shown on upper-left.

5.4.2.2 Flexible Lateral Boundary Condition

Impacted tests using an automated drop tower (Instron CEAST9350) were conducted. The two parameters that are varied are the drop height (or velocity) and the total drop mass. The latter is defined by the sum of the mass of the dropping frame (tup), load transducer, hammer, and additional masses that are attached to the frame. For varying the drop height, the desired values are entered into the software and the machine which automatically coils a pair of power springs to simulate the velocity corresponding to the input height. For varying the total drop mass, kitted detachable weights of +0kg, +1kg, +2kg, and +3kg were added to the Instron tup resulting in total drop masses of 2.667kg, 3.667kg, 4.667kg, and 5.667kg, respectively. A schematic of the test configuration is shown in Figure 5-20.

Eight samples were made per particular setting. Samples which exhibited precracking or did not break in the middle were discarded as invalid data. The results for the flexural strengths are shown in Figure 5-22.

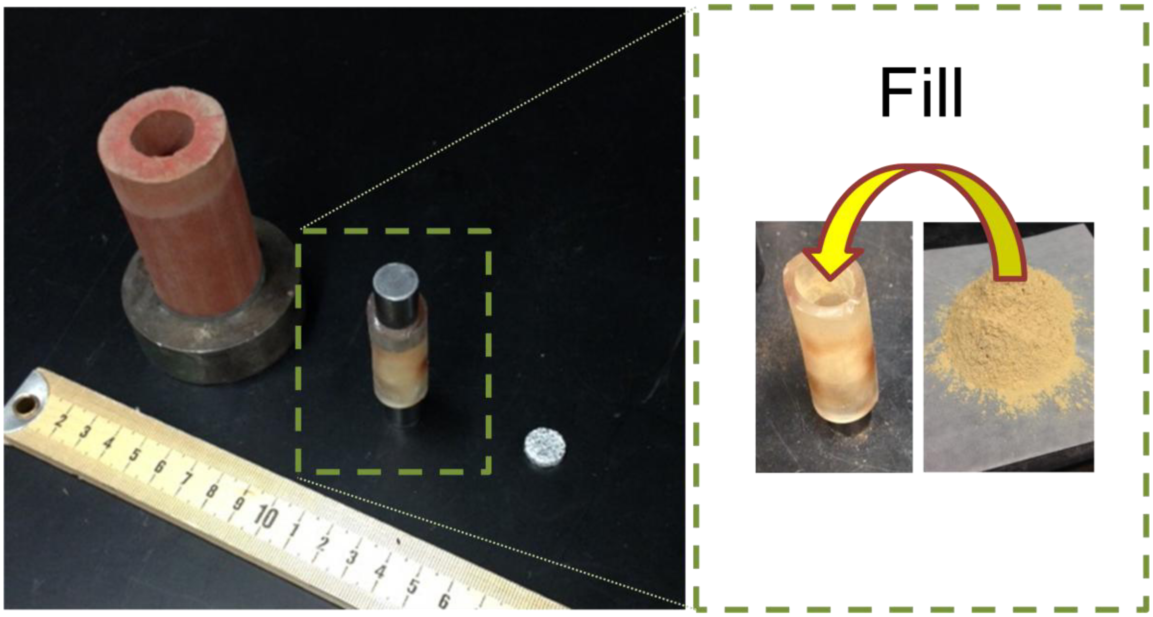

Figure 5-19 Montmorillonite Flexible Lateral Boundary Impact Subassembly. Equipment used for the impact formation process for montmorillonite. On photograph at left, positioned from left to right: the elastomeric jacket secured to a steel base, the assembly of the pistons and flexible tube containing montmorillonite powder, and a disc-shaped protective cushion made of aluminum foil. The right-hand inset shows the filling process from the open end of the flexible tube. Ruler is shown for scale; the jacket (a vacuum hose) has outer diameter 38.1mm; the piston and cushion diameter is 12.7mm.

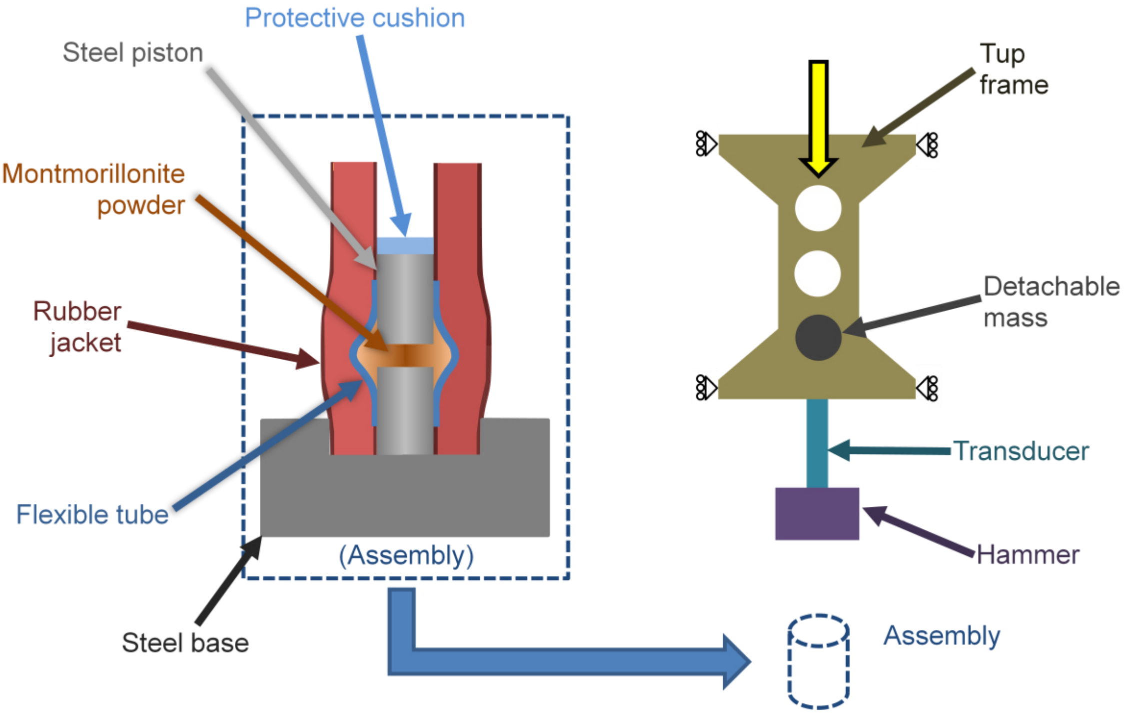

Figure 5-20 Montmorillonite Flexible Lateral Boundary Impact Compaction. Schematic of the arrangement of the test configuration for impact-formed montmorillonite powder under the CEAST 9350 drop tower. Width of the steel base is 63.6mm.

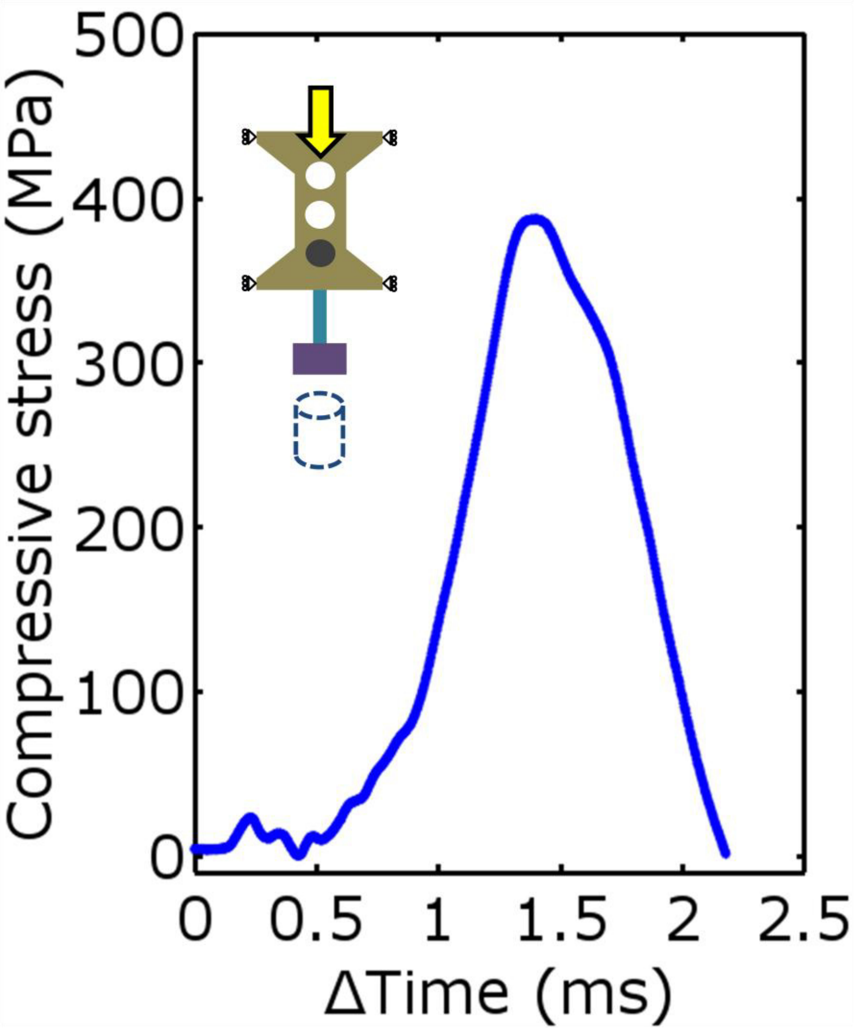

Figure 5-21 Montmorillonite Impact Time History. A representative and typical stress time history of the impact pulse of a 120J drop, showing a characteristic duration of ~1ms. The time abscissa is arbitrary elapsed (Δ) time. A schema of the drop test is shown at upper-left.

Table 5-13 Montmorillonite Impact-Formed with Flexible Lateral Boundary

Sample	Drop Height (m)	Drop Mass (m)	Peak Pressure (MPa)	Width (mm)	Depth (mm)	Flexural Strength (MPa)
1928 *	2.6	3.8	291	4.31	2.26	7.30
1929	3.4		349	5.25	1.69	38.07
1930			409	5.73	2.45	16.81
1931	3.0		427	5.24	2.16	26.28
1992 *	2.6	2.8	192	3.00	2.37	16.12
1993 *			181	2.97	1.49	28.23
1994			174	3.96	2.57	14.17
1995			188	2.61	1.84	34.36
1996			185	3.57	2.30	24.23
1997			170	3.61	2.13	17.63
1998			176	3.71	2.24	17.03
1999			205	3.67	1.55	32.93
2000		3.8	273	4.06	2.18	22.47
2001			315	4.26	2.08	38.65
2002 *			254	3.76	2.17	52.12
2003			266	3.97	1.77	76.24
2004 *			247	3.88	2.61	17.42
2005			270	3.96	1.77	44.69
2006			284	4.02	1.90	22.57
2007			292	4.23	2.21	25.94
2008 *		4.8	322	4.07	1.70	31.74
2009 *			328	4.19	2.10	34.52
2010			294	3.87	1.79	29.88
2011 *			352	4.37	1.68	43.73
2012			343	4.34	2.19	26.69
2013			238	3.23	1.50	21.42
2014			287	3.99	2.17	23.22
2015			341	4.51	1.80	45.09
2016		5.8	355	4.65	2.04	36.99
2017 *			431	4.73	1.83	82.99
2018			413	4.90	2.04	29.50
2019 *			390	4.42	2.09	30.25
2020			459	4.84	1.65	47.11
2021			450	3.62	1.22	37.86
2022 *			459	4.68	1.90	49.93

Table 5-13 Montmorillonite Impact-Formed with Flexible Lateral Boundary (continued)

2023	2.6	5.8	459	4.92	1.86	51.74
2024	1.8	4.8	239	3.35	2.42	28.69
2025 *			256	3.72	2.51	14.23
2026			261	3.42	2.21	23.35
2027 *			229	3.12	2.64	16.53
2028 *			254	3.78	2.32	25.16
2029			246	3.46	2.48	21.07
2030			254	3.88	2.33	22.12
2031			288	2.72	2.25	19.44
2032 *	3.4		389	4.60	1.95	23.47
2033			400	3.81	2.01	42.47
2034			382	3.29	2.01	39.09
2035			460	4.03	0.87	54.15
2036			460	3.68	0.66	49.21
2037			357	3.43	1.85	39.91
2038 *			455	4.72	2.16	43.79
2039 *			431	4.60	2.18	29.91
2040			429	4.02	2.02	35.97

Beam support length was 4.99mm.
Flexible tube diameter was 12.7mm.
Initial particle size range was 25-45μm.
* Failure did not occur at midspan, or visible defects were spotted before test.

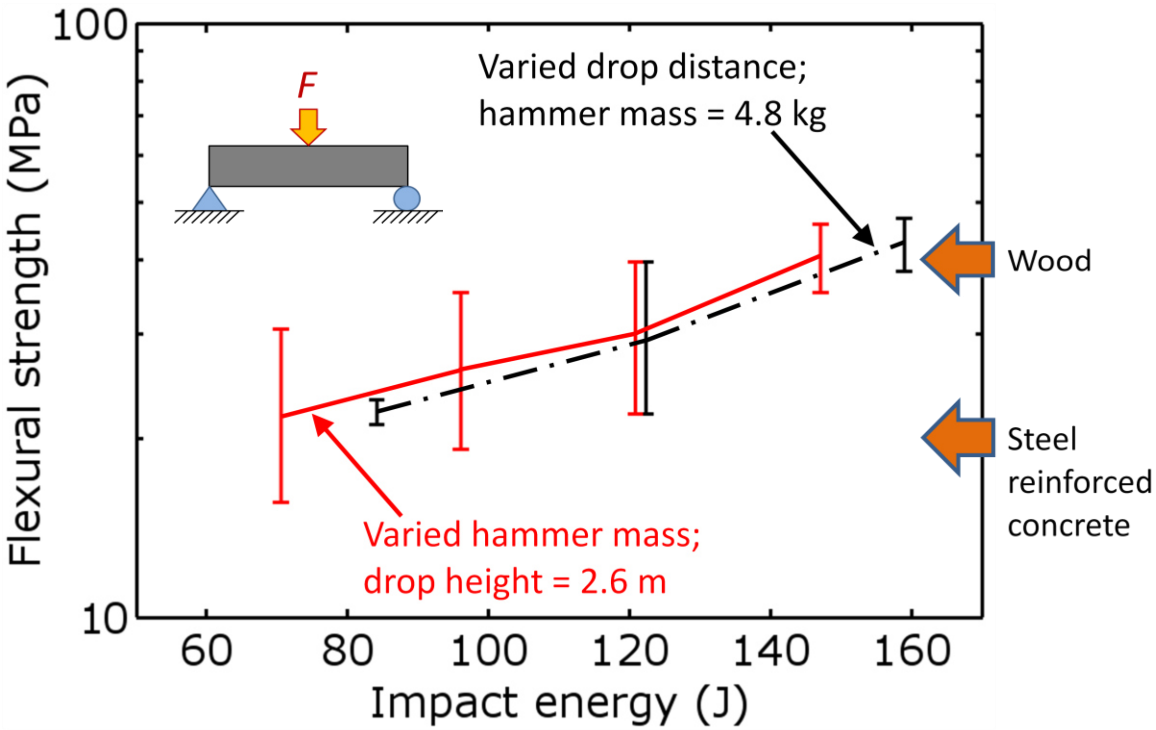

Figure 5-22 Montmorillonite Flexural Strength vs. Impact Energy, Flexible. Two series showing the trends of resultant flexural strength versus impact energy for impact-formed solid montmorillonite. The series labeled at bottom and top varied the drop weight and hammer mass, respectively, during the formation process. Initial particle size of the montmorillonite was 25-45μm. Schematic of three-point bending is shown at upper-left; reference materials shown at right.

The observed flexural strengths in coupons formed from shock loading show more variability than their quasi-statically formed equivalents. We hypothesize the dynamic nature of compression was responsible for the variation. During shock, waves travel through the sample and undulate between a maximum and minimum compressive stress, where the latter can be interpreted as a transient unloading. Reapplication of loading resumes the shearing process, if the sample configuration is perfectly undisturbed, or begins a cracking process, if a slight imperfection occurred between the two peak loads.

A combination where cracking and shearing of particles occur simultaneously may be also possible. In quasi-static loading, thin wafers showing relatively high strength is related to the role radial confinement plays in suppressing microcracks. However, elastic rebound from static friction can also occur upon further spreading of the compressed sample and surface microcracks can still occur from particle breakage. Shock loading is distinguished by the fact that, as the hardened clay spreads over the loading interface, elastic rebound occurs more incrementally and particle breakage is reduced by the vibration acting on the interface. This is equivalent to the commonly observed reduction of friction between vibrating surfaces. The equivalence in strength observed with most of the quasi-statically-pressed samples nonetheless suggests peak stress mainly determines the flexural strength.

The similarity between resultant flexural strengths between quasi-static and impact forming methods affirms the notion that the bonding process is time-invariant. Rate sensitivity is not detected because electrostatic interactions, if responsible for the bonding, occur at the speed of light and are therefore a function of separation distance instead of time. At most, a standing wave can occur throughout the compacted sample. With a characteristic thickness of ~1mm and assuming the speed of sound ~1km/s, a phonon will traverse through the compact in $t = \sim 10^{-3}\, m \div \sim 10^{3}\, m/s = \sim 1 \mu m$. Because this value is much less than the duration of the main peak in the impact time history (Figure 5-21), the compressive stress is probably uniform, and at most a standing wave, at all time intervals during the impact compression process.

5.5 Controlling Water Content in Montmorillonite

Although it is expected theoretically that drying montmorillonite particles to 600°C still allows secondary bonding to take place between montmorillonite particles, the main results of the foregoing work with the reduced boundary condition need be corroborated to support the claim that dry Martian clay particles can experience secondary bonding under high compression pressure. In particular, we seek to determine whether strong secondary bonding is possible in ultra-dry particles. We investigated three controls involving water in the montmorillonite clay.

5.5.1 Drying Temperature Effects

We refer to the drying of montmorillonite particles before compaction processing as performed in §5.3.1.4. The water loss corresponds to a decrease in the diffuse double layer around a particle. Two possibilities account for the decrease in flexural strength with increasing pre-processing drying temperature. The first is that small amounts of water may adhere between particles through surface tension, when those particles are forced together during compression. This would support the notion of hydrogen bonding being responsible for strength. The second is that water is only responsible for the friction and lubricity of particles during compression, but not their intact strengths.

Assume that hydrogen bonding is dependent on the presence of water. Based on the arguments of an ‘ice-like’ arrangement of the first few layers of the diffuse double layer (see §5.1 and references therein), we may also assume that water is responsible for most of the lubrication between particles under external shearing forces. Then, we can expect a drop in flexural strength for increased drying of montmorillonite particles if the processing only invokes a rigid lateral boundary condition. This in fact was observed; refer to the finding that heating montmorillonite particles prior to compaction lowers the strength from ~9MPa to ~2MPa in §5.3.1.4. However, strengths are very high if compacting the clay with the reduced lateral boundary condition. The sensitivity to the boundary condition shows that inter-particle contact is the main role of the double layer in clay, and stands against the notion that water-aided hydrogen bonding is responsible for strength in such compacted samples.

5.5.2 Control of Water during Compaction

All compaction work was carried out in the ambient environment. The time lapse between furnace drying and compaction was anywhere between 15min to several hours, during which atmospheric water could have adsorbed onto the clay particles' surfaces and served as an inadvertent agent of lubrication and bonding. Although some dry solids can bond in the ultra-dry state—evidenced by compacted sodium chloride's integrity in a vacuum [28]—it is unknown whether montmorillonite can rigorously bond with zero water content. In order to demonstrate this, we need to establish a trend in how strong the resultant compact is when one introduces or dries different amounts of water from the sample during the compression.

We dried montmorillonite to 600°C overnight in the furnace (Carbolite CTF 12/75/700), to establish the same baseline set of material from which strong solids were produced with the reduced lateral boundary condition. Disc-shaped precursors of diameter 8.7mm were then made by pressing the dried powder inside of an 8.71mm die (that is, with the rigid lateral boundary). The pellets, once extracted from the die, were rehydrated with various amounts of water in two steps. First, one drop of water (~0.030g) was dripped directly on the face of a pellet using a pipette, while concentrically positioned on the face of an oversized 19.05mm-diameter piston. This ‘floods’ the sample beyond its plastic limit and represents the maximum added water content. Second, the pellets were air-dried at 80°C for between 8 min to ~1.5h in order to attain water contents ranging from 2wt% to 8wt%; the water content is checked intermittently every 5min. Nominal water contents were 2.3wt%, 7.8wt%, and 16.8wt% besides the furnace-dry state. For the penultimate option, no drying was performed at all.

Rehydrated (or dry) pellets were compressed on the same oversized piston inside the 19.05mm die to 800MPa using a load-displacement testing machine (Instron 5582) with a loading rate of 3mm/min. The lower loading rate is to account for thin dimension of the sample. We applied a gentle torsion to liberate one piston from the compacted montmorillonite, which adheres to the other piston. A few dabs with tissue remove the small amounts of water around the periphery of the compact, still adhering to one piston. This piston with the attached sample is dried for a final time at 100°C in an oven for 2h. After this final drying, the compact is ground into a beam specimen and tested in three-point bending setup.

The entire procedure was repeated for three initial particle size bins: <20μm, 25-45μm, and 53-90μm. A plot of the overall results is shown in Figure 5-23, while the individual data points can be seen in a linear plot in Figure 5-24.

Table 5-14 Montmorillonite Compacted with Various Water Contents

Sample	Measured Water Content (wt%)	Target Water Content (wt%)	Initial Particle Size (μm)	Width (mm)	Depth (mm)	Flexural Strength (MPa)
1615	(dry)	0	<20	4.20	0.54	26.40
1616				3.45	0.36	15.40
1617				3.64	0.39	16.22
1618				4.17	0.32	24.72
1619				4.50	0.35	22.00
1620				3.23	0.36	21.64
1621				3.60	0.28	25.19
1644			25-45	3.20	0.55	44.85
1645				3.29	0.56	26.48
1646				3.17	0.51	30.96
1647				3.46	0.52	20.32
1648				3.59	0.53	27.61
1649				3.12	0.48	20.72
1650				3.40	0.50	15.50
1651				3.31	0.49	15.73
1622			53-90	3.14	0.53	12.14
1623				3.50	0.64	11.07
1624				4.08	0.80	17.74
1625				4.16	0.89	15.88
1626				4.00	0.72	11.59
1627				3.94	0.88	13.15
1628				4.41	0.90	6.91
1724	2.90	2	<20	3.76	0.57	34.99
1725	2.79			4.14	0.55	14.88
1726	2.11			4.43	0.53	45.77
1727	2.54			3.79	0.52	12.49
1728	1.94			4.38	0.56	8.23
1729	2.09			4.34	0.51	20.29
1730	2.40			4.27	0.54	14.85
1731	1.80		25-45	3.87	0.60	9.94
1732	2.20			2.87	0.59	4.50
1733	1.73			4.45	0.58	15.50
1734	1.92			3.29	0.51	5.42
1735	2.23			4.63	0.76	23.90
1736	1.41			4.90	0.75	7.96
1737	2.55			4.56	0.73	11.05
1738	1.71			4.41	0.60	22.49
1739	1.84		53-90	4.49	0.69	10.71
1740	2.63			3.80	0.56	2.51

Table 5-14 Montmorillonite Compacted with Various Water Contents (continued)

1741	1.81	2	53-90	3.83	0.88	4.69
1742	2.86			3.48	0.83	9.62
1743	2.70			3.37	0.80	5.73
1744	1.96			2.57	0.77	4.57
1745	1.92			2.77	0.80	5.91
1702	7.80	8	<20	7.80	0.52	5.78
1703	9.81			9.81	0.70	12.42
1704	9.42			9.42	0.66	8.59
1705	6.83			6.83	0.71	2.47
1706	9.73		25-45	9.73	0.52	9.39
1707	6.60			6.60	0.61	3.42
1708	6.54			6.54	0.68	4.02
1709	6.50			6.50	0.59	1.43
1710	6.50		53-90	6.50	0.76	4.39
1711	10.00			10.00	0.62	2.44
1712	2.12			2.12	0.75	2.76
1713	7.63			4.74	0.66	7.69
1714	10.30			4.28	0.62	1.91
1715	8.79			4.76	0.71	2.43
1716	8.70			4.38	0.71	5.16
1717	7.20			4.05	0.72	2.46
1652	22.48	16	25-45	3.00	0.44	6.83
1653	23.37			3.30	0.75	21.01
1654	20.40			4.30	0.79	8.00
1655	23.82			2.91	0.72	7.00
1668	11.96			3.12	0.69	10.43
1669	16.23			2.50	0.56	8.59
1670	13.73			3.44	0.55	9.85
1671	13.83			3.15	0.74	6.94
1672				2.88	0.77	7.32
1673	17.22			3.87	0.72	4.92
1674				3.35	0.77	15.98
1675	10.47			2.18	0.71	8.38
1676	15.85			266	0.62	17.42
1677	15.04			2.48	0.80	4.48

Compression pressure = 800MPa.
Drying temperature prior to compression = 600°C.
Compression performed with free lateral boundary condition.

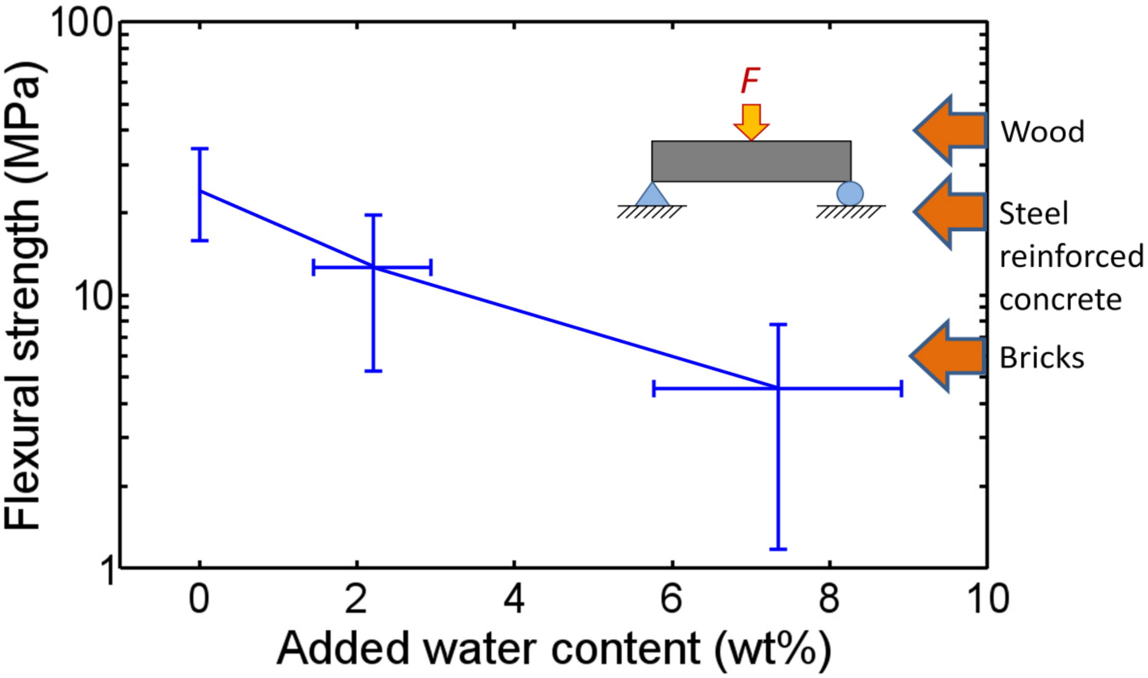

Figure 5-23 Montmorillonite Flexural Strength *vs.* Added Water. Flexural strength of rehydrated montmorillonite compacted to 800MPa followed by subsequent air-drying, plotted as a function of the added water during rehydration. The horizontal error bars show the standard deviations of the actual water contents with respect to the nominal (target) water content. Comparison references are shown at right; test schema at upper-right.

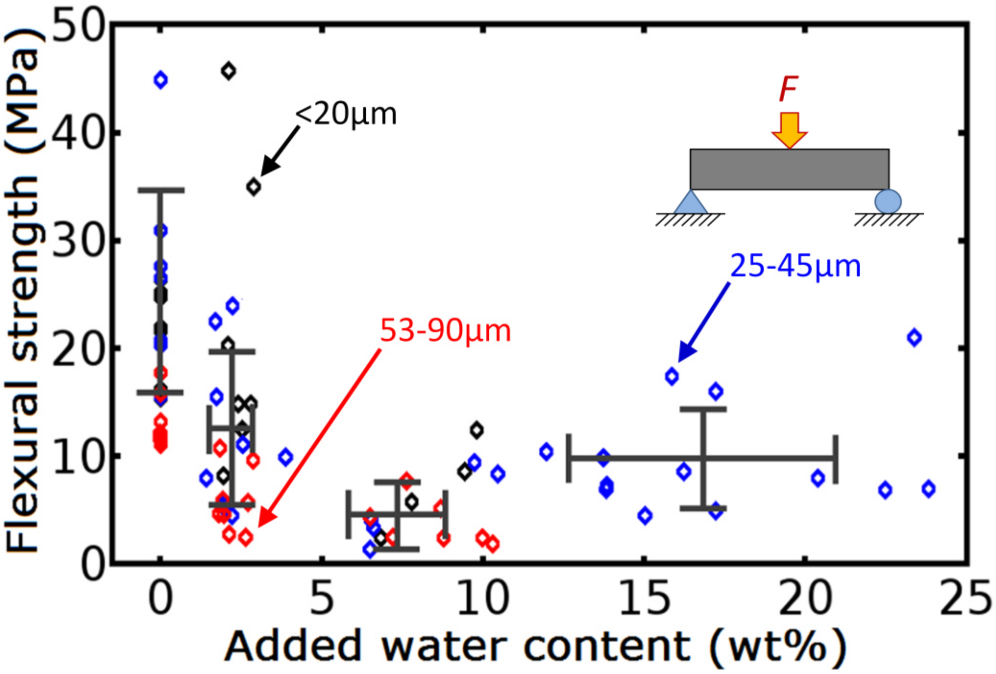

Figure 5-24 Montmorillonite Flexural Strength vs. Added Water, Scattergram. Linear plot of flexural strength of rehydrated montmorillonite compacted to 800MPa followed by subsequent air-drying, plotted as a function of the added water during rehydration. The horizontal error bars show the standard deviations of the actual water contents with respect to the nominal (target) water content. Individual data points are included, with the color corresponding to the initial particle size bin. Test schema at upper-right.

The results in Figure 5-23 indicate that for ultra-high compression pressures of 800MPa, the strength of the resulting compact decreases for all levels of added water. This stands in contrast to most geotechnical practice, which uses much lower pressures for compaction, because the macroscopic minimization of voids is more dependent on the lubricity between particles for ground improvement applications; that can explain the existence of an optimum moisture content, usually somewhere near the plastic limit of the clay. In contrast, if one takes the limit of strength when compressing to ultra-high pressures, the thickness of the diffuse double layer will determine the spacing of the particles after drying, because the ice-like adsorbed layers persist (e.g. [1][4]). Away from the ice-like or two-dimensional liquid layers, the water exhibits higher viscosity. Given the particle motions are local, the increase in effective particle 'size' due to the increase in the diffuse double layer does not guarantee the closure of defects because water can transmit compressive stress and effectively substitute solid volumes during consolidation. Once dry, the water void becomes an air void, decreasing strength.

5.5.3 Control of Water after Compaction

An air-drying oven subjected 25-45μm montmorillonite particles to 100°C for 5h. We then quasi-statically compacted the dried clay powder inside a normal, full 19.05mm die, *i.e.* with the rigid lateral boundary condition. Compression pressure on the pistons was 360MPa. The samples were not rehydrated at any time, but testing was performed at ambient. Then, instead of cutting and grinding the compacted solid into a beam specimen after compression, it is 'cured' inside a furnace (Carbolite CTF 12/75/700) to 350°C for 12h. Note that this is similar to the 'curing' temperature pursued for the earliest Mars-1a samples (see §4.3.1.1) as an artifact of the PVC melt-processing procedure. Note also the furnace temperature is also lower than the sintering temperature of clay (about 1000°C [1]), which in turn is still yet lower than the dehydroxylation temperature (about 400-500°C [1]). After heating, the discs were cut and ground into beam specimens and tested in 3-point bending. The mean strength from 4 valid tests was 23.42MPa, which is significantly higher than the flexural strength values observed with 100°C-dried particles without post-compression curing.

Upon water loss from the clay particles, the diffuse double layer retreats to the point where most interlayer water is lost, save for a few points of contact at the vertices, asperites, or extremities of particles. The water loss from the sample entails a decrease in the number of hydrogen bonds in the sample. If hydrogen bonds were responsible for strength, a compacted sample should lose strength upon heating. Instead, compacts gained strength. A shrinking diffuse double layer is concomitant with the decrease of the zeta potential, making particles bond into a more integral solid. Recall that flocculation in a liquid suspension is due to same decrease in zeta potential. Secondary forces, such as the transiently electrostatic Van der Waals forces, are generally responsible for the flocculation seen in particles with a reduced diffuse double layer. The same phenomenon holds true in the dry condition, as demonstrated by this control.

5.6 Sample Size Effects of Compacted Montmorillonite Flexural Strengths

The feasibility of scaling the size of samples is possible through a process approach, as was demonstrated by the gain in compacted thickness from the free to the flexible lateral boundary conditions, but the strengths are subject to inherent statistical variation due to defect populations in solids. As done for Mars-1a, we perform a statistic analysis of the strength using two-parameter Weibull analysis, a standard tool for describing the failure distribution of brittle solids[29]. We can follow the same approach as done for Mars-1a in § [30]. For an elementary assessment of this, we examined the following samples:

- 575, 576, 581, 582, 586-592, 702-705, 2047-2052 (rigid boundary quasi-static, 25-45μm, 360MPa)
- 1296-1301, 1303-1310, 1327-1334 (free boundary quasi-static, 25-45μm, >800MPa)
- 1415-1430 (free boundary quasi-static, <20μm, 1000MPa)
- 1863-1865, 1874-1893, 1912, 1917 (flexible boundary quasi-static, 25-45μm, 360MPa)
- 1474-1495 (free boundary impact, <20μm and 25-45μm, 114J impact energy)
- 1929, 1930, 2008-2023, 2032-2040 (flexible boundary impact, 25-45μm, >120J impact energy)

For the two-parameter Weibull model, we have [31]

$$\sigma_0 V^{-\frac{1}{m}} = R$$

where m and σ_0 are the Weibull parameters of fitting, R is the flexural strength, and V is the volume of the sample. Plotting $\log R$ as a function of $\log V$, the scatter can be shown in Figure 5-25.

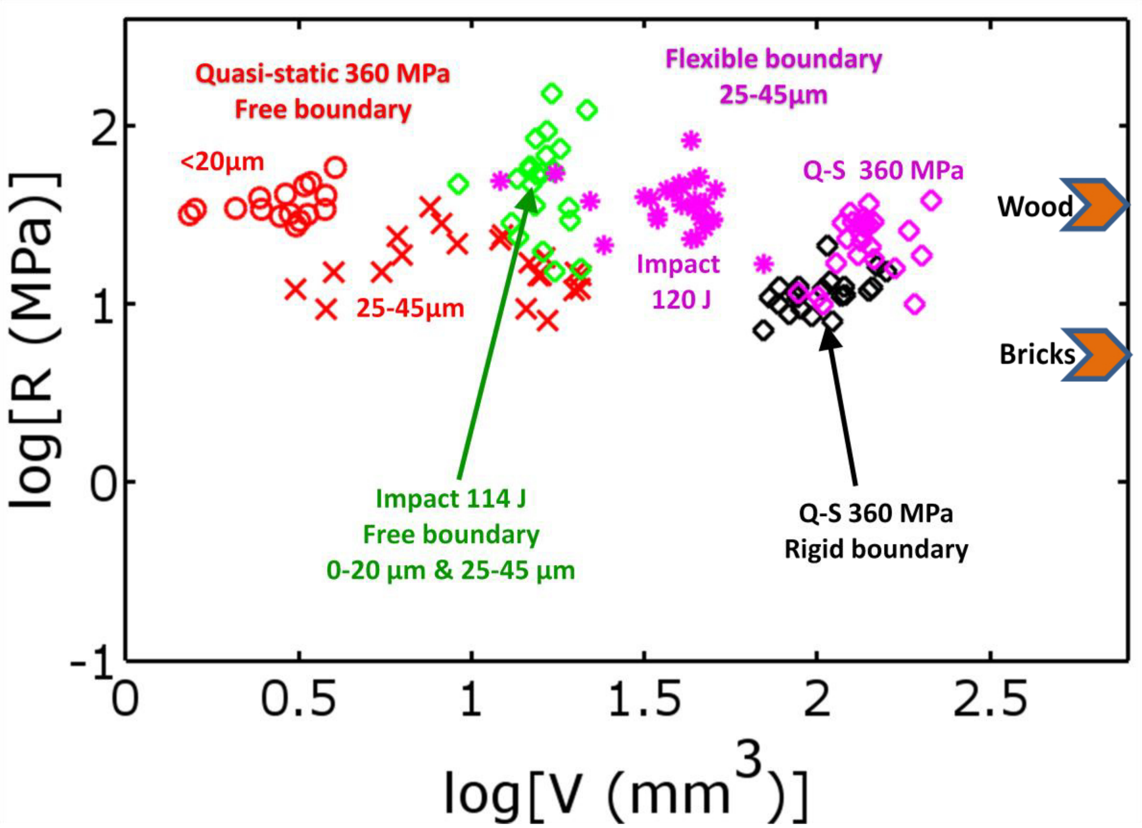

Figure 5-25 Montmorillonite Flexural Strength *vs.* Sample Volume. Empirical scatter plot of experimental flexural strengths versus the sample volume, taken from configurations containing at least 15 samples. Reference flexural strengths are shown on the right. The vertical axis bottom ordinate is chosen as the lower limit of fragility anticipated by manual handling.

No significant trends were detected within each process configuration. For example, the strongest-appearing trend appear to be the red circles on the left of Figure 5-25, but exhibits positive slope. Increasing flexural strengths for increasing volumes runs contrary to the hypothesis of defect population statistics, which states that larger flaws cause lower strengths in larger solids. This is advantageous, because there is no detrimental size sensitivity for the size variation.

Although Weibull analysis can be used to extrapolate strengths, we caution that the process configuration exerts significant impact on the resultant flexural strengths and may affect the results significantly. A possible exception is as follows: the red x's and pink diamonds in Figure 5-25 represent very close process configurations, each belonging to one of the reduced lateral boundary conditions and all else identical. If one were to regard these as a single data set, the line drawn would appear to be quite horizontal. Thus, the reduced boundary condition is robust against size effects to at least one order of magnitude and offers confidence that processing with a reduced boundary can be scaled up without deleterious consequence on mechanical strength.

5.7 Model of Montmorillonite

5.7.1 Particle Shearing

In light of the work presented in the latter parts of this chapter, we are interested in the reason why severely dried montmorillonite can develop strength under reduced lateral boundary conditions. A simple, zeroth-order model suffices from a microscopic point of view. Assume the following:

1. The in-plane strength of a clay particle is sufficiently strong to preclude in-plane failure of its lamellar sheets (refer to SEM in Chapter 6).
2. A stack of clay lamella fails under catastrophic, linear elastic, mode-II shearing during compression (refer to SEM in Chapter 6).
3. A montmorillonite lamella can be approximated by bulk, isotropic properties of silicates.
4. An ensemble of particles is compressed in isostress.

The critical shear stress of a lamellar stack is [32]

$$\tau_{cr} = \sqrt{\frac{2E\gamma}{\pi a(1-\nu^2)}}$$

where E is the modulus of elasticity, γ the surface energy between lamellae, a the flaw size, and ν Poisson's ratio. Literature references motivate estimates of $E = 50GPa$, $\gamma = 0.2J/m^2$, and $\nu = 0.3$ [33][34][35][36]. Furthermore, from the SEM micrographs in Chapter 6, assume $a = 1\mu m$. Using Mohr's circle, the resulting critical compression pressure is

$$\sigma_{cr} = 2\tau_{cr} \approx 170MPa$$

without lateral constraint. If we introduce a frictionless lateral constraint (*i.e.*, side rollers in a 2-D depiction), Mohr's circle solves

$$\sigma_{cr} = 3.5\tau_{cr} \approx 290MPa$$

The range of pressures from 170MPa-290MPa is significant not only in that it lies below the maximum compressive pressure during forming, but also for the shape of this curve. In order to compare the reduced lateral boundary conditions, we construct normalized curves *via* several steps. First, the stress ordinates near zero are discarded. Second, the displacement readings were normalized with respect to their final values. Third, the end slope of the free lateral boundary was brought to match that of the flexible lateral boundary; doing this accounted for stiffness differences in the final geometry of the sample. Finally, the peaks were translated to coincide with one another. Each reduced lateral boundary condition averaged three curves to minimize kinks in the data.

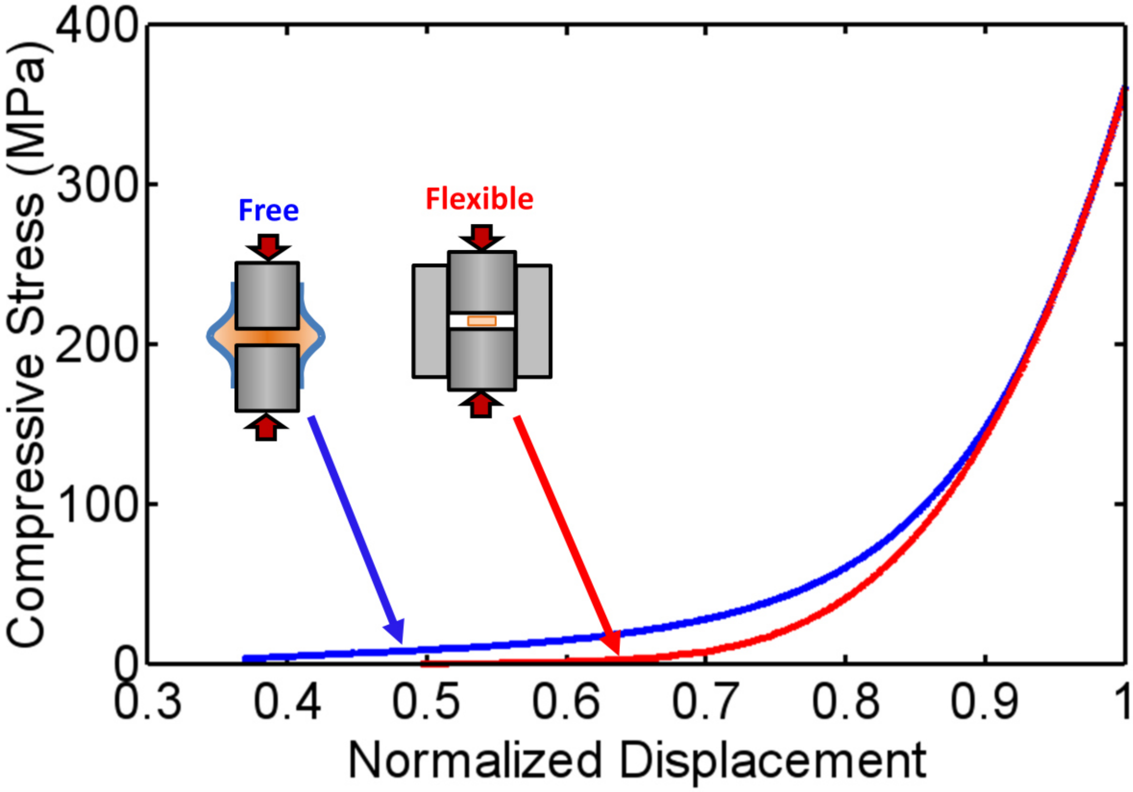

Figure 5-26 Montmorillonite Forming Load *vs.* Displacement. Compression forming load vs. displacement trace for the reduced lateral boundary conditions, labeled by depictions: the blue curve represents the flexible lateral boundary, and the red curve represents the free lateral boundary.

We note that without constraint (in red), the hardening develops earlier and 170MPa is a good approximation for the onset of the linear-elastic regime. With the flexible tube, the hardening visibly occurs earlier in the displacement history from the partial confinement of the flexible tube.

In the load-displacement trace of the compression during forming, the onset of a linear-elastic slope occurs roughly at about this range. Shearing-assisted motion of the clay particles minimizes the system free energy and residual voids in the sample. At full density, the sample is approximately linear elastic. Thus, the onset of a linear elastic regime indicates particles shear in this range of compressive stress. Macroscopically, the top-down behavior describes hardening of clays and is amenable to top-down constitutive models that have already been developed (*e.g.*, [37]).

5.7.2 Theoretical Cohesive Strength of Montmorillonite

The analysis follows the calculation of theoretical cohesive strength for Mars-1a in §4.6.3, but a key difference is that information about secondary bonds, often referred to as nonbonding potentials, are available in the literature. The potentials describe electrostatic interactions that govern the behavior of two neighboring atoms not covalently bonded.

The nature of force interactions between adjacent surfaces on a molecular scale is complex and transcendental. Calculations for the specific values for ΔF_0 discussed in §4.6.2, can proceed with a *6-12* Lennard-Jones potential, which can be regarded as a specific case of the general Mie potential [38]. For a silicate material with hydroxyl groups, one expresses the nonbonding energy using the expression by Greathouse *et al.* [39]

$$E_{nonbond} = \frac{q_1 q_2}{4\pi\epsilon_0 r} + 4\epsilon_{1-2}\left[\left(\frac{\sigma_{1-2}}{r}\right)^{12} - \left(\frac{\sigma_{1-2}}{r}\right)^{6}\right]$$

where q_1 and q_2 represent the magnitude of the atomic charges on the surface, ϵ_0 is the permittivity of free space, r is the distance between surfaces, ϵ_{1-2} is the shape parameter controlling well depth that governs stability of the bond, and σ_{1-2} is the effective atomic radius. The term 'bond' in this context temporarily refers to a covalent bond.

Based on SEM observations in Chapter 6, assume a square clay mineral layer as a platelet with dimensions 2 X 2 X 0.1µm. The volume is $4 \times 10^{-19}\ m^3$. Thus the platelet has a mass of, assuming the bulk density $\rho = 2.35 g/cm^3$

$$2.35\frac{g}{cm^3} \times 4 \times 10^{-19}\ m^3 = 9.4 \times 10^{-13} g$$

The formula for montmorillonite is given as $Na_2(Mg_2Al_{14})(Si_2O_5)_{16}(OH)_{16}$[39], leading to a molar weight of 2923.09g/mol, and the platelet thus contains

$$\frac{9.4 \times 10^{-13} g}{2923.09 g/mol} = 3.22 \times 10^{-16} mol$$

The shape parameter is uses a value of 0.1554kcal/mol. Thus, per platelet

$$\varepsilon_{1-2} = 0.1554\frac{kcal}{mol} \times 3.22 \times 10^{-16} mol = 2.09 \times 10^{-13}\ J$$

But, only a fraction of particles are in true contact, suppose 1/8th of this value (2.61E-14J). The average of the charge values for the montmorillonite components is -1.11 elementary charges, or -1.78E-19C, while the effective atomic radii are identically ~3.17Å [39]. Thus

$$E_{nonbond} = \frac{(1.78 \times 10^{-19} C)^2}{4\pi\left(8.85 \times 10^{-12}\frac{C^2}{Nm^2}\right) r} + 4(2.61 \times 10^{-14} J)\left[\left(\frac{3.17\text{Å}}{r}\right)^{12} - \left(\frac{3.17\text{Å}}{r}\right)^{6}\right]$$

which can be simplified as

$$E_{nonbond} = \frac{A}{r} + \frac{B}{r^{12}} - \frac{C}{r^6} \quad where \begin{array}{ll} A = 2.854 \times 10^{-28} & N - m^2 \\ B = 1.059 \times 10^{-127} & J - m^{12} \\ C = \ 1.052 \times 10^{-70} & J - m^6 \end{array}$$

The strength of the connection is given by the maximum force, which is the derivative of the energy profile. We first take the root of the rate of change of force, F, with respect to separation distance, r:

$$\frac{dF}{dr} = \frac{d^2E}{dr^2} = \frac{2A}{r^3} + \frac{156B}{r^{14}} - \frac{42C}{r^8} = 0$$

giving $r = 3.94\text{Å}$. The force is then

$$F = \frac{dE}{dr} = -\frac{A}{r^2} - \frac{12B}{r^{13}} + \frac{6C}{r^7} \approx 0.43mN$$

This is interpreted as the maximum force required to separate two platelets, *i.e.* ΔF_0 using the notation in §4.6.2. The theoretical strength then estimates

$$\sigma_u = \frac{0.42 \times 10^{-3}\ N}{(2 \times 10^{-6}\ m)^2} \approx 210\ MPa$$

as a result. As for the case with Mars-1a, the theoretical strength of montmorillonite exceeds the experimental data for the real solid, but the gap between theory and experiment is a little lower. Discarding the 1/8th areal contact assumption estimates $\sigma_u \sim 1.7GPa$, which is one to two orders of magnitude higher than the experimental results. This is still less than the classic ~E/10 assumption for a silicate material if assuming E~60GPa for a typical silicate. The discrepancy owes to the use of non-bonded potentials, lowering the calculated theoretical strength.

This chapter, in part, contains material that has been submitted for publication in 2016 with authors Brian J. Chow, Tzehan Chen, Ying Zhong, Cheng Zhang, Juan A. Ramirez, Cruz M. Galarza, and Yu Qiao. The dissertation author was the experimental investigator and first author of this paper.

5.8 References

1. Grim, R. E. Clay Mineralogy (2nd ed.). McGraw-Hill (1968).

2. Worall, W. Clays: Their Nature, Origin, and General Properties. Maclaren and Sons (1968).

3. Pusch, R., Yong, R. N. Microstructure of Smectite Clays and Engineering Performance. Taylor & Francis (2006).

4. Osipov, V. I. "Nanofilms of Adsorbed Water in Clay: Mechanism of Formation and Properties," *Water Resources* **39**, *7*, 709-721 (2012).

5. Das, B. Principles of Geotechnical Engineering (7th ed.). (2010).

6. Lambe, T., Whitman, R. V. Soil Mechanics. Wiley (1969).

7. Brownell, W. Structural Clay Products. Springer-Verlag (1976).

8. Smalley, M. Clay Swelling and Colloid Stability. Taylor and Francis (2006).

9. Teich-McGoldrick, S. L., Greathouse, J. A., Jove-Colon, C. F., Cygan, R. T. "Swelling Properties of Montmorillonite and Beidellite Clay Minerals from Molecular Simulation: Comparison of Temperature, Interlayer Cation, and Charge Location Effects," *J. Phys. Chem. C* **119**, *36*, 20880-20891 (2015).

10. Terzhagi, K. "The Physical Properties of Clays," *Tech. Eng. News* **9**, 10-36 (1928).

11. Hendricks, S., Jefferson, M. E. "Structure of Kaolin and Talc-Pyrophyllite Hydrates and Their Bearing on Water Sorption of Clays," *Am. Mineralogist* **23**, 863-875 (1938).

12. Macey, H. "Clay-Water Relationships and the Internal Mechanism of Drying," *Trans. Brit. Ceram. Soc.* **41**, 73-121 (1942).

13. Mering, J. "The Hydration of Montmorillonite," *Trans. Faraday Soc.* **42B**, 205-219 (1946).

14. Vemulapalli, G. "Why Does a Stream of Water Deflect in an Electric Field?," *J. Chem. Edu.* **73**, *9*, 887 (1996).

15. Plummer, H. G., Reardon, L. J. Principles of Brick Engineering: Handbook of Design. Structural Clay Products Institute (1939).

16. Ehlmann, B. L., Edwards, C. S. "Mineralogy of the Martian Surface," *Annu. Rev. Earth Planet. Sci.* **42**, 291-315 (2014).

17. Ehlmann, B. L., Mustard, J. F., Murchie, S. L., Bibring, J.-P., Meunier, A., Fraeman, A. A., Langevin, Y. "Subsurface water and clay mineral formation during the early history of Mars," *Nature* **479**, 53-60 (2011).

18. Moore, H. J., Hutton, R. E., Scott, R. F., Spitzer, C. R., Shorthill, R. W. "Surface Materials of the Viking Landing Sites," *J. Geophys. Res.* **82**, *28*, 164-184 (1977).

19. Clark III, B. C., Arvidson, R. E., Gellert, R., Morris, R. V., Ming, D. W., Richter, L., Ruff, S. W., Michalski, J. R., Farrand, W. H., Yen, A., Herkenhoff, K. E., Li, R., Squyres, S. W., Schröder, C., Klingelhöfer, G., Bell III, J. F. "Evidence for montmorillonite or its compositional equivalent in Columbia Hills, Mars," *J. Geophys. Res.* **112**, *E06S01* (2007).

20. Boynton, W. V., Taylor, G. J., Karunatillake, S., Reedy, R. C., Keller, J. M. "Elemental abundances determined via the Mars Odyssey GRS," in *The Martian Surface: Composition, Mineralogy, and Physical Properties (Bell III, J. F., ed.)*, Cambridge University Press (2008), pp. 105-124.

21. Allen, C. C., Jager, K. M., Morris, R. V., Lindstrom, D. J., Lindstrom, M. M., Lockwood, J. P. “Martian Soil Simulant Available for Scientific, Educational Study,” *Eos* **79**, *34*, 405-412 (1998).

22. Nyström, C., Alderborn, G., Duberg, M., Karehill, P.-G. "Bonding Surface Area and Bonding Mechanism- Two Important Factors for the Understanding of Powder Compactibility," *Drug Dev. Ind. Pharm.* **19**, *17-18*, 2143-2196 (1993).

23. Qin, L., Rudolph, V., Weigl, B., Earl, A. "Interparticle van der Waals force in powder flowability and compactibility," *Int. J. Pharm.* **280**, *1-2*, 77-93 (2004).

24. Autumn, K., Sitti, M., Liang, Y. A., Peattie, A. M., Hansen, W. R., Sponberg, S., Kenny, T. W., Fearing, R., Israelachvili, J. N., Full, R. J. "Evidence for van der Waals adhesion in gecko setae," *Proc. Natl. Acad. Sci.* **99**, *19*, 12252-12256 (2002).

25. Velde, B. Introduction to Clay Minerals: Chemistry, Origins, Uses and Environmental Significance. Chapman & Hall (1992).

26. Muthuvel, I., Krishnakumar, B., Swaminathan, M. "Novel Fe encapsulated montmorillonite K10 clay for photo-Fenton mineralization of Acid Yellow 17," *Indian J. Chem.* **51A**, 800-806 (2012).

27. "Bentonite," Mindat.org, Hudson Institute of Mineralogy, 2016. URL: http://www.mindat.org/min-9141.html. [Accessed 2016].

28. Karehill, P. G., Nyström, C. "Studies on direct compression of tablets XXI. Investigation of bonding mechanisms of some directly compressed materials by strength characterization in media with different dielectric constants (relative permittivity)," *Int. J. Pharm.* **61**, 251-260 (1990).

29. Hertzberg, R. W. Deformation and Fracture Mechanics of Materials (2nd ed.). Wiley (2004).

30. Al-Fawzan, M. "Methods for Estimating the Parameters of the Weibull Distribution," King Abdulaziz City for Science and Technology, Saudi Arabia (2000).

31. Pelleg, J. Mechanical Properties of Ceramics. Springer (2014).

32. Tada, H., Paris, P. C., Irwin, G. R. The Stress Analysis of Cracks Handbook. ASME (2000).

33. Manevitch, O. L., Rutledge, G. C. “Elastic Properties of a Single Lamella of Montmorillonite by Molecular Dynamics Simulation,” *J. Phys. Chem. B* **108**, 1428-1435 (2004).

34. Helmy, A. K., Ferreiro, E. A., de Bussetti, S. G. “The surface energy of montmorillonite,” *J. Colloid Interface Sci.* **268**, *1*, 263-265 (2003).

35. Wiederhorn, S. M. “Fracture Surface Energy of Glass,” *J. Am. Ceram. Soc.* **52**, *2*, 99-105 (1969).

36. Davidge, R. W., Tappin, G. “The Effective Surface Energy of Brittle Materials,” *J. Mat. Sci.* **3**, 165-173 (1968).

37. Lade, P. V., Kim, M. "Single Hardening Constitutive Model for Soil, Rock and Concrete," *Int. J. Solids Structures* **32**, *14*, 1963-1978 (1995).

38. Israelachvili, J. Intermolecular and surface forces. Academic Press (1985).

39. Greathouse, J. A., Durkin, J. S., Larentzos, J. P., Cygan, R. T. "Implementation of a Morse potential to model hydrxyl behavior in phyllosilicates," *J. Chem. Phys.* **130**, *134713* (2009).

6 Characterization of Simulants

The main characterizations on simulants supporting the work in Chapters 3, 4, and 5 are thermogravimetric analysis (TGA), scanning and transmission electron microscope characterization (SEM & TEM), X-ray diffraction (XRD), CHNS/O elemental analysis, evolved gas analysis (EGA) using a combination of TGA and mass spectrometry (MS), and also elemental CHNS/O detection analysis.

6.1 TGA Analysis

A TGA machine (PerkinElmer Pyris 1 TGA) measures the mass loss of a sample while it is heated to high temperature. The sample usually gives off volatiles from adsorbed species on the surface or from within the mineral particles. In the case of IOH, the TGA machine calcines the polymers.

6.1.1 IOH Polymer Content

We used TGA to check the amount of polymer actually present in the IOH samples discussed in Chapter 3. The amount introduced was initially determined by using a balance, but the solvent method may slightly change the resultant mass percentage of polymer content in the sample.

For the TGA test, the temperature was set at 550°C at a heating rate of 20°C/min and sample was held for 1h at maximum temperature. As the TGA graph shows (Figure

6-1), the PES content in JSC-PES50 was 10.9wt%, which is much lower than the initial polymer content in the mixture. For JSC-PES33, JSC-PES20, JSC-PES20-V, the PES contents are 8.7wt%, 5.7wt%, and 7.9wt%, respectively, which is also much lower than the polymer content in the initial mixture. This is consistent with observations of the polymer squeezing out during mold compression.

One also seeks to determine whether JSC-1A lunar simulant contains any trace volatiles. A 30mg sample of unsieved, as-received JSC-1A is tested in the TGA, with results displayed in Figure 6-2. The machine settings used a maximum temperature of 550°C, a ramp rate of 5°C/min, and a dwell time at maximum temperature of 1h. The purge gas is nitrogen.

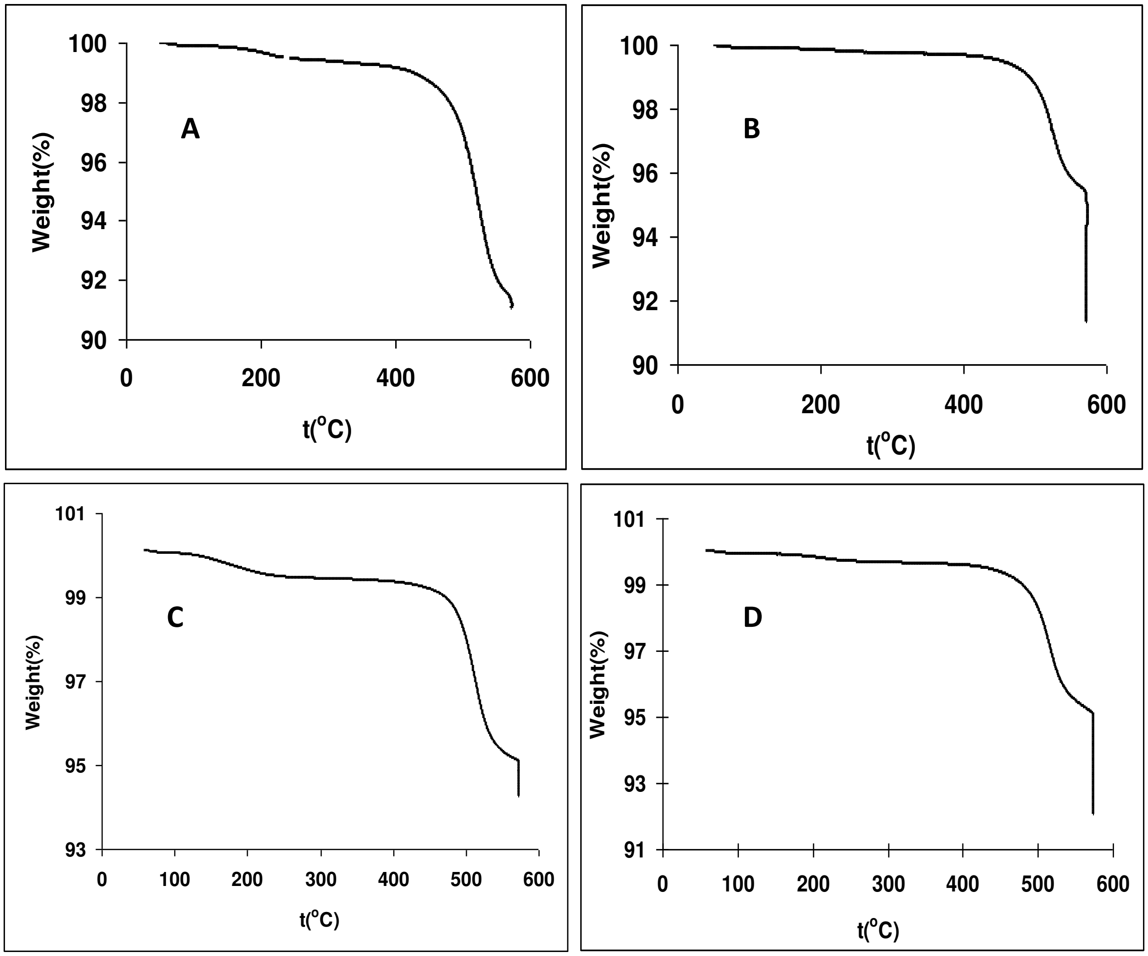

Figure 6-1 TGA of PES IOH. Panels show curves for JSC-PES50 (A), JSC-PES33 (B), JSC-PES20 (C), and JSC-PES20-V (D). Graphs courtesy of Gang Wang.

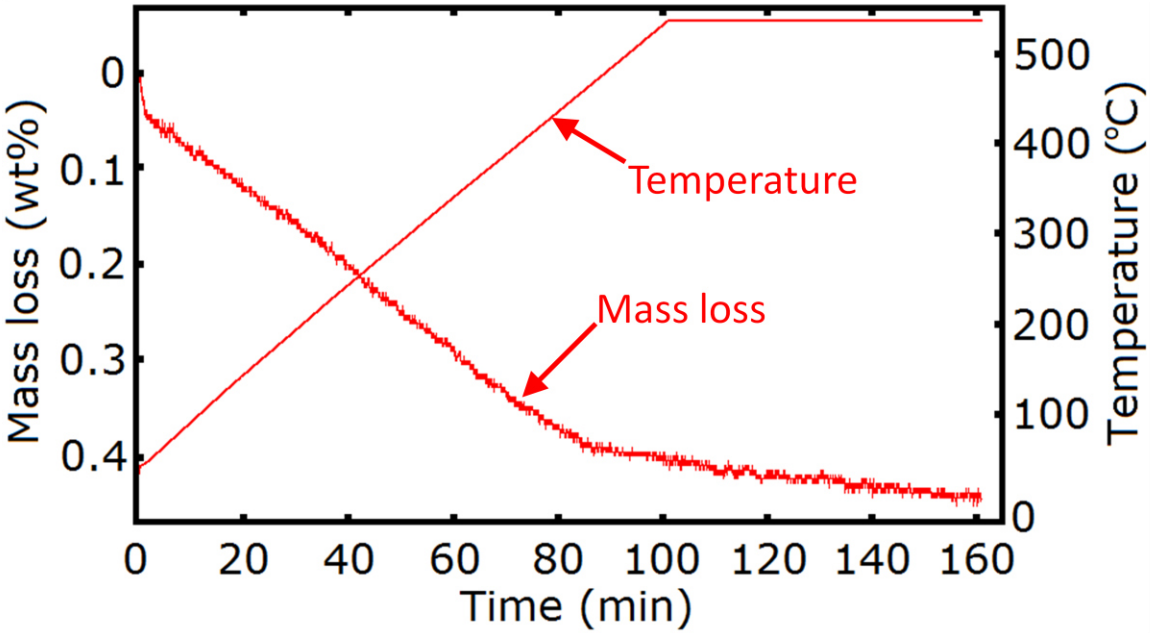

Figure 6-2 TGA of JSC-1A. Mass loss for a 30mg sample of neat JSC-1A simulant as a function of time.

In Figure 6-2, the mass loss for a sample of JSC-1A is less than 0.5wt%, as expected, because JSC-1A does not have a high specific surface area for adsorbate molecules such as water. One also observes that there exists a change in the rate of mass loss just before the maximum temperature of ~550°C was reached. This change in rate may be due to exhaustion of available adsorbed molecules on the surface of particles, or may also relate to the onset of maximum temperature. We can check the latter by increasing the ramp rate such that the time spent heating is minimized relative to the dwell time. Such was the case with Sample 173, an IOH with 10wt% PMMA. Initial sample mass was 28mg, ramp rate was set to 50°C/min, with a 1h dwell time at maximum temperature.

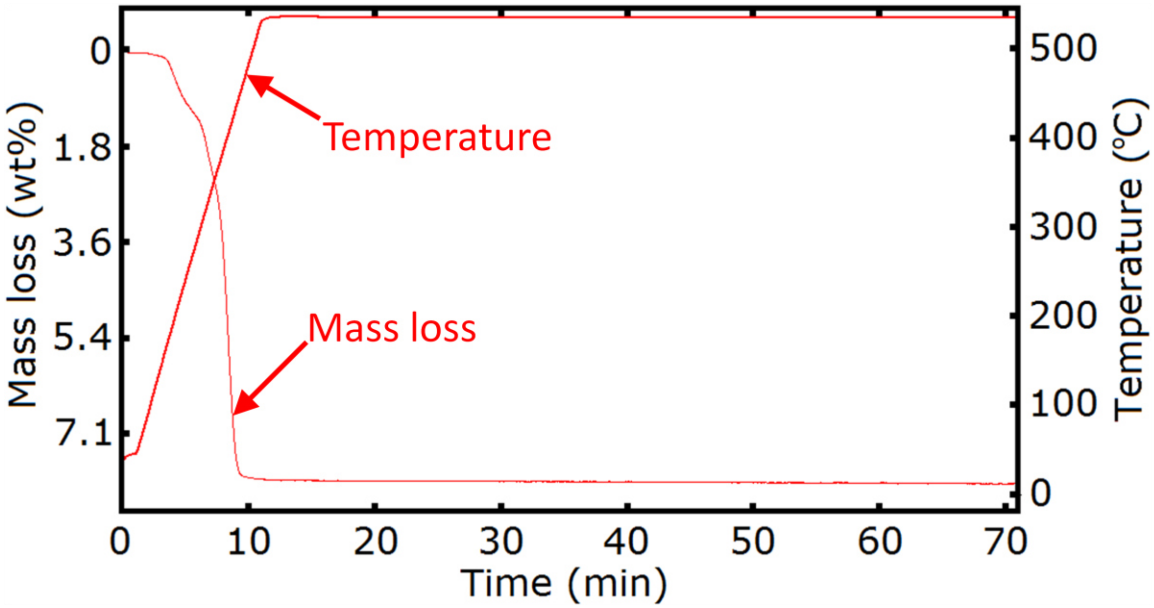

Figure 6-3 TGA of PMMA IOH. Mass loss for Sample 173, a 28mg sample of JSC-1A / PMMA hybrid made from *in situ* polymerization.

Figure 6-3 represents a typical mass loss curve for a polymer IOH hybid. The first steep drop corresponding to a temperature of about 100°C represents the loss of non-polymeric volatiles, such as water. The second drop, beginning around 300°C, signifies pyrolysis of the polymer. The mass loss with the *in situ* polymerized PMMA Sample 173 is clearly correlated with the presence of a temperature ramp. A more accurate way to measure the polymer phase or volatiles is not to dwell at the set point for a long time, but rather to extend the temperature ramp until the rate of mass loss trails off.

For *in situ* polymerized samples, the mass loss was generally in deficit of the initial amounts of monomer added during processing. For the solvent-processed samples (PES and PSU binders) or hot-pressed samples (with PVC and sulfur binders), the readings generally matched the initial amounts added during processing.

6.1.2 Volatile Characterization of Mars-1a and Montmorillonite

To simulate water content, one determines a suitable drying temperature for the Mars-1a and montmorillonite simulants in Chapter 4 and 5. Simulants were dried for 12h inside a different furnace before performing TGA.

TGA analysis on several Mars-1a (Orbitec JSC Mars-1a, <1mm) soil samples is shown in Table 6-1. The Mars-1a is as-supplied, without any drying or calcining done. The machine's ramp rate was 5°C/min to a maximum temperature of the TGA was 600°C for 20min, followed by furnace cooling to ambient. Nitrogen gas purged the sample.

Table 6-1 TGA of Mars-1a Simulant Particles

Trial	Sample Initial Mass (mg)	Mass Loss (mg)	Relative Mass Loss (wt%)
1	24.17	5.13	21.22
2	19.99	4.21	21.58
3	21.24	4.60	21.66

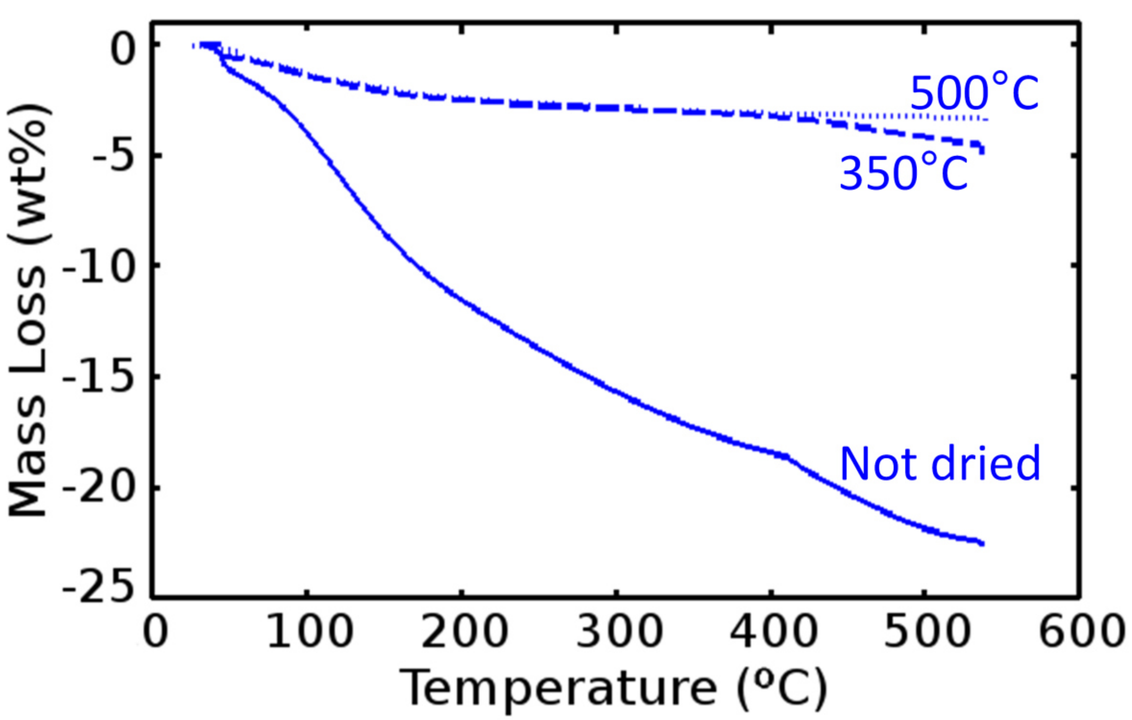

Figure 6-4 Mars-1a TGA to 550°C. TGA curve plotting mass loss as a function of temperature for Mars-1a simulant (25-45μm bin) dried to different temperatures as indicated by the labels.

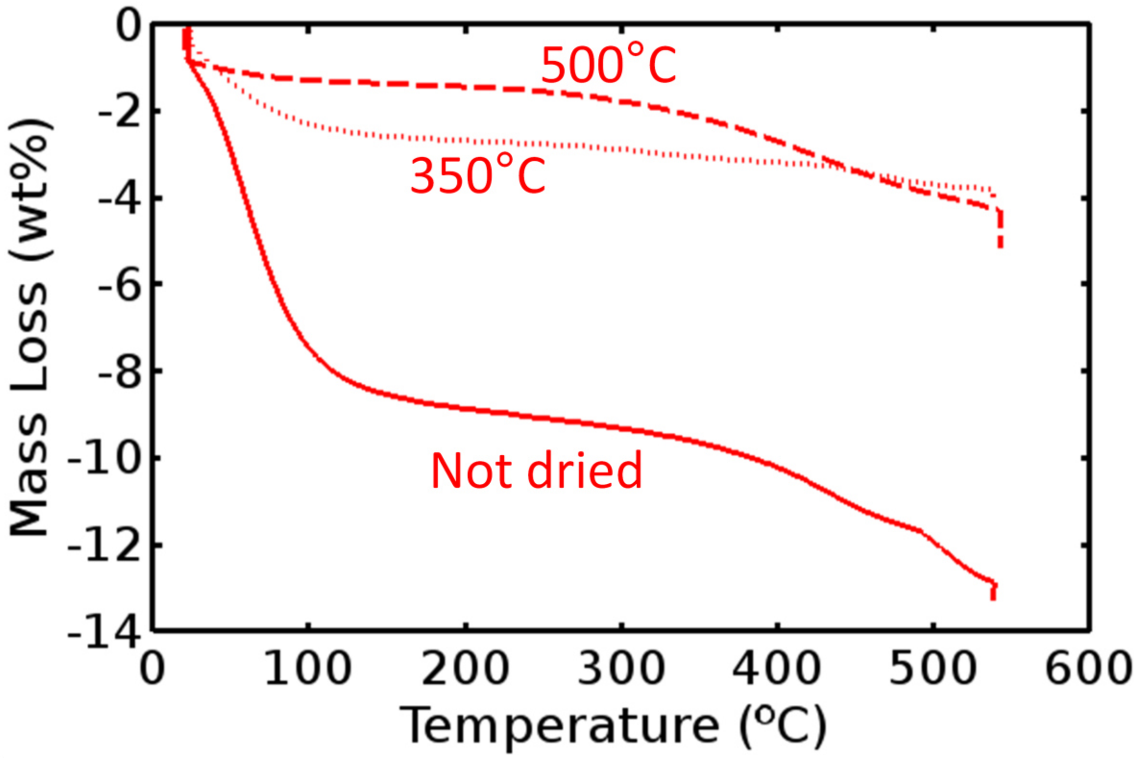

Figure 6-5 Montmorillonite TGA to 550°C. TGA curve plotting mass loss as a function of temperature for montmorillonite simulant (25-45μm bin) dried to different temperatures as indicated by the labels.

Figure 6-4 and 6-5 both show that the amount of volatile material decreases with increased drying temperature. Owing to the formation environments generating both minerals, water accounts for the majority of the volatile species [1] [2].

Montmorillonite has two steep drops in the TGA trace when it is not dried. The first begins around 50°C to about 100°C–this drop corresponds to the loss of free water and adsorbed interlayer water [2]. The second centers around ~500°C—this drop signifies the loss of hydroxyl water from the interior of the clay mineral layers.

Like montmorillonite, Mars-1a also exhibits two steep drops when it is not dried. The first begins around 100°C-200°C and is analogous to the release of surface-adsorbed water. The higher temperature may pertain to the higher specific area of npOx that encloses water molecules inside of pores and gaps. The second drop occurs around 400°C-500°C and represents the evolution of carbon dioxide from carboniferous material, as indicated by the EGA in §6.5.1. Given that most carbonates decompose far in excess of 500°C, they are not plausible candidates for the source of evolved gas. Hydroxyl water is not released, because rock-forming silica, *inter alia*, bound at the molecular level raise the transformation temperature substantially from that of neat FeOOH species [3]. Soot-like or graphitic carbon is relatively rare in igneous environments, at best constituting a minor fraction of the carboniferous material. Carbohydrates derived from plant matter are the most likely candidate, because the EGA trace in Figure 6-43 correspond to simultaneous releases of water vapor and carbon dioxide.

In most cases, the drying temperature results in a total mass loss corresponding quite closely with the remaining amount left on the ‘not-dried’ curve. Montmorillonite dried at 500°C appears not to follow this rule, giving evidence that interlayer water (and possibly structural hydroxyl water) in it is partially rehydrated upon exposure to atmospheric moisture between transport of the sample from the drying furnace to the TGA. The rehydration does not necessarily restore the structure of the clay mineral layer's interiors, which changes irreversibly above 500°C [1].

6.1.3 Total Volatile Contents in Mars-1a and Montmorillonite

Simulants generated comprehensive TGA plots with a slow ramp of 5°C/min to a maximum temperature setpoint of 1000°C. Maximum temperature held for 5min. Simulant that was dried at 600°C for 12h was also tested.

The time between removing the sample from the drying furnace to placing it inside the TGA was on a timescale similar to that of the compaction testing. Nevertheless, the TGA still shows some readsorbed water content.

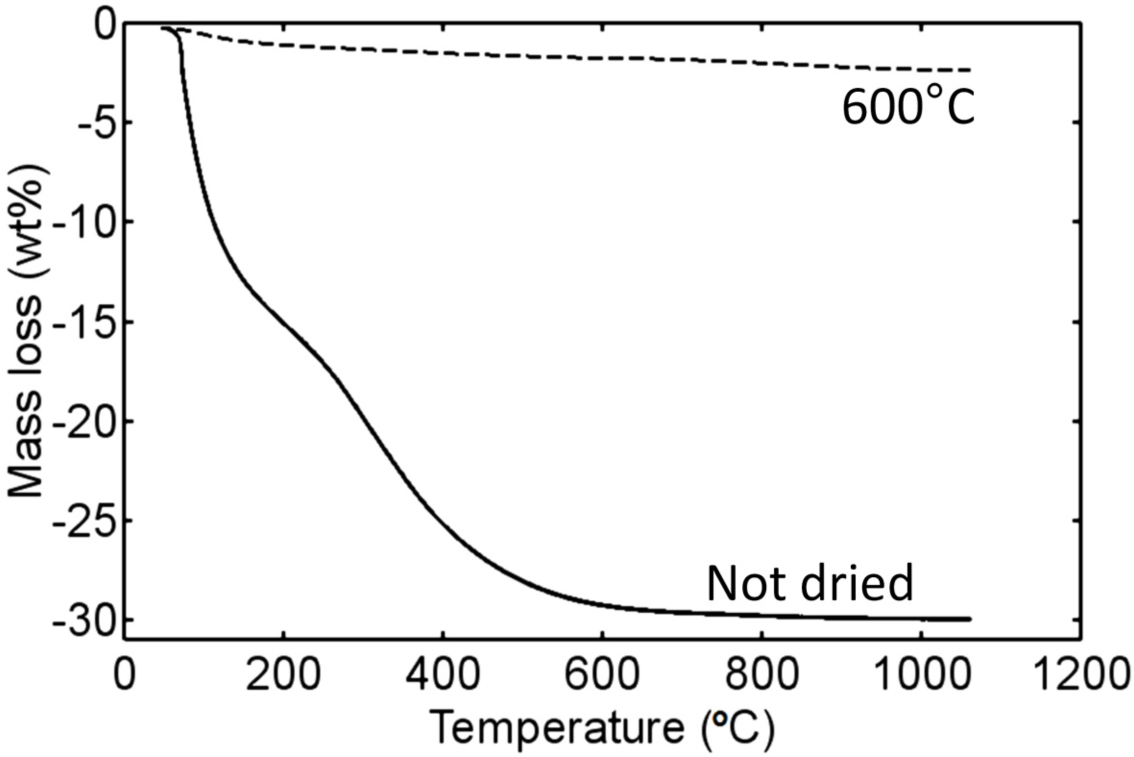

Figure 6-6 Mars-1a TGA to 1000°C. TGA of Mars-1a mass loss as function of temperature. One sample was dried to 600°C for 12h and the other was not dried. The machine setting is a high-temperature ramp to 1000°C at 5°C/min.

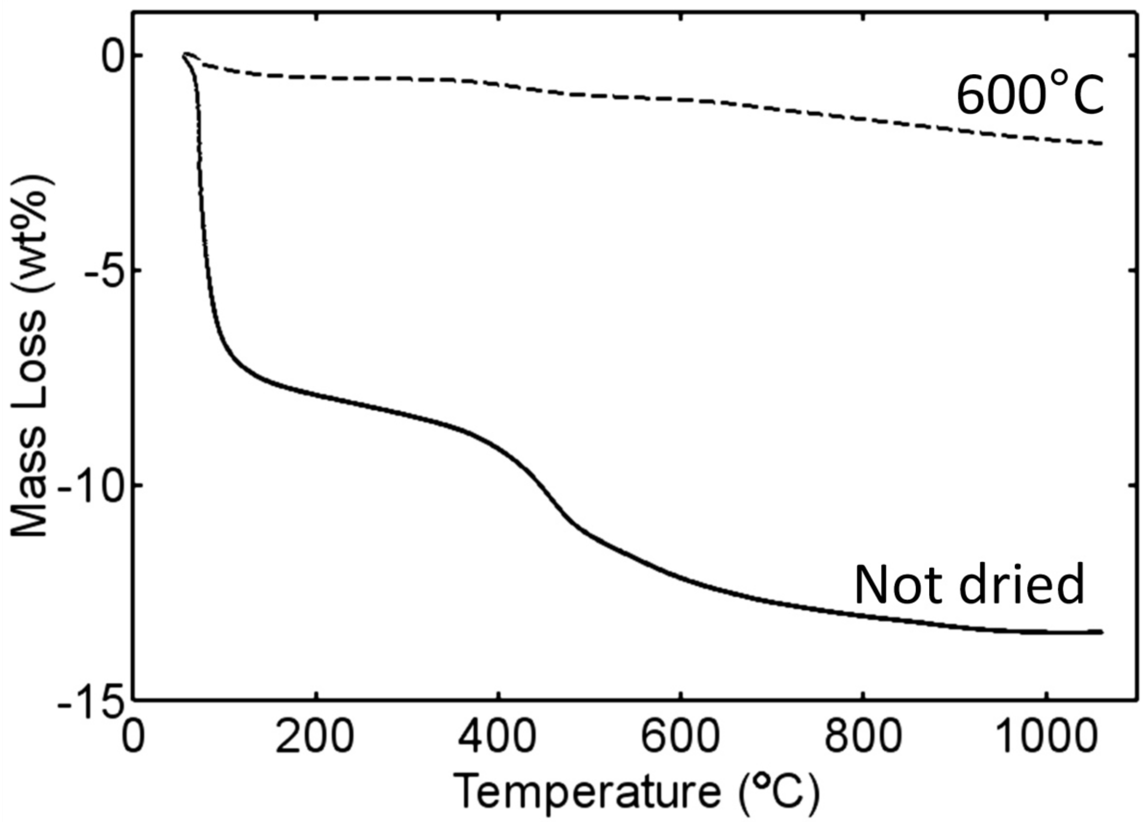

Figure 6-7 Montmorillonite TGA to 1000°C. TGA of montmorillonite mass loss as function of temperature. One sample was dried to 600°C and the other was not dried. The machine setting is a high-temperature ramp to 1000°C at 5°C/min.

Figure 6-6 and 6-7, although merely extensions of Figure 6-4 and 6-5, help to more completely support the notion that drying to an elevated temperature reduces the volatile content in the simulant to levels found in relatively dry Martian soils.

With some degree of conservatism, Martian soil water content can be estimated as <5wt%. With reference to the TGA analysis for Mars-1a, we determined 350-600°C to be an ideal drying temperature. However, in consequent procedures, the drying temperature can be as low as 80°C. The effect of prior drying temperature on flexural strength is tested in Chapter 4 and 5.

Recalling that various forms of iron oxyhydroxide (FeOOH) comprise most of npOx, one would expect a high-temperature phase transformation to occur at temperatures as low as 200°C [6]. However, silicate material derived from the weathering of basalt disperses the FeOOH on a molecular level, and impedes the phase change to well above 600°C [6]. The author reports anecdotally that out of an estimated several dozen crucibles (batches) of Mars-1a particles dried to 600°C, only on one occasion did a small amount of <20μm size fraction undergo a full phase transformation to hematite. The phase transformation is readily indicated in the visible spectrum, with hematite bearing a cherry-red color [6].

6.1.4 Characterization of Goethite Analogue

TGA was also performed for goethite in relation to Mars-1a. Figure 6-8 plots three traces for a 25wt% goethite simulant dried to two different temperatures.

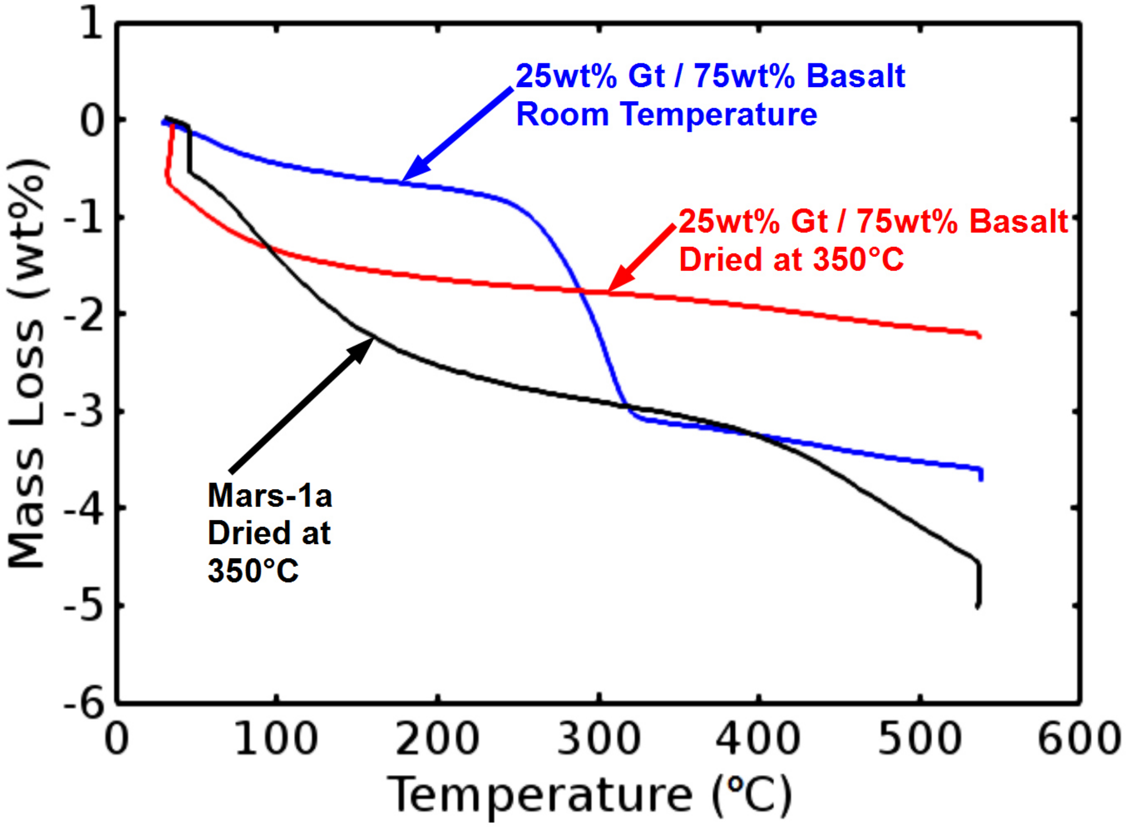

Figure 6-8 Goethite Analogue TGA. TGA curves for goethite analogues, with Mars-1a shown for reference.

Phase transformation from goethite to hematite under dry heating accompanies the liberation of hydroxyl groups, released as water vapor from the solid. The clear, steep drop in the room-temperature curve (*i.e.*, not dried) located in the 250°C-300°C matches descriptions in the literature [4]. This drop is erased as goethite is dried to 350°C, because the transformation already completes during the drying stage.

6.1.5 Post-Test TGA and Simulant Water Content

Montmorillonite from the 25-45μm bin was dried in a furnace at 600°C for 12h, followed by compaction at 360MPa using the flexible lateral boundary condition (see Chapter 5). The compact was further shaped into a beam and tested under 3-point bending. A small sample was extract from the fracture surface, and sent to TGA. The proportion of water lost in a 16mg sample was 3.6wt%, although the data for this sample is unavailable. Another sample was prepared from the fractured face of Sample 1917 and the post-flexure test TGA curve is displayed in Figure 6-9. The setpoint temperature was 600°C with a ramp rate of 5°C/min; setpoint dwell time was 30min. Sample mass was 35mg.

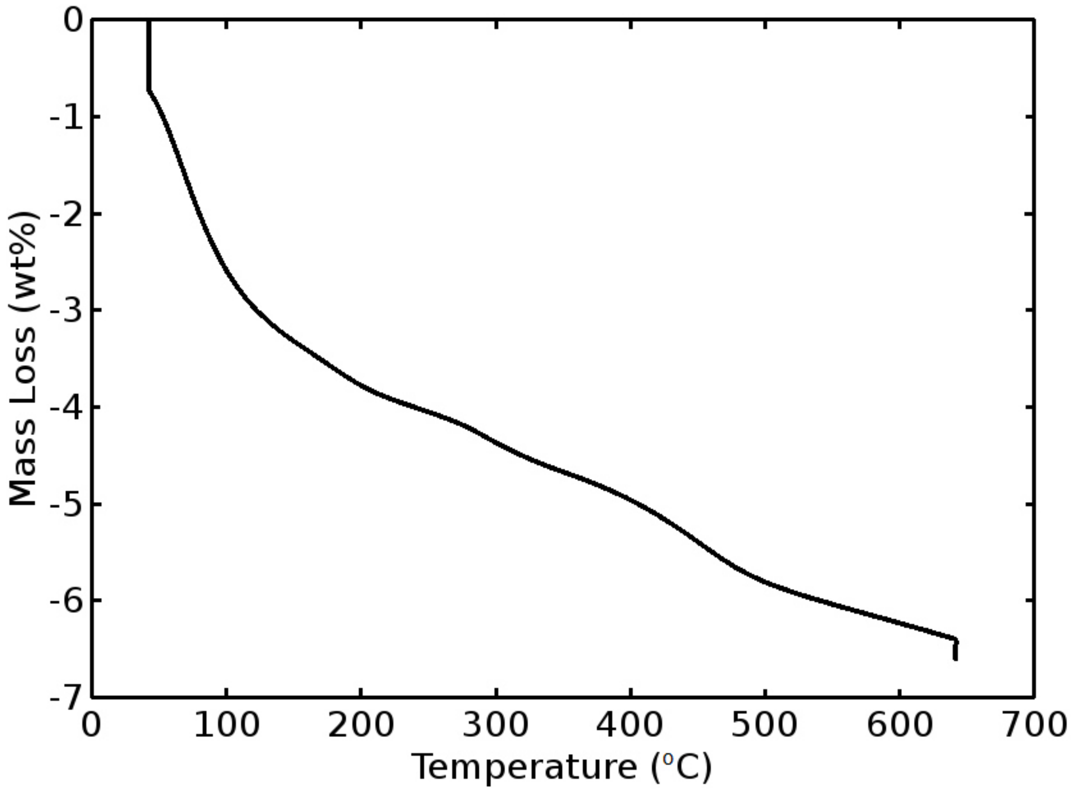

Figure 6-9 Montmorillonite Post-Test TGA. Mass loss *versus* temperature for compacted montmorillonite Sample 1917.

The weight loss from Sample 1917 was approximately 6.6wt%. Note the time elapsed between the furnace-drying of a sample to three-point bend testing is 1-2h; more time is needed to extract a sample for TGA. This is considerably more time than required for the compaction process only. Thus, the freshly dried curve from Figure 6-7 is more likely to represent the water content of the montmorillonite during the compaction phase. The range of water content rehydrated in a furnace-dried montmorillonite is between 2wt% and 6.6wt%.

Several lines of evidence have reinforced the notion that water-aided hydrogen bonding is not responsible for strength, in light of the controls with water performed in Chapter 5. Water contents between 2wt% and 6.6wt% is already representative of the Martian surface water content [5].

In reality, furnace-drying to past the dehydroxylation temperature (~450°C) is rather ultra-conservative because the hydroxyl structure is stable on the cold atmosphere of Mars. Supposing that boiling water can be achieved either at 100°C or in a vacuum at room temperature, the near-vacuum environment of Mars' surface would need 700K – 100K = 600K to drive off the hydroxyl groups. Doing so conservatively assumes linearity between absolute temperature and activation energy. Given the actual Martian surface temperatures are between 200K and 300K, one can preclude with high confidence that the hydroxyl water is stable inside Martian clay mineral layers. Ordinarily dry clay minerals are sufficient to make structural parts, in part due to better lubricity between the clay mineral layers.

6.2 SEM and TEM Analysis

Selected fractured beam coupons from Chapter 3, 4, and 5 are iridium-sputtered (Emitech K575X) for 8-15s and micrographed at 5-10kV from a working distance of 5-12mm with SEM (FEI/Phillips XL30 or FEI SFEG UHR). Compacted Mars-1a characterized by TEM (Hitachi HD-2000) were ground with a mortar and pestle for 60s using <1N force.

Melt-processed Mars-1a and sodium perchlorate is characterized by SEM in Appendix L.

6.2.1 Fracture Surface of a 5wt% PES IOH

In order to determine the wettability of the binding polymer phase against JSC-1A simulant, SEM characterization was performed on fracture surfaces of tested samples. This sample was not serialized.

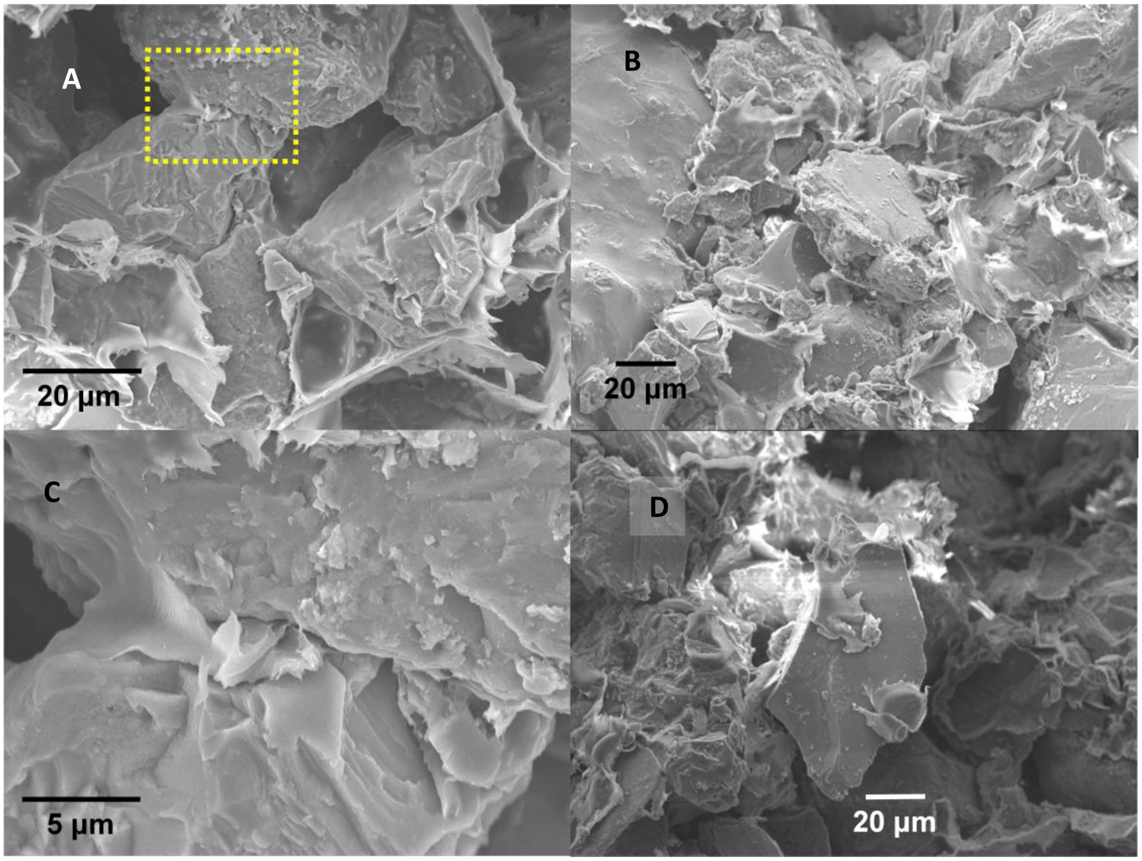

Figure 6-10 SEM of PES IOH. Micrographs of a post-test 5wt% PES – JSC-1A IOH fracture surface. The dotted yellow box is magnified on the lower-left panel.

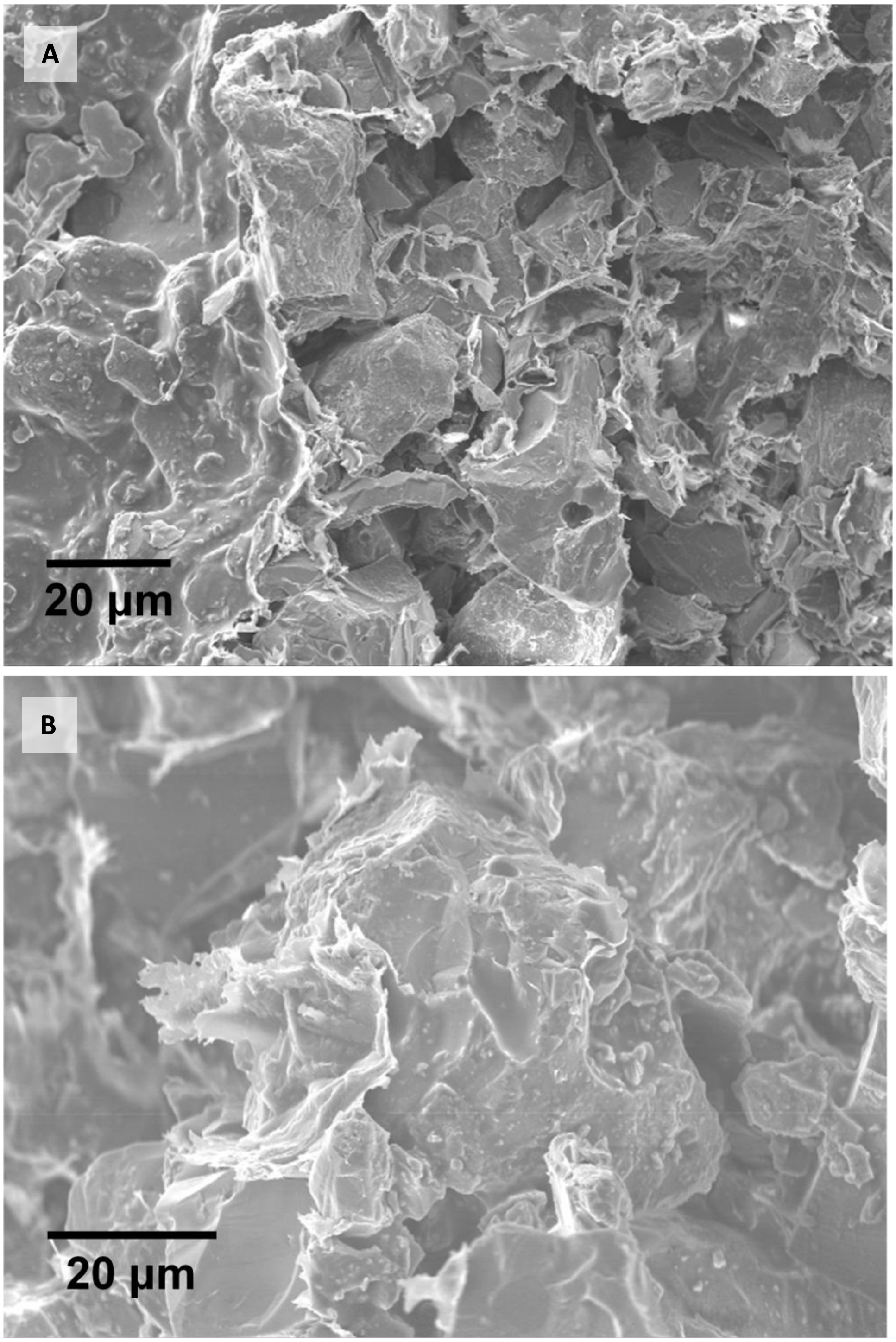

Figure 6-11 SEM of PES IOH 2. Micrographs of a post-test 5wt% PES – JSC-1A IOH fracture surface.

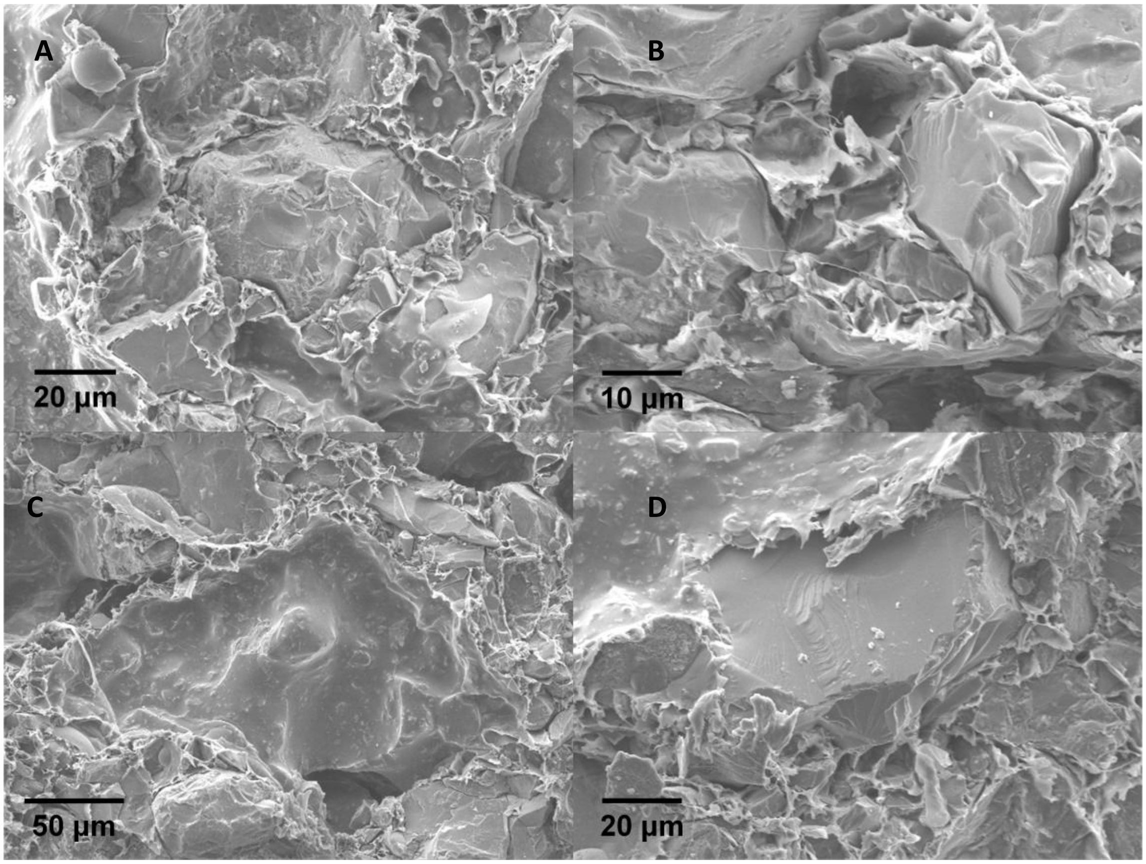

Figure 6-12 SEM of PES IOH 3. Micrographs of a post-test 5wt% PES – JSC-1A IOH fracture surface.

Figure 6-10 through 6-12 present visual evidence of the binding phase being merely a loosely-adhering coating to the simulant particles of the sample. Particles that are exposed generally do not show adherence to particles, especially around fine features such as cracks and depressions. This suggests that the polymer was not present in these features prior to mechanical removal. The boundaries around the particles appear to be cleanly separated from the binder; collectively these suggest non-wettability of the binding polymer phase. The suggestion is further corroborated by the self-comparison contact angle investigation in Appendix A.

6.2.2 Fracture Surface of Sulfur Binder

Bound sulfur was characterized within Mars-1a simulant on fracture surfaces of Samples 211, 225, 245, and 247 in ascending order of sulfur content.

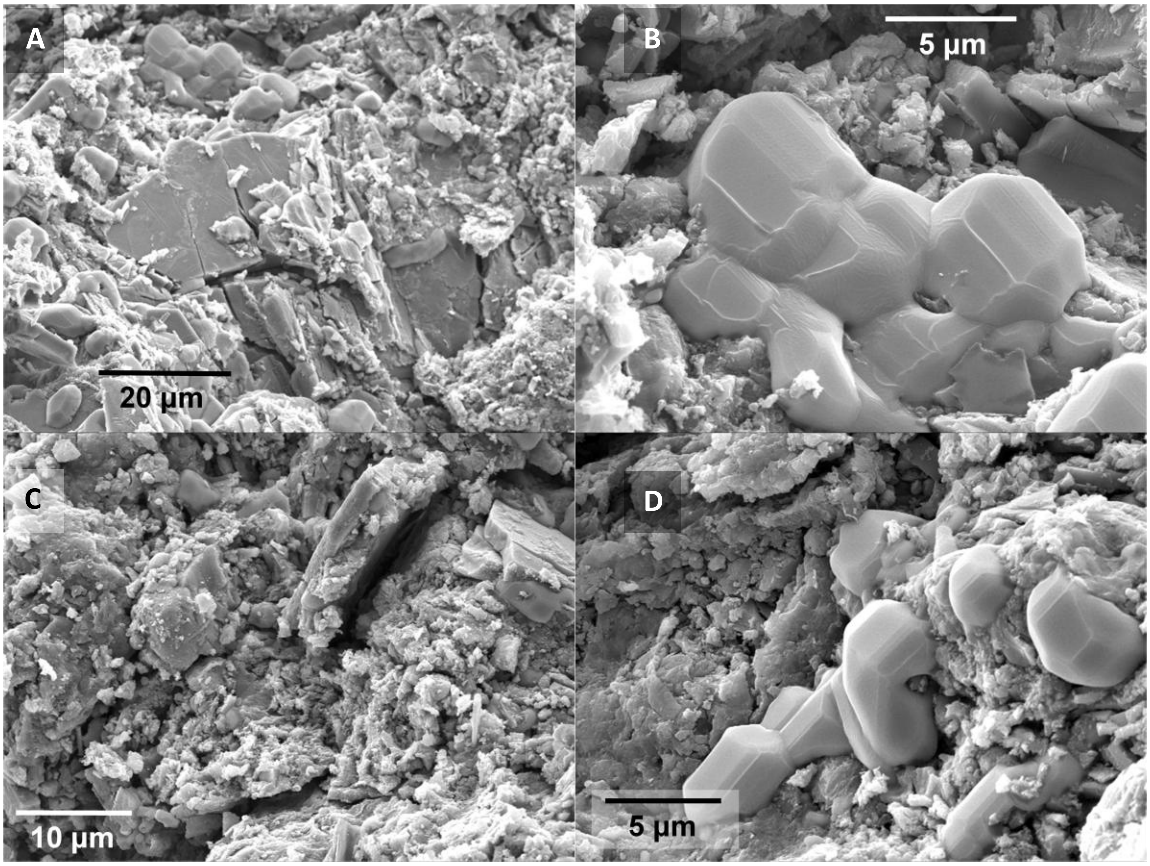

Figure 6-13 SEM of 10wt% Sulfur/Mars-1a. Micrographs of Sample 211 post-test fracture surface. This sample was a 10wt% sulfur-Mars-1a hybrid quasi-statically compressed to 270MPa inside a rigid lateral boundary.

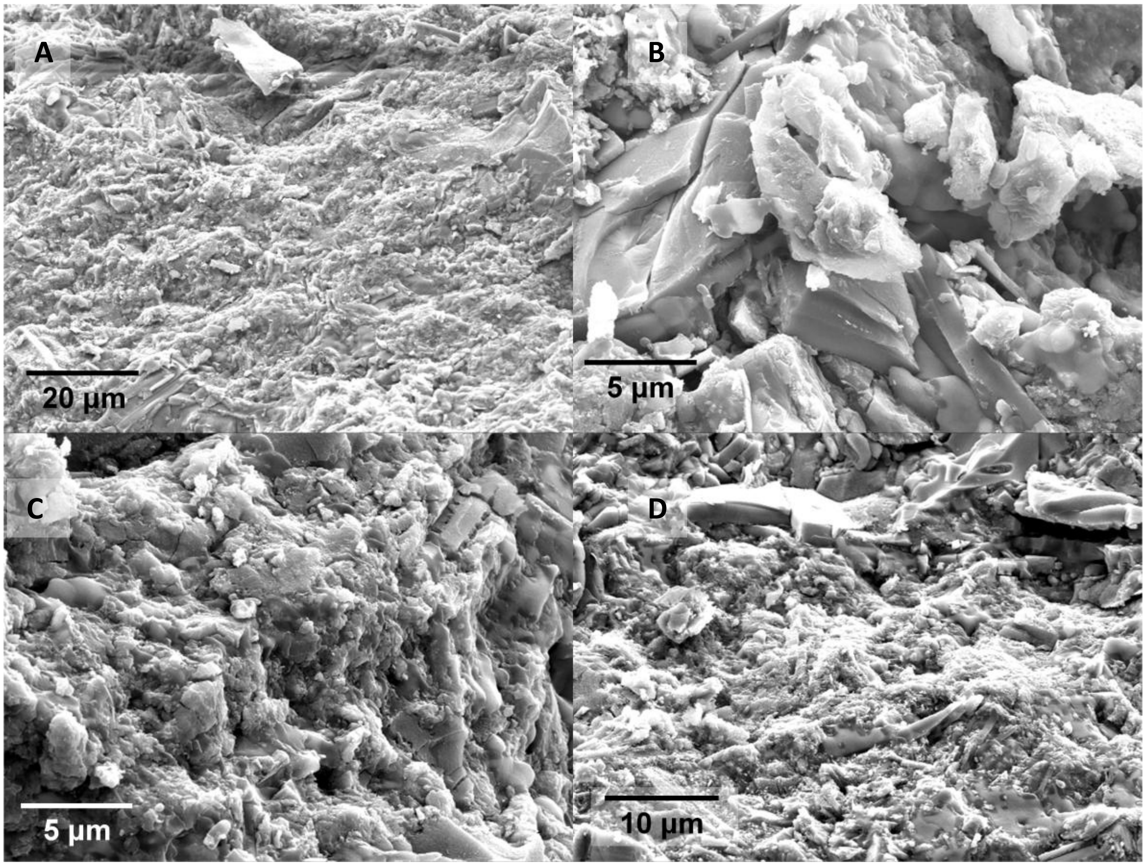

Figure 6-14 SEM of 20wt% Sulfur/Mars-1a. Micrographs of Sample 225 post-test fracture surface. This sample was a 20wt% sulfur-Mars-1a hybrid quasi-statically compressed to 270MPa inside a rigid lateral boundary.

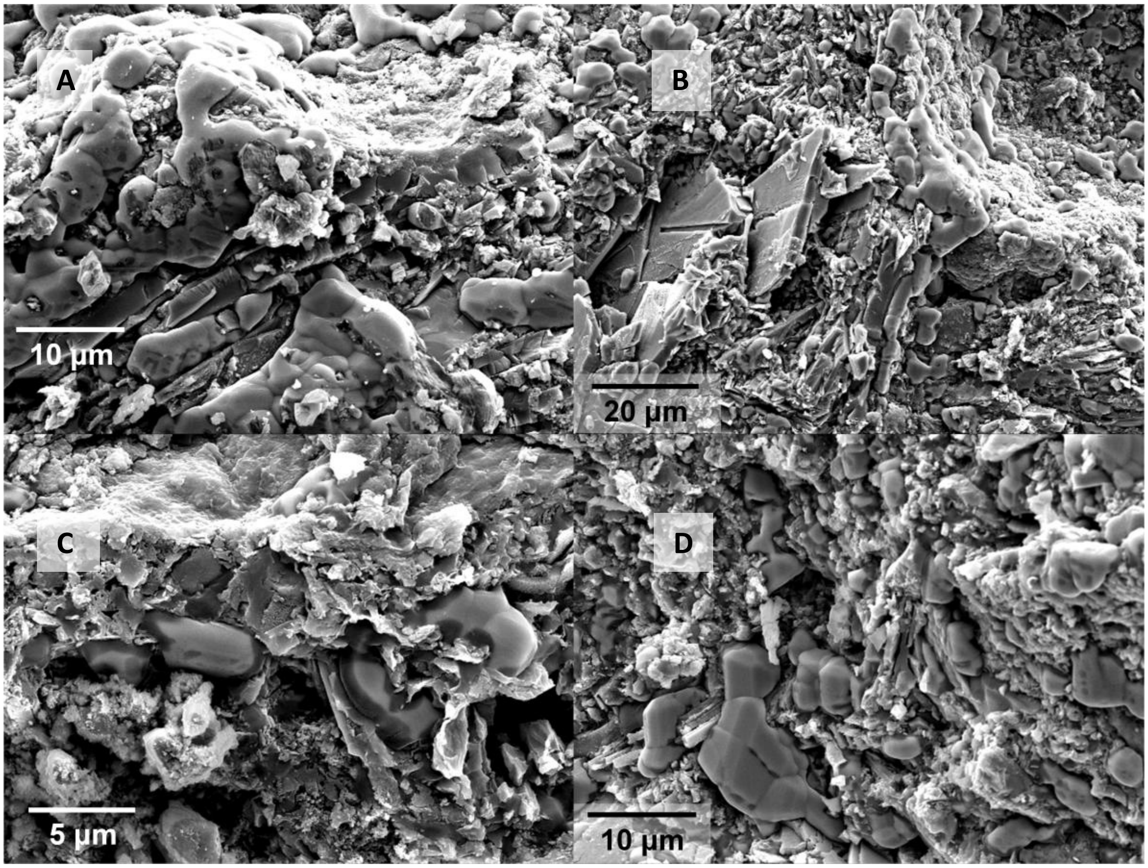

Figure 6-15 SEM of 30wt% Sulfur/Mars-1a. Micrographs of Sample 245 post-test fracture surface. This sample was a 30wt% sulfur-Mars-1a hybrid quasi-statically compressed to 270MPa inside a rigid lateral boundary.

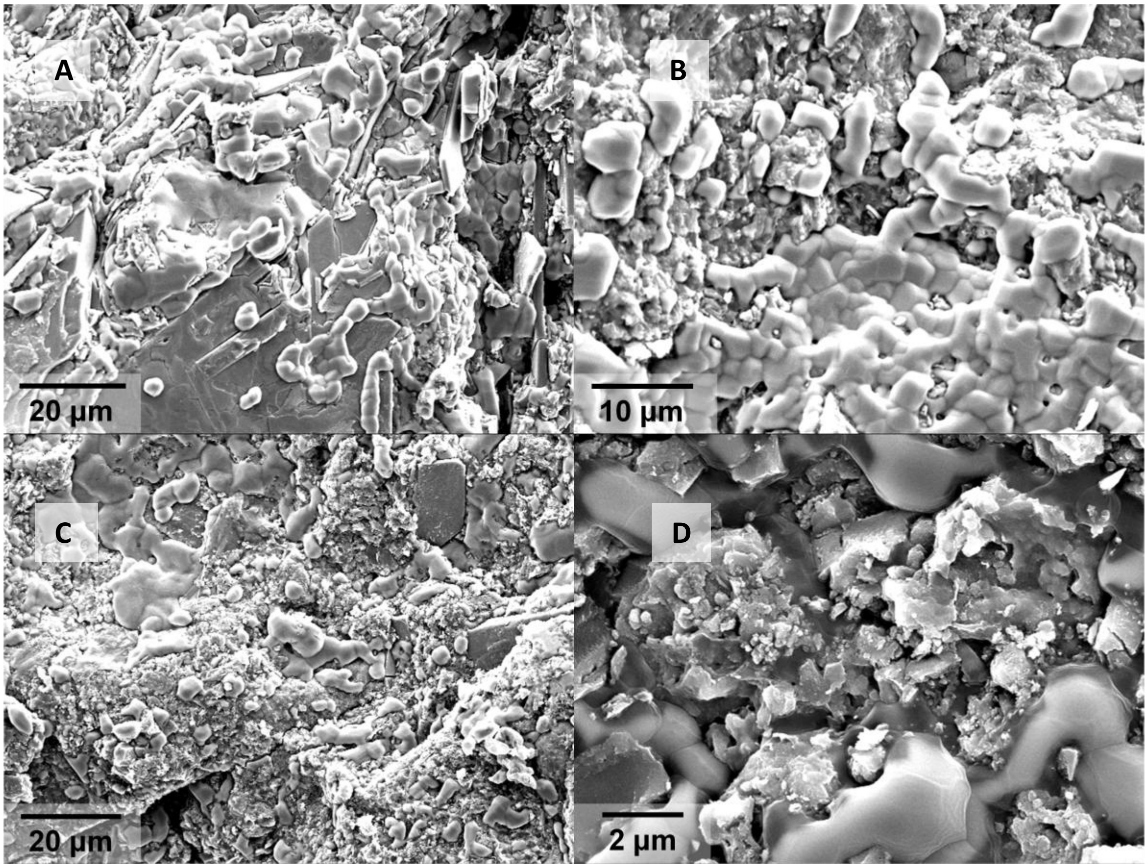

Figure 6-16 SEM of 40wt% Sulfur/Mars-1a. Micrographs of Sample 247 post-test fracture surface. This sample was a 40wt% sulfur-Mars-1a hybrid quasi-statically compressed to 270MPa inside a rigid lateral boundary.

When the binder content is low, the sulfur phase appears finely dispersed and nearly indistinguishable from the Mars-1a simulant. Due to its high melting viscosity and crystalline habit in the SEM, sulfur does not mix with the simulant particles and appears distinct from Mars-1a background. The convex shape of the sulfur (*e.g.*, Figure 6-16C), along with the contact angles suggesting phobia (*e.g.* Figure 6-13B) indicates that sulfur, too, is not wettable with basaltic substrates.

6.2.3 Fracture Surface of PVC and PMMA IOH

Characterization was performed on fracture surfaces of a 4wt% PVC IOH (Sample 313) and a 10wt% PMMA IOH (Sample 322). This sample was not serialized.

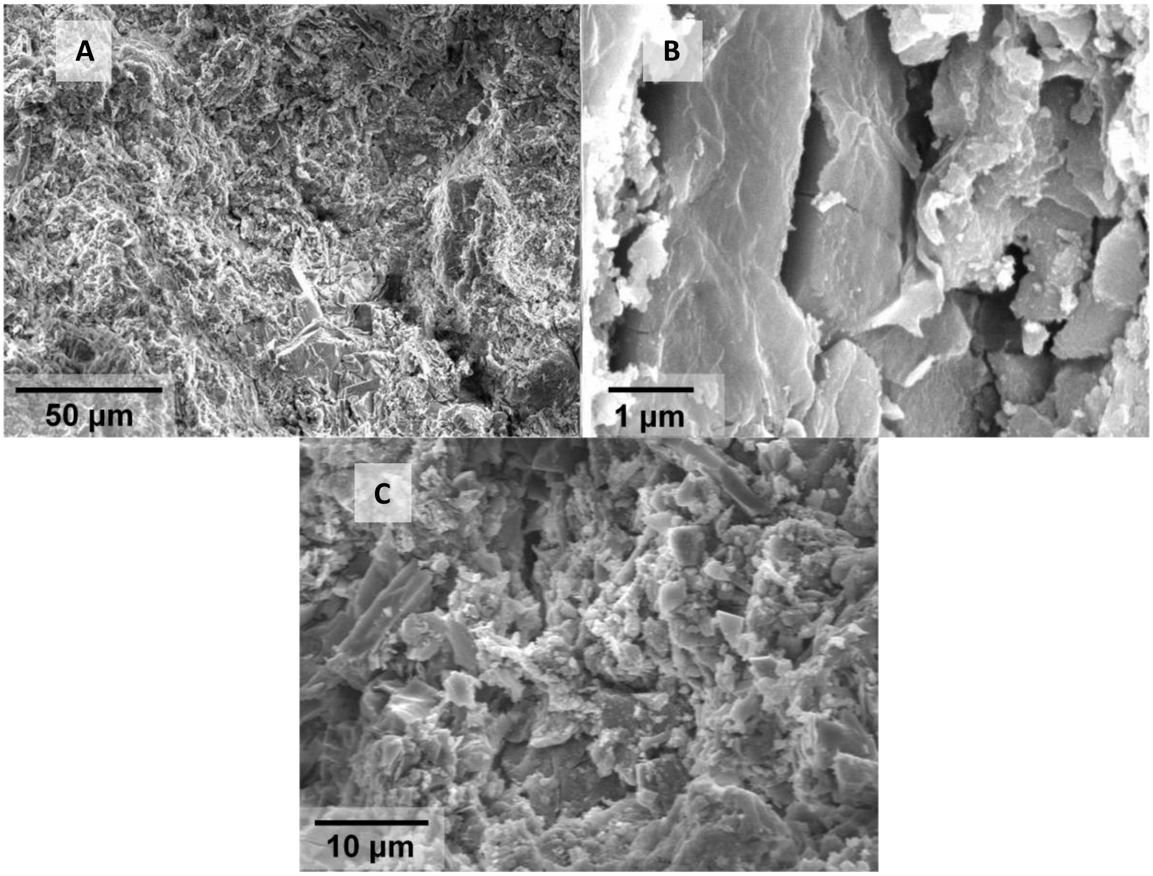

Figure 6-17 SEM of 4wt% PMMA/Mars-1a. Micrographs of Sample 313 post-test fracture surface. This was a 4wt% PVC-Mars-1a hybrid quasi-statically compressed to 270MPa inside a rigid lateral boundary.

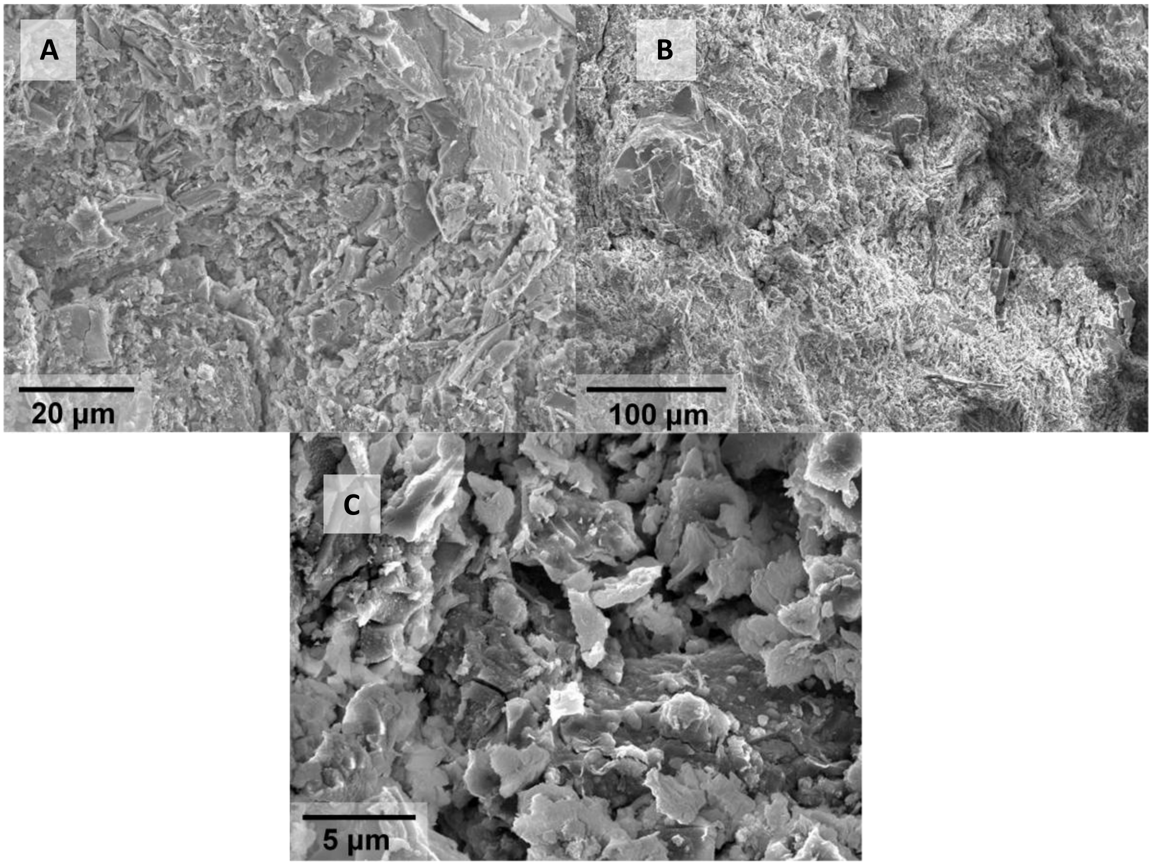

Figure 6-18 SEM of 10wt% PMMA/Mars-1a. Micrographs of Sample 322 post-test fracture surface. This sample was a 10wt% PMMA-Mars-1a hybrid quasi-statically compressed to 360MPa inside a rigid lateral boundary.

The fracture surface morphology from the SEM images appear typical for what is expected from Mars-1a, without outstanding features. The small amounts of polymer seen in Figure 6-17B show some resistance to pull-out, and the particle junctions intact. However, adjacent to the PVC, the face of the simulant particle is still bare. This observation negates a fundamental, microstructural improvement in the melt-processing configuration above other methods for introducing binder into the sample.

6.2.4 Elemental Analysis of Dried Montmorillonite Powder

Montmorillonite powder from the <20μm bin was dried at 350°C and characterized by SEM and elemental analysis. A control powder, which was not dried, was also examined.

The analysis helps to support the discussion in Chapter 5, in regards to the cleanliness of clay when dried to elevated temperatures. Relative to the variation between the dried and non-dried samples, the carbon content remains insignificant.

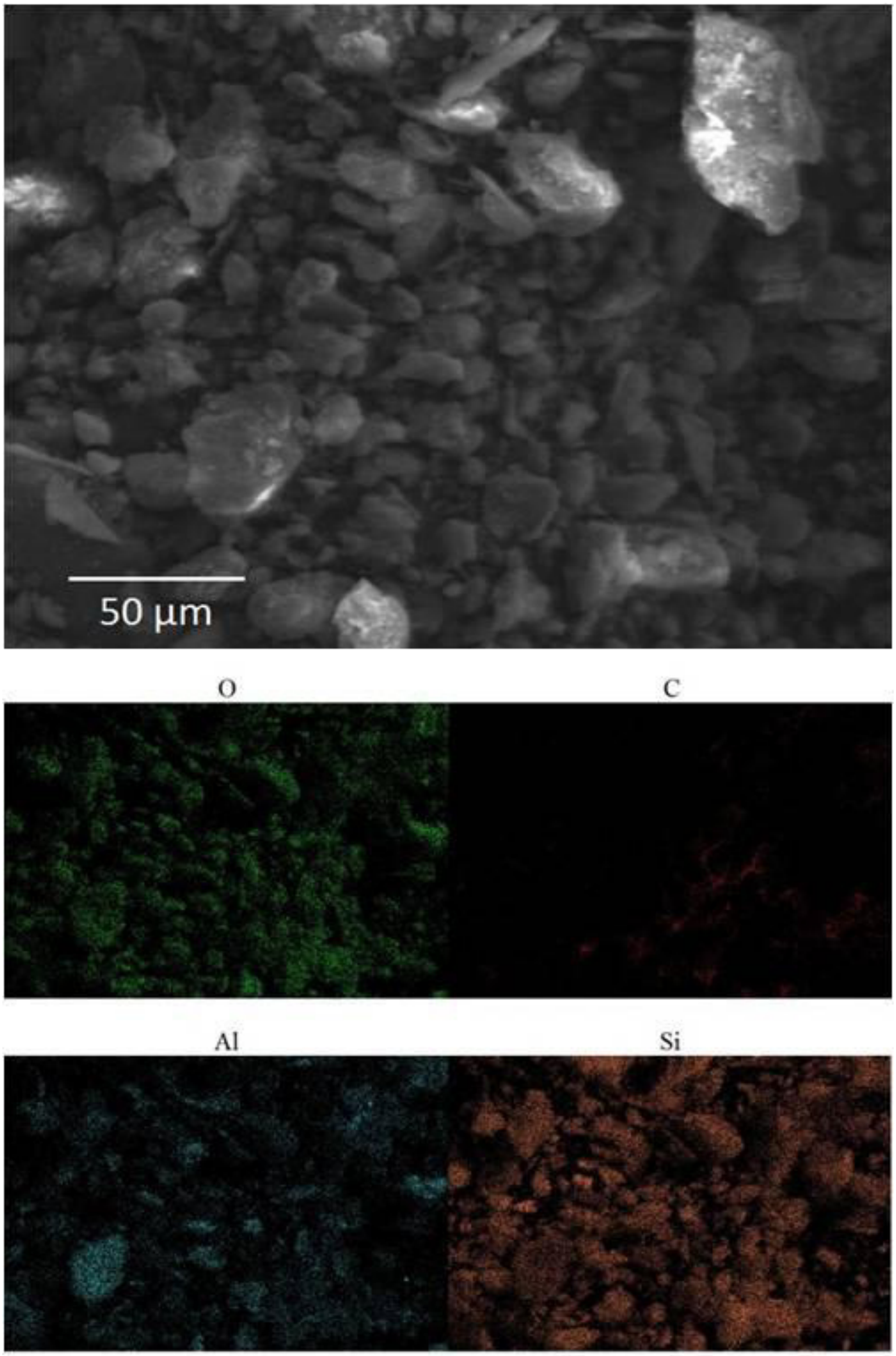

Figure 6-19 Elemental Maps of Dried Montmorillonite. SEM micrograph (top) and elemental maps (bottom) for <20µm montmorillonite particles dried to 350°C for 12h in open atmosphere. Three main rock-forming elements and carbon were examined.

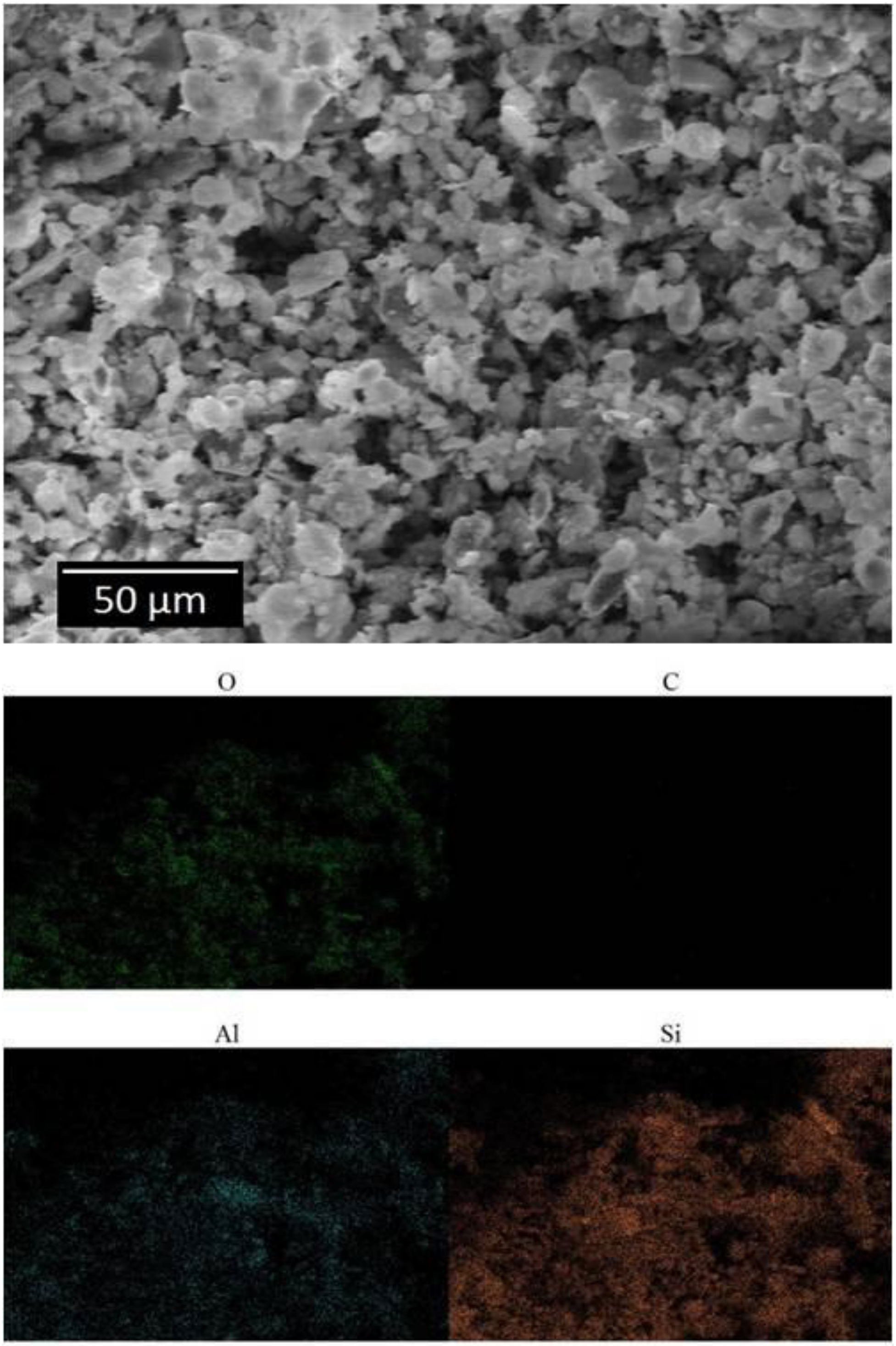

Figure 6-20 Elemental Maps of Non-Dried Montmorillonite. SEM micrograph (top) and elemental maps (bottom) for <20µm montmorillonite particles not subjected to drying. Three main rock-forming elements and carbon were examined.

Table 6-2 Carbon Content of Dried *vs.* Non-Dried Montmorillonite

Element	Concentration in 350°C-Dried Montmorillonite (wt%) [2-σ error]	Concentration in Non-Dried Montmorillonite (wt%) [2-σ error]
C	1.70 [0.08]	1.19 [0.09]
O	45.01 [0.12]	32.17 [0.13]
Si	34.90 [0.06]	42.36 [0.03]
Al	10.95 [0.03]	13.76 [0.04]

6.2.5 Mars-1a Compressed to Different Pressures

We consider Samples 424 and 467. Simulants were not sieved, but dried to 350°C for 12h prior to compressing at 360MPa and 720MPa, respectively, under quasi-static conditions. Samples were compressed with a rigid lateral boundary.

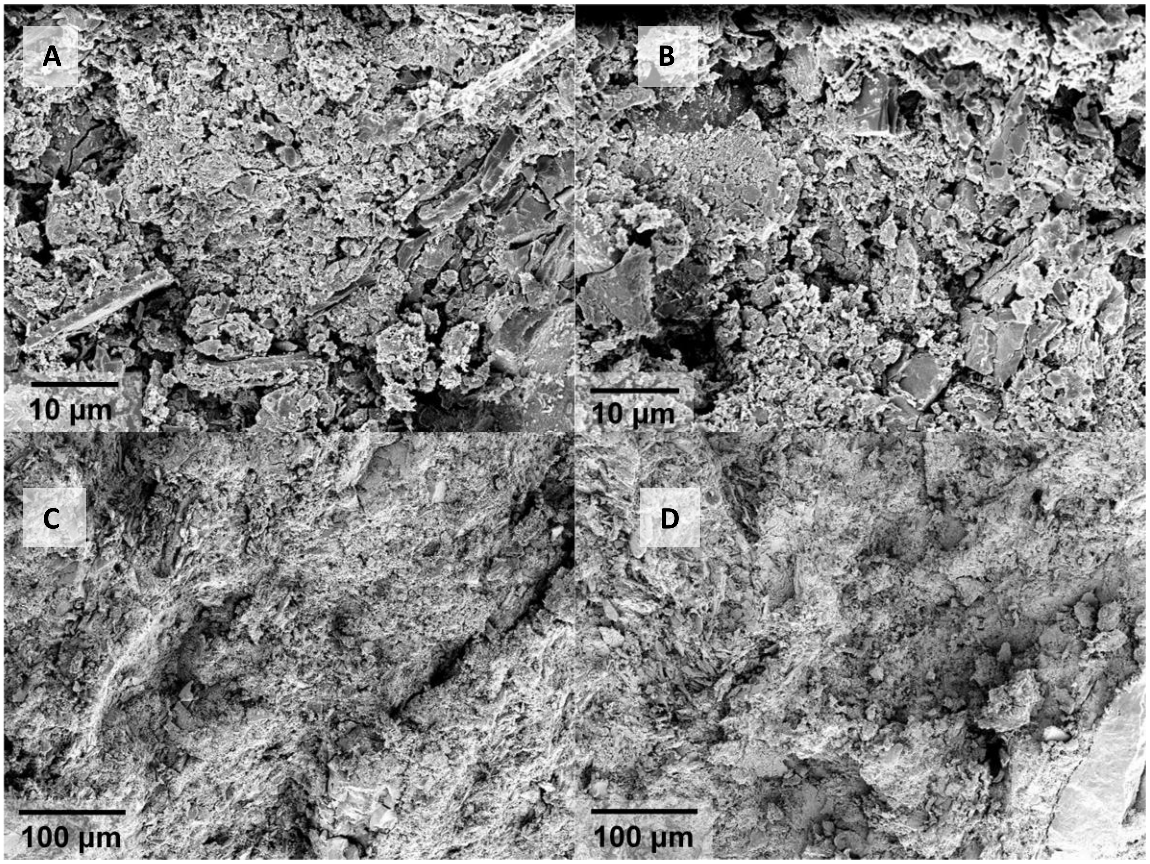

Figure 6-21 SEM of Mars-1a Compressed to 360MPa. Micrographs of Sample 424 post-test fracture surface. This sample was Mars-1a simulant quasi-statically compressed to 360 MPa inside a rigid lateral boundary.

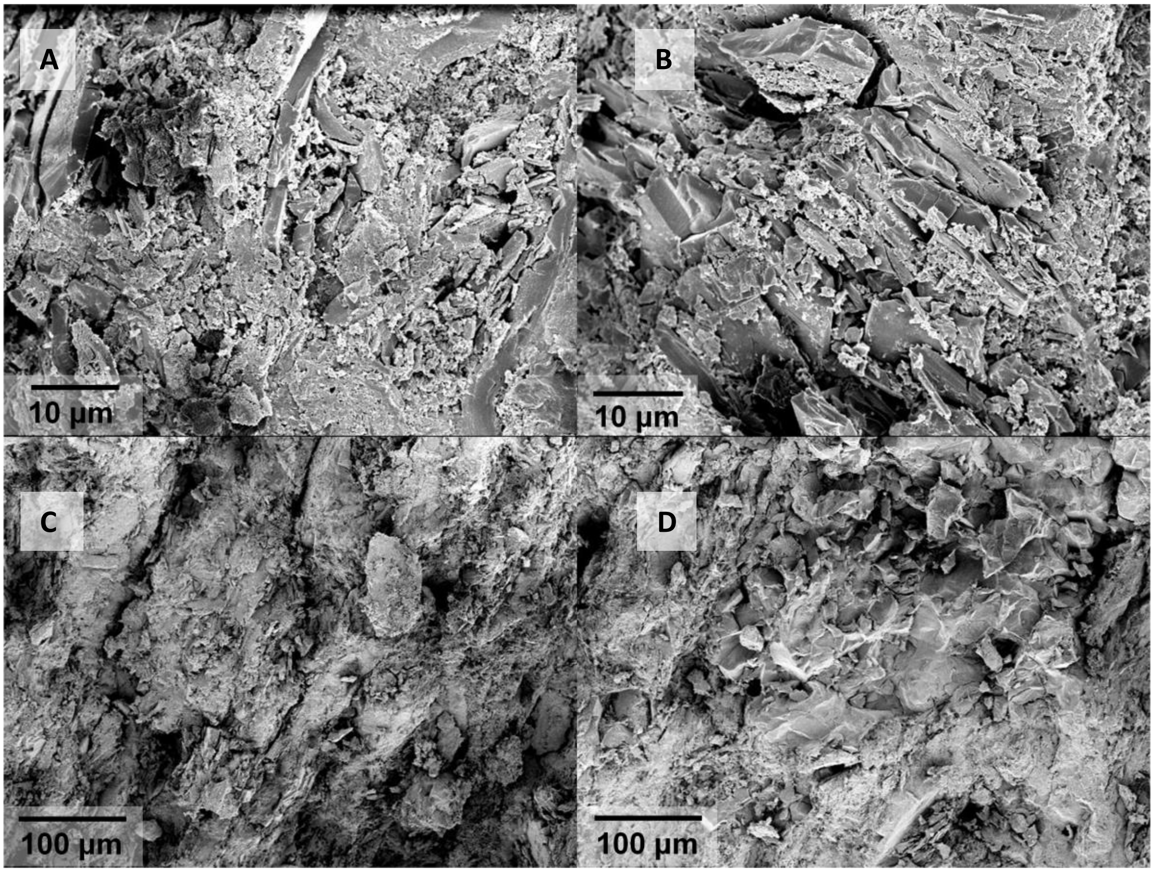

Figure 6-22 SEM of Mars-1a Compressed to 720MPa. Micrographs of Sample 467 post-test fracture surface. This sample was Mars-1a simulant quasi-statically compressed to 720 MPa inside a rigid lateral boundary.

We can verify the hypothesis that particle crushing continues under high pressures, rather than completely seizing from the friction against the rigid lateral boundary. The continuance of particle crushing at higher pressures signifies that further particle motions are possible to redistribute the npOx more optimally among finely divided particles. The analysis is conducted by manipulating the panels in Figures 6-21 and 6-22.

With the naked eye, one draws boundaries around the most discernible particles, regardless of size, until the count reaches about 120 particles. This effort is strictly on a first-attempt basis to ensure statistical objectivity.

Manual counting is preferred in light of difficulties encountered by image processing software. Additional justification is provided by the fact that, as of the time of this writing, human recognition still serves as an effective countermeasure against automated software for Internet security purposes. The National Institutes of Health image manipulation program Image J was used to draw and calculate the areas of particles. Working distances of ~4mm used for taking the SEM micrographs allow a near-parallel optical assumption.

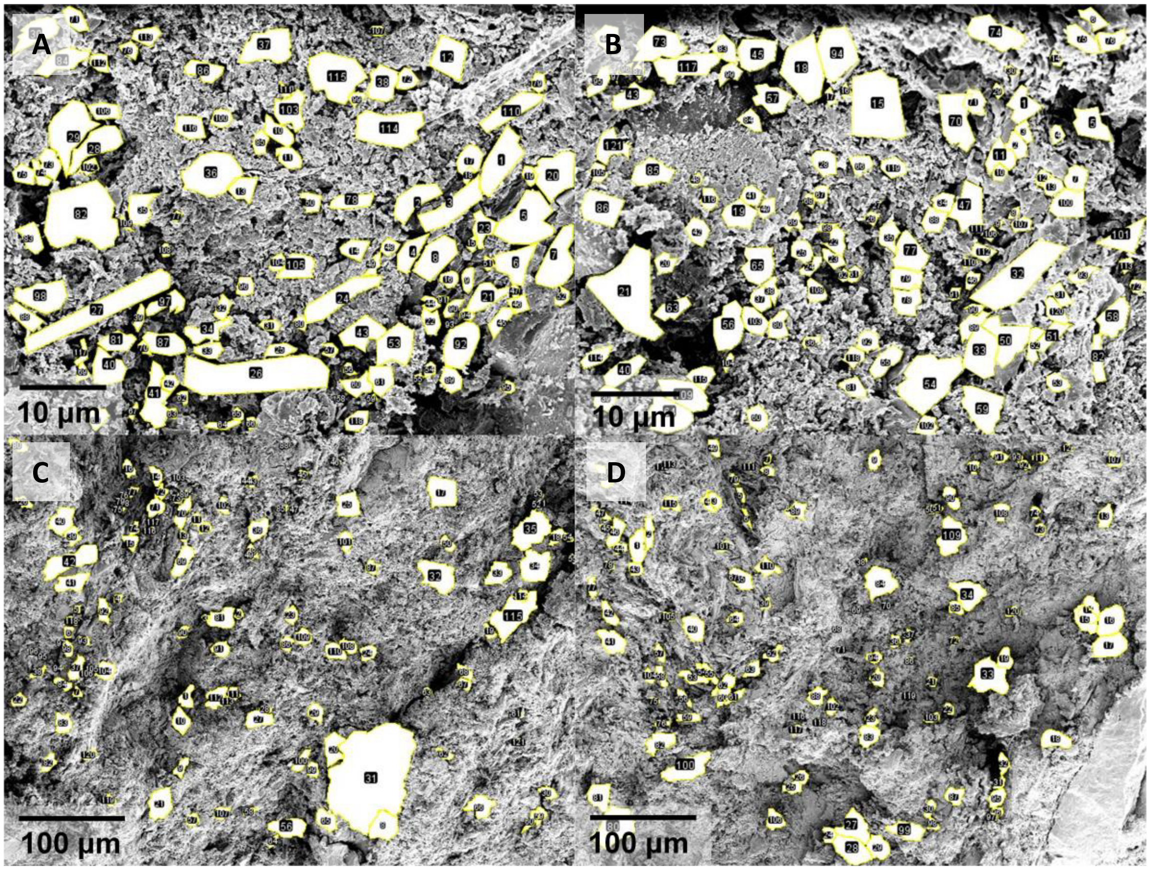

Figure 6-23 Particle Count of Mars-1a Compressed to 360MPa. Particles drawn from micrographs of Sample 424 (compressed to 360MPa) using Image J on a strictly first-attempt basis. Each panel counts ~120 particles (figure total ~480 particles).

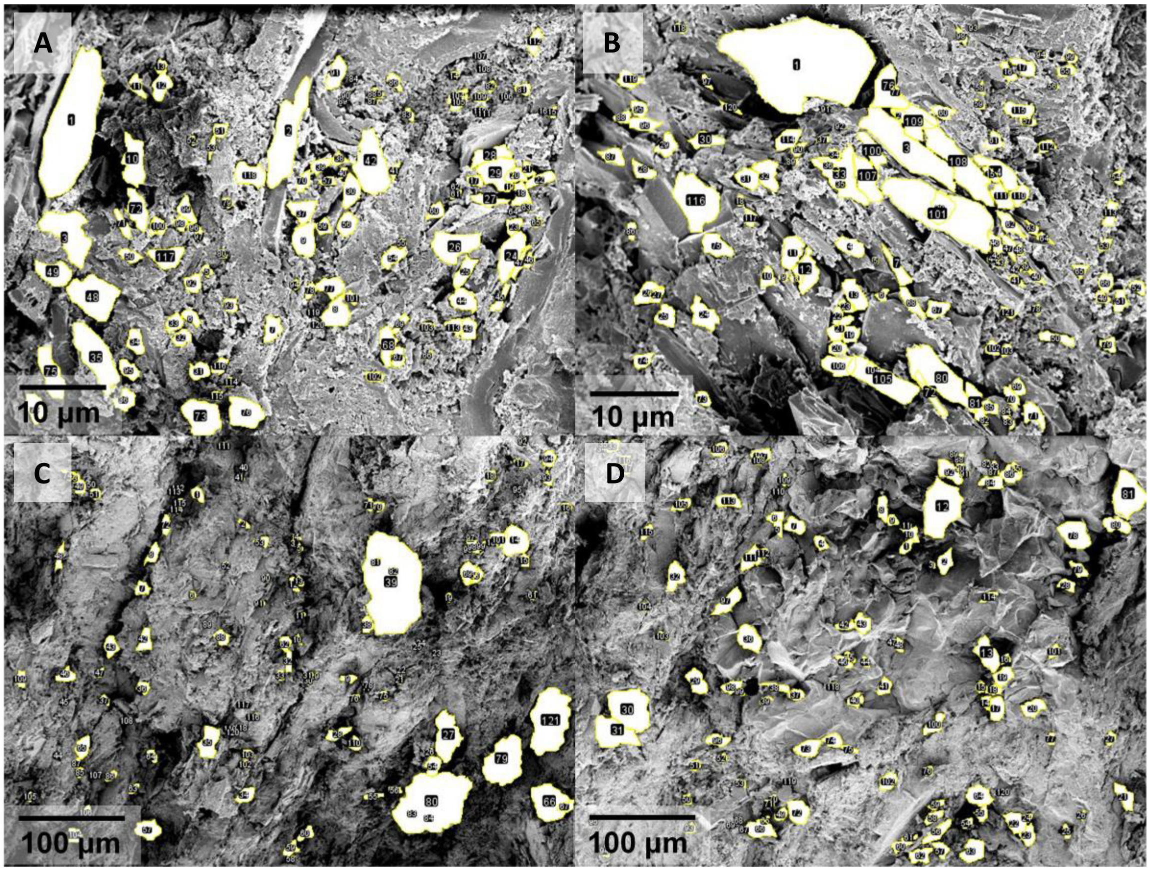

Figure 6-24 Particle Count of Mars-1a Compressed to 720MPa. Particles drawn from micrographs of Sample 467 (compressed to 720MPa) using Image J on a strictly first-attempt basis. Each panel counts about 120 particles (figure total ~480 particles).

From the drawn particles in Figure 6-23 and 6-24, distributions of the particle diameters are generated by taking the square roots of the areas calculated using Image J. A probability density function (PDF) describes the frequency of occurrence per range of particle size. Integrating the PDF gives the cumulative density function (CDF), which describes the weight fraction of all particles smaller than a particular size. Data plotting conforms to a 15-bin histogram evenly divided between the minimum and maximum sizes found.

The Weibull PDF and CDF describe the distribution of crushed particles in most practical cases [6] [7]. To curve-fit the distribution, one first linearizes the CDF equation (*e.g.*, [8]). Knowing that an ordinary least-squares estimator is not robust against some realistic variations and outliers [8], the parameters are extracted from the data instead *via* a modified Theil-Sen estimator. Whereas a normal Theil-Sen estimator takes the median of all slopes and *y*-intercepts from all pair-wise combinations of points in a scattergram [10], perform the following:

1. Assign each point in the linearized (Weibull) scatter plot a ‘weight’ with multiplicity an integer of the non-normalized PDF count ordinate.
2. Determine the slope and *y*-intercepts as the mean of all pair-wise non-unique combinations (they are non-unique because multiple points overlap at the same coordinate from Step 1).

Step 1 is necessary because the ordinary Theil-Sen estimator fails to capture the peak of the distribution accurately from brief inspection of the output. Step 2 is necessary because the multiplicity of points in Step 1 increases the susceptibility for the median to fall somewhere between steep jumps near the peak of the histogram. Both steps are necessary to ensure an accurate fit upon inspection, and can be regarded as a ‘backdoor’ equivalent for the ordinary Theil-Sen process in circumstances where a univariate PDF represents the frequency of occurrence. Plots generated with this method are shown in Figure 6-25.

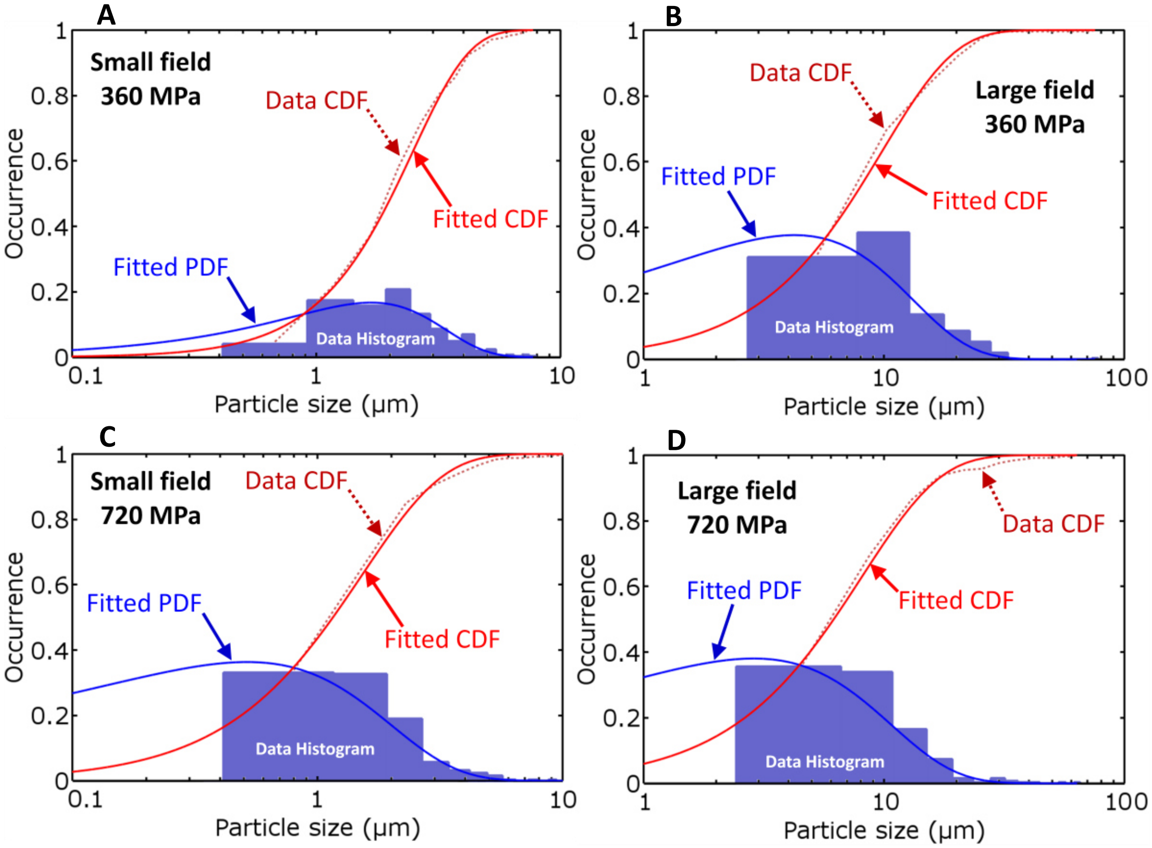

Figure 6-25 Weibull Fitting for Particle Counts. Distribution curves represent crushed particles in compressed Mars-1a. The distributions in panel A and B compress, yielding the distributions in C and D, respectively. Each panel refers to ~240 particles (figure total: ~960 particles) combining two panels of the same view scale in Figure 6-23 and 6-24.

Statistical tests of the linearized histogram data show very strong correlation $(R^2 > 0.984)$ and virtually certain statistical significance by Pearson's moment correlation coefficient $(p \approx 0)$. This strongly indicates that the distribution changes are statistically significant not only within themselves, but also in relation between one another.

The movement of the distribution PDF peak towards the left shows that further crushing indeed takes place under a rigid lateral boundary. Distributions tend to be much more sensitive towards in the tails of the distribution, when a univariate PDF representing a complex system shifts from external causes (*e.g.*, [11]). Thus the movement of the PDF peak towards smaller sizes is relatively well-pronounced in the smaller field of vision compared to the larger one. Physically speaking, the continued production of small particles is non-trivial at high pressures.

Friction does not completely arrest the compression process, and further strengthening can occur from different loading conditions, such as that with reduced lateral boundaries. The apparent plateau in some graphs displayed in Chapter 4 is therefore attributed to only a partial arrest from increased friction, but does not represent a complete nor theoretical plateau. For this particular application, SEM transcends the detection power of testing mechanical strength alone.

The peak movement can be qualitatively described by the equations in §4.6.1, but the quantitative aspect is expected to be subject to some error, as it is merely a single-crush approximation. The significance of verifying crushing at high pressures enables the development of high strengths through reduction of flaw sizes, assuming junctions between particles represent flaws and even distribution of npOx between particles.

6.2.6 Supporting Mars-1a Characterization

The following SEMs are supporting previous micrographs of the fracture surfaces of binder-free Mars-1a, for reference purposes. Sample 660 and Sample 764 were characterized.

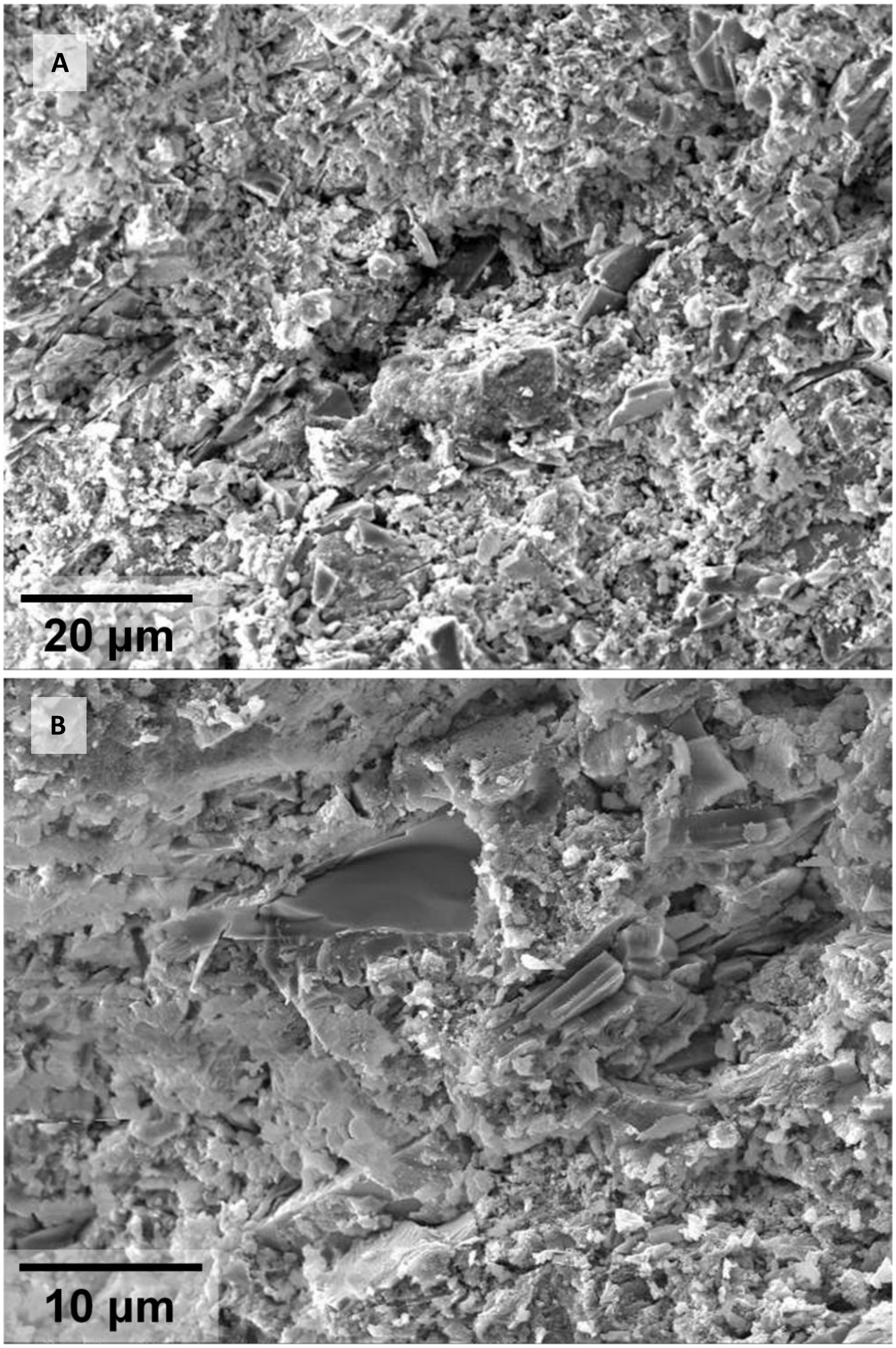

Figure 6-26 SEM of Compacted Mars-1a. Sample 660 fracture surface. Initial particle size was <20µm, particles were dried to 350°C, and compression pressure was 360MPa using the rigid lateral boundary condition.

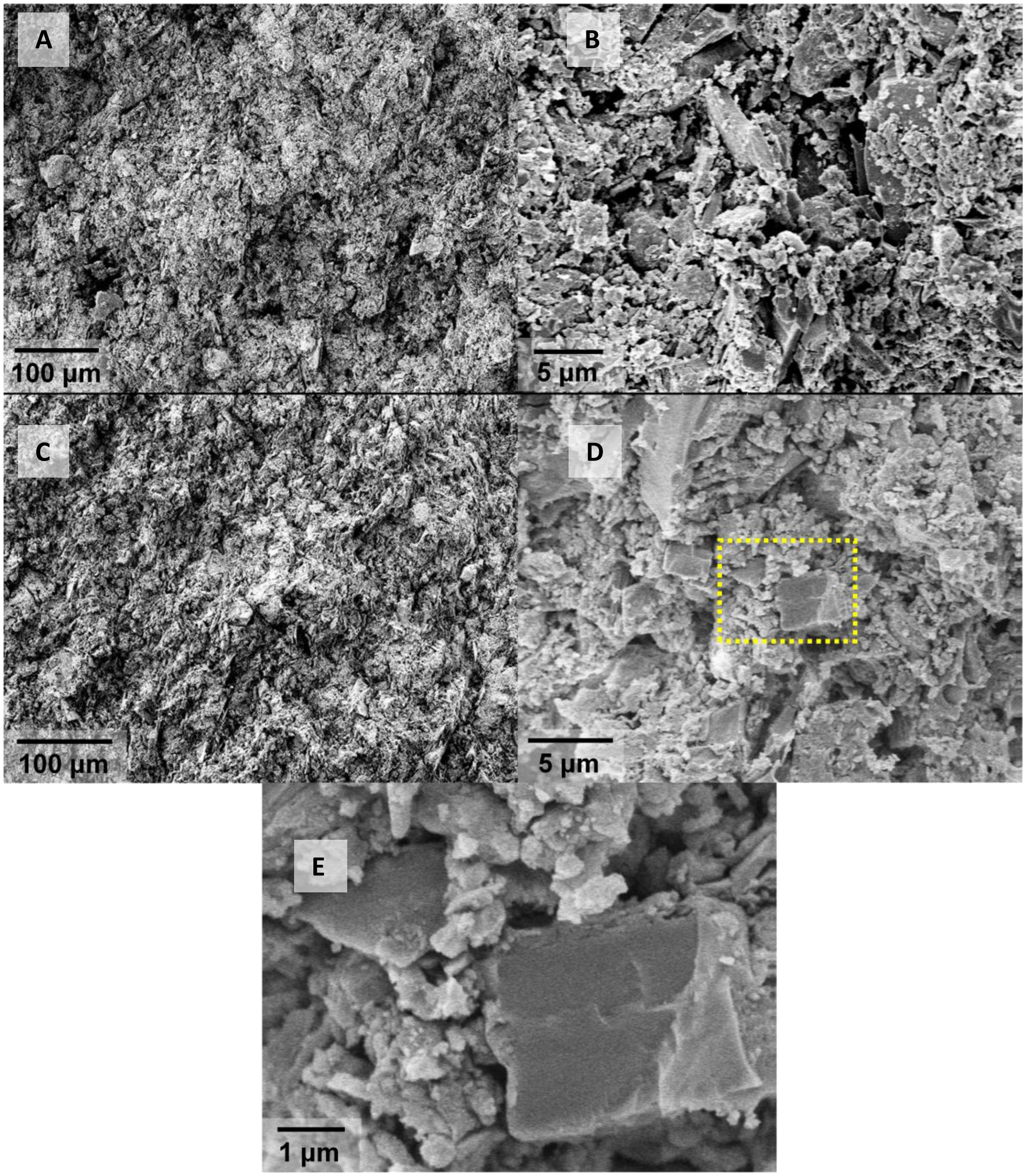

Figure 6-27 SEM of Compacted Mars-1a 2. Sample 764 fracture surface. Initial particle size was 25-45µm, particles were dried to 500°C, and compression pressure was 360MPa using the rigid lateral boundary. Bottom panel is an inset of the middle-right, shown by the dashed box.

A motif noticeable from previous characterizations notes the presence of plate-like or tabular basaltic particles in the crushed sample. The alignment of these particles is most often orthogonal to the direction of the applied uniaxial load. This is again observed in the large field-of-view panels of Figure 6-27.

6.2.7 Montmorillonite Compacted under Rigid Lateral Boundary

Like Mars-1a, montmorillonite was also compacted with a rigid lateral boundary. Sample 768 represents this configuration.

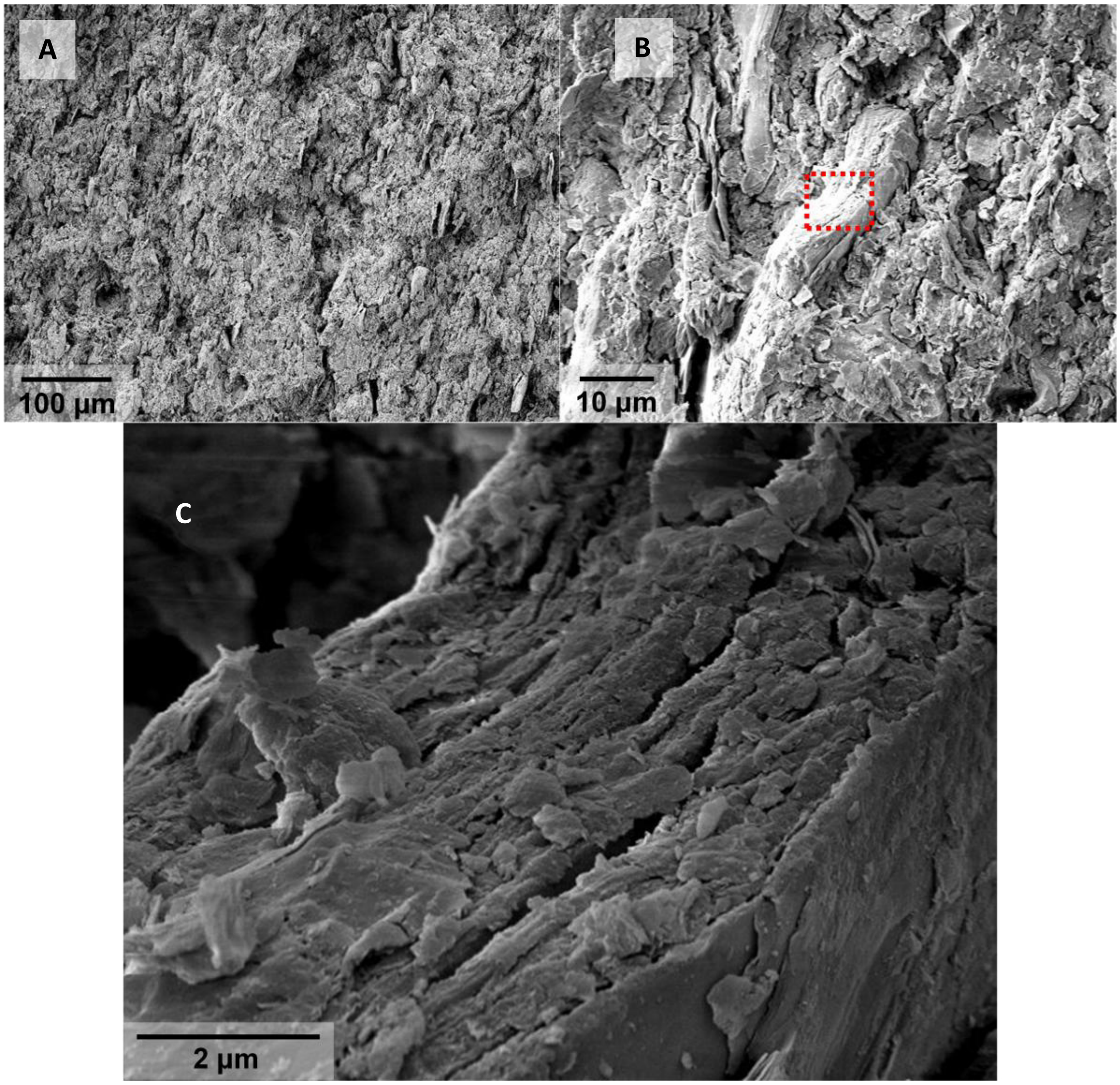

Figure 6-28 SEM of Compacted Montmorillonite. Micrographs show fracture surface of Sample 768. Initial particle size is 25-45µm, drying temperature was 500°C, and compression pressure was 360MPa using the rigid lateral boundary. Lower panel (C) is an ultrahigh resolution inset of dashed box (B).

As is well-known and expected, the clay particles align under uniaxial loading; the loading occurs perpendicular to the alignment of clay particles.

6.2.8 Mars-1a Compacted under Reduced Lateral Boundary Conditions

TEM was selected for the purposes of providing visual evidence of solid bridging between Mars-1a simulant particles. The TEM was performed on Sample 1095. Light grinding (~1N for 60s) in a mortar and pestle ensured the particle size was small enough to be compatible with TEM while preserving bonded aggregate linkages.

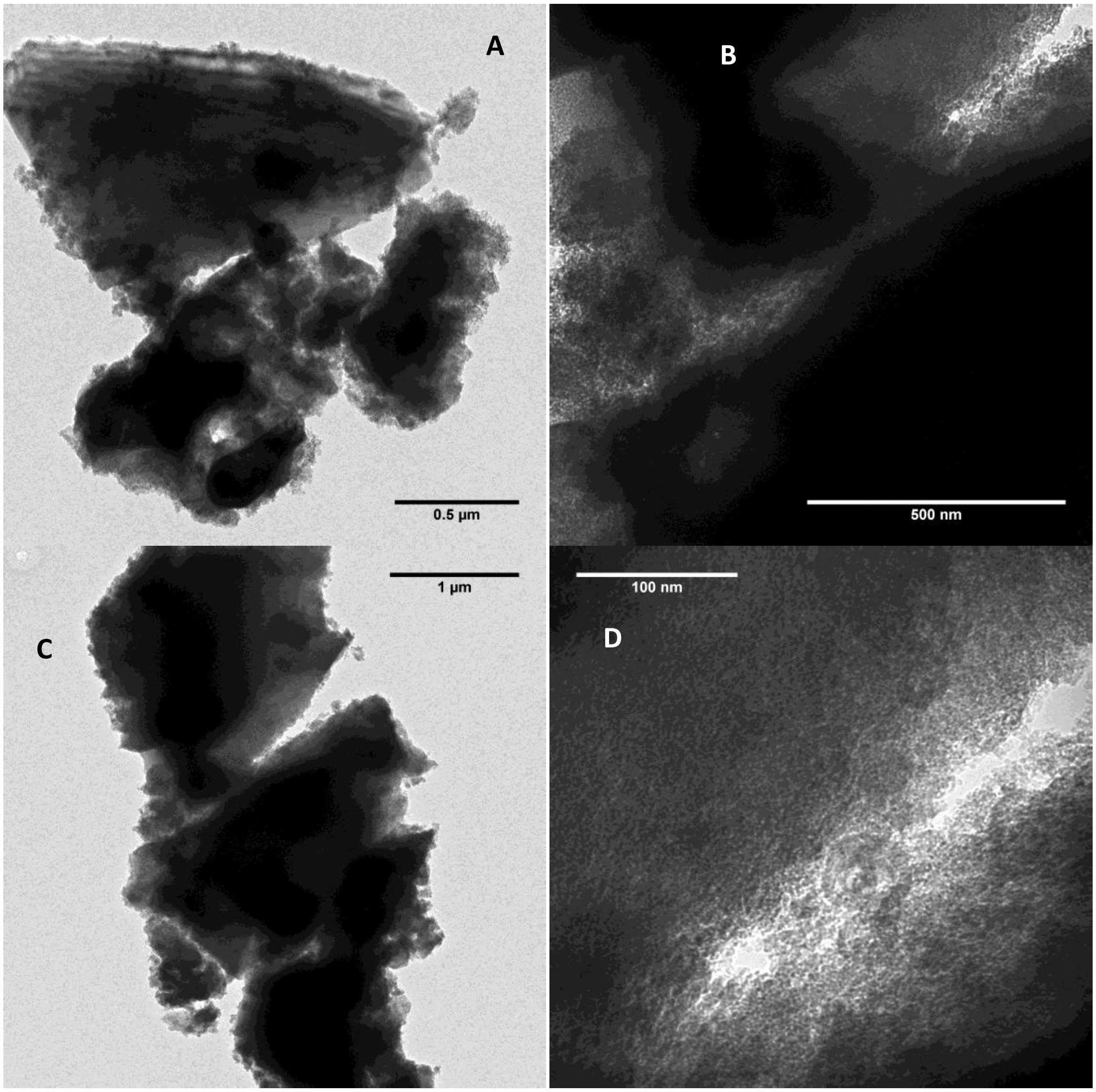

Figure 6-29 TEM of Compacted Mars-1a. Particles are from Sample 1095. Compression pressure was 25-45µm, particles were dried at 350°C, and compression pressure was 720MPa with the rigid lateral boundary.

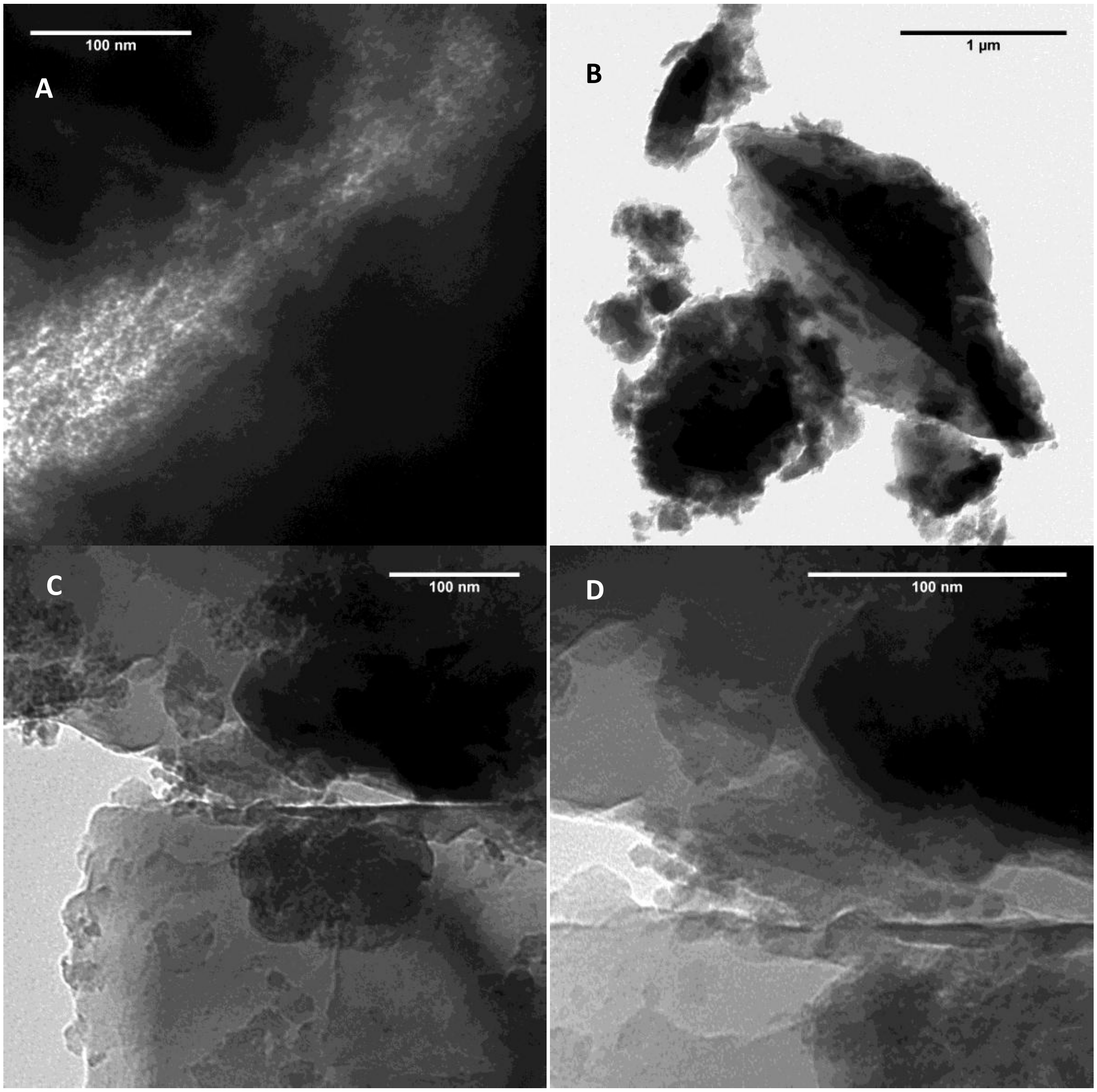

Figure 6-30 TEM of Compacted Mars-1a 2. Particles are from Sample 1095. Compression pressure was 25-45µm, particles were dried at 350°C, and compression pressure was 720MPa with the rigid lateral boundary.

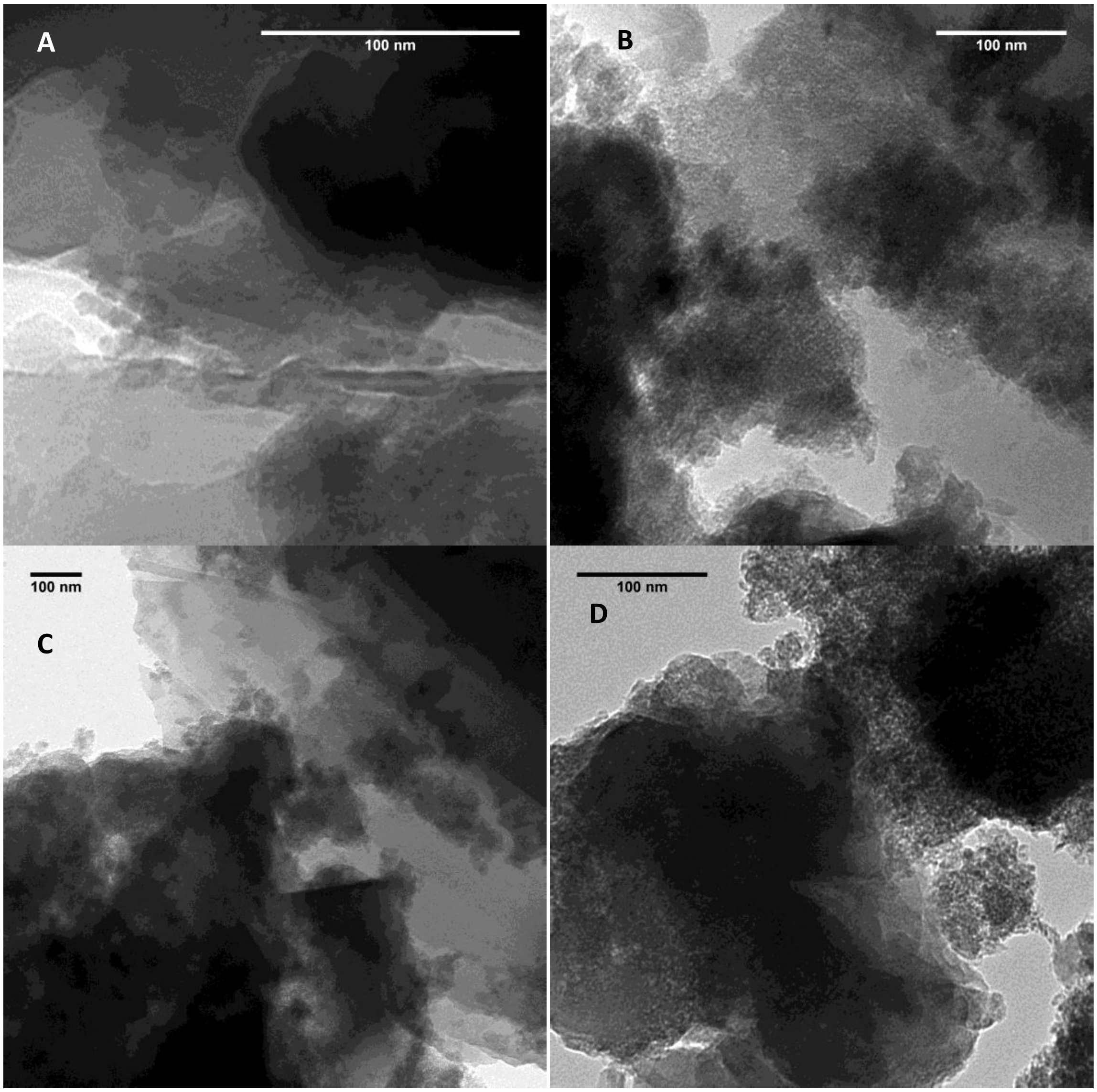

Figure 6-31 TEM of Compacted Mars-1a 3. Particles are from Sample 1095. Compression pressure was 25-45µm, particles were dried at 350°C, and compression pressure was 720MPa with the rigid lateral boundary.

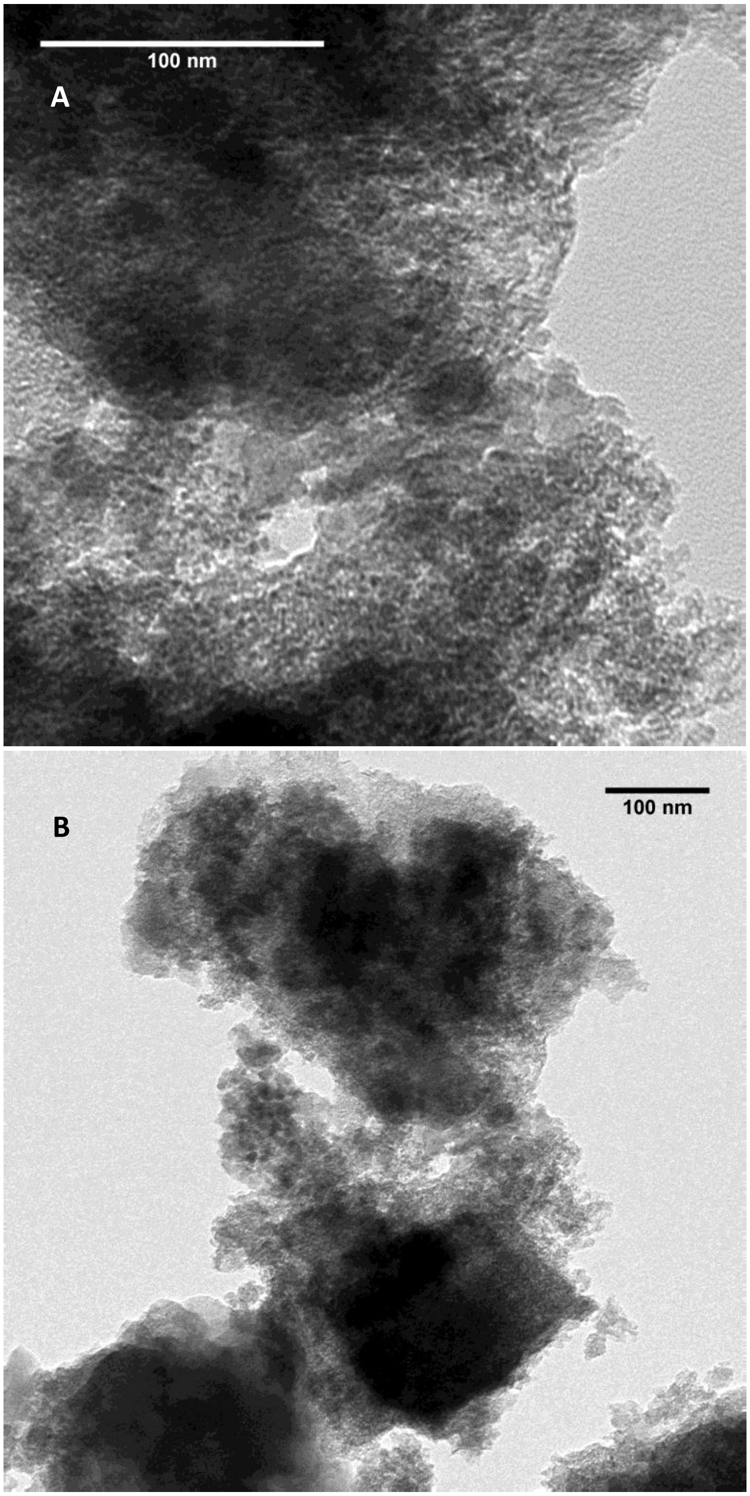

Figure 6-32 TEM of Compacted Mars-1a 4. Particles are from Sample 1095. Compression pressure was 25-45μm, particles were dried at 350°C, and compression pressure was 720MPa with the rigid lateral boundary.

In the smaller fields-of-view in Figure 6-29 through 6-32, the npOx is translucent and surrounds the darker basaltic phase in Mars-1a. Solid bridging appears as the translucent npOx bridging the dark regions together, giving credence to npOx as mechanical cement binding Mars-1a together under pressure.

6.2.9 Montmorillonite Compacted under Reduced Lateral Boundary

6.2.9.1 Rehydrated Montmorillonite

SEM characterization supports the discussion in §5.5. To review, montmorillonite was rehydrated to different water contents and compressed to 800MPa with the free lateral boundary condition. In descending order of added water content, they are Sample 1652, 1706, 1733, and 1648.

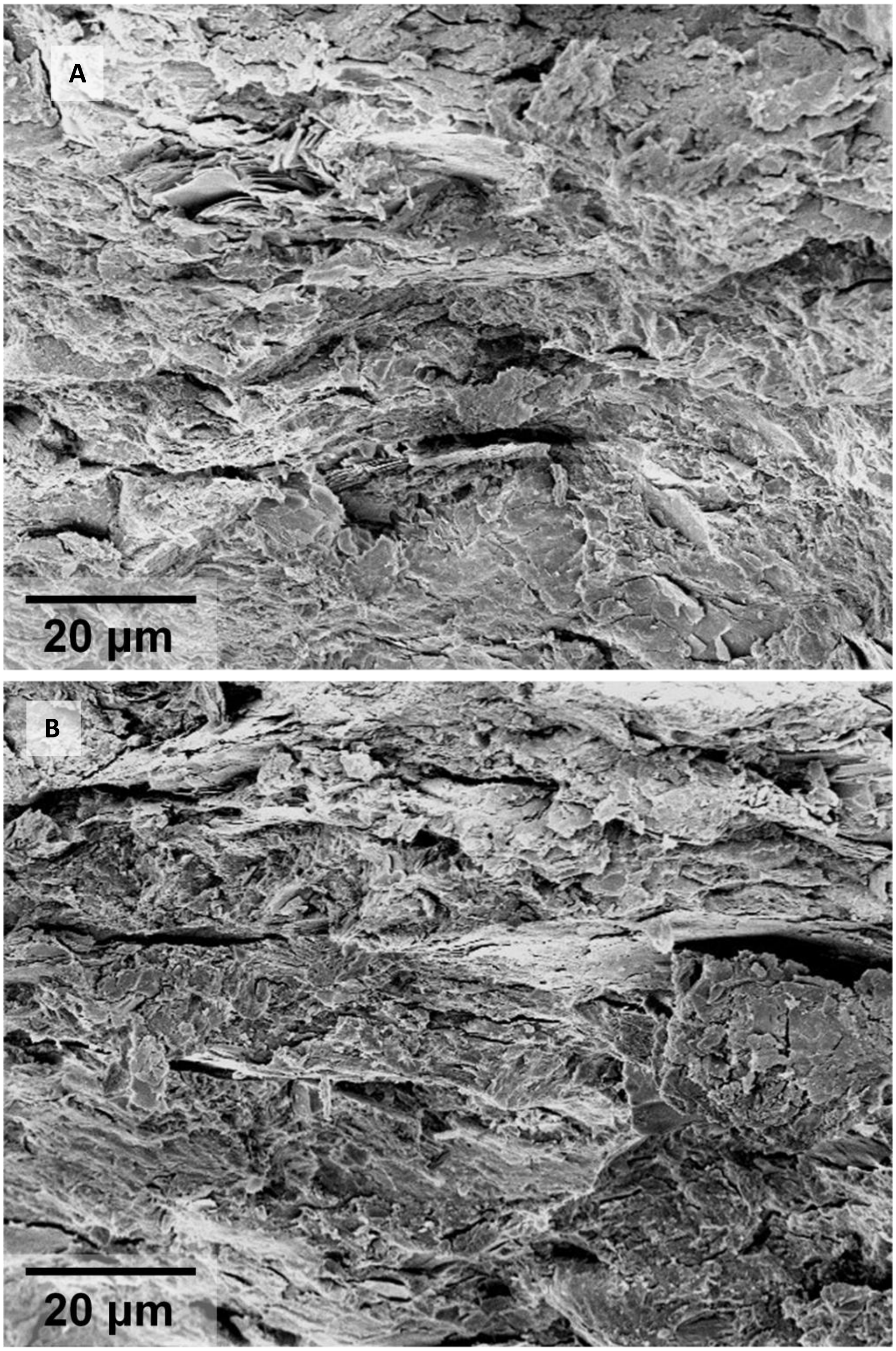

Figure 6-33 SEM of Montmorillonite Compacted with 22wt% Added Water. Micrographs show fracture surface of Sample 1652. This sample was rehydrated to ~22wt% water. Initial size bin was 25-45µm, and compression pressure was 800MPa with the free lateral boundary condition.

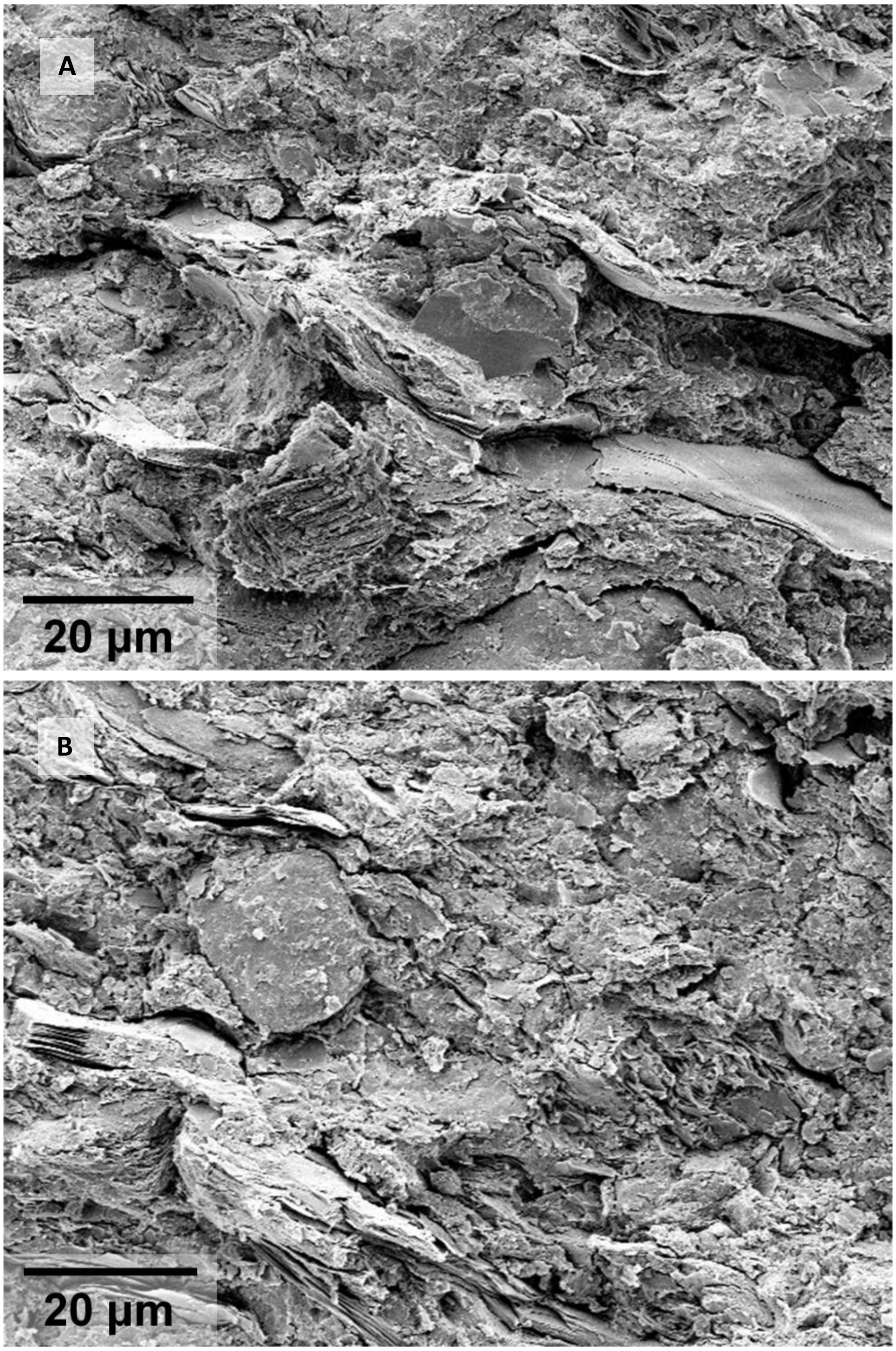

Figure 6-34 SEM of Montmorillonite Compacted with 10wt% Added Water. Micrographs show fracture surface of Sample 1706. This sample was rehydrated to ~10wt% water. Initial size bin was 25-45µm, and compression pressure was 800MPa with the free lateral boundary condition.

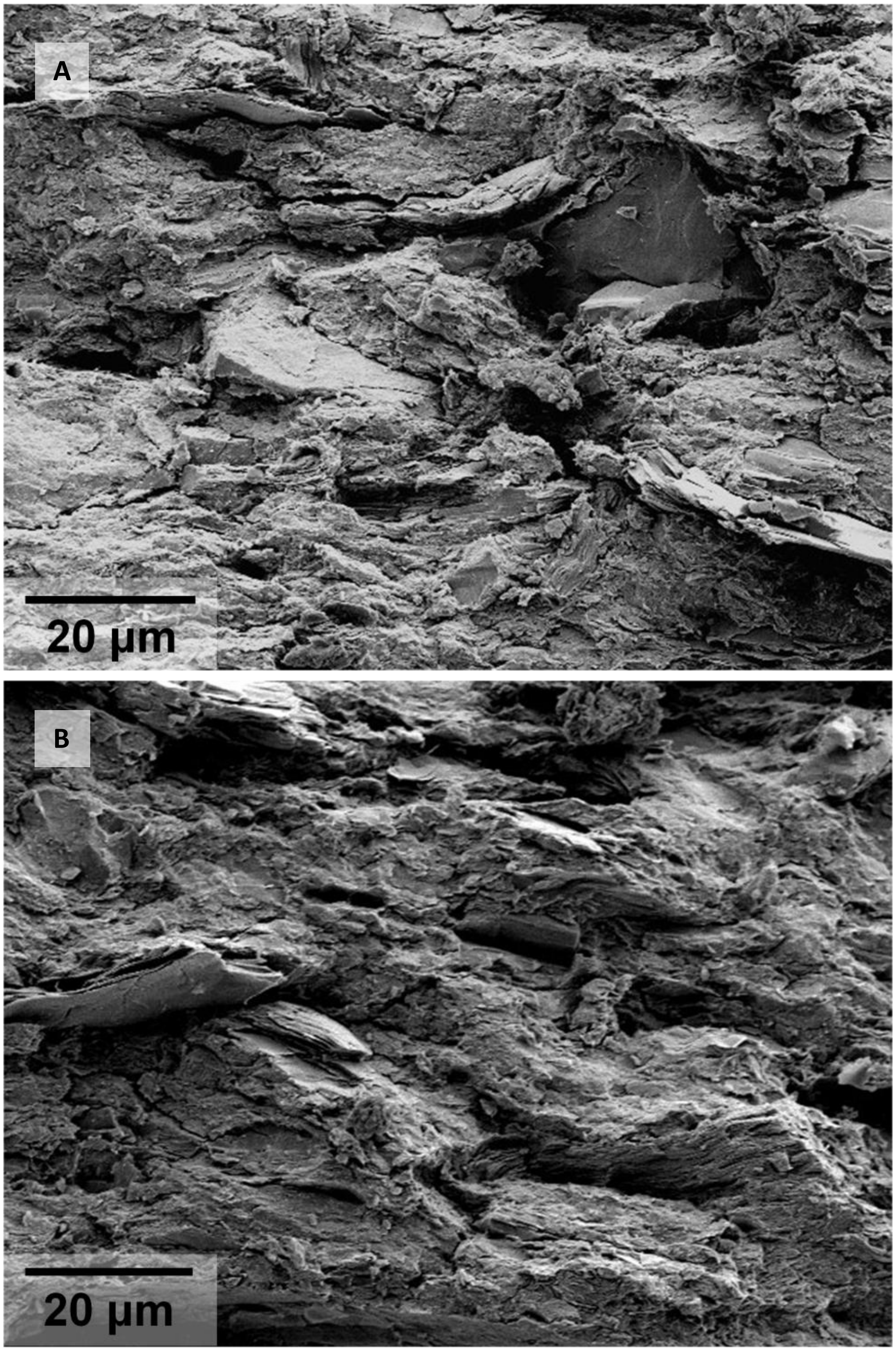

Figure 6-35 SEM of Montmorillonite Compacted with 2wt% Added Water. Micrographs show fracture surface of Sample 1733. This sample was rehydrated to ~2wt% water. Initial size bin was 25-45µm, and compression pressure was 800MPa with the free lateral boundary condition.

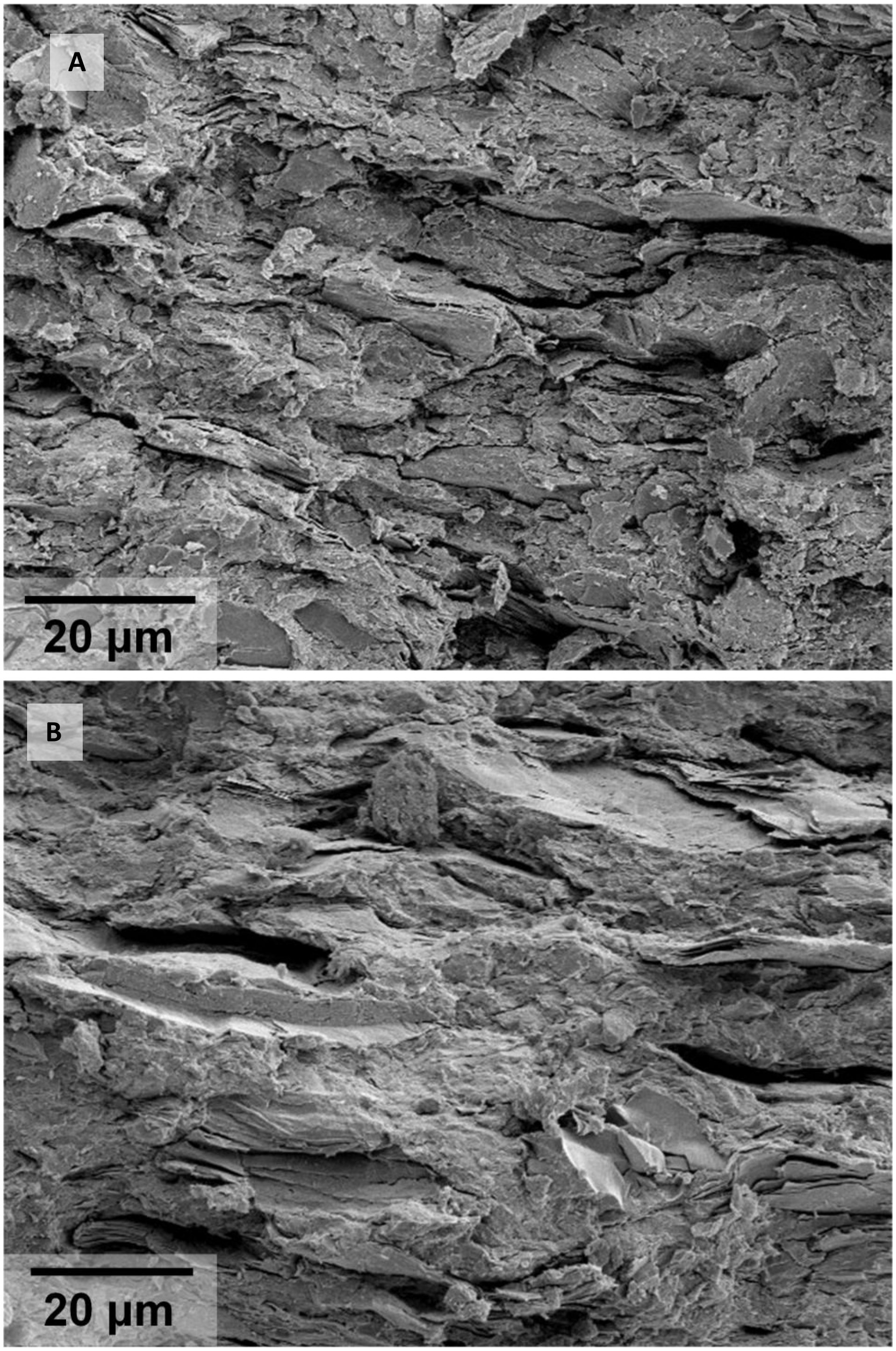

Figure 6-36 SEM of Montmorillonite Compacted with No Added Water. Micrographs show fracture surface of Sample 1648. This sample was not rehydrated. Initial size bin was 25-45μm, and compression pressure was 800MPa with the free lateral boundary condition.

In the SEM micrographs, the alignment generally occurs in the clay mineral layers orthogonal to the direction of applied load. The proposed discussion in §5.5 remains open about the possibility that void spaces vary with double layer water interfering with the compression process. Rather, the SEM points to a different phenomenon. Under higher added water contents, one notices that the morphology of the fracture surface is more planar. This is likely attributed to decreasing in-plane strength of clay mineral layers in the montmorillonite with increased hydration. Such attribution implicitly assumes that the effective stress is virtually the same as applied stress, which is likely because the stress is ultrahigh and the sample extremely thin, such that the water consolidates out immediately. The reason is not clear why in-plane strength of clay mineral layers might decrease with increased hydration. It may be related to the phenomenon of environmentally-assisted cracking, or the reactive mechanical stress due to the ice-like adsorbed water adjacent to the clay mineral layer that renders the latter in a state of tension [9].

6.2.9.2 Montmorillonite Compacted under Flexible Lateral Boundary

SEM characterization helps to support the discussion regarding strength increase in §5.4.1. To review, the montmorillonite powder compacts under 360MPa with much higher strength under a flexible lateral boundary condition, than with the rigid lateral boundary.

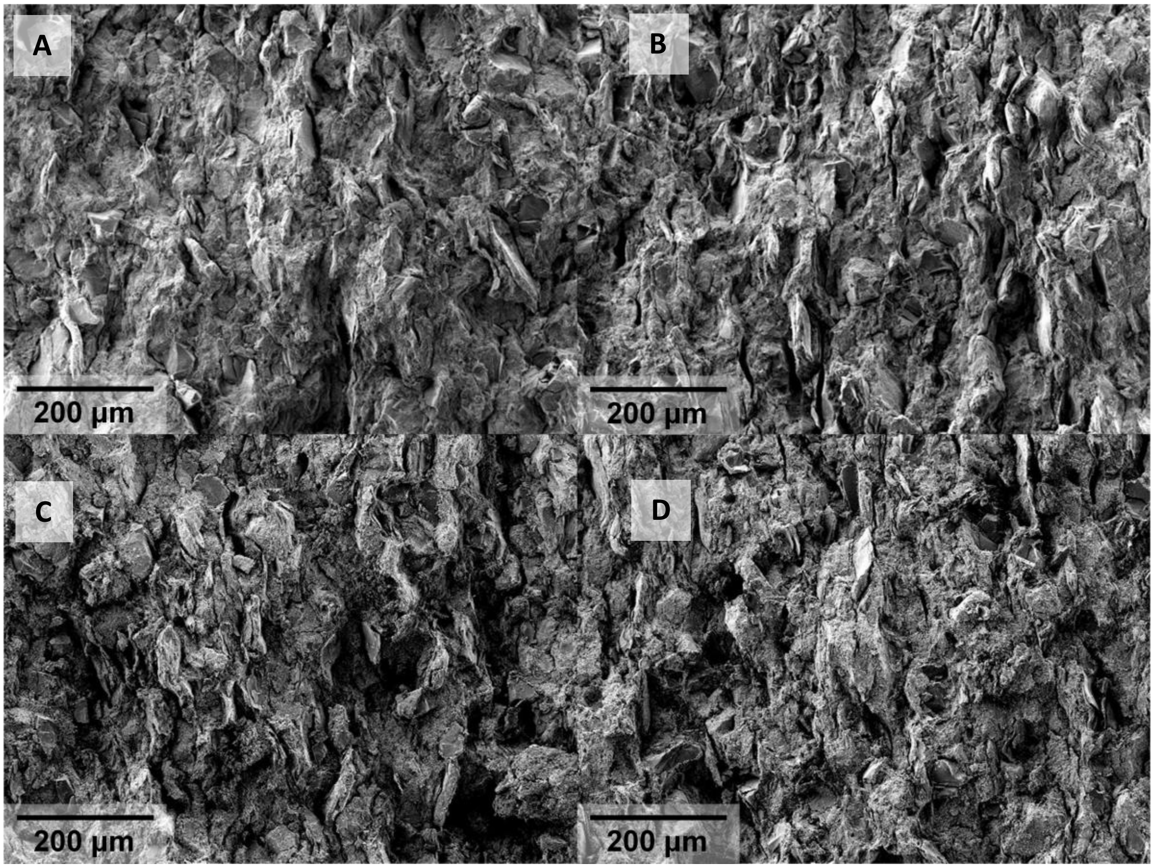

Figure 6-37 SEM of Montmorillonite Compacted with Flexible Lateral Boundary. Micrographs show fracture surface of Sample 1859. Initial size bin was 53-90µm, and compression pressure was 360MPa with the flexible lateral boundary condition.

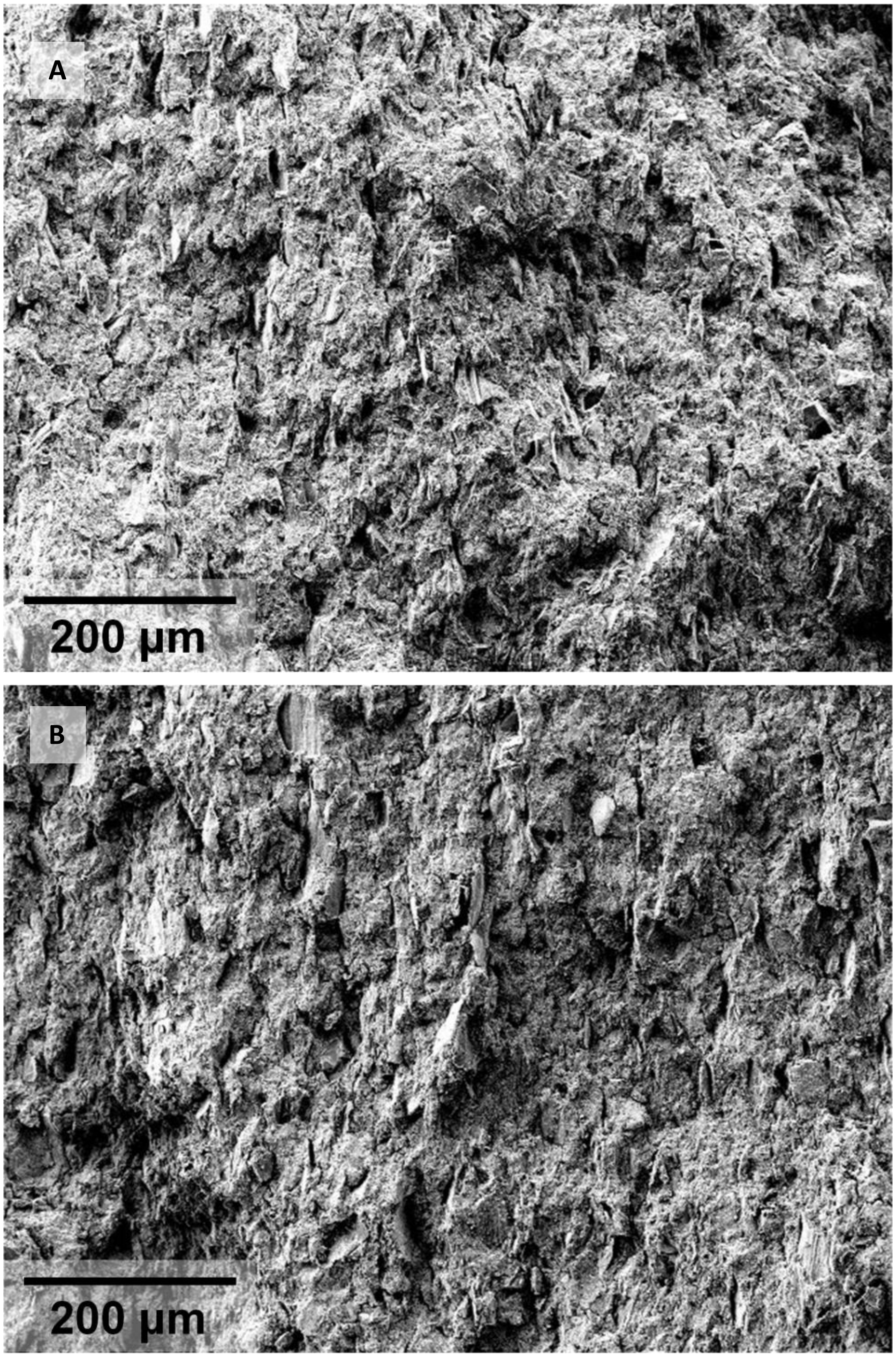

Figure 6-38 SEM of Montmorillonite Compacted with Flexible Lateral Boundary 2. Micrographs show fracture surface of Sample 1893. Initial size bin was 25-45µm, and compression pressure was 360MPa with the flexible lateral boundary condition.

The clay lamellae align in all SEM micrographs. The parallel arrangement of the clay mineral layers helps to produce a more optimal arrangement than otherwise. Alignment is expected in most stress histories even with a rigid boundary condition, as evidenced by practice in the field where the boundary of soil outside the blow of a Proctor hammer is relatively confined. However, the difference with a uniaxial compression occurring under reduced lateral boundary is that lateral motion exists to especially enhance the sliding and shearing of the particles into a stronger, denser final state. Particle motions and deformations occur in the bulk sample because the deviatoric stress increases in uniaxial loading with the lateral boundary removed. Note that although the pistons confined samples by friction, their polished surfaces enabled resulting compacts to exhibit sufficient mechanical differences.

6.2.10 Mars-1a under Impact Compaction

The SEM micrographs here support the discussions in §4.4, where strength increases were generally observed. Sample 1973 represents a specimen formed under impact, with a flexible lateral boundary.

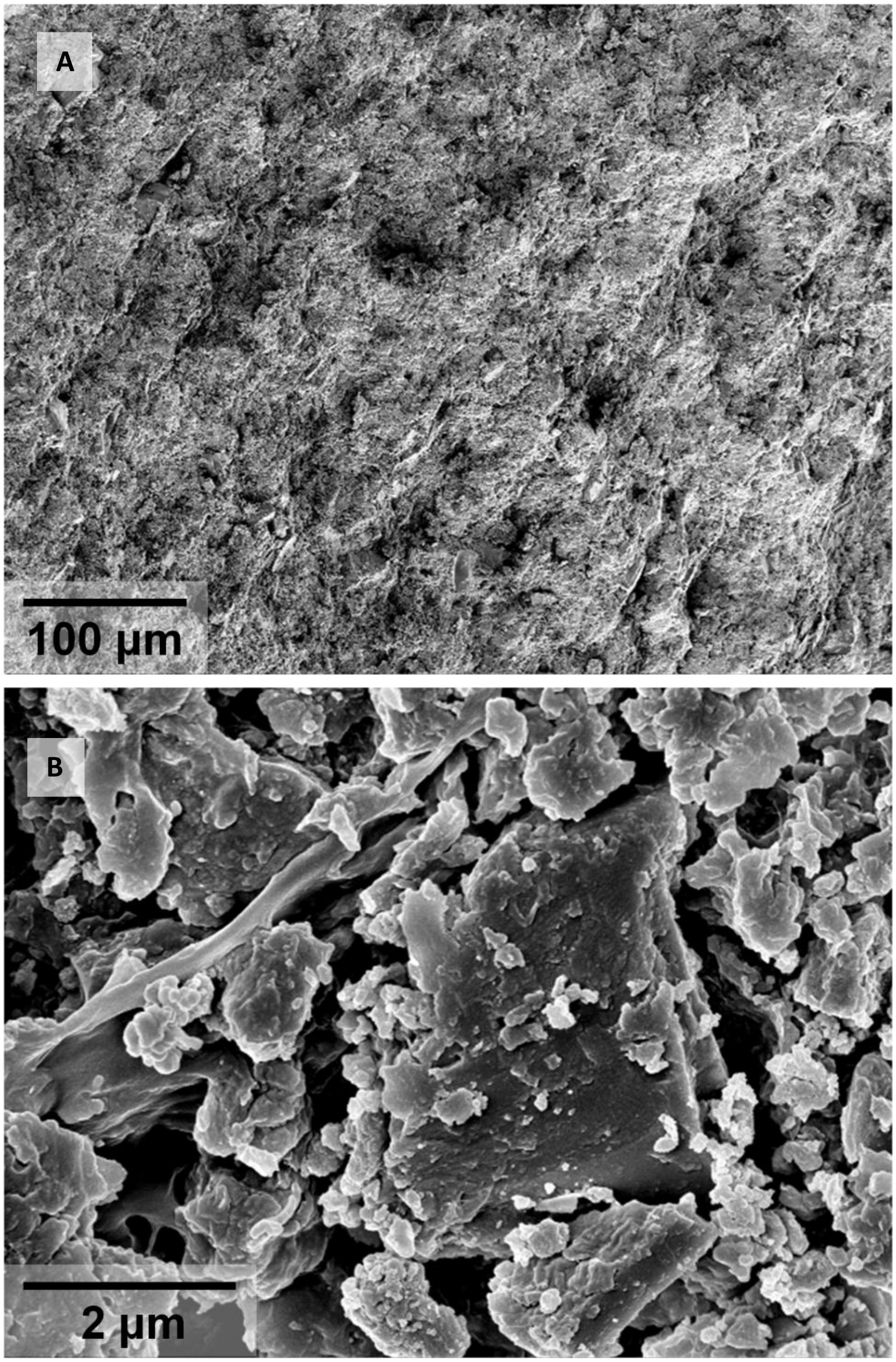

Figure 6-39 SEM of Impact-Formed Mars-1a. Fracture surface of Sample 1973. This was Mars-1a of initial size bin 25-45µm and dried at 600°C prior to compaction. Impact was 140J with the flexible lateral boundary.

Here the lighter npOx particles more fully populate the surfaces the of the basalt particles, suggesting that impact enables more motion of small particles to break free and redistribute among the fracture surfaces of particles. Notice also the voids still present in the small field-of-view. Inertia, however small, promotes seizure of the broken particles owing to npOx bridging under a fast rate of loading. The crushing of particles must still occur with high stress, or possibly exacerbated from closer-to-adiabatic conditions during impact [8] [13]. Note also the npOx itself appears compacted. If motility of the particles is the sole cause of densification, then more crushing occurs than particle motion under impact, leading to a relatively high local void ratio. However, the npOx solid bridging is consequently strong when interface stress between particles increases in this depopulated, skeletal network. Thus, impact-formed specimens are similarly strong as quasi-static specimens when compacted with reduced lateral boundaries.

6.2.11 Montmorillonite under Impact Compaction

The SEM micrographs here support the discussions in §5.4, where strength increases were generally observed. Sample 2034 represents a specimen formed under impact, with a free lateral boundary.

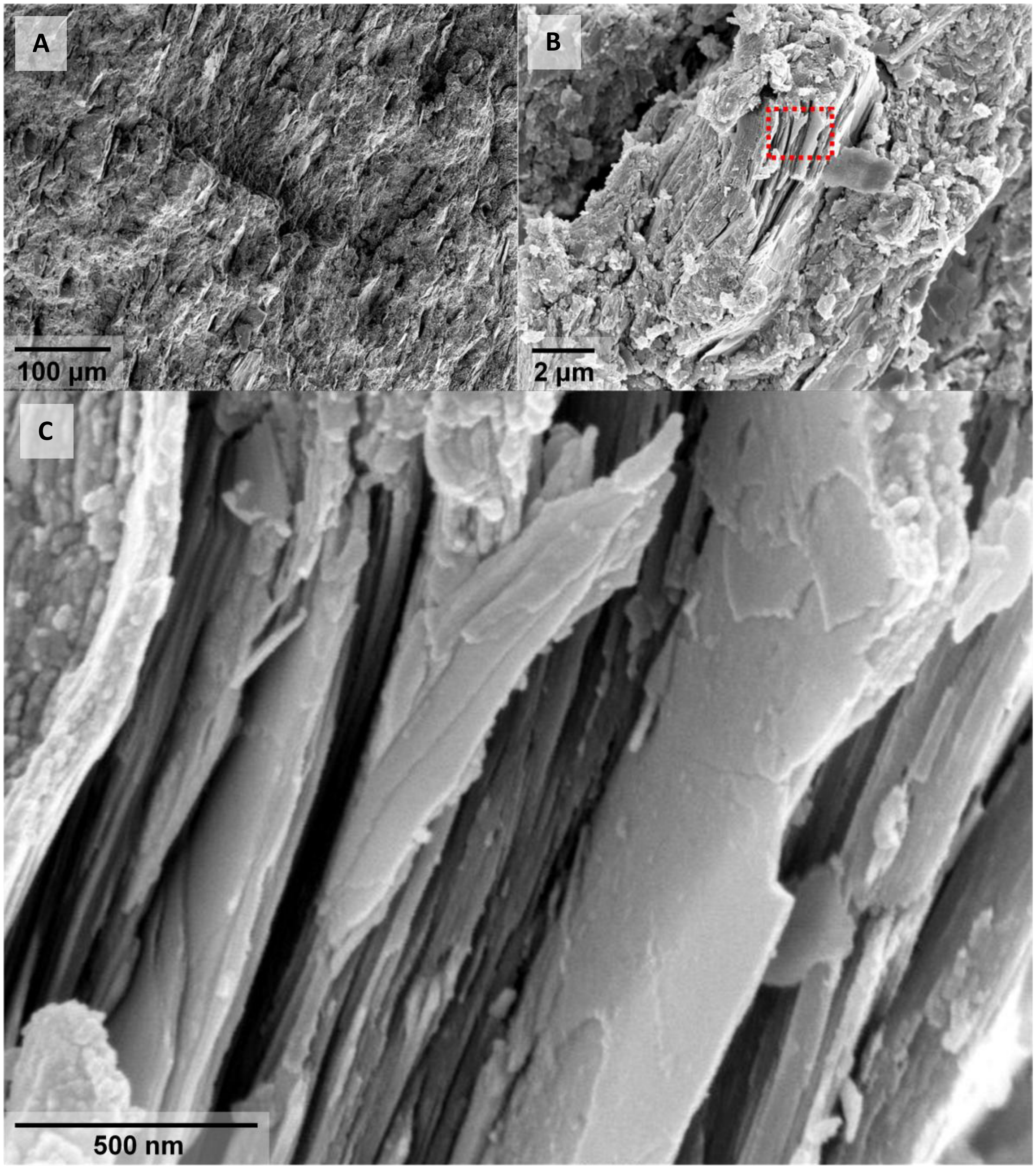

Figure 6-40 SEM of Impact-Formed Montmorillonite. Fracture surface of Sample 2034. This was montmorillonite, of initial size bin 25-45µm, and particles dried to 600°C prior to compaction. Impact was 159J with flexible lateral boundary. Bottom panel is an ultrahigh resolution magnification of the dashed box inset in the upper-right panel (B).

The alignment of particles, to the unaided eye, appears more homogeneous than the montmorillonite mineral layer alignments observed elsewhere. Then, impact compaction can apparently achieve a very high degree of particle-to-particle contact. Of course, a truly parallel configuration is ideal.

The ultrahigh resolution inset shows that the clay particle in-plane strength suffers from the severe loading. The molecular clay mineral layer sheets crack, split, and pull out from their neighboring layers. Although it might not be unique to the shock conditions experienced by particles subject to impact, the pullout of layers seen in the inset suggests that the decrease in in-plane strength may distribute strain energy more evenly in the entire sample, leading to higher strength.

6.3 XRD Analysis

The XRD analysis supports the discussion on the development of mechanical strength in Chapter 4 and 5. In powder X-ray diffraction, comminuting of finely-divided particles broadens the peaks, corresponding to a loss of long-range order [2] [4]. Because the SEM analyses give some compelling evidence for the crystalline disruption in particles from high-pressure compaction, select XRD analysis is warranted.

Mars-1a simulant and montmorillonite clay were ground inside a mortar and pestle for 60s under <1N force. Ground particles mixed with petroleum jelly into a paste-like consistency, followed by smearing the paste on a glass slide and insertion into the XRD machine (Rigaku Miniflex-II) for analysis. Samples were analyzed with scan time of 1s at a rate of 0.02s under Cu-Kα radiation.

6.3.1 Mars-1a

Of interest are the specimens compacted with reduced lateral boundary conditions. One is compacted quasi-statically with the flexible lateral boundary; the other is impacted with the free lateral boundary. The control case represents no grinding or compression of Mars-1a simulant. Initial bin size was 25-45μm, dried to 600°C for 12h.

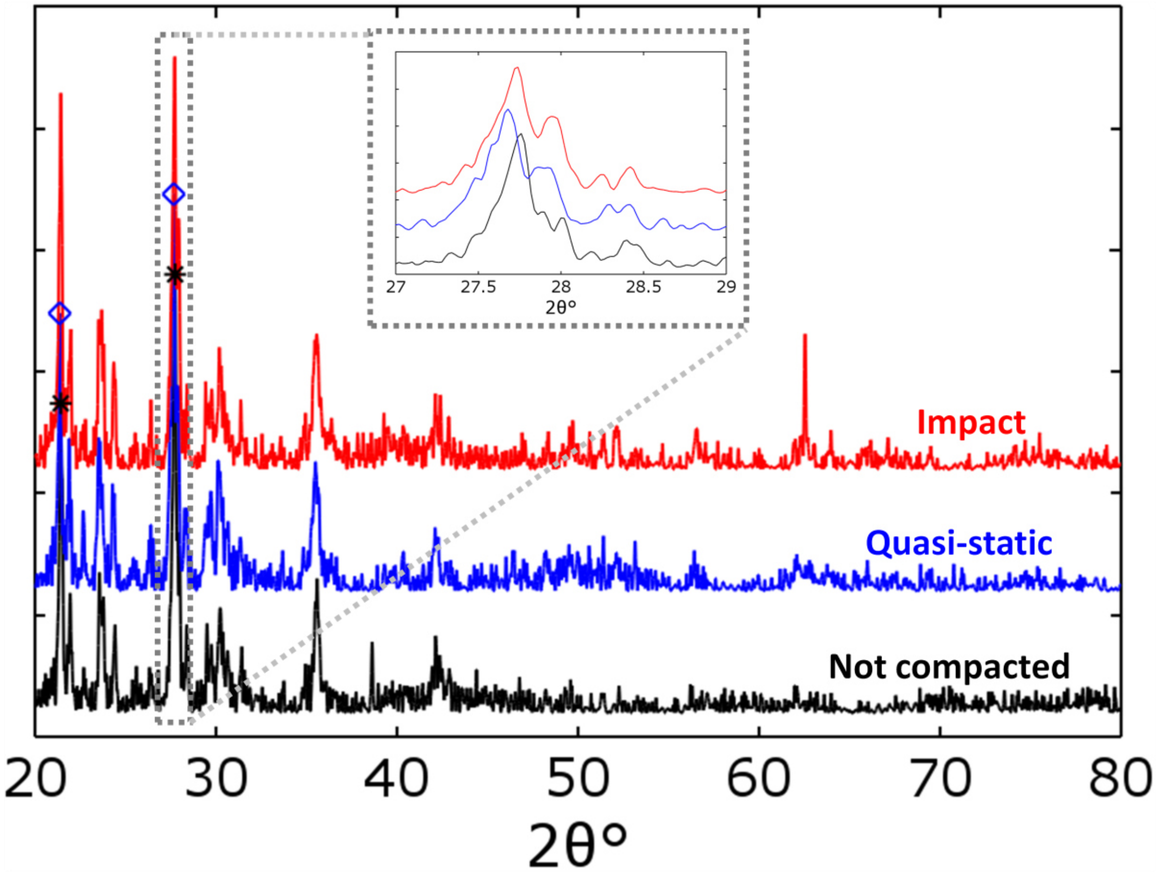

Figure 6-41 XRD of Mars-1a. Diffractograms are shown as labeled for different states. Asterisks and diamonds show peaks for the bottom and middle traces, respectively. Dashed box shows inset of the main peak. The bottom trace was not compacted. The middle trace was quasi-statically compressed to 360MPa with the flexible lateral boundary. The top trace was impacted with the free lateral boundary; impact energy was 114J. All three simulants were dried to 600°C for 12h prior to XRD.

The main peak in Figure 6-41 is likely a pyroxene mineral [14], which is typical in basaltic rock. This main peak generally decreases once Mars-1a is compacted quasi-statically or by impact, indicating the loss in long-range order associated with particle crushing at extremely small scales. This is also jives with the statistics of the SEM counting exercise, which showed that small particles are generated more frequently. SEM also exposed some conchoidal fracture surfaces on the basaltic particles, likely indicating the presence of some amorphous material. The XRD subtracts out the background and does not account for poorly-crystalline or amorphous phases.

If significant crystalline changes were to occur, certain axes would be more susceptible than others (by analogy of slip planes). The peak shifts in the left and right direction are most likely machine error, because they occur throughout the domain. However, some peaks can merge or split into two, such as the peaks in the inset. Merging and splitting of peaks indicates that some disruption occurs in the crystalline direction. A split is probably represented by unopened cracks oriented normal to the spacing direction. A merge is probably represented by merged voids across adjacent repeat units. Some features of goethite are visible near the 21° and 36° [4]. Goethite's crystal structure resembles an expanded lattice full of voids [4], likely facilitating deformation and fracture.

The discussion in §4.4.2.2 hypothesized that phase transformation during long timescales could account for the higher strengths achieved by shock, while earlier discussion in §4.3.2 entertained the opposite notion. Here, the XRD shows that the transformation likely occurs in the impact-loaded sample. The feature near 62° is most prominent, and likely is related to the mineral magnetite or hematite [4]. However, principal features for those neat minerals are not entirely consistent with our diffractogram [4]. Recall that the iron oxides and FeOOH are dispersed with silica and other rock-forming compounds from the weathering process, making the mineral somewhat unique compared to the neat compounds described thus far by others.

6.3.2 Montmorillonite

Of interest are the specimens compacted with reduced lateral boundary conditions. The control case represents no compression of montmorillonite powder. The initial bin size was 25-45μm, dried to 600°C for 12h.

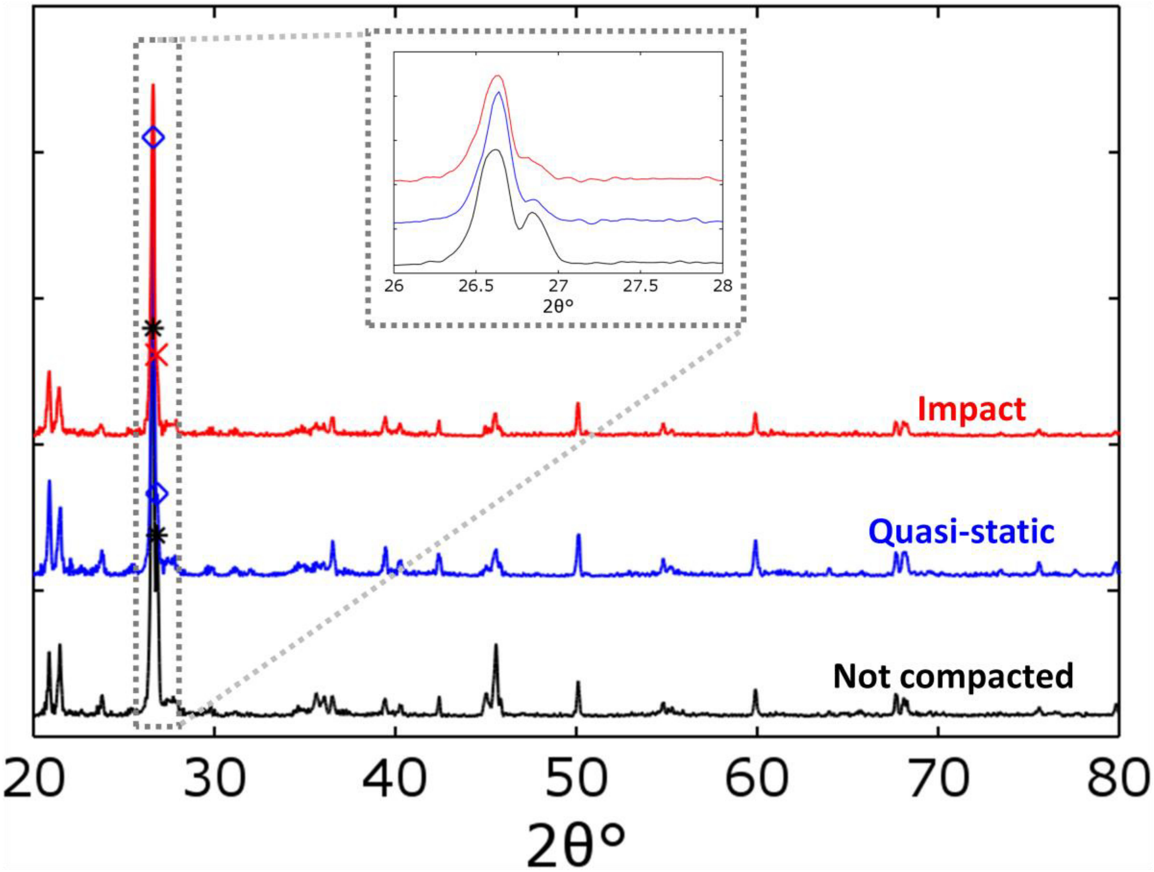

Figure 6-42 XRD of Montmorillonite. Diffractograms are shown as labeled for different states. Asterisks, diamonds, and x's show peaks for the bottom, middle, and top traces, respectively. Dashed box shows inset of the main peak. The bottom trace was not compacted. The middle trace was quasi-statically compressed to 360MPa with the flexible lateral boundary. The top trace was impacted with the free lateral boundary; impact energy was 114J. All three powders were dried to 600°C for 12h prior to XRD.

As with Mars-1a, changes can be seen. The main peak in the inset represents covalently bonded layers in montmorillonite between adjacent silica units for the in-plane direction. To the immediate right of the main peak is a subsidiary peak in the not-compacted montmorillonite. This characteristic distance probably corresponds to an out-of-plane measure [2]. In both compacted cases, this subsidiary peak diminishes likely as a result from mechanical separation. A less significant peak located at ~46° diminishes after compaction and lends further credence to mechanical disruption, although its crystalline identification is more speculative.

6.4 CHNS/O Analysis of Mars-1a and Montmorillonite

Mars-1a and montmorillonite possibly contain trace organic material that can contribute part of the TGA response. However, a TGA machine by itself (PerkinElmer Pyris 1 TGA) does not detect the chemical makeup of the evolved gas. We corroborate the findings from the TGA analysis to elemental analysis using CHNS/O.

CHNS/O analysis (PerkinElmer 2400 Series II) was performed on samples courtesy of Numega Resonance Labs. Each letter stands for the elements that can be detected in the sample. The sample first calcines in pure oxygen, evolving elemental oxide gases [15]. The gases are mixed and travel through a column at different rates owing to differences in adsorption. At the end of the column, gases are detected automatically by their thermal conductivity [15].

Carbon is the identifying element present, by definition, in all organic matter. Carbon-containing solids will combust in the presence of atmospheric oxygen. The hypothesis remains that organic content in the sample is not responsible for the binding effect of the particles, because montmorillonite and Mars-1a were found to strengthen upon compaction regardless of their drying temperature.

As-supplied Mars-1a simulant and montmorillonite powder dried to 350°C and 500°C for 12h were subject to a carbon and hydrogen analysis, along with control samples that were not dried. The results are shown in Table 6-3.

Table 6-3 Effects of Drying Temperature on Carbon Content

Simulant	Drying Temperature (°C)	Number of Trials	Average Carbon Content (wt%)	Average Hydrogen Content (wt%)
Mars-1a	None (25)	3	3.16	1.76
	350	3	0.68	0.77
	500	3	0.30	0.82
Montmorillonite	None (25)	3	0.21	1.15
	350	3	0.24	0.76
	500	3	0.21	0.09

Precision and accuracy in measurement is 0.3wt%.

Mars-1a in the raw, undried state contains an organic content of ~7.9wt%, assuming an empirical formula for sugar, CH_2O, for conversion of mass. The assumption that the organic matter is in the form of carbohydrates arises from the visual observation of small root-like matter present in the unsieved Mars-1a soil, taken directly from the vendor container. Another candidate is graphitic, or soot-like carbon from drying at elevated temperatures; this case leads to carbonaceous content matching the result of 3.2wt%. Given the measurement precision is 0.3wt%, heating to 350°C is sufficient to drive off most of the organic content, and 500°C is sufficient to drive off all of the organic content.

One proceeds to vary the drying temperature between 230°C and 500°C for Mars-1a simulant particles. The compression procedure is identical as that done previously, using a 19.05mm dye as in Chapter 4 with the rigid lateral boundary. Beam specimens are tested in 3-point bending.

Table 6-4 Compacted Mars-1a Dried at Different Temperatures

Sample	Drying Temperature (°C)	Width (mm)	Depth (mm)	Strength (MPa)	Average Strength (MPa)
724	230	4.65	1.97	8.35	7.79
725		4.59	1.97	7.95	
726		4.75	2.73	7.55	
727		4.29	2.72	8.34	
728		4.26	2.11	8.91	
729		4.35	2.10	6.78	
730		4.60	2.03	7.83	
731		4.05	2.02	6.63	
764	500	4.66	1.74	7.44	7.71
765		4.16	1.74	7.07	
766		4.86	1.36	7.62	
767		4.23	1.36	8.75	

Note: Particle size for all Mars-1a prior to compression was 25-45μm.

The mechanical testing presented in Table 6-4 and Chapter 4 for Mars-1a and in Chapter 5 for montmorillonite shows that the compact strength is independent of either carbon or water content.

6.5 EGA (TGA/MS) Analysis

TGA analysis can be extended to evolved gas analysis (EGA), courtesy of the UC Santa Barbara TEMPO Facility. Out of the total volatile content, the portion that is water is unknown. An EGA uses a TGA in combination with a mass spectrometer (MS) to provide the identification of the gaseous species. Samples were dried to different temperatures for 12h in an open quartz tube furnace (Carbolite CTF 12/75/700). The TGA was purged with both compressed air and argon gas; the ramp rate was 10°C/min to 1000°C.

6.5.1 Mars-1a

Two loose simulant samples underwent EGA. The first was dried to 200°C, while the second was dried to 600°C.

The data is plotted combining both TGA and MS curves. Small amounts of noise in the data are smoothed by using Tikhonov regularization using derivative value 4 and the midpoint rule of integration [17].

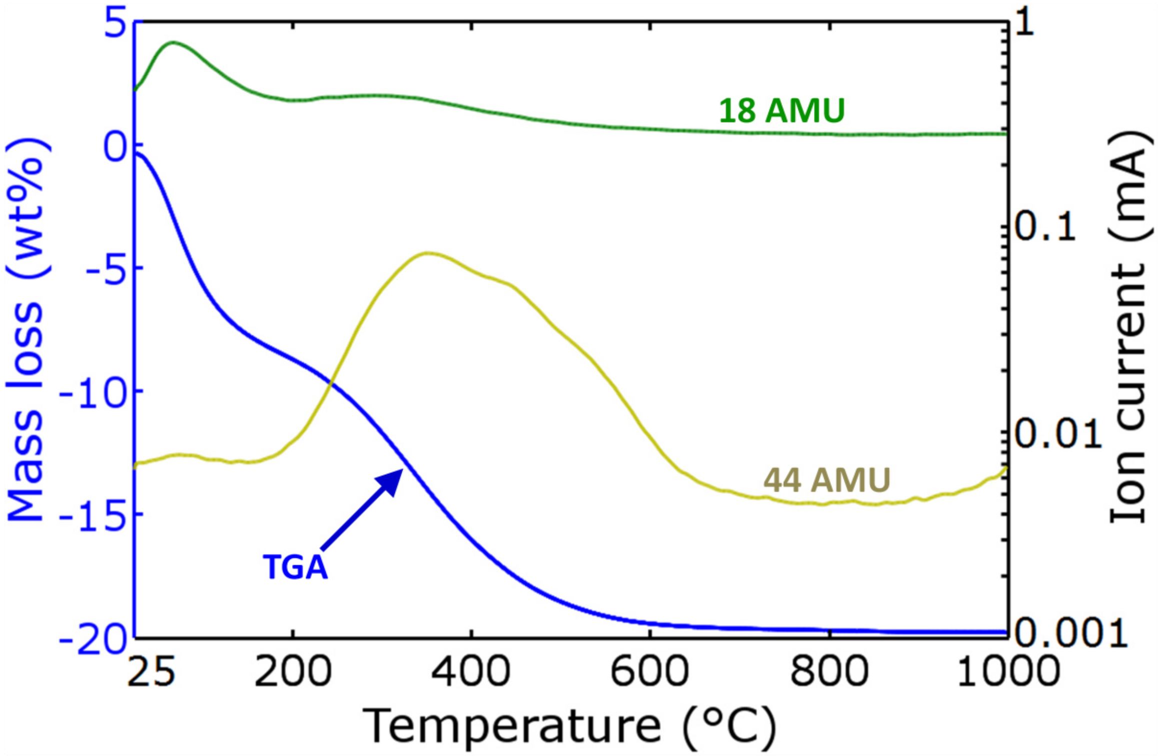

Figure 6-43 EGA of Mars-1a Dried at Lower Temperature. EGA plot of loose Mars-1a simulant dried at 200°C for 12h. The EGA curves comprised of a TGA curve along with two MS curves; ion current is plotted on a logarithmic axis. Ramp rate is 10°C/min to 1000°C.

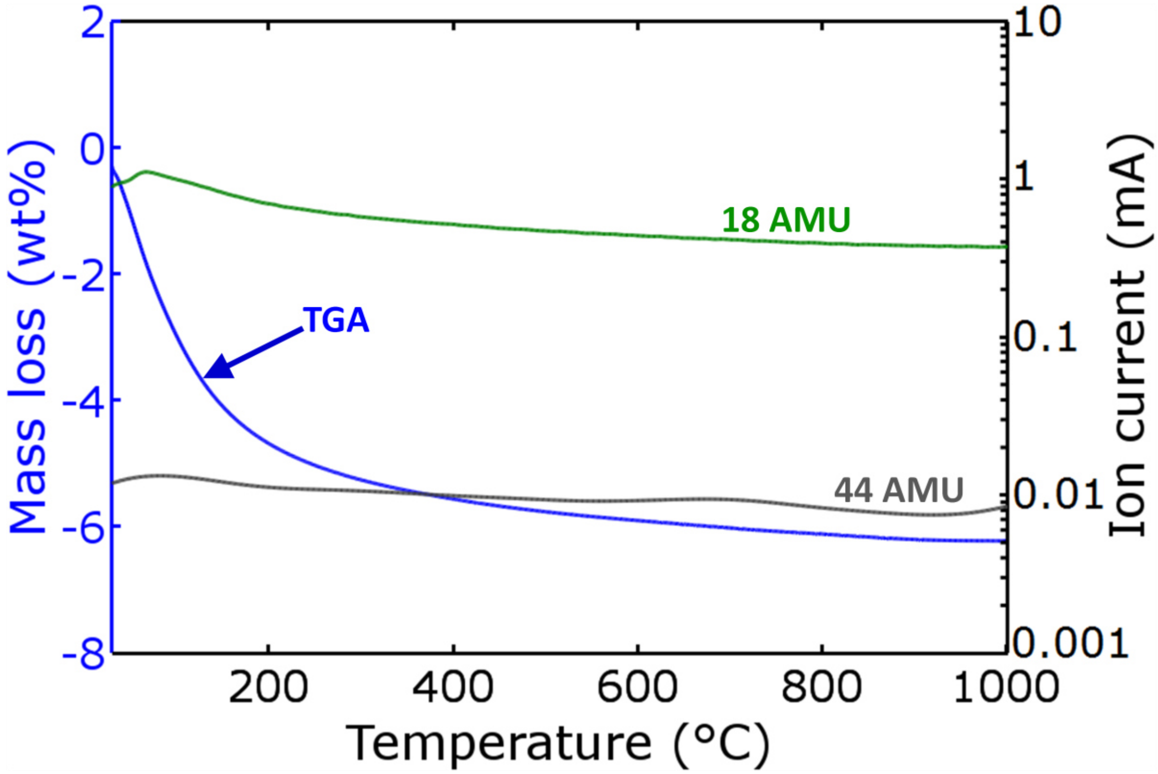

Figure 6-44 EGA of Mars-1a Dried at Higher Temperature. EGA plot of loose Mars-1a simulant dried at 600°C for 12h. The EGA curves comprised of a TGA curve along with two MS curves; ion current is plotted on a logarithmic axis. Ramp rate is 10°C/min to 1000°C.

Charged molecules striking a target plate in the MS cause the ion current, and is reasonably linear in response to the number of collisions per unit time [15]. The main species of interest are water, carbon dioxide, and sulfur dioxide. Carbon dioxide evolves from calcined organic matter, while sulfur dioxide is associated with the volcanic origin of the simulant. Assuming that gaseous triatomic molecules are strongly bonded together, one adopts the assumption that the ionic weight is approximately the same as the molecular weight [16]. Water (18AMU) and carbon dioxide (44AMU) were present, while the sulfur dioxide (64AMU) was negligible. In addition, strong traces of oxygen, nitrogen, and argon were detected from the purge gases. While adsorption of oxygen, nitrogen, and argon may contribute fine amounts to the mass loss in a TGA, they are of no interest as far as mechanical properties are concerned.

In the EGA plot for 200°C-dried simulant (Figure 6-43), two peaks in the 18AMU trace and one large peak in the 44AMU trace is visible. The 18AMU peaks integrate by subtracting the background linearly between room temperature and 500°C, giving 204.88mC of total charge. The 44AMU peaks integrate by subtracting the background between 150°C to 750°C, giving 80.49mC. Note all integrations are taken with respect to time, which is linear with temperature for the ramp. Thus the carbon dioxide-to-water mole ratio is approximately 39.3:100.

Upon drying to 600°C (Figure 6-44), the same analysis procedure with careful inspection subtracts between room temperature and 200°C in the 18AMU trace, with the result 129.96mC. The 44AMU trace is mostly background, but one may interpret two broad features between room temperature to 200°C and 500°C to 900°C, which leads to 1.99mC—a small amount. Consequently, the carbon dioxide-to-water mole ratio reduces significantly to 1.5:100.

A few stoichiometric assumptions are useful for comparisons. For 200°C-dried simulant, the carbon dioxide total weight fraction is 49wt%. However, this is the evolved gas. If the carbon is naturally present in the form of sugars having empirical formula CH_2O, the proportion is then ~40wt%. If present as graphitic or soot-like material as a result of drying, then it can be as low as 21wt%. The average (~31wt%) is in good agreement with the CHNS/O analysis figure of ~8wt% divided by the totally evolved ~30wt% from the TGA (Figure 6-6). For 600°C-dried material, the three different scenarios reduce to 4wt%, 2wt%, and 1wt%, respectively.

Recalling no significant strength changes for different levels of heating, we infer that carbon contamination has a minimal or negligible effect on the compact strength in Mars-1a simulant.

6.5.2 Montmorillonite

Two montmorillonite (Sigma-Aldrich) powder samples—dried to 350°C and 600°C—underwent EGA.

The data is plotted combining both TGA and MS curves. Small amounts of noise in the data are smoothed by using Tikhonov regularization using derivative value 4 and the midpoint rule of integration [17].

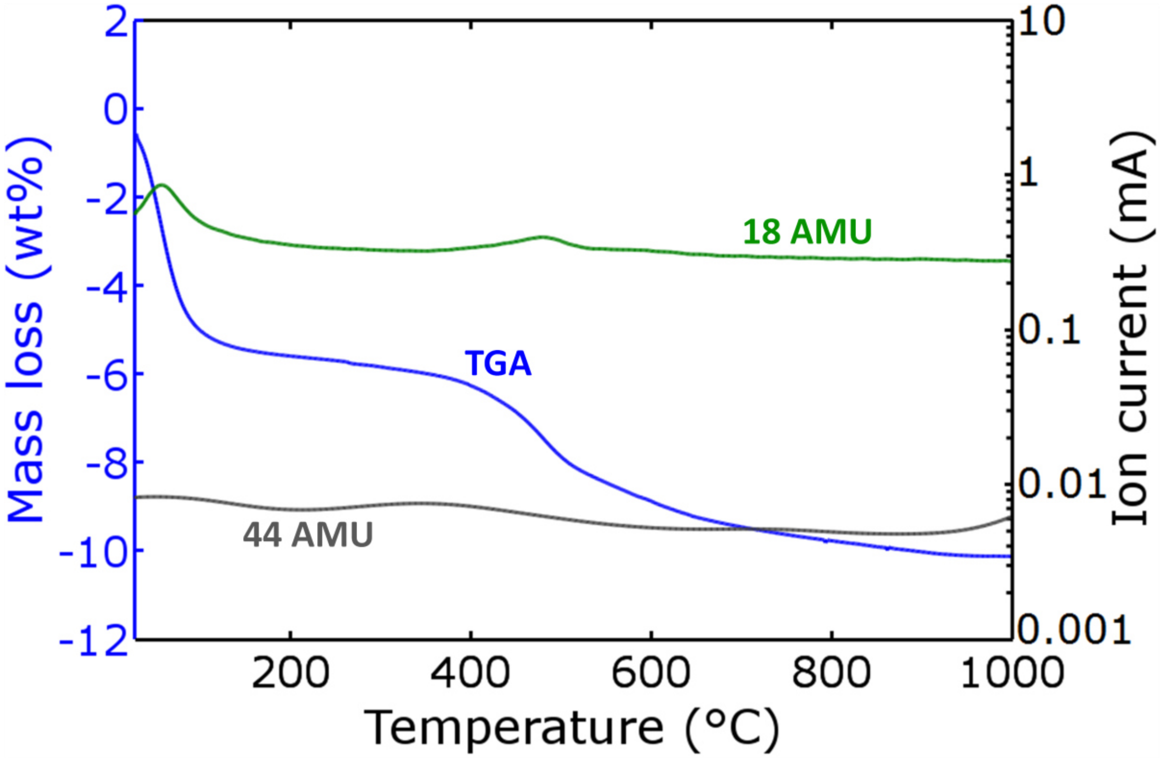

Figure 6-45 EGA of Montmorillonite Dried at Lower Temperature. EGA plot of montmorillonite powder dried at 350°C for 12h. The EGA curves comprised of a TGA curve along with two MS curves; ion current is plotted on a logarithmic axis. Ramp rate is 10°C/min to 1000°C.

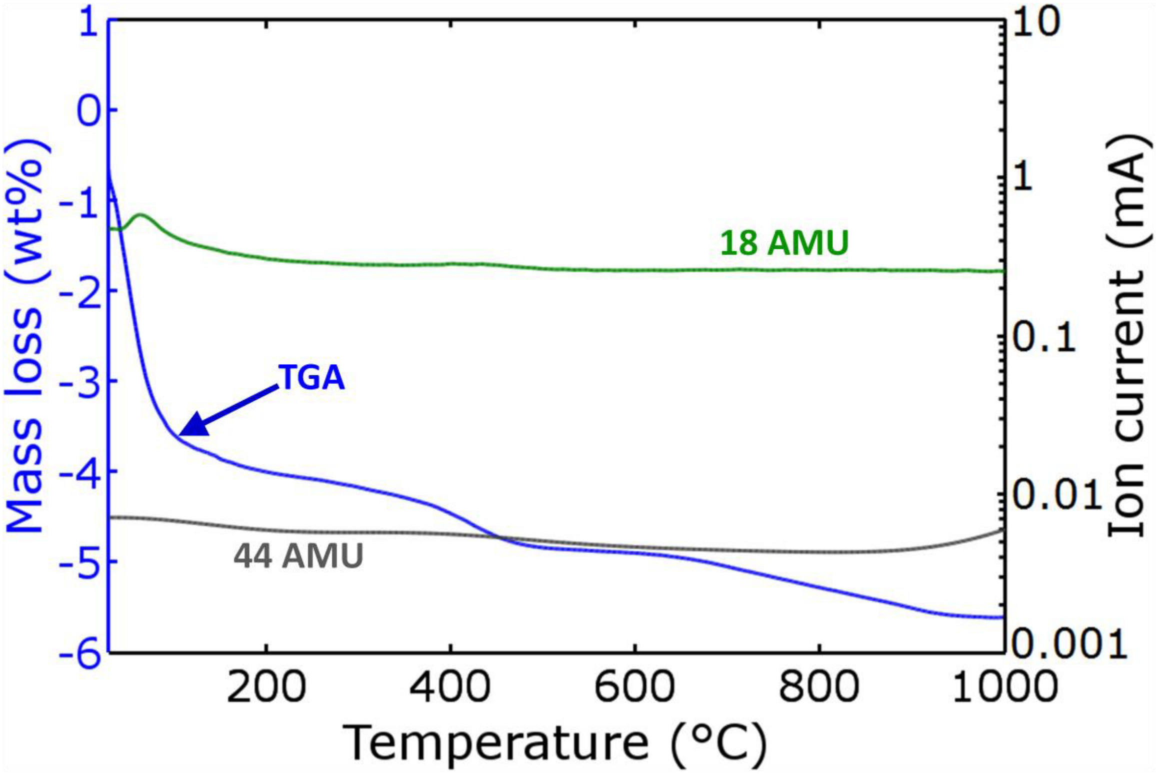

Figure 6-46 EGA of Montmorillonite Dried at Higher Temperature. EGA plot of montmorillonite powder dried at 600°C for 12h. The EGA curves comprised of a TGA curve along with two MS curves; ion current is plotted on a logarithmic axis. Ramp rate is 10°C/min to 1000°C.

Refer to the discussion for the Mars-1a simulant EGA in §6.5.1. Identical assumptions and methodologies apply.

EGA curves for montmorillonite powder dried to 350°C produce familiar shapes. The 18AMU trace contains two peaks, integrated from room temperature to 150°C and 350°C to 600°C against the background to yield 128.97mC of charge. The 44AMU trace assumes one broad peak integrated from 200°C to 600°C, giving 1.45mC. We expect the montmorillonite to be clean because it is of a synthetic source (Sigma-Aldrich K10 69866). The carbon ratio is therefore negligible and can be discarded as background, suggesting that the analyses for Mars-1a are also conservative to some degree.

The 18AMU trace for montmorillonite powder dried to 600°C integrates two regions from room temperature to 150°C and 300°C to 500°C against the background to give 40.659mC. The 44AMU trace is easily disregarded as background in light of the previous finding.

This chapter, in part, contains material that has been submitted for publication in 2016 with authors Brian J. Chow, Tzehan Chen, Ying Zhong, Cheng Zhang, Juan A. Ramirez, Cruz M. Galarza, and Yu Qiao. The dissertation author was the experimental investigator and first author of these publications.

6.6 References

1. Allen, C. C., Jager, K. M., Morris, R. V., Lindstrom, D. J., Lindstrom, M. M., Lockwood, J. P. “Martian Soil Simulant Available for Scientific, Educational Study,” *Eos* **79**, *34*, 405-412 (1998).

2. Grim, R. E. Clay Mineralogy (2nd ed.). McGraw-Hill (1968).

3. Cornell, R. M., Schwertmann, U. The Iron Oxides: Structure, Properties, Reactions, Occurrences and Uses (2nd ed.). Wiley-VCH Verlag (2003).

4. Joshi, R. C., Achari, G., Horsfield, D., Nagaraj, T. S. "Effect of heat treatment on strength of clays," *J. Geotech. Eng.* **120**, 1080-1088 (1994).

5. Boynton, W. V., Taylor, G. J., Karunatillake, S., Reedy, R. C., Keller, J. M. "Elemental abundances determined via the Mars Odyssey GRS," in *The Martian Surface: Composition, Mineralogy, and Physical Properties (Bell III, J. F., ed.)*, Cambridge University Press (2008), pp. 105-124.

6. Kondolf, G. M., Adhikari, A. "Weibull vs. Lognormal Distributions for Fluvial Gravels," *J. Sedimentary Res.* **70**, *3*, 456-460 (2000).

7. Vogel, L., Peukert, W. "Breakage behaviour of different materials - construction of a mastercurve for the breakage probability," *Powder Tech.* **129**, *1*, 101-110 (2003).

8. Pelleg, J. Mechanical Properties of Ceramics. Springer (2014).

9. Al-Fawzan, M. "Methods for Estimating the Parameters of the Weibull Distribution," King Abdulaziz City for Science and Technology, Saudi Arabia (2000).

10. Wang, X., Yu, Q. “Unbiasedness of the Theil-Sen Estimator,” *J. Nonparam. Stat.* **17**, *6*, 685-695 (2005).

11. Hansen, J. E., Sato, M., Ruedy, R. "Perception of climate change," *Proc. Natl. Acad. Sci.* **109**, *37*, 14726-14727 (2012).

12. Osipov, V. I. "Nanofilms of Adsorbed Water in Clay: Mechanism of Formation and Properties," *Water Resources* **39**, *7*, 709-721 (2012).

13. Timoshenko, S. P., Goodier, J. N. Theory of Elasticity. McGraw-Hill (1970).

14. Ray, C. S., Reis, S. T., Sen, S. "Characterization and Glass Formation of JSC-1 Lunar and Martian Soil Simulants," in *Space Technology and Applications International Forum - STAIF 2008*, Albuquerque, New Mexico (2008).

15. PerkinElmer, "2400 Series II CHNS/O Elemental Analysis," 2011. URL: https://www.perkinelmer.com/lab-solutions/resources/docs/BRO_2400_SeriesII_CHNSO_Elemental_Analysis.pdf. [Accessed 2016].

16. J. Stickel, "Data-smoothing package," in *GNU Octave version 4.0.0 manual: a high-level interactive language for numerical computations (Eaton, J. W., ed.)* (2015).

17. White, F. A., Wood, G. M. Mass Spectrometry: Applications in Science and Engineering. Wiley-Interscience (1986).

18. Taylor, H. A., Brinton, H. C., Wagner, T. G., Blackwell, B. H., Cordier, G. R. "Bennett Ion Mass Spectrometers on the Pioneer Venus Bus and Orbiter," *IEEE Trans. Geosci. Rem. Sen.* **GE-18**, *1*, 44-49 (1980).

7 Closing Discussions

7.1 Permeability as a Measure of Habitability

Structural materials intended for building habitats can be expected to contain atmospheric gas to an acceptable limit. We conduct a few tests here to determine the permeability of Mars-1a and montmorillonite. These two materials are chosen because they occupy prominent roles in the results from Chapters 4 and 5. Determination and calculation of permeability drew from the framework of the Rilem-Cerembureau method [1][2].

We generated compacted solids with quasi-static loading and the flexible lateral boundary condition process described in §4.4.1.2 and §5.4.1.2. Instead of following through with cutting of raw post-compressed solid into beams, samples were instead ground into discs directly used as specimens for the permeability test. The disc followed the profile of a 12.7mm-diameter reference piston, and grinding utilized both 26μm and 13μm abrasive. Edges of the discs lightly chamfered with the latter size to ensure integrity of the disc. Vacuum grease (Dow Corning) sealed the circumference of the disc inside flexible tubing of matching size (Tygon R-3603 Saint Gobain AAC00037). A hose clamp crimped the tubing against the sample, completing the seal. Quality of the seal was ensured through performing separate control tests with a metal piston; when gas pressurized the flexible tubing inlet, no gas escaped across the sample to the outlet.

Upstream of the sample connected to a 138kPa nitrogen gas source, while the downstream tubing led to an upside-down graduated cylinder filled with water. A schematic of the test stand is shown in Figure 7-1. Given the gaseous absolute (or dynamic) viscosity μ, sample thickness t parallel to flow, cross-section area A normal to flow, and upstream and downstream pressures P_i and P_o, respectively, the Rilem equation for determining permeability is [1]

$$k = Q\left(\frac{2\mu t}{A}\right)\left(\frac{P_o}{P_i^2 - P_o^2}\right)$$

At standard temperature, one is given for nitrogen gas $\mu = 0.0000176\ Pa - s$.

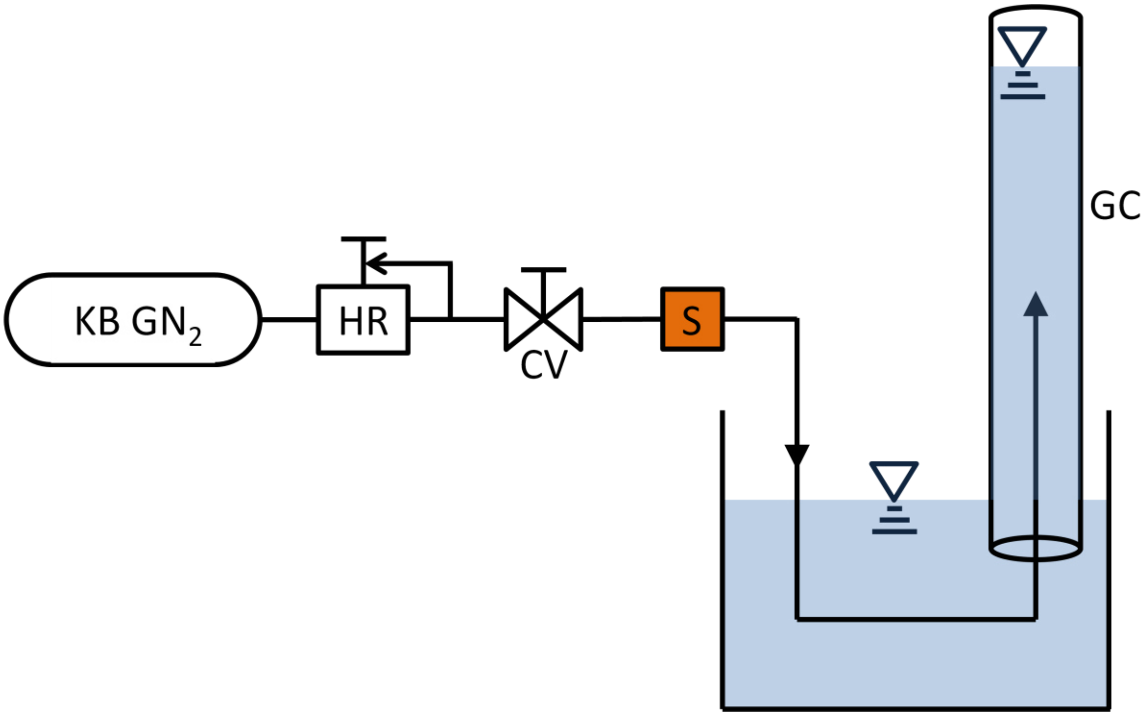

Figure 7-1 Schematic of Permeability Test Stand. Abbreviations are as follows: KB GN$_2$ denotes the nitrogen K-bottle; HR denotes the hand regulator with output set at 138kPa; CV is a close valve; S is the sample, secured as described in the procedure; GC denotes the graduated cylinder. Flow direction and arbitrary water levels are shown as indicated during test.

Table 7-1 Permeability of Compacted Mars-1a and Montmorillonite

Simulant	Sample	Thickness (mm)	Cross-sectional Area (mm^2)	Elapsed Time (s)	Volume (ml)	Permeability ($\times 10^{-16}$ m^2)
Mars-1a	1924	2.88	143.6	908	101	1.70
	1925	2.61	141.5	785	85	1.52
	1926	2.70	138.3	737	86	1.73
	1927	2.62	139.6	971	120	1.76
Montmorillonite	1920	3.61	136.9	1809	90	1.00
	1921	2.92	135.6	1900	80	0.69
	1922	2.82	134.0	4322	102	0.38
	1923	2.56	122.9	6023	91	0.24

To account for the calculated permeability values, we may naturally assume small channels consisting of connected voids on the order of the smaller particle sizes observed. If the packing of particles is very dense, like a body-centered cubic structure for atoms in a crystal, each particle would contribute one defect effectively serving as a flow channel. Following the equation to calculate mean particle size of the uncrushed distribution in §4.6.1, the large-field SEM particle count in §6.2.5 has $x_0 \approx 9\mu m$ and $\alpha \approx 1.4$ to give

$$\mu \approx \frac{9\ \mu m}{1.4}\,\Gamma\left(\frac{1}{1.4}\right) = 8.2\ \mu m$$

This value of mean diameter is adopted for montmorillonite as well. Dividing the area of the cross-sectional area by the square of $8.2\mu m$ gives a result on the order of 10^6 particles on the face of the cross-section. Reasonably, the defect size is on the order of particle size such that the flow channel radius, r, is ~10^{-6}m. Combining Poiseuille's well-known equation for flow through a cylindrical tube with the Rilem equation yields an expression in terms of the permeability coefficient:

$$k = \frac{\pi}{r}\left(\frac{r^4}{A_s}\right)\left(\frac{P_o}{P_i + P_o}\right)$$

where A_s is the cross-sectional area of the sample. Applying tortuosity factors of 10 and 100 for Mars-1a and montmorillonite clay will generate calculated permeability coefficients on the order of 10^{-16} and 10^{-17}m^2, respectively, in agreement with the experimental data.

To put the results into physical perspective, the experimentally calculated gas permeability coefficient of 10^{-16} and 10^{-17}m^2 is similar to those measured for igneous rocks, such as granite or gneiss [3][4]. This suggests that compressed tiles, arranged orthogonal to the direction of resistance against mass transport, can be an effective barrier for containing an atmosphere under pressure. Numerous geotechnical applications exist for montmorillonite as a liquid barrier [5], and this work extends the application to a dry montmorillonite holding gas.

7.2 Energy Efficiency of Compaction

The very feasibility of extraterrestrial habitat construction essentially draws upon sustainability paradigms on Earth. That is, given a limited amount of energy, one should maximize output. The compaction process developed in Chapter 4 and 5 is purely mechanical forming, avoiding the chemical or calcination processes burdening other alternatives such as the polymeric IOHs investigated in Chapter 3. A brief survey of the literature of the time of this writing still exposes the popularity of melting or sintering within the prototyping community (*e.g.* [6][7]).

Qualitatively, thermal sintering is energy-consuming because only a fraction of thermal energy is spent breaking and forming bonds at the necessary interfaces, while the rest is dissipated as heat phonons. As we have discussed in this work, mechanical forming naturally assists particles to more optimal locations. While immobile defects may serve as crack initiators, if dispersed finely as seen in SEM they tend to distribute strain more evenly and strengthen the solid instead.

The drying and sieving steps were experimental variables and do not reflect pragmatic implementations of compaction strengthening. Drying of the particles prior to compression was served merely to simulate the actual Martian soil. Flexural strengths of the beams made from initially random particle sizes was nearly equivalent to those made from some of the finer sieved sizes. Although broader-scale sieving in the field is expected, the compression forming accounts for the great majority of the overall energy expenditure.

One can inspect the volumetric efficiency of the quasi-static compression *via* their load-displacement curves. Forming curves for Mars-1a and montmorillonite are shown in Figure 7-2.

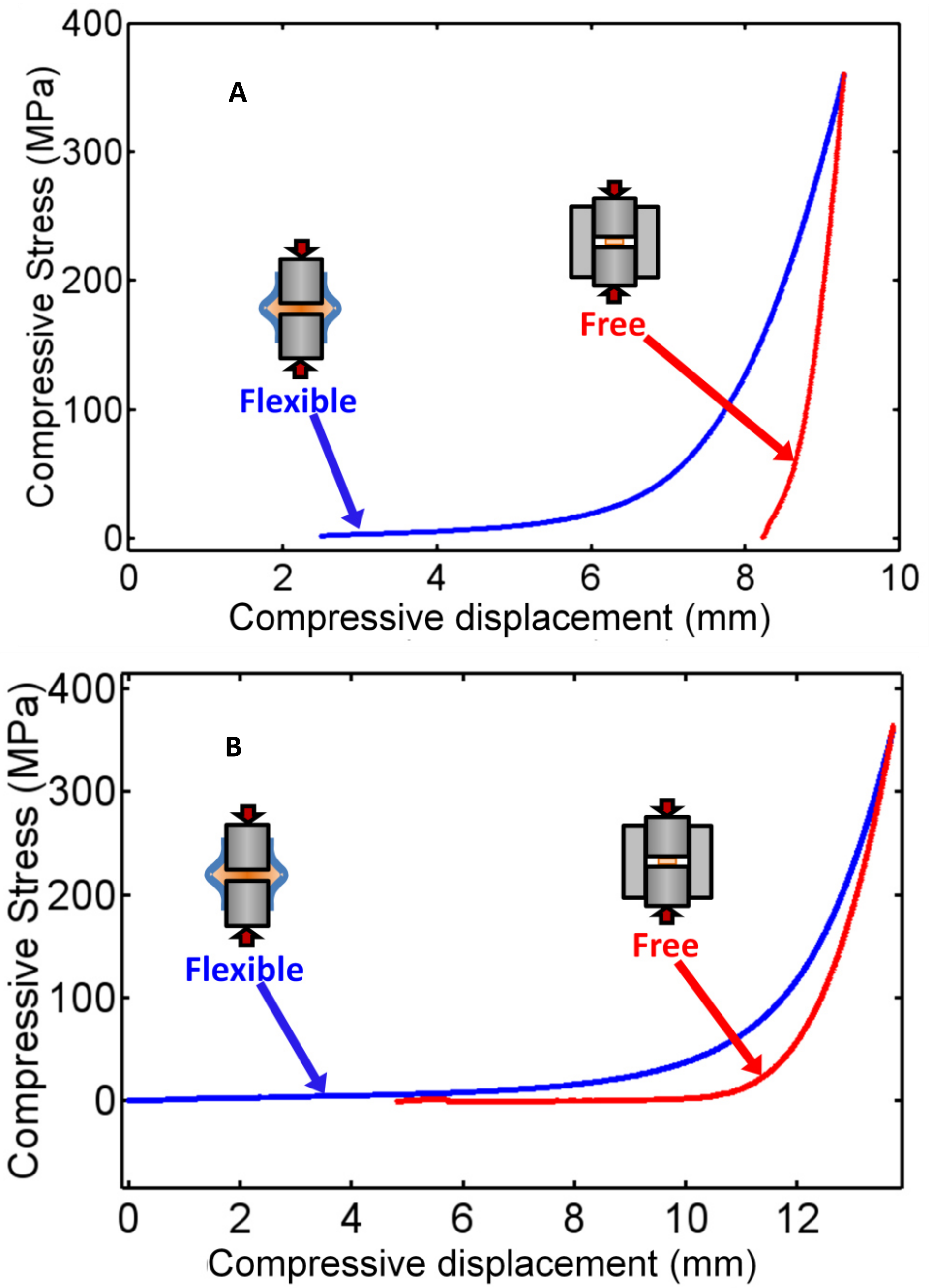

Figure 7-2 Forming Load *vs.* Displacement Curves. Shown graphs are Mars-1a (A) and montmorillonite (B), all quasi-statically compressed with reduced lateral boundary conditions. Specific boundary conditions with diagram are labeled for each curve. Piston diameter is 19.05mm^2. Each curve is calculated from the mean of three representative curves.

Calculation of energy assumes, quite practically, that the elastic energy from unloading is not regenerative. Trapezoidal integration of the flexible boundary curve represented the realistic amount of energy expended to compress the sample. Consider the flexible lateral boundary curves from Figure 7-2 and numerically integrate them. These curves are chosen because quasi-static loading with the flexible lateral boundary achieved the highest combination of sample volume and strength. The discs made for the permeability tests (Table 7-1) represent the typical dimensions of the entire useful, hardened region in the raw compact (Figure 4-25). For the integrated energy E and typical sample volume V, we have for Mars-1a:

$$\frac{E}{V} = \frac{124.5\,J}{380\,mm^3} \approx 330\,MJ/m^3$$

and for montmorillonite:

$$\frac{E}{V} = \frac{166.3\,J}{394\,mm^3} \approx 422\,MJ/m^3$$

These quantities are one order of magnitude less than energy expenditures associated with melting of silicates, which is usually >4GJ/m^3 [8][9]. Although thermal methods can be potentially improved through rapid heating and synergetic electricity such as spark plasma sintering, mechanical compaction still represents a benchmark due to its simplicity of processing and equipment.

7.3 Future Work

Any single answer to a testable hypothesis offers the potential to generate more open questions for the purposes of further investigation. The discussions in the experimental chapters give a preview to some of the possible questions that remain.

In the results with IOH, the wettability and adhesion of the polymer to the surfaces of particles was non-optimal. By inspection using SEM, only melt-processing showed marginally satisfactory adhesion to particles. It remains an open problem to develop a method of binding polymers to particle surfaces without complicated (surface treatment) or energy-consuming (heating) steps, although some progress has been made [10][11].

When Mars-1a and montmorillonite were compressed without binders, the rigid lateral boundary condition gave the best shape control, being a perfect disc. Whether it is possible to control the shape of the immediately compacted solids using the reduced lateral boundary conditions without further subtractive grinding is not known. So far, it appears that lateral expansion must take place randomly and flash material must be generated for a strong solid to occur.

Mars-1a and montmorillonite were subject to maximum stresses of 1.5GPa with the free lateral boundary condition. The surface hardness of the steel piston (~60R_C) limits the compressive stress to approximately this level (~2GPa). No cermet or ceramic anvils were utilized to probe higher compression pressure. Particle crushing was continued when the compression pressure increased from 360MPa to 720MPa; it is unknown whether an upper limit exists where particle crushing starts to decrease or arrest from either a hydrostatic stress state (similar to the rigid lateral boundary) or a deviatoric stress state (similar to the reduced lateral boundaries). The decrease may be expected from the limit where flaws run out and the particles consist of near-perfect lattices somewhere in the nanoscale region.

Tensile strengths primarily referred to the in-plane direction normal to the uniaxial load direction; using fracture mechanical convention, this is the radial-longitudinal crack opening direction. SEM micrographs clearly show that alignment of particles, montmorillonite more strongly so than Mars-1a. The strength anisotropy for different directions remains to be quantified. Testing anecdotes, however, noted the radial-tangential strength tends to be similar to the radial-longitudinal strength.

Flexural strength generally correlates well with closely associated mechanical and physical properties, such as density, permeability, elastic modulus, compressive strength, splitting (Brazilian) tensile strength, and many others. Most of these properties, and their correlations with each other, remain to be quantified.

During impact compaction with reduced lateral boundaries, Mars-1a and montmorillonite showed a change in appearance to a darker albedo in places where the solid was strongest (Figure 4-25). The correlation of the albedo change to the microstructure, density, or mechanical properties was not established. The XRD showed a new phase formed in Mars-1a under impact compaction, but this phase is not known.

The origin of Mars-1a as an altered basaltic rock is difficult to replicate with neat analogues, because the weathering process introduces silicates and other rock-forming minerals into the npOx over the course of many years. Whether it is possible to synthesize Mars-1a from raw basalt flour, such as JSC-1A, on much shorter timescales is not known. Such processes for artificial weathering may be practical for unaltered basalt particles in the Martian regolith.

The degrees to which different nanoscale materials strengthen under the compaction methods employed in this work remain open to quantification. A commonality between clay minerals such as montmorillonite and Mars-1a is that they are both consequences of aqueous alteration. There is some motivation to explore easily-cleaved ceramic particulates which are not necessarily dependent upon water for their formation. Some salts, such as sodium chloride [12] and magnesium carbonate (Appendix I), are already known to compact to strong solids.

Geotechnical parameters, including the degree of saturation and void ratio, are not measured precisely in Mars-1a and montmorillonite during compaction forming. Measurements taken from Samples 2016-2023 and 2032-2040, impact-formed at relatively high energy, indicate an average density of ~1.74g/cm^3. Solid montmorillonite has density ~2.65g/cm^3 [5], giving a void ratio of 0.52. Given the TGA drying imparts total water content ~5wt%, we arrive at a degree of saturation of ~0.25, which agrees with the lack of visible water or corrosion on the steel piston during or after compaction. Quantitative measurements during compaction are warranted because the extent of void closure under high pressure remains an open problem for dry clays [13].

Experience shows that unloading curves after forming show some hysteresis that minimizes with increased compressive stress of loading. The model developed for montmorillonite shearing is zeroth-order, being linear-elastic and applicable for the highest stresses. The existence of the hysteresis, on the other hand, affirms voids are continuously being filled (entailing energy absorption) and that this process is never quite complete.

The long-term stability of the compacted materials should be further explored. Montmorillonite, in particular, is notable for its ability to swell with adsorbed water, and this may affect long-term properties. The current study, so far, only explores about a dozen samples of Mars-1a left at ambient conditions for about 190 days in Appendix H.

7.4 Significance and Conclusion

The experimental results indicate that JSC-1A can be bonded successfully using a very small amount of binder with in-situ polymerization. However, the remnant quantity after polymerization is variable, owing to some volatility of the monomer. Other methods to bond JSC-1A generally meet difficulties with strength or binder wettability. If these issues were to be resolved, the required binders still do not satisfy a complete ISRU framework.

Compaction of Mars-1a and montmorillonite simulants met much more success. Changing the lateral boundary condition employed for uniaxial loading significantly influences the resultant flexural strength of the compact. When dried to temperatures in excess of 350°C, Mars-1a strengthens under compaction inside a rigid lateral boundary, but montmorillonite does not. The montmorillonite requires lateral expansion associated with the reduced lateral boundaries to strengthen. Neither carbon contamination nor trace water was found to be responsible for strength in either Mars-1a or montmorillonite. Electrostatic interactions and secondary bonding in high-specific surfaces—in excess of 500m^2/g—attributes the strengthening of the compact. Crushing, shearing, translation, and rotation occur within the samples to optimally distribute particles in the state of lowest system free energy.

The laboratory-scale processes developed for the reduced lateral boundaries can be scaled as an engineering problem. As an example, to further scale a flexible lateral boundary apparatus under a quasi-static, uniaxial load, one can design a number of possible devices illustrated in Figure 7-3.

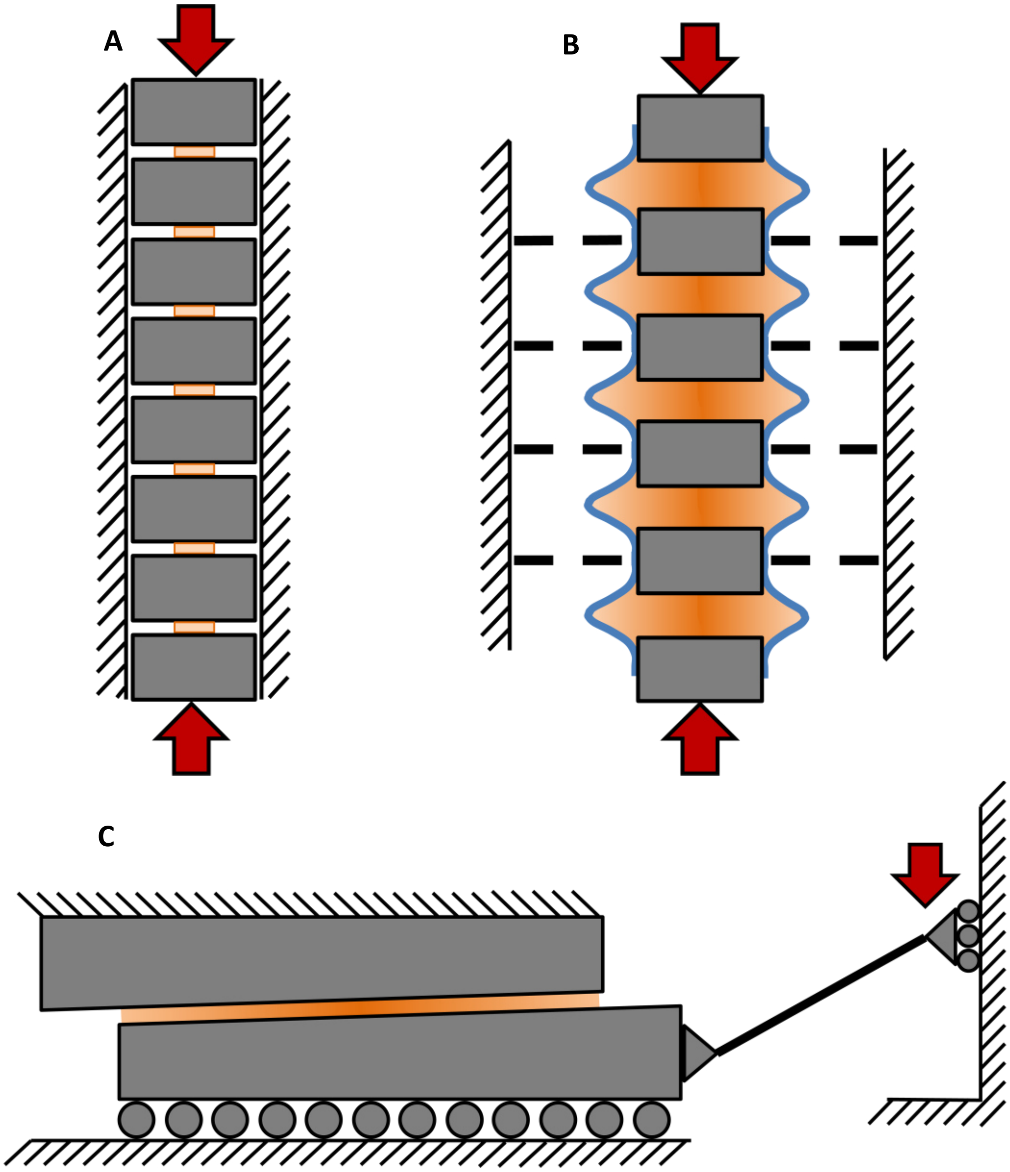

Figure 7-3 Examples of Implementation. Some simple mechanical devices that can be used for further scaling of the compaction process using reduced lateral boundaries. Both free (A) and flexible (B) lateral boundaries can be placed in series; dashed lines represent horizontal stabilizers. Increased amounts of force for a free lateral boundary produce larger samples; the simple machine (C) geometrically multiplies force twice, although the actuation source can be hydraulically boosted in several stages, perhaps achieving 0.1-1GN normal force on the sample at the inclined face.

The ability of Mars-1a to form strong solids without added binders, although remarkable in itself, is also significant for several other reasons. The direct formation of structural components in a single step offers a novel possibility for complete ISRU in Martian construction. Finding npOx phases are responsible for strengthening of Mars-1a dramatically transforms the perspective of iron oxides from undesirable rust—with small, niche applications in pigmentation and catalysis—to a potentially large-scale structural material with flexural strength higher than concrete. Whereas natural cementation processes, such as fluvial concretion [14][15], act over geologic timescales with the help of water, this work shows that ultradry npOx acts as mechanical cement capable of bonding instantaneously.

Likewise, the potential for montmorillonite to strengthen is significant because dry clays are sometimes difficult to strengthen from compaction. This difficulty was especially pronounced for ultra-dry montmorillonite exposed to temperatures of >350°C for 12h: rigid lateral boundaries produced fragile specimens. However, when a reduced lateral boundary condition was employed, the strengths were quite high. On absolute terms, impact with the free lateral boundary produced the strongest montmorillonite solids, with two of them (Samples 1475 and 1488) testing >100MPa flexural strength. This exceeds the unfired strength of most technical ceramics; for instance the strongest alumina greenware approaches 50MPa flexural strength [16][17]. Whereas compaction in geotechnical engineering requires optimum moisture content [5] for highest density and presumably strength, this work shows that in the regime of ultrahigh pressures, strength is optimal when moisture content is near or exactly zero.

The findings in this work represent a contribution towards the realization of complete ISRU construction paradigm on Mars. The compaction of Mars-1a and montmorillonite is practical for habitats, because solids are capable of holding gas. It is also sustainable, because energy efficiency of compaction is about one order of magnitude less than heat-based processes. Realization of compaction should not be realized exclusively with bulk machinery; rather, it should be portable to rapid prototyping, where incremental layers are compacted on top of one another. Such technology, or any as-yet unforeseen engineering development, holds the promise for expanding human presence on Mars and the cosmos beyond.

7.5 References

1. "Measurement of the Gas Permeability of Concrete by the Rilem-Cembureau Method," *Mat. Struct.* **32**, 176-178 (1999).

2. Springer, D. S., Loaiciga, H. A., Cullen, S. J., Everett, L. G. *RILEM* (1999).

3. Brace, W. F., Walsh, J. B., Frangos, W. T. "Permeability of Granite under High Pressure," *J. Geophys. Res.* **73**, *6*, 2225-2236 (1968).

4. Wang, H., Xu, W., Zuo, J. "Compact rock material gas permeability properties," *Physica B* **449**, 10-18 (2014).

5. Das, B. M. Principles of Geotechnical Engineering (7th ed.). Cengage Learning (2010).

6. Cesaretti, G., Dini, E., De Kestelier, X., Colla, V., Pambaguian, L. "Building components for an outpost on the Lunar soil by means of a novel 3D printing technology," *Acta Astronautica* **93**, 430-450 (2014).

7. Kading, B., Straub, J. "Utilizing in-situ resources and 3D printing structures for a manned Mars mission," *Acta Astronautica* **107**, 317-326 (2015).

8. Meechoowas, E., Tapasa, K., Jitwatcharakomol, T. "Alternative Soda-lime Glass Batch to Reduce Energy Consumption," *Key Eng. Mater.* **545**, 24-30 (2013).

9. Lin, T. D., in *Lunar Bases and Space Activities of the 21st Century* (1985).

10. Chen, T., Chow, B. J., Shi, Y., Zhao, C., Qiao, Y. "An inorganic-organic hybrid of lunar soil simulant and polyethylene," *ASCE J. Mater. Civil Eng.* **27**, *06015013*, 1-4 (2015).

11. Chen, T., Chow, B. J., Qiao, Y. "Two-stepped size gradation of particle size in an organic-inorganic hybrid," *Sci. Eng. Compos. Mater.* **22**, 643-637 (2015).

12. Karehill, P. G., Nyström, C. "Studies on direct compression of tablets XXI. Investigation of bonding mechanisms of some directly compressed materials by strength characterization in media with different dielectric constants (relative permittivity)," *Int. J. Pharm.* **61**, 251-260 (1990).

13. Mun, W., McCartney, J. S. "Constitutive Model for the Drained Compression of Unsaturated Clay," *J. Geotech. Geoenviron. Eng.*, in press.

14. Cornell, R. M., Schwertmann, U. The Iron Oxides: Structure, Properties, Reactions, Occurrences and Uses (2nd ed.). Wiley-VCH Verlag (2003).

15. Arvidson, R. E., Squyres, S. W., Bell III, J. F., Catalano, J. G., Clark, B. C., Crumpler, L. S., de Souza Jr., P. A., Fairén, A. G., Farrand, W. H., Fox, V. K., Gellert, R., Ghosh, A., Golombek, M. P., Grotzinger, J. P., Guinness, E. A., Herkenhoff, K. E., Jolliff, B. L., Knoll, A. H., Li, R., McLennan, S. M., Ming, D. W., Mittlefehldt, D. W., Moore, J. M., Morris, R. V., Murchie, S. L., Parker, T. J., Paulsen, G., Rice, J. W., Ruff, S. W., Smith, M. D., Wolff, M. J. "Ancient Aqueous Environments at Endeavor Crater, Mars," *Science* **343** (2014).

16. Ha, J.-S. "Effect of atmosphere type on gelcasting behavior of Al2O3 and evaluation of green strength," *Ceram. Int.* **26**, 251-254 (2000).

17. Xie, R., Zhang, D., Zhang, X., Zhou, K., Button, T. W. "Gelcasting of alumina ceramics with improved green strength," *Ceram. Int.* **38**, 6923-6926 (2012).

Appendix A Polymer Wettability Testing

Qualitative tests were performed to judge the contact angles of the polymers tested in Chapter 3 against simulant. The 2 main polymers tested were polysulfone (PSU) and polyetherketoneketone (PEKK).

About 1cm^2 of a single layer of beads is positioned on plagioclase feldspar and basalt substrates, polished to a mirror finish. The substrates are then placed inside a quartz tube furnace for a certain amount of time under nitrogen gas, heated to 350°C at a rate of 50°C/min. After the elapsed time, the furnace is turned off and the sample allowed to air cool.

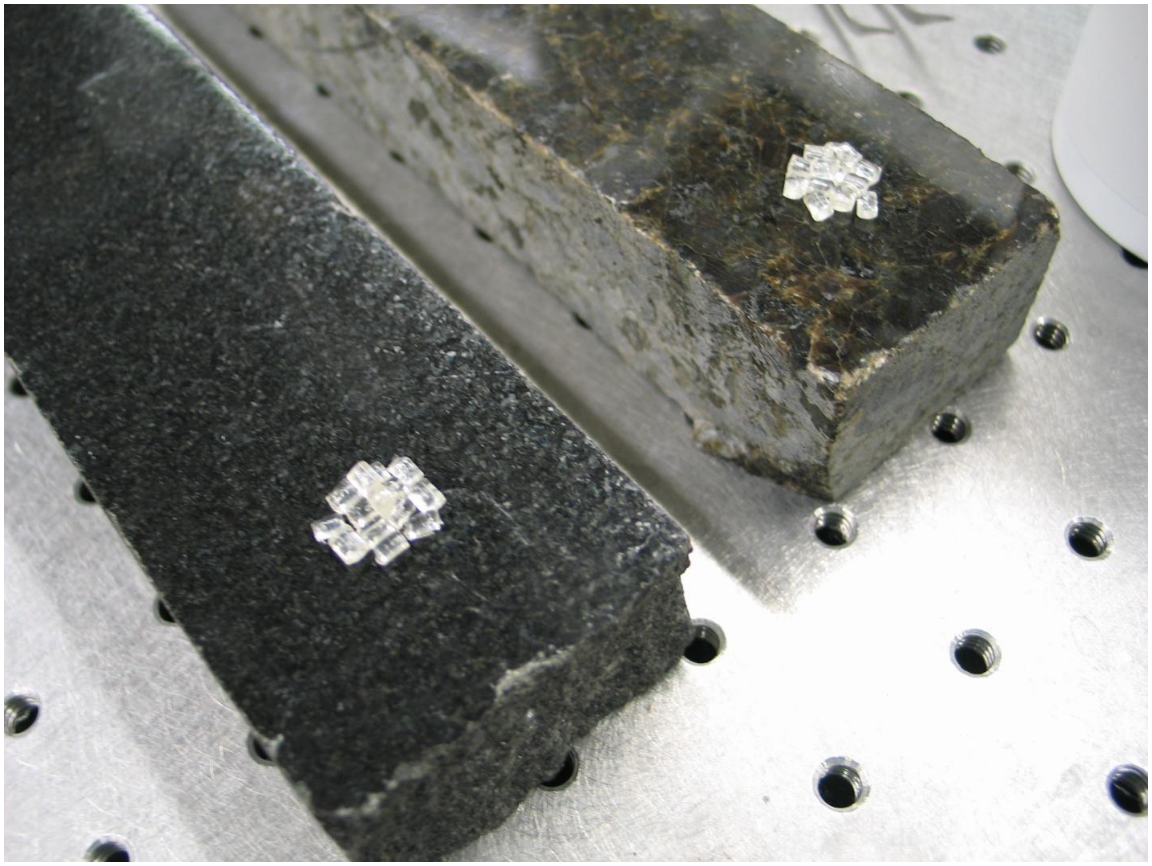

Figure A-1 Photo of Wettability Test 1. Samples of PSU positioned on substrates. Width of each substrate is 4cm.

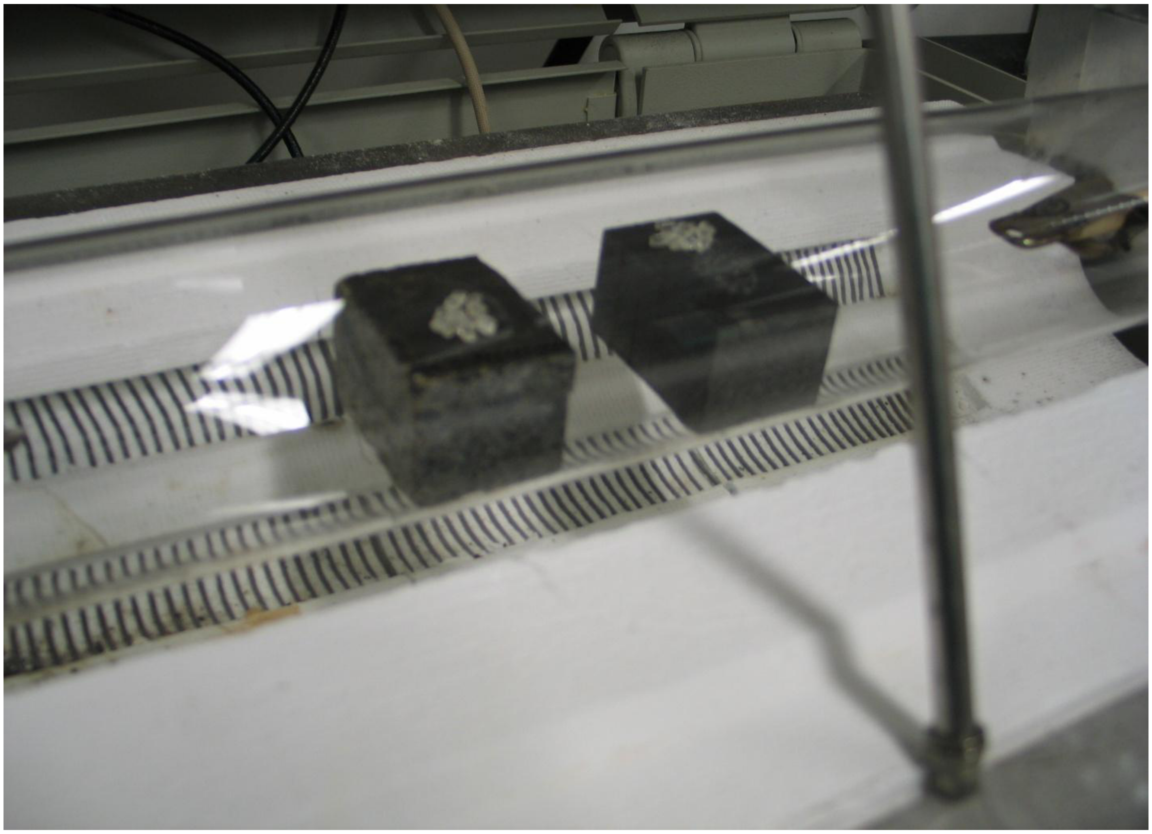

Figure A-2 Photo of Wettability Test 2. PSU samples positioned inside quartz tube furnace. Width of view is approximately 30cm.

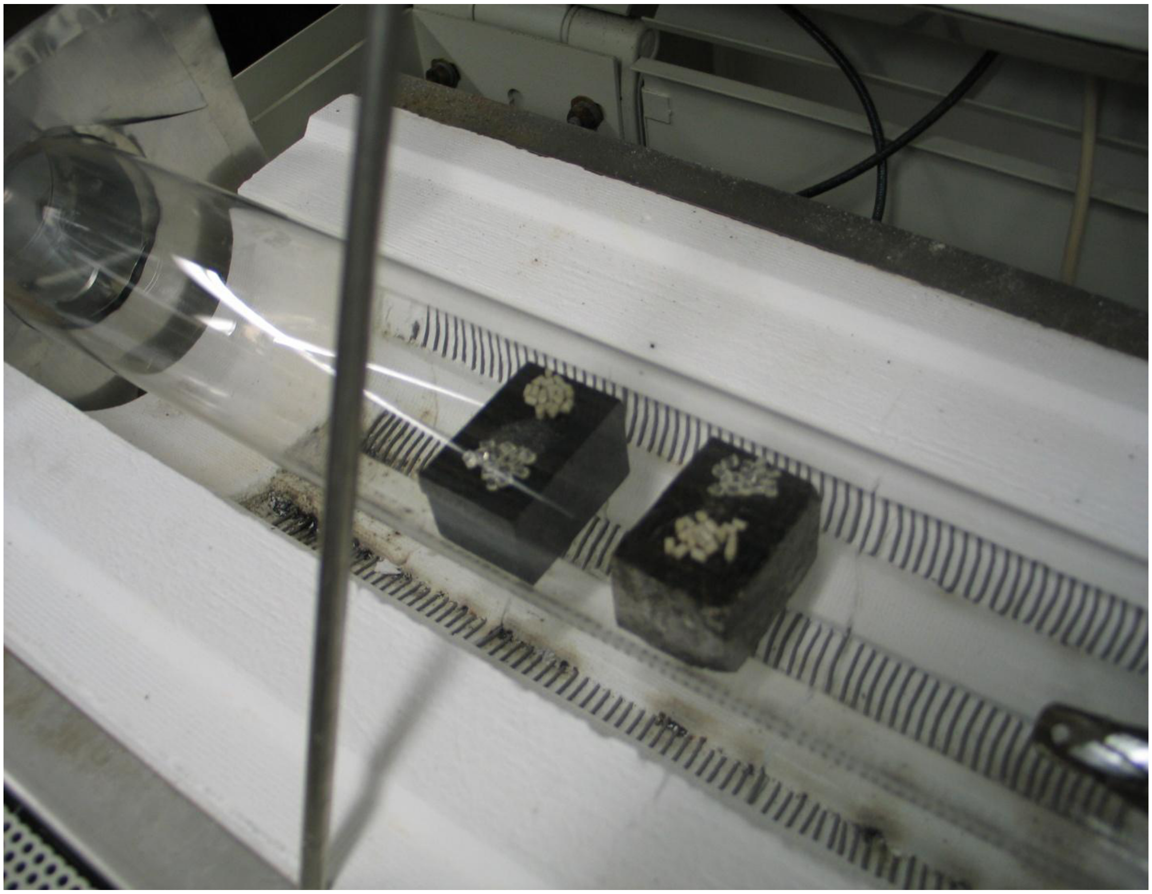

Figure A-3 Photo of Wettability Test 3. PEKK and PSU samples positioned inside quartz tube furnace. Width of view is approximately 40cm.

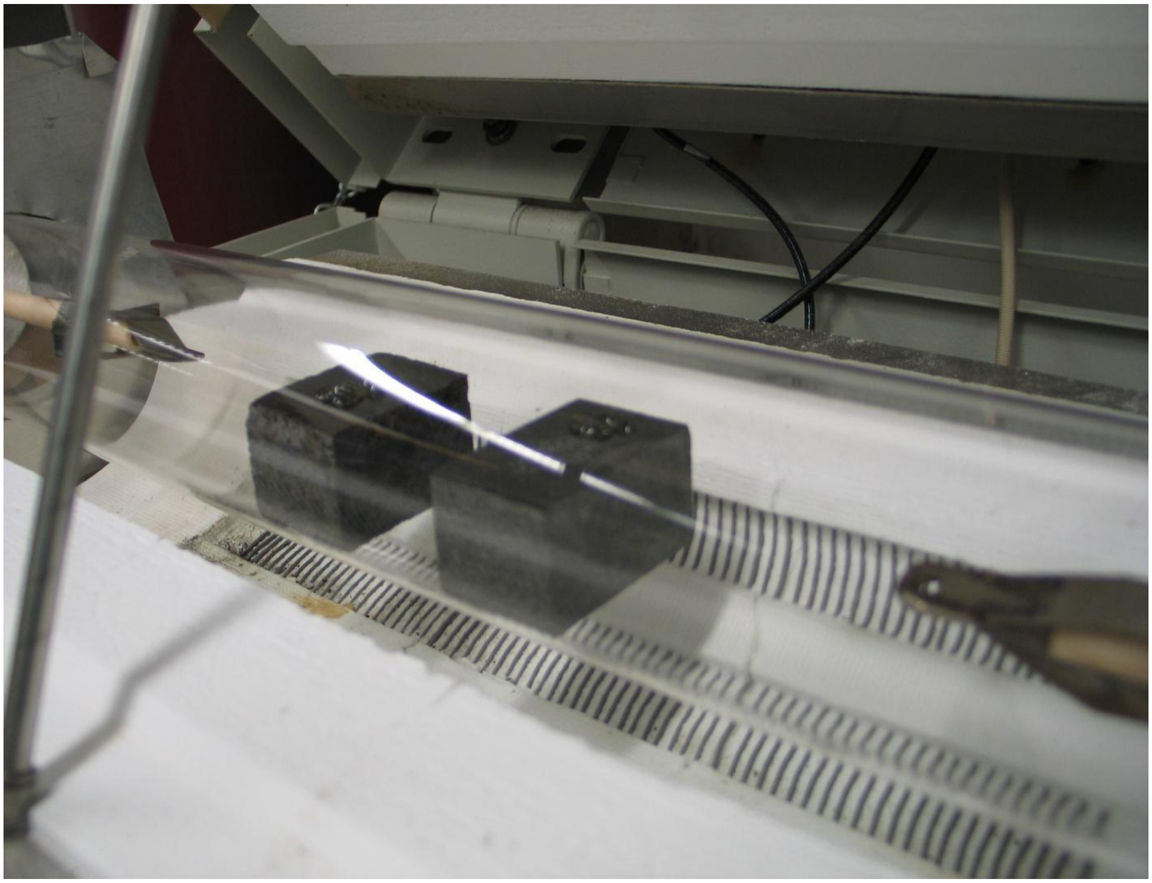

Figure A-4 Photo of Wettability Test 4. PSU samples after melting in quartz tube furnace. Width of view is approximately 40cm.

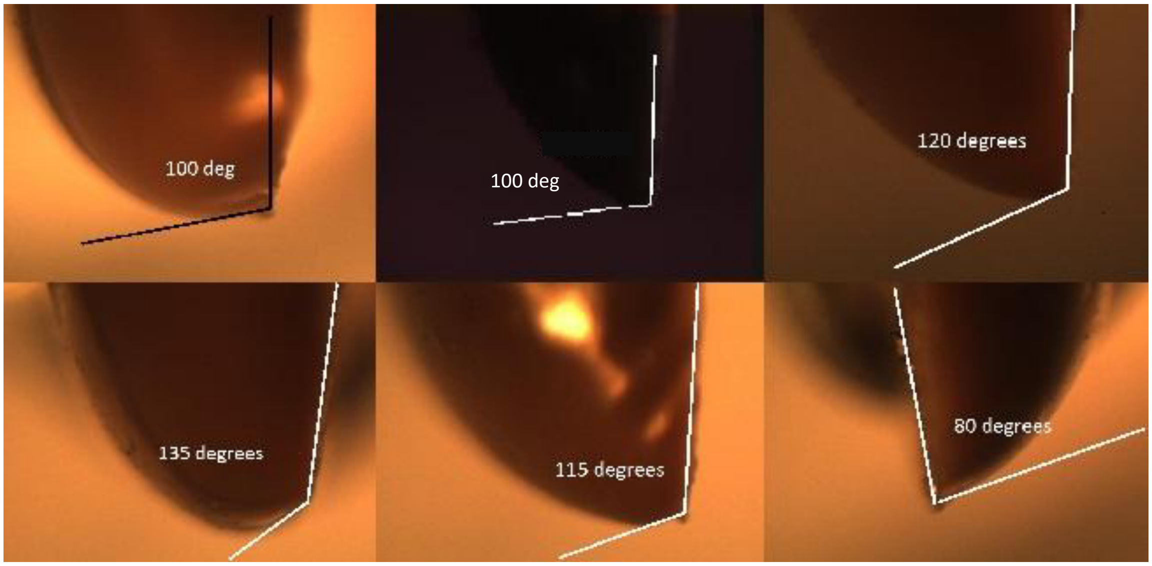

Figure A-5 Wetted Angles 1. Measured contact angles between PEKK and both substrates. Width of view in each panel is ~5mm.

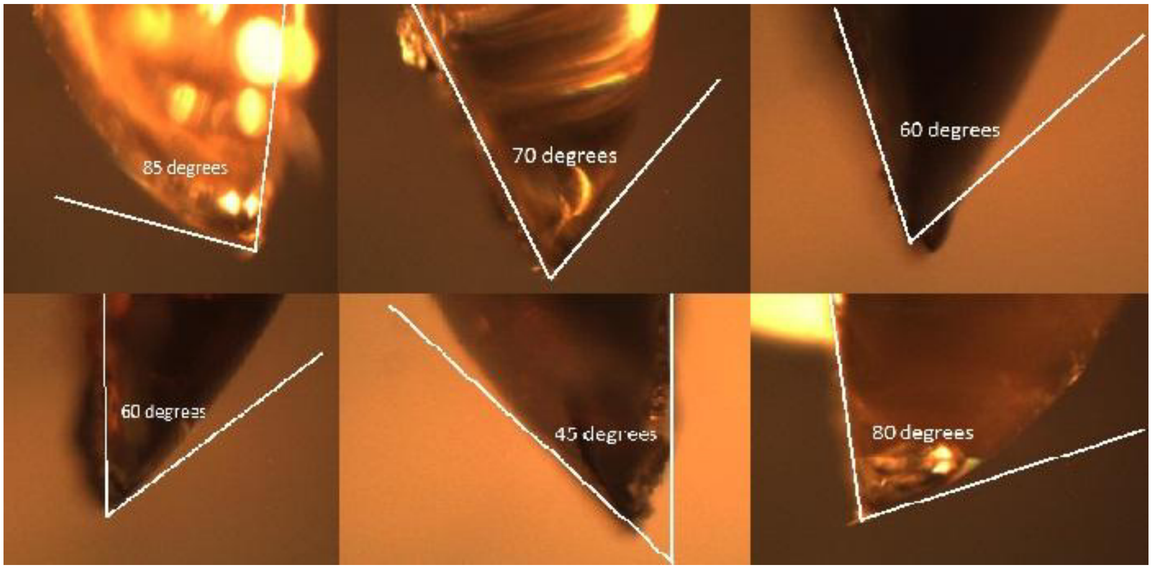

Figure A-6 Wetted Angles 2. Measured contact angles between PSU and plagioclase feldspar substrate. The darker colored samples have been oxidized (top right, bottom left, bottom center). Width of view in each panel is ~5mm.

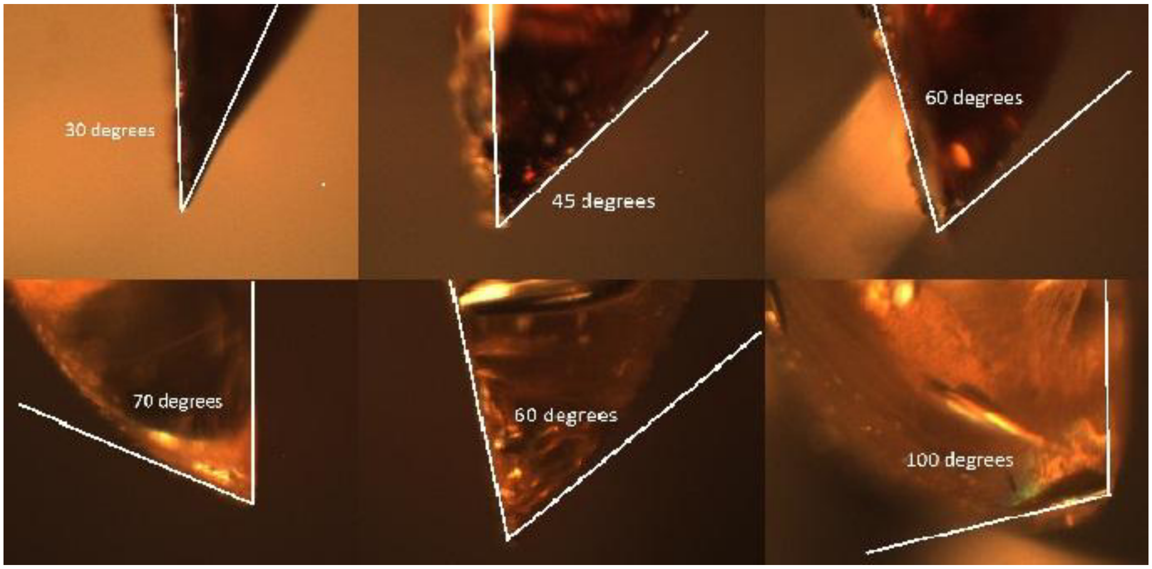

Figure A-7 Wetted Angles 3. Measured contact angles between PSU and basalt substrate. The darker colored samples have been oxidized (top row). Width of view in each panel is ~5mm.

As shown above, the Young-Laplace contact angles which do not exceed 90° are exhibited by both PSU and PEI samples. PES, PEEK, and PEKK all exceed 90° and thus exhibit phobia against heated basalt and plagioclase feldspar substrates. On average, we note

PEKK (all substrates' average): 108°
PSU-plagioclase, 1 hr elapsed furnace time (w/ signs of oxidation): 55°
PSU-plagioclase, 15 min elapsed furnace time (w/o signs of oxidation): 78°
PSU-basalt, 1 hr elapsed furnace time (w/ signs of oxidation): 45°
PSU-basalt, 15 min elapsed furnace time (w/o signs of oxidation): 77°

It is consistently noticed that a partially oxidized sample appears to show a decrease in the contact angle, since such effects on polymers would lower the secondary bonds (Van der Waals) forces between polymer molecules as chain scission occurs. At the same time, the presence of reacted oxygen would tend to form more strong dipoles in the pyrolytic by-products which would adhere locally to the local covalent bonds of the silicate, which itself has local dipoles despite being electrically neutral.

Experimentally, it has not been yet determined whether the amount of time under the 350°C temperature has any effect on the contact angle. Analogies with water drops, provided that the water does not evaporate, support the hypothesis that the contact angle is not a function of time, but the viscosity of the polymer at 350°C could play a role. The accidental leak of the quartz tube, by imperfect sealing, probably accounts for the low contact angles seen in Figure A-6 and A-7. Overall, the prevailing observation is that the polymers develop moderate phobia against silicate substrates under melting temperature. The test is conservative because large drops, which mechanically have lower tendency towards phobia than small drops, were tested.

Appendix B Elementary Analysis of Mars-1a

An elementary analysis was then performed using EDX (FEI/Phillips XL30) on Mars-1a simulant (Orbitec JSC Mars-1a), both before and after the TGA analysis (PerkinElmer Pyris 1 TGA). One sample from the in-situ polymerization investigation using 3wt% methyl methacrylate (MMA) content is included for reference. Results are shown in Table C-1. The analysis does not assume the presence of carbon contamination and it persists as a confounding variable from conclusions with this data.

Table B-1 Elementary Analysis of Mars-1a

Element	Pre-TGA at% Mars-1a only	Post-TGA at% Mars-1a only	Pre-TGA at% Mars-1a / 3wt% MMA adj.
C	21.06	-	19.15
O	62.27	70.57	62.28
Mg	0.81	0.62	1.30
Al	5.37	8.79	5.11
Si	6.45	13.46	7.25
Ca	0.57	0.93	0.71
Ti	0.55	0.71	0.89
Fe	2.57	4.92	2.65

Appendix C Flexural Strength of a Typical Reinforced Concrete Beam

We choose a typical example found in the introductory literature, such as Limbrunner and Aghayere [1]. Take the case of the design beam on p.44, in conformance with the American Concrete Institute standards. For reference, this beam is 508mm deep and 304.8mm wide with a single row of rebar located 444.5mm from the top surface. Assuming 27.58MPa as the compressive strength $f_c^{'}$of the unreinforced concrete we estimate the Young's modulus E as

$$E \approx 24.9GPa$$

For the steel,

$$E_s \approx 200GPa$$

with area

$$A_s = 2038.7mm^2$$

Let χ be the ratio of the Young's modulus of steel to that of concrete, for use in transformed sections. Defining y as the distance from the top surface down into the beam, the centroid is

$$\bar{y} = \frac{(154838mm^2 \times 254mm) + (14361mm^2 \times 445mm)}{169200mm^2} = 270.17mm$$

The moment of inertia for the beam is

$$I \approx 3.807 \times 10^9 mm^4$$

The ultimate moment in the example was calculated to be ~292kNm. Thus, an equivalent failure stress σ_f in a simple beam is

$$\sigma_f = \frac{292348Nm \times 0.23783m}{3.807 \times 10^{-3} m^4} = 18.2MPa$$

which can be regarded as the equivalent flexural strength of the reinforced beam.

If using only the Whitney stress block, one more directly estimates

$$\sigma_f = 0.85 f_c^{'} = 0.85 \times 27.58MPa = 23.4MPa$$

as the flexural strength of the beam. Although designs can vary considerably in equivalent strength, we shall assume 20MPa as a typical strength of a steel-reinforced concrete beam.

Appendix D Particle Size Distribution Analysis

The size distributions of Mars-1a and montmorillonite clay were determined by using a stack of sieves shaken mechanically. The divisions are outlined in Table D-1. It is not thought that the drying process at 350°C changes the Mars-1a particle size distribution from the as-ordered condition. On the other hand, since mechanical crushing inside of the steel dye and manual grinding are both known to increase the number of small particles, there is strong motivation to seek potential changes from the particle size distribution of the undisturbed sample to that of the crushed and manually ground samples. Manual grinding conventionally refers to use of the mortar and pestle.

The procedure began with sieving of the Mars-1a using a mechanical shaker. The different particle sizes were stored, with some chosen for experimentation. Those subject to experimentation were dried at 350°C overnight, compressed to 360MPa in a steel dye, cured at 230°C while still compressed inside the steel dye for 30min, and finally dry-cut.

A histogram of distribution of the overall particle sizes from Table D-1 for Mars-1a was compiled. Using a two-parameter Weibull distribution we minimize the sum of the errors raised to the power *n*, where *n = 40* for high sensitivity against large differences. Figure D-1 shows the calculated distribution for the two parameter Weibull curve describing the frequency of occurrence, PDF, as a function of particle size, *x*:

$$PDF(x) = \frac{\alpha x^{\alpha-1}}{\beta^{\alpha}} e^{\left(\frac{x}{\beta}\right)^{\alpha}}$$

where α and β be the shape and spread parameters, respectively. The result for the overall particle size distribution is then $\alpha = 1.28$ and $\beta = 249.61$ when the abscissa is plotted in units of μm, and the ordinate is plotted in units of wt%μm^{-1}. Table D-2 shows some results from calculation of average particle sizes over the size intervals defined by the mesh sieves.

The primary motivation for using a Weibull curve is due to its closely related application in characterizing the fracture of materials. As long one assumes the origin of soil particles as mechanical in nature, the Weibull curve should be able to describe the statistics of the particle sizes. On the other hand, the distribution derived by assuming constant strength as a function of size is the lognormal distribution. This is older knowledge in the literature, and the Weibull distribution appears to best fit the data.

Table D-1 Particle Size Distribution of Simulants

Size (µm) ↓	Mars-1a				Montmorillonite (80.2g)
	Trial 1 (40.0g)	Trial 2 (385.1g)	Trial 3 (370.3g)	Trial 4 (362.7g)	
> 560	7.0wt%	8.8wt%	8.6wt%	8.3wt%	0wt%
500 – 560	2.5wt%	3.0wt%	2.6wt%	2.8wt%	0wt%
112 – 500	60.0wt%	61.4wt%	60.6wt%	61.2wt%	3.6wt%
90 – 112	7.3wt%	6.5wt%	6.7wt%	6.8wt%	3.7wt%
53 – 90	11.5wt%	11.0wt%	10.8wt%	10.8wt%	16.6wt%
45 – 53	3.0wt%	2.4wt%	2.4wt%	2.4wt%	20.1wt%
25 – 45	5.3wt%	4.9wt%	5.0wt%	5.3wt%	54.1wt%
20 – 25	1.5wt%	1.1wt%	1.0wt%	0.7wt%	1.5wt%
< 20	1.8wt%	1.0wt%	1.9wt%	1.7wt%	0.4wt%

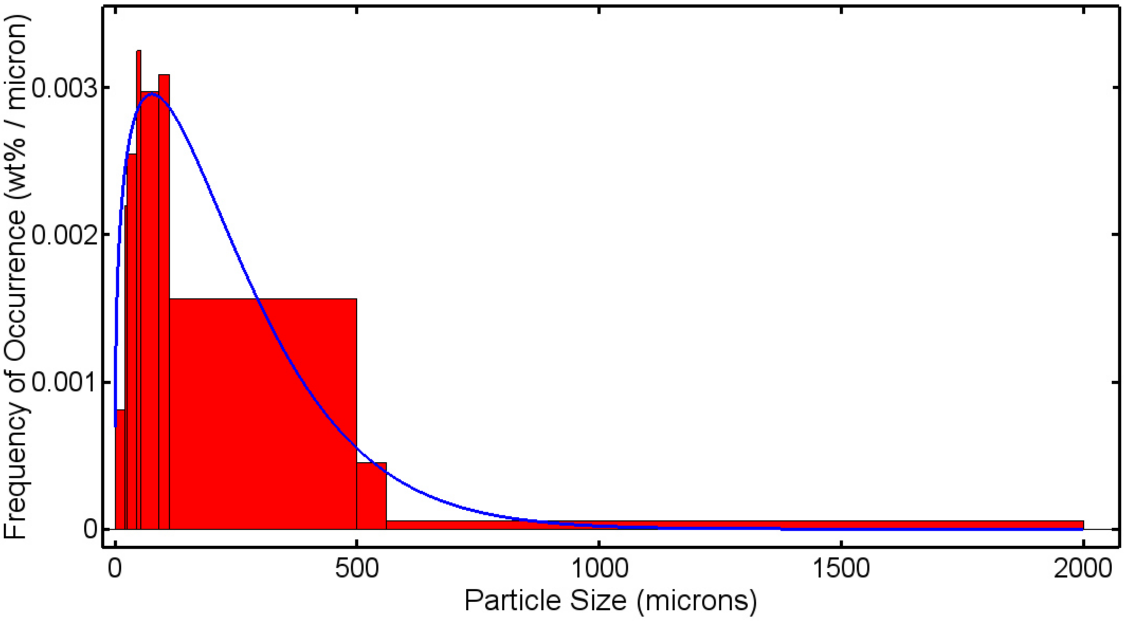

Figure D-1 Particle Histogram and Distribution. Particle size histogram of data, plotted with two-parameter Weibull distribution with $\alpha = 1.28$ and $\beta = 249.61$.

Table D-2 Particle Size Bins in Mars-1a

Size Range (μm)	0.2-20	20-25	25-45	45-53	53-90	90-112	112-500	500-560	560-2000
Average Occurence (10^{-3}wt%μm^{-1})	1.95	2.50	2.72	2.87	2.94	2.91	1.57	0.46	0.04
Average Size (μm)	8.30	22.42	34.29	48.80	64.21	101.78	292.28	529.09	902

Appendix E Flexural Strength of Silted Fines

A second method of sieving relied on the settling of a liquid suspension of particles. This has the advantage of separating out particles generally less than 2μm in size, and the sizes in suspension can extend towards well within the nanoscale regime (reported minima range from 20-200nm in spherical diameter). When the particle is small enough, it no longer silts out and remains indefinitely suspended by Brownian motion. The settling velocity is expressed as a function of particle diameter and viscosity *via* Stoke's equation. Flocculation is purposely avoided by selection of the dispersant liquid to maximize the zeta potential differential from the surface towards the free liquid.

Ethanol adequately settles a portion of Mars-1a, while still maintaining a particle supernatant suspension after 30min. For the same time scale, water is chosen as the fluid for settling the same fraction of montmorillonite (Sigma-Aldrich) clay. However, because montmorillonite is a smectite which has the capacity to swell and uptake water, persistent interlayer water hinders effective solid-solid bonding processes of the fines.

All suspensions were separating by means of distilling the liquid phase, leaving only the particles in the flask. The particles then were dried at 350°C in a quartz tube furnace under normal atmosphere, and compressed in steel dyes at 360MPa. The discs produced were then sectioned into beam-shaped coupons and tested in three-point bending. A list of strengths from uncured fines is shown in Table E-1.

After the low strengths exhibited by Samples 662–665 for montmorillonite, rinsing with 200ml of ethanol and 200ml of acetone was marginal at increasing the strength.

Crushed basalt and iron oxide powder were also processed using the same method of fluid settling and distillation. However, none of these developed high enough strength and disintegrated upon removal from the loading dye.

Table E-1 Mars-1a Fines Silted from Ethanol

Sample	Length (mm)	Width (mm)	Depth (mm)	Strength (MPa)
621	15.22	2.56	2.65	12.70
622		3.80	2.97	14.30
623	9.78	3.45	3.35	15.16
624		3.81	2.64	11.05
625	9.78	3.74	3.35	12.23
626	15.22	5.66	3.43	8.57
627	9.78	4.00	4.06	6.67
628	15.22	4.90	3.99	9.95
629	9.78	5.11	4.11	5.27
630	15.22	7.89	3.88	4.04
631 *		6.54	1.98	14.25
632 *		5.52	1.65	18.23
633		6.48	3.23	11.14
634		5.77	3.23	15.17
635 *		4.78	3.91	26.55
636 *		5.54	3.93	28.82

*Samples were cured at 230°C for 30min.

Appendix F Compressive Strengths and Density

Chapter 1 argued that flexural strengths were used as a proxy for most other measures of strength in ceramic materials, as well as certain physical properties. Nonetheless, compressive strengths and density of a limited number of samples were attempted on a number of occasions. Great difficulties and drawbacks beset the procedure for compression-forming an intact cylinder for compression testing. These samples were made by a different process with a rigid lateral boundary condition, entailing high wall friction and consuming much more material than a flexural test.

Compressive strengths were measured by compressing solid cylindrical samples between parallel test platens. Standard testing requires the cylinder height to be at least twice the diameter, but only a fraction of the samples achieved this geometry. Achieving the necessary aspect ratio is a loose motivation because the sample strength is sacrificed by the friction against the die wall for long, slender samples. Wax added to the die wall ameliorates some friction, but still resulted in binding of the sample, causing difficulty of release. The samples were made by a cylindrical split die, with matching pistons. In general, several lifts were required to achieve height-to-diameter ratios of roughly unity.

Density was measured by dividing the weight by sample volume. Archmedes' method doesn't apply because samples slake under water.

Diameter of cylinders was 12.7mm. The heights were variable and dependent on the compressibility of the soil particles and friction of the cell. Lubricant was used as a quick-release for the samples. Table F-1 and Figure F-1 summarize the results for compressive strength and density.

Table F-1 Some Compressive Strengths and Densities

Sample	S	CP (MPa)	IPS (μm)	h (mm)	d (mm)	W (g)	ρ (g/cm^3)	σ_c (MPa)
1176	M*	360	90-112	4.76	13.03	1.00	1.57	64.49
1177			53-90	9.53		2.36	1.85	15.31
1178			45-53	9.37		1.98	1.58	19.60
1179			25-45	7.80		1.53	1.47	27.18
1180			20-25	5.13		1.02	1.49	45.74
1181			<20	5.05	12.98	1.00	1.50	43.78
1215	Mars -1a	720	90-112	14.21	13.11	3.36	1.75	56.72
1216			53-90	11.16		2.53	1.68	54.91
1217			45-53	14.83	12.89	3.11	1.61	37.20
1218			25-45	15.38	13.12	3.35	1.61	21.52
1219			20-25	9.42	12.98	2.11	1.70	74.45
1220			<20	7.59	12.95	1.61	1.61	65.29
1238			90-112	6.48	12.98	1.49	1.73	34.20
1239			53-90	16.02	13.03	3.65	1.71	32.53
1240			45-53	5.97	13.04	1.36	1.71	65.77
1241			<20	5.30	12.97	1.22	1.74	116.11
1381		360	53-90	29.30	13.33	6.54	1.60	21.19
1382				30.04	13.11	6.62	1.63	24.05
1383			112-500	28.48	13.41	6.93	1.72	13.20
1384				32.94	13.21	7.99	1.77	9.70
1385			25-45	32.13	13.19	6.87	1.56	15.02
1386	M			33.57	13.21	6.41	1.39	21.25

* = montmorillonite

Abbreviations in top row: SN = sample number, S = simulant, CP = compression pressure, IPS = initial particle size, h = height, d = diameter, W = weight, ρ = density, σ_c = compressive strength.

Compression pressure was 360MPa, achieved in 3-4 lifts.

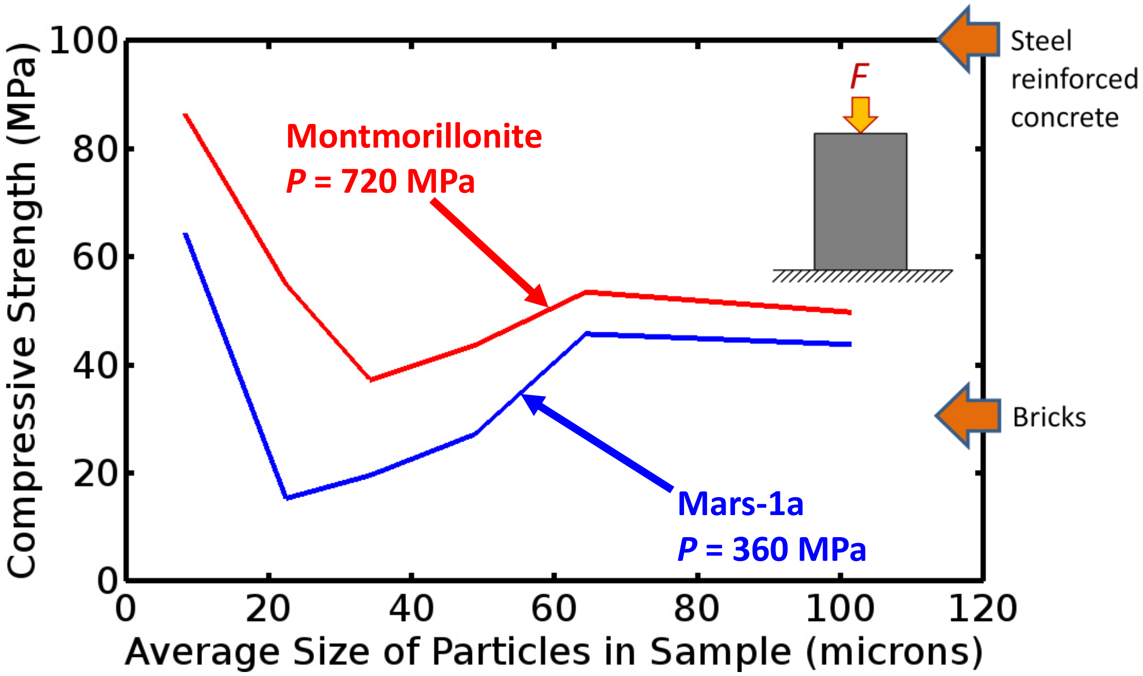

Figure F-1 Compressive Strengths. Plots are a function of particle size for two compression pressures (indicated as *P*) for both montmorillonite and Mars-1a. Compression pressures are indicated by the labels. Compression test schema shown at upper-right; reference materials shown at right.

Appendix G Compaction of CMS-1 Simulant

The same procedures for Mars-1a in §4.3 were adopted for a different simulant known as Ceralink CMS-1. The CMS-1 is found to have higher soluble content under a water distillation test. The precipitates form under increased temperature of water, leading one to suspect carbonates and sulfates, *inter alia*, as possible soluble species in CMS-1. The relevance of water is linked to the procedure of mixing the sample prior to compression.

Water processing was performed by adding a volume of water from a graduated cylinder to the sample in a mortar and pestle, and grinding the mixture to effectively disperse the water with the simulant particles. Hydrophilic wettability was generally observed to be greater in the Mars-1a than the CMS-1 simulant. In fact, before water tends to bead on the CMS-1 particles' surface for longer periods before eventually absorbing into the particle interstices.

Table G-1 Flexural Strength of Compressed CMS-1 Simulant

Sample	Processing Added Water Content (wt%)	Width (mm)	Depth (mm)	Length (mm)	Flexural Strength (MPa)
388	None	7.75	4.95	15.22	1.44
389		7.67	4.84		1.27
390		7.72	5.21		2.18
391		7.69	4.94		1.22
396	14.3	5.13	4.30		14.20
397		5.13	4.22	11.98	11.02
398	9.1	6.27	4.94	15.22	15.67
399		6.26	4.59		11.77

Compression pressure on pistons = 360MPa.
Pre-compaction drying temperature = 600°C.
Post-compaction curing temperature = 225°C.

Appendix H Long-Term Performance of Mars-1a

Mars-1a of the 53-90μm bin size is dried at 350°C for 12h. Disks are made immediately after drying by compressing them in a cylindrical die (*i.e.*, rigid lateral boundary condition), and left on a lab table for 6mo. Afterwards, the discs are made into beams and tested per the procedure in §4.3.1. Table H-1 shows the results upon exposure to ambient San Diego air (32.880°N, 117.233°W) between August 27th, 2014 and February 26th, 2015. The moisture cycles experienced at ambient do not affect the flexural strength of compacted Mars-1a.

Table H-1 Compacted Mars-1a Exposed to Ambient Conditions

Sample	Width (mm)	Height (mm)	Flexural Strength (MPa)
1242	6.24	1.91	8.12
1243	5.51	1.91	7.94
1244	5.27	1.32	8.70
1245	5.46	1.36	9.20
1246	5.86	1.80	5.13
1247	5.56	1.81	7.85
1248	5.93	1.87	8.73
1249	6.06	1.88	7.30

Compression pressure = 360MPa.
Initial particle size = 53-90μm.
Drying temperatures of particles before compression = 350°C.
Length between beam supports = 15.22mm.

Appendix I Other Simulants and Combinations Thereof

Both JSC Mars-1a and basalt fines are simulants of Martian soil. Neat basalt, however, cannot form bricks and can therefore be regarded as an “impurity” to the flexural strength as determined in §4.3.1.6.

Besides these two, there are many other possible simulants. Montmorillonite is tested in Chapter 5. Ceralink CMS-1 is tested in Appendix G. None of these include the evaporite salts, which can include carbonates and sulfates spread over wide regions of Mars.We test the salts magnesium sulfate and magnesium carbonate, and mix goethite simulant with basalt fines. Table I-1 and Figure I-1 and I-2, summarize the findings.

Other salts are present. We report a few miscellaneous findings for calcium carbonate and calcium sulfate dehydrate (gypsum). The former has very little flexural strength, ~1 MPa, when compressed quasi-statically with the rigid lateral boundary to 360MPa. Calcium sulfate dehydrate develops flexural strength comparable with coarse Mars-1a particles, ~6-9MPa, when processed identically.

Table I-1 Simulant Combinations

Sample	Simulant A ↓ (raw)	Simulant B ↓ (fines)	Length (mm)	Width (mm)	Depth (mm)	Flexural Strength (MPa)	
965	25wt% Gt*	Basalt	15.22	5.77	1.59	1.35	Avg 1.46
966	25wt% Gt*			6.19		1.56	
967	50wt% Gt*		9.78	4.33	1.42	2.55	
969	75wt% Gt*		15.22	6.06		2.93	Avg 3.01
970	75wt% Gt*			6.34		3.09	
971	100wt% Gt*	None	9.78	4.44	0.59	4.56	
981	25wt% MC*	Basalt	15.22	5.71	1.21	5.41	Avg 5.33
982	25wt% MC*			5.95	1.20	5.25	
983	50wt% MC*		9.78	5.07	1.17	11.29	Avg 11.43
984	50wt% MC*		15.22	6.27		11.57	
985	75wt% MC*			7.00	1.37	15.95	Avg 16.40
986	75wt% MC*			5.67	1.38	16.85	
987	100wt% MC*	None	9.78	7.08	1.55	13.76	Avg 17.44
988	100wt% MC*			6.34	1.55	21.12	
1000	25wt% MS*	Basalt	15.22	6.66	1.14	3.53	Avg 3.55
1001	25wt% MS*			5.48	1.15	3.56	
1002	50wt% MS*			5.51	1.10	8.73	Avg 8.37
1003	50wt% MS*			5.08	1.08	8.01	
1004	75wt% MS*			5.12	1.15	16.35	Avg 18.44
1005	75wt% MS*			4.78	1.12	20.52	
1006	100wt% MS*	None		5.52	1.18	39.36	Avg 33.05
1007	100wt% MS*			4.28	1.14	26.74	
1039	25wt% Gt*	Basalt		4.68	1.47	0.95	Avg 1.08
1040	25wt% Gt*			4.69	1.46	0.94	
1041	25wt% Gt*		9.78	5.05	1.38	1.22	
1042	25wt% Gt*			5.04	1.39	1.22	
1043	50wt% Gt*		15.22	5.14	1.40	1.77	Avg 1.61
1044	50wt% Gt*			4.87	1.40	1.46	
1045	50wt% Gt*			5.23	1.28	1.60	
1046	50wt% Gt*			5.22	1.25	1.60	
1047	75wt% Gt*			5.58	1.33	2.84	Avg 2.70
1048	75wt% Gt*			4.91		2.85	
1049	75wt% Gt*		9.78	5.91	1.15	2.20	
1050	75wt% Gt*			4.58	1.10	2.91	
1051	100wt% Gt*	None		3.78	0.98	3.43	

*Gt = goethite; MC = $MgCO_3$; MS = $MgSO_4$.
Compression pressure = 360MPa.

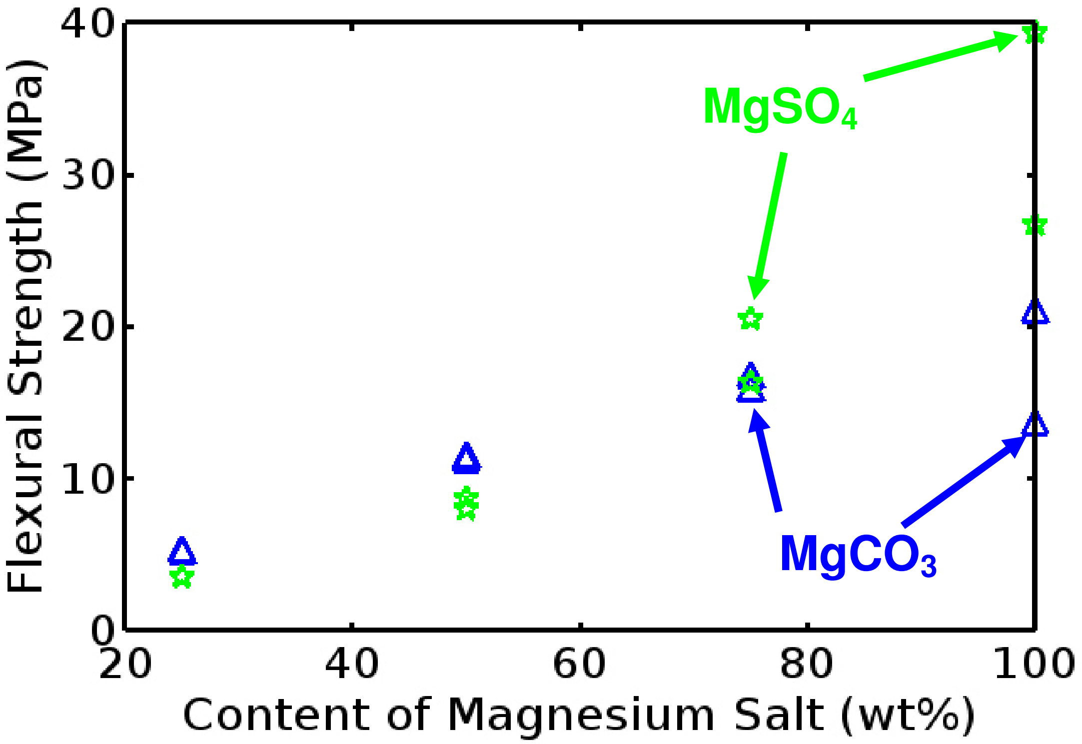

Figure I-1 Magnesium Salt Flexural Strength. Flexural strength of combinations of magnesium salts with basalt compressed quasi-statically to 360MPa with rigid lateral boundary.

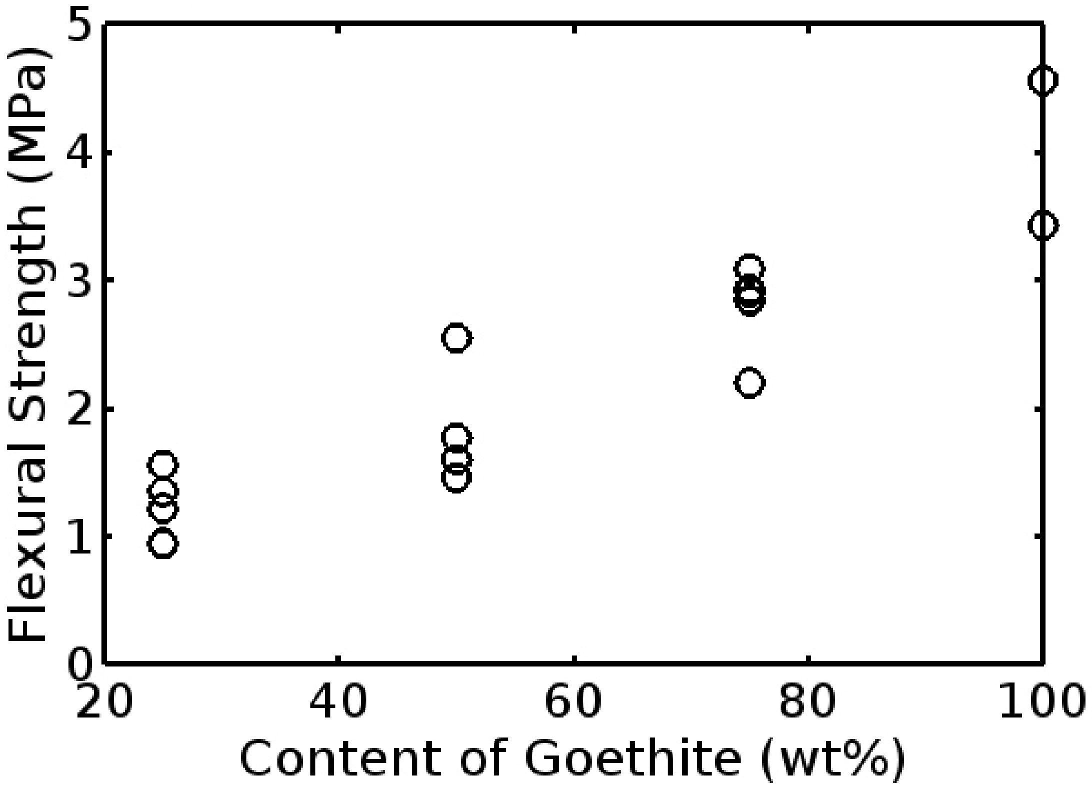

Figure I-2 Goethite Flexural Strength. Flexural strength of combinations of goethite with basalt compressed quasi-statically to 360MPa with rigid lateral boundary.

Appendix J Structure and Uses of Montmorillonite

J.1 Lamellar and Interlamellar Structure

Montmorillonite is a mineral belonging to the smectite group. Smectite minerals at the molecular level consist of stacked lamellae. Each lamella in turn consists of two tetrahedral silica sheets sandwiching a central octahedral silica-hydroxyl sheet [1]. There are about half a dozen common smectite clay minerals, whose identities are essentially determined by the elements inside of the tetrahedra and octahedra [2] [3]. In the case of montmorillonite, there is only silicon inside of the tetrahedra and aluminum inside the octahedral. Aluminum fills two out of every three possible octahedral sites in montmorillonite, and thus the term dioctahedral is sometimes used to describe its configuration [4]. The total thickness of a silica lamina unit is about 9.6Å [2] [3].

The lamina herein is considered to be a silica structural group. The most related minerals are talc and pyrophyllite, being related phyllosilicate minerals. In these minerals the hydroxyl groups–located interior of the silica layers—do not form interlamellar hydrogen bonds directly [3]. In montmorillonite, there is a charge imbalance from the substitution of magnesium in talc with aluminum, and this introduces cation affinity to restore charge balance [2]. Thus, the prevailing charge of the montmorillonite lamina is always negative on the exterior silica face [1]. The interior aluminum six-coordinated octahedra are positively charged, but this is more than offset by the greater negative charge of either silica four-coordinated tetrahedra sheet on adjacent sides [1]. The overall effect of the charge imbalance ultimately gives rise to cations and the presence of water, with hydrogen bonds associated with the interlamellar structure [1].

Each clay platelet is referred to as a “lamella” or “clay mineral layer.” Between clay mineral layers, the interlamellar structure of montmorillonite is largely dictated by the presence of cations which preserves electrical neutrality between lamellae. Stacks of lamellae constitute an apparent 'particle' of clay, with the number of lamellae in each particle stack between 3 to 10 [5]. The cations are present in the form of hydrated groups with water molecules. A number of different cation species can be absorbed. The most commonly discussed examples are Ca and Na cations, as they are naturally abundant, but pure water can also occupy the interstitial space and these are termed ‘hydrogen montmorillonites’ [1]. Depending on the adsorbed species, the interlamellar distance changes and thus influences the amount of swelling observed in the sample [1] [3].

Na and Mg hydrated cations cause a swelling in pure montmorillonite due to an increase in interlamellar spacing. In this case the water molecules take on a loosely-bound hexagonal position, when viewed from a 2-dimensional cross section of an interlamellar space, for up to three cation layers [3] [5]. Up to two layers can form for K and Ca, and the latter exhibits the peculiar property of decreasing the interlamellar space upon an increase of one to two adsorbed complexes. In open air, the number of interlamellar hydrates formed for a Na montmorillonite is determined by the relative humidity, where 20-40% indicates one layer of hydrate, 40-60% two layers, and greater than 60% three layers of hydrate [3] [5]. In water, the maximum number of hydrate layers possible for the particular cation is established.

Calcium hydrated complexes are more strongly bound and the complexes are restricted from movement. The other cation species, including Na, form relatively weaker bonds with water molecules. Research suggests that some of these water molecules lie outside the complexes and form their own hydrogen bonds, and these cations consequently may move freely [3] [5]. The result is a higher diffusion coefficient for Na montmorillonites, and higher compressive pressures for Ca montmorillonite required to drive out a given amount of interlamellar water [3] [5].

Interlamellar spacing of the montmorillonite varies between 15Å for monovalent cations to 15.2Å for divalent cations [3] [5]. The distance changes within one angstrom for multiple layers, except for Ca where is there is a contraction of about 1Å [3] [5].

Surface properties exterior to lamellar stacks influences macroscopic mechanical properties. The technique of aqueous suspension may be used to separate particles smaller than 2μm in diameter [2] [3]. The thicknesses of the particles are variable and indeterminate, since the plate diameter direction is dominant for fluid separation. The size ranges from 0.20-0.02μm when separating from an aqueous suspension [2] [3]. The size distribution, from related histograms on illite and bentonite, apparently follow a Rayleigh or Rayleigh-like distribution with a maximum located between 0.10 and 0.12μm [2] [3].The Rayleigh distribution is a particular case of a two-parameter Weibull distribution [6].

Interparticle bonds are influenced by hydrogen bonding due to interfacial water, valence bonds, Coulomb attraction by sorbed cations [3]. Per bond, the strongest bonds are the valence bonds and they arise due to true contact between particles beginning at a pressure of about 200MPa [3].

J.2 Overview of Compressed Earth Structural Materials

The discussion about the microstructure and aspects of water absorption in montmorillonite clay extends to the practical realm in structural engineering. By far, the predominant civil engineering focus is in geotechnical matters where volume changes influence the elevation profile of a foundation over long periods of time [7] [8]. Compaction is a means to improve foundations for buildings and infrastructure [8]. As reviewed in the Chapter 1, such compaction pressures (0.1–10MPa) are relatively low in the context of our current work. The literature review also shows a large amount of research into the mechanics and strength properties if motivated by geotechnical applications as well. Very often, only shear strength is assumed and not tensile strength.

For masonry applications, clay finds considerable use as well. The methods and processes for clay as a structural material—such as in a plate or block—are predominantly traditional. Clay is an important constituent for adobe, earthen structures, and fired brick masonry structures. Other civil applications of clays range from waste containers to catalysts and composites. Note that many traditional processes do not regard montmorillonite per se as distinct from the other clays.

J.2.1 Civil Structures

Civil structures made from clay have existed as a mainstay form of house construction since prehistoric times all over the world. The most prominent example of heritage clay technology in the United States exists in the form of adobe structures in the southwest by the Anasazi [9] and many other communities worldwide [10]. The modern equivalent is pressed-earth bricks using machines. Pressed bricks continue to be used in modern construction, most notably in the developing world [11]. Compressed-earth blocks arguably represent the most similar extant technology to the present work, albeit with some major differences.

The term 'adobe', which can be synonymous with mud or soil, most commonly refers to a sun-dried brick, composed of sand, silt, and clay. Often, these were reinforced with straw fibers to suppress catastrophic cracking upon drying. The clay particles mineral-wise are composed of a naturally-occurring combination of kaolinite, illite, smectites, chlorite. Size-wise, the clay includes fines of calcite, quartz, dolomite, feldspar, and gypsum.

Techniques for forming adobe structures were traditionally puddled or rammed-earth [9]. Adobe soils composed typically of 70% sand and 30% fines (silt and clay) are mixed with water to form slurry. In the puddling procedure, the slurry is composed of typically 80 wt% adobe soil and 20wt% water; the mixture may be cast into rectangular molds, or transported to the work site and plastered by hand [9]. Rammed earth structures were traditionally made from a wooden mold consisting of parallel plates and tamping of moist adobe soil containing 10 wt% moisture using rams. Once consolidated, the mold was repositioned to allow adjacent *in situ* work.

Modern technology presses adobe earth bricks directly from a mold, unlike their slip-cast ancient counterparts. In modern formulations about 4wt% asphalt emulsion is added to impart hydrophobicity [9]. Portland cement added in the 5-10wt% range or lime in the 10-20wt% range is also shown to stabilize against water resistance [9]. In all cases the bricks are still dried for several days in open sun. The water content in the moist soil is typically less than 10wt%, with some manufacturers using less than 6wt%.

Machines press adobe soil in molds to form bricks. Tiles are also offered by some manufacturers. Hydraulic or levers impart a pressure on the moist soil to consolidate bricks. An impressive array of different industrial machinery existed from the 1950s to the present, some of them manually operated for adaptation in the developing world [9]. Many of the brick-making machines are in the form of vehicular trailers for portability.

Analysis of the strength of the adobe bricks suggest that clay is an important strengthener, but does not account for all of the strength due to the presence of slightly water-soluble binders such as calcium carbonate. Structural materials using calcium carbonate binders, or *caliche*, all have well-known sedimentary petrological analogues. A mechanical test which presses adobe soil to 3.9MPa found compressive strengths of 7.3MPa, with a modulus of rupture of about 0.4MPa for a 9 x 25 x 36cm brick [9]. This is quite high, as the normal compressive strength of adobe is ~1MPa [10]. Another study measured a compressive strength of about 24MPa and a modulus of rupture of 1.7MPa for a 10 x 25 x 36cm brick containing 5wt% portland cement [9].

Rammed-earth structures have also found modern applications, having been used in a myriad of edifices ranging from commercial buildings to houses and barns. The process uses a similarly moist soil to produce entire walls with forms and tamps. Molds in the shape of a wall are used, commonly build from wood, steel, or aluminum. A relatively thin layer of adobe soil is added. For reference, in one case about 18cm of soil are added for a wall thickness of 41cm [9]. Repeated blows of a hammer ram the earth into shape by pressing the soil and working particles horizontally when the hammer strikes a different, adjacent location, causing densification. Ramming, or tamping, of the soil leads to a 25-30% reduction in volume from the original height when sufficiently compacted [9]. Once compacted, the mold is moved upwards (if necessary), and another layer of adobe soil is added directly on top of the compacted layer, and the process repeats. Tests show that the mechanical properties of rammed-earth are slightly lower than those of pressed bricks, with a compressive strength of up to 5.5MPa upon drying for several weeks [9]. The compressive strength increases with age beyond a few weeks, however, because of the relatively slower rate of drying in a single-piece wall.

A survey of different companies involved in the manufacture of either pressed brick or rammed earth structures shows that they use a particle size gradation of below 10wt% clay, 10wt% to 50wt% silt, and the balance sand [9]. The clay composition among brick makers is also highly variable, with no clear modes except a near-complete absence of chlorite clay and, on the average, a slight paucity of smectite compared to mixed illite/smectite, neat illite, or neat kaolinite [9].

Another major use of clay in civil structures is for conventional bricks. The technology of firing clay to high temperatures to strengthen it is also quite antique. Clay is mixed with a filler material (such feldspar and flint) in total proportion of ~50wt% [4] and mixed with water to the plastic limit. A brick can also be formed from 6-8wt% added water, and this is termed ‘dry’ pressing [4]. The filler acts to control volume changes and to lower the melting temperature during firing. Firing temperature is usually about 1000°C [4] [12]. Resultant flexural strengths of fired clay bricks is typically 6-14MPa [13]. The characteristic red color of firebrick comes from the formation of iron (III) oxide, which can actually assume a range of colors from orange to black depending on defect density [4].

J.2.2 Other Uses

Clay finds important uses in waste isolation due to its ability to seal. Engineered barriers made from smectite are used in both chemical and nuclear waste containment [3]. Chemical landfills have bottom and top layers comprising compacted smectite clay. Nuclear containers can feature dense clay blocks surrounding the waste container to serve as a mechanical and chemical buffer [14]. Calcium cation-containing smectite – in this case bentonite - clay is added to a small percentage of sodium carbonate to promote cation exchange and precipitate $CaCO_3$ as a binding agent [3]. No water is added and the mixture is compressed under a pressure of 50 to 150MPa [3] [14].

One of the oldest and most traditional applications of clay is in the form of pottery. Porcelain is produced from a combination of pure kaolin clay, quartz, and alkali feldspar fired to high temperatures [5]. Good mechanical properties are attributed to the presence of interlocking mullite grains formed from the firing process [5] [12].

Clays have been more recently applied to polymer nanocomposites, which forms a voluminous segment in the literature of nanocomposites. Melt processing with an easily melted binder such as PVC can be used [15]. Smectite clay, most often montmorillonite, is suspended in a solution with polar molecules, ions, and/or organophilic reagents [16] [17]. The intercalated species is either a polymer or a monomer that is later polymerized and exfoliates the sample [16]. The intercalation-exfoliation process can be done in a single step, achieving tensile strengths of 100MPa [18].

J.3 References

1. Grim, R. Clay Mineralogy (2nd ed). McGraw-Hill (1968).

2. Worall, W. Clays: Their Nature, Origin, and General Properties. Maclaren and Sons (1968).

3. Pusch, R., Yong, R. N. Microstructure of Smectite Clays and Engineering Performance. Taylor & Francis (2006).

4. Brownell, W. Structural Clay Products. Springer-Verlag (1976).

5. Velde, B. Introduction to Clay Minerals: Chemistry, Origins, Uses and Environmental Significance. Chapman & Hall (1992).

6. Ang, A. H.-S., Tang, W. H. Probability Concepts in Engineering. Wiley (2007).

7. Noorany, I., Stanley, J. V. "Settlement of Compacted Fills Caused by Wetting," in *Proc. Vertical and Horizontal Deformations of Foundations and Embankments, ASCE* **2**, College Station, TX (1994), pp. 1516-1530.

8. Das, B. Principles of Geotechnical Engineering (7th ed.). Cengage Learning (2010).

9. Smith, E. W., Austin, G. S. "Adobe, pressed-earth, and rammed-earth industries in New Mexico," Bulletin 127, Authority of State of New Mexico (1989).

10. Silveira, D., Varum, H., Costa, A., Martins, T., Pereira, H., Almeida, J. "Mechanical properties of adobe bricks in ancient constructions," *Constr. Build. Mat.* **28**, 36-44 (2012).

11. Chu, Y. "Five Innovative Materials for Sustainable Structural Engineering," *Mechanical Engineering: The Magazine of ASME,* 14-15 (August 2016).

12. Callister, W. D. J. Materials Science and Engineering: An Introduction. Wiley (2003).

13. Plummer, H. G., Reardon, L. J. Principles of Brick Engineering: Handbook of Design. Structural Clay Products Institute (1939).

14. Johannesson, L.-E., Borgesson, L. "Compaction of bentonite blocks," Swedish Nuclear Fuel and Waste Management Co. (1998).

15. Kalendova, A., Zykova, J., Kovarova, L., Slouf, M., Gerard, J. F. "The Effect of processing on the PVC/Clay Nanocomposites Structure," in *CP1255, Vth International Conference on Times of Polymers (TOP) and Composites* (2010).

16. Annabi-Bergaya, F. "Layered clay minerals. Basic research and innovative composite applications," *Micro. Meso. Mat.* **107**, 141-148 (2008).

17. Uddin, F. "Clays, Nanoclays, and Montmorillonite Minerals," *Metall. Mat. Trans. A* **39A**, 2804-2814 (2008).

Appendix K Alternate Clay Minerals

The literature reviews from Chapter 1 and Chapter 6 reveal that many clay minerals exist on Mars, as they do on Earth. Prominent clay minerals well-known to the geotechnical and geological disciplines are kaolinites and illites. We also include nontronite and saponite as other clays in testing.

K.1 Variety of Clays

The selection of Australian nontronite (Clay Minerals Society NAu-1), montmorillonite (Sigma-Aldrich), kaolinite (Sigma-Aldrich), saponite, and mixed illite-smectite were dried and compacted into solids.

Raw saponite occurs in dark-brown inclusions from an eroded hillside outcrop near the Hollywood Bowl in Los Angeles, CA (34.114°N, 118.337°W). The mineral is soapy to the touch, hence the name. Mixed illite-smectite occurs openly exposed around fluvial channels on the UC San Diego campus (32.878°N, 117.232°W). Localities are determined using the website mindat.org.

All clays were sieved, dried to 350-500°C, compacted quasi-statically with the rigid lateral boundary condition, and tested in 3-point bending.

Flexural strengths are listed in Table K-1 and plotted as a function of average initial particle size in Figure K-1.

Table K-1 Flexural Strengths of Various Compacted Clays

Sample	Clay Mineral	DT (°C)	IPS (μm)	CP (MPa)	b (mm)	d (mm)	L (mm)	FS (MPa)
732	NAu-1	350	25–45	360	4.59	1.22	15.22	4.04
733					4.37	1.23		3.80
734					4.35	1.05		4.76
735					4.54	1.05		4.11
736					4.08	1.07		3.42
737					4.31	1.07		3.70
738					4.13	0.72		4.27
739					4.21	0.70		5.53
740	Kaolinite				4.54	0.73		7.55
741					4.16	0.71		8.71
742					4.25	0.97		8.56
743					4.03	0.97		7.23
744					4.39	0.74		8.55
745					4.74	0.74		7.92
746					4.56	1.11		6.10
747					4.21	1.08		6.04
748	NAu-1		53–90		4.94	2.43		2.50
749					4.85	2.41		1.38
750					4.94	2.47		2.09
751					4.61	2.47		2.98
752					4.59	2.58		2.76
753					4.12	2.56		1.78
754					5.19	2.60		2.21
755					4.38	2.60		2.75
756	Kaolinite				4.71	1.24		4.73
757					4.50	1.25		4.87
758					5.24	1.15		5.60
759					5.11	1.15		5.74
760					4.54	1.18		6.14
761					4.52	1.14		3.89
762					4.81	1.56		5.07
763					4.11	1.57		5.18
768	M	500	25–45		4.68	1.35		4.55
769					4.58	1.33		4.79
770	NAu-1	350	20–25		4.43	1.48		4.94
771					4.28	1.47		4.44
772					4.44	1.15		4.67

Table K-1 Flexural Strengths of Various Compacted Clays (continued)

773	NAu-1	350	20-25	360	4.07	1.15	15.22	5.09
774					4.41	1.50		6.67
775					4.20	1.50		5.56
776					4.91	1.48		5.09
777					4.43	1.47		3.58
778	Kaolinite				5.04	0.83	9.78	5.20
779					4.51	0.83	15.22	5.14
780					4.17	0.99	9.78	7.54
781					4.17	0.99	15.22	6.70
782					4.79	1.38		6.17
783					4.36	1.39		5.96
784					4.49	1.38		6.14
785					4.69	1.38		5.88
790	M	500	45–53		5.06	1.75		1.92
791					4.61	1.80		1.83
792					4.16	1.80		1.52
793	NAu-1				4.73	1.56		0.99
794					4.44	1.60	9.78	1.55
795					5.36	1.61		1.16
796	Kaolinite				6.19	1.39		0.61
797					5.02	1.46	15.22	2.13
798					4.50	1.46		1.19
799	M		25-45		4.89	1.49		2.10
800					4.61	1.49		1.56
801					6.94	1.68	9.78	3.15
802					5.36	1.49	15.22	2.69
803					4.78	1.50		2.55
804					5.02	1.85		1.99
805					4.80	1.83		2.27
806	NAu-1				5.01	2.10		1.24
807					5.13	2.11		1.30
808					4.00	1.46	9.78	0.86
809					4.84	1.31		1.06
810					1.51	1.39	15.22	0.78
811	Kaolinite				4.69	1.26	9.78	1.18
812					5.06	1.67		0.42
813					1.24	1.67	15.22	0.77
814	M	350		90	4.71	2.35		0.98
815					4.47	2.36		0.96

Table K-1 Flexural Strengths of Various Compacted Clays (continued)

816	M	350	25-45	180	4.65	1.82	15.22	2.86
817					4.69	1.79		2.61
818				270	5.30	1.43		4.42
819					4.73	1.42		4.45
820				360	5.52	1.54		8.25
821					4.93	1.51		6.26

Abbreviations in the top row are as follows: DT = drying temperature, IPS = initial particle size, CP = compression pressure, b = beam width, d = beam depth or thickness,
L = length between beam supports, FS = flexural strength.
Abbreviations for clay minerals are as follows: NAu-1 = Australian nontronite,
M = montmorillonite.
Note: Clays found in the natural environment are referred to by their catalog name, or if procured by field trip, are referred to by name and location.
* Compacted with the free lateral boundary condition.

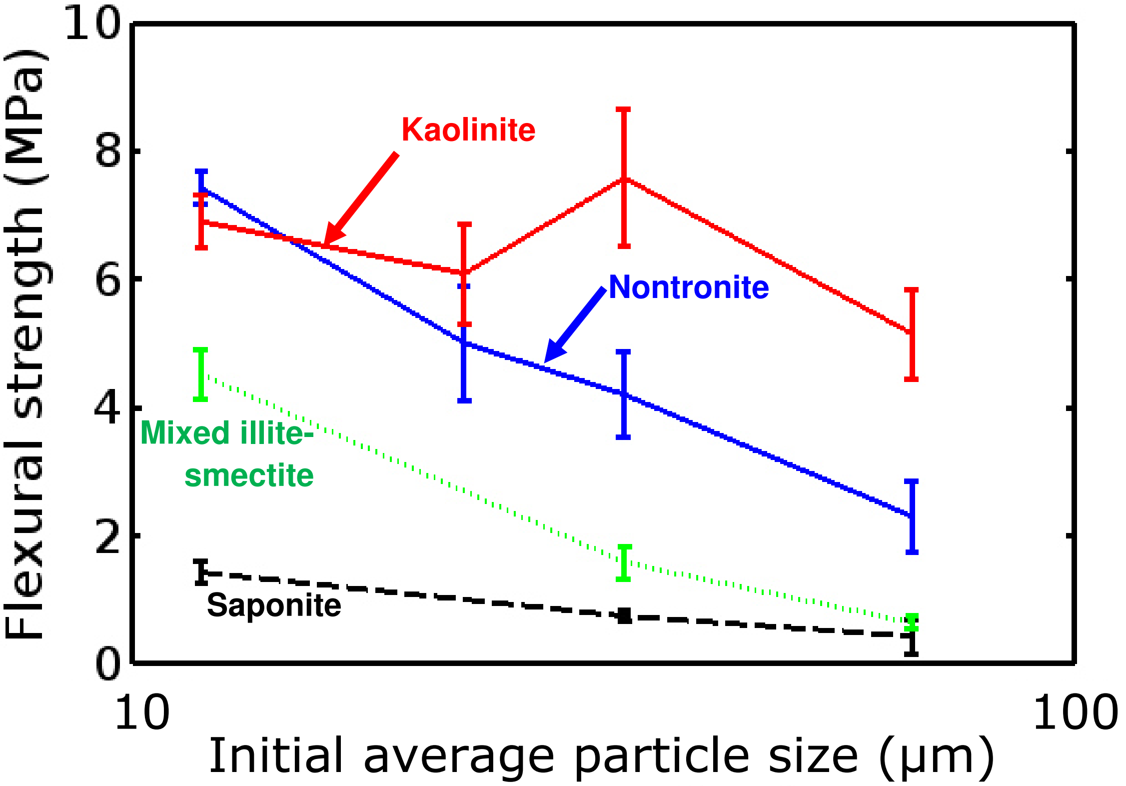

Figure K-1 Other Clay Minerals' Flexural Strength. Flexural strength as function of initial particle size for alternative clay samples dried to 350°C for 12h and compressed under 360MPa pressure.

K.2 Miscellaneous Samples of Kaolinite

For Samples 1315-1322, compaction employed the rigid lateral boundary condition: loose particles are placed inside of a 19.05mm-diameter bore and a matching piston is compressed against the particles. The resulting disc is most often cut into two flexure specimens and tested in 3-point bending.

Samples 1335-1349 are assigned to higher forming pressure with the free lateral boundary condition. Loose particles are placed on a flat surface. Then, a guided 8.71mm-diameter piston impinges the loose pile at 1000MPa. The resulting disc is sanded into a flexure specimen and tested in 3-point bending.

Table K-2 Miscellaneous Kaolinite Flexural Strengths

Sample	Compression Pressure (MPa)	Length (mm)	Width (mm)	Depth (mm)	Flexural Strength (MPa)	Average Strength (MPa)
1315	360	15.22	4.86	0.62	1.83	1.48
1316			4.74	0.62	1.63	
1317		9.78	4.63	1.11	1.31	
1318			4.72	1.05	2.37	
1319		15.22	4.83	0.81	1.51	
1320		9.78	4.81	0.82	1.32	
1321		15.22	5.07	0.93	0.99	
1322			4.85	0.92	0.89	
1335	1000	4.99	3.58	0.26	4.70	8.12
1336			4.24	0.40	11.92	
1337			3.87	0.32	6.61	
1338			2.71	0.24	3.84	
1347			3.96	0.20	8.03	
1348			4.39	0.28	10.66	
1349			3.79	0.25	11.06	

Initial bin size = 25-45μm.

Drying temperature of particles prior to compression = 500°C.

K.3 Miscellaneous Combinations

Figures K-2 through K-4 graph flexural strengths of miscellaneous combinations of clay minerals. These are montmorillonite mixed with basalt, nontronite with saponite, and kaolinite with montmorillonite, respectively. Experimental parameters are indicated in the captions. In Figure K-4, the 1000MPa data was achieved using the same free lateral boundary condition procedure as the one in §K.2. The data for this section is not serialized.

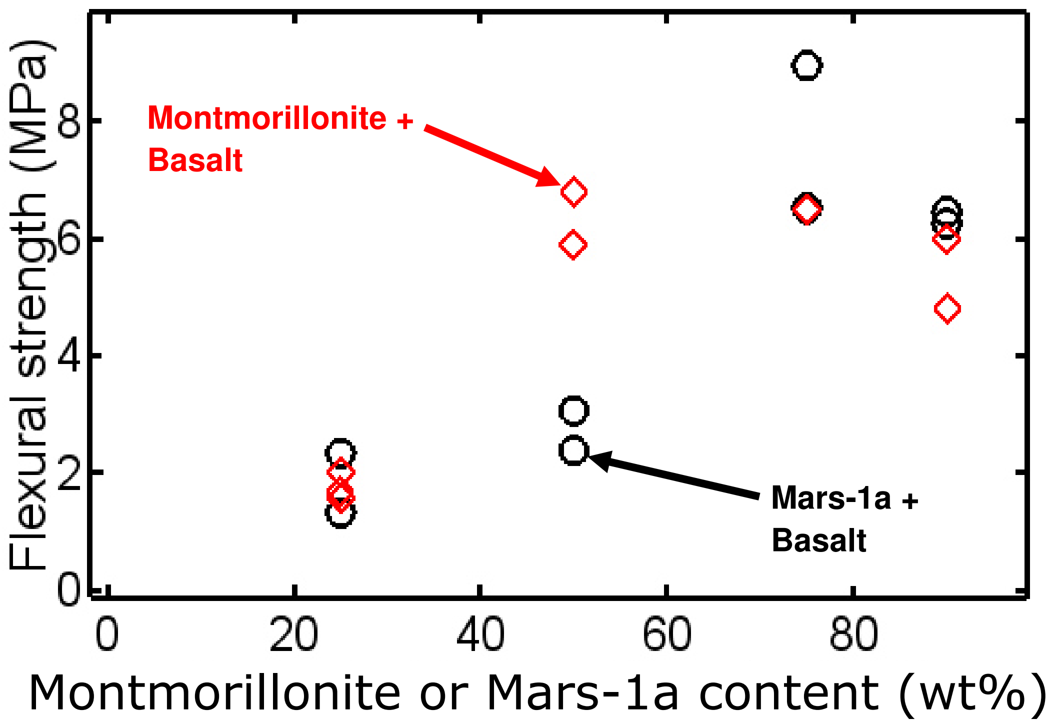

Figure K-2 Basalt Mixtures' Flexural Strength. Data scattergram of the flexural strengths of montmorillonite mixed with basalt. Initial particle size is 25-45μm. Drying temperature for particles prior to compression is 350°C. Compression pressure is 360MPa. Data shown for Mars-1a mixed with basalt is included for reference.

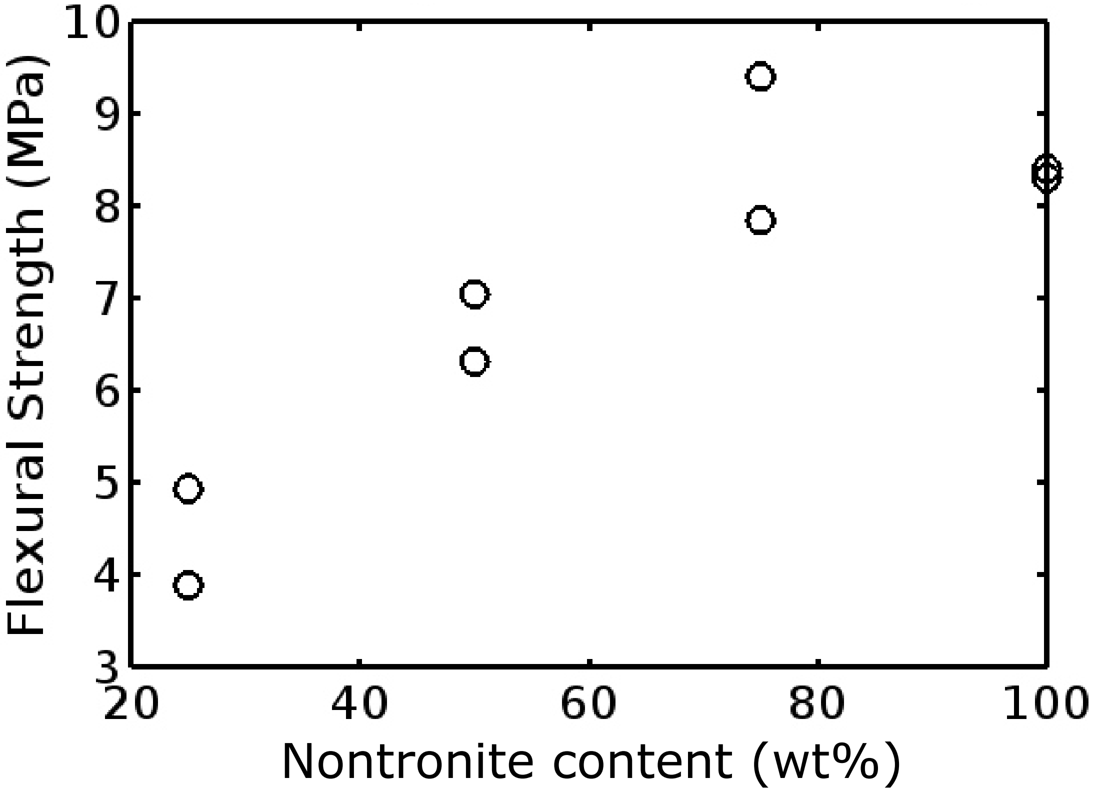

Figure K-3 Nontronite/Saponite Flexural Strength. Flexural strengths of nontronite mixed with saponite. Initial particle size is 20-25µm. Particles were dried to 350°C prior to compression forming. Compression pressure was 360MPa. Each point represents a single experimental datum.

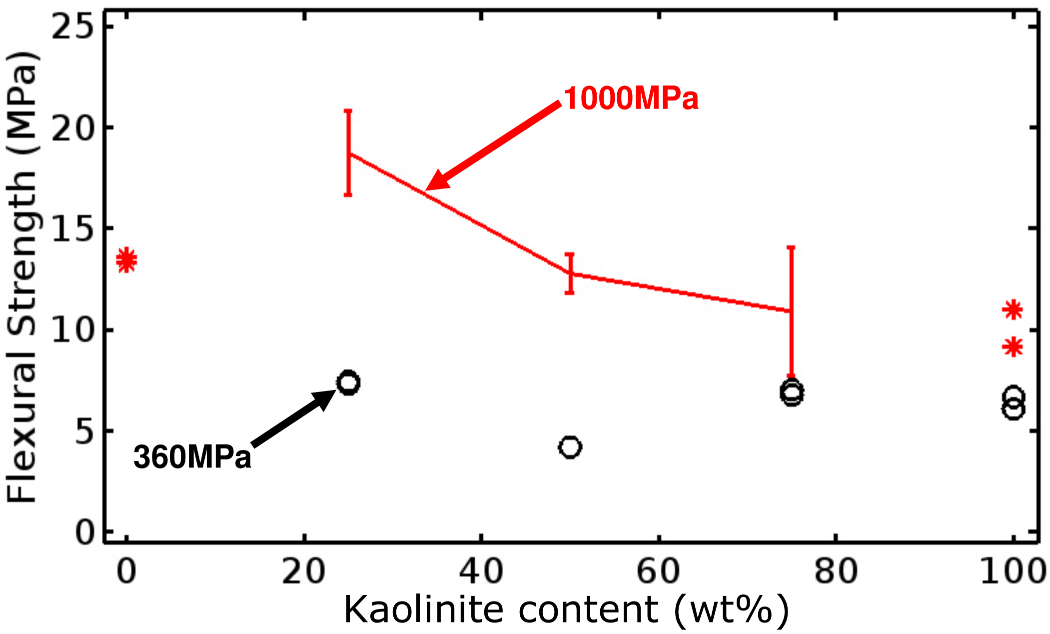

Figure K-4 Kaolinite/Montmorillonite Flexural Strength. Flexural strengths of montmorillonite and kaolinite mixtures compressed to a pressure of 360MPa (in circles) and 1000MPa (asterisks and error bars). Initial particle size is 20-25μm for the 360MPa data and 25-45μm for 1000MPa data. Particles were dried to 350°C prior to compressing at 360MPa, and 600°C prior to compressing at 1000MPa. Each point represents a single experimental datum; error bars represent one standard deviation.

Appendix L SEM of Fracture Surface of Mars-1a/NaPC Hybrid

Bound sodium perchlorate salt (NaPC) in Mars-1a was characterized on fracture surfaces of Samples 299, 301, 303, and 305 in ascending order of salt content.

In general, the shape of the Mars-1a simulant particles show the same morphology characteristics as previously seen in other Mars-1a IOHs at low binder contents. It is difficult to distinguish the salt binder from the rest of the simulant. While elementary analysis is usually undertaken to distinguish the salt phase from the simulant phases, there is little motivation to do so in light of the relatively low mechanical strengths and resource scarcity for sodium perchlorate salt as a building material.

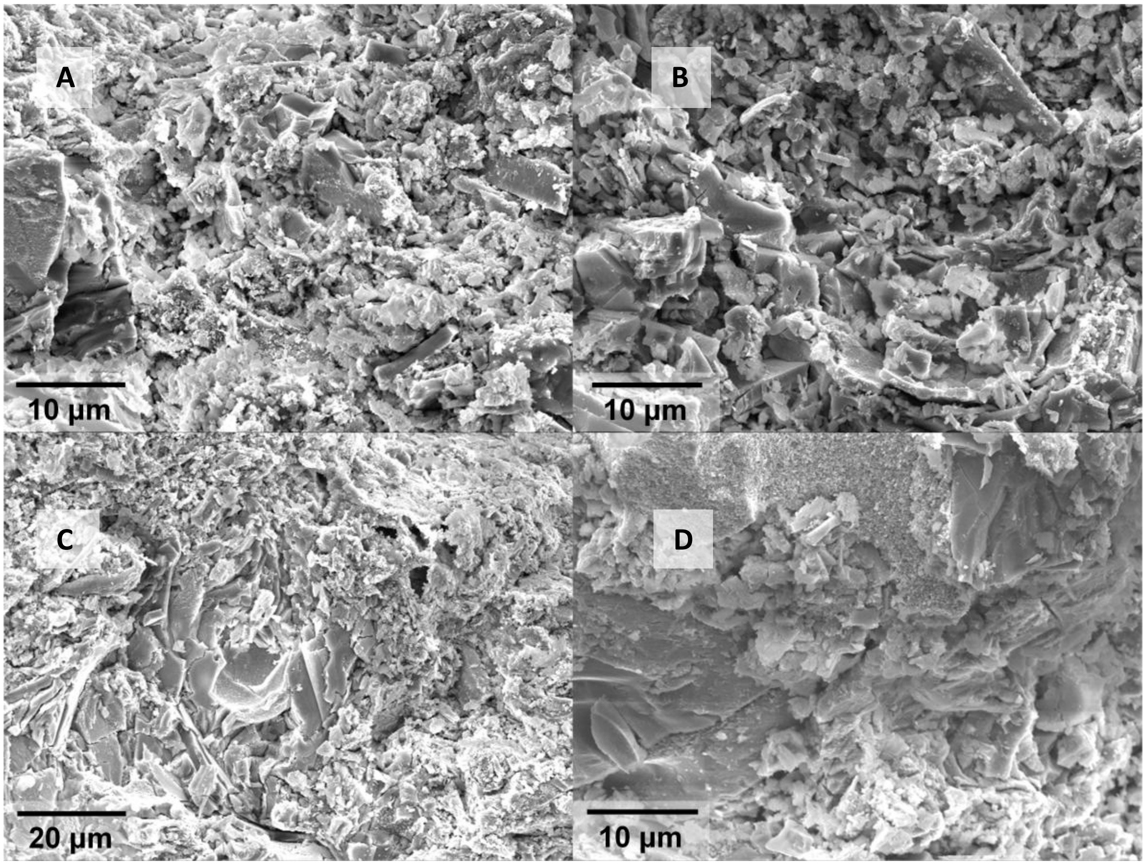

Figure L-1 SEM of 6wt% NaPC/Mars-1a. SEM micrographs of Sample 299 post-test fracture surface. This sample was a 6wt% NaPC-Mars-1a hybrid quasi-statically compressed to 270MPa inside a rigid lateral boundary.

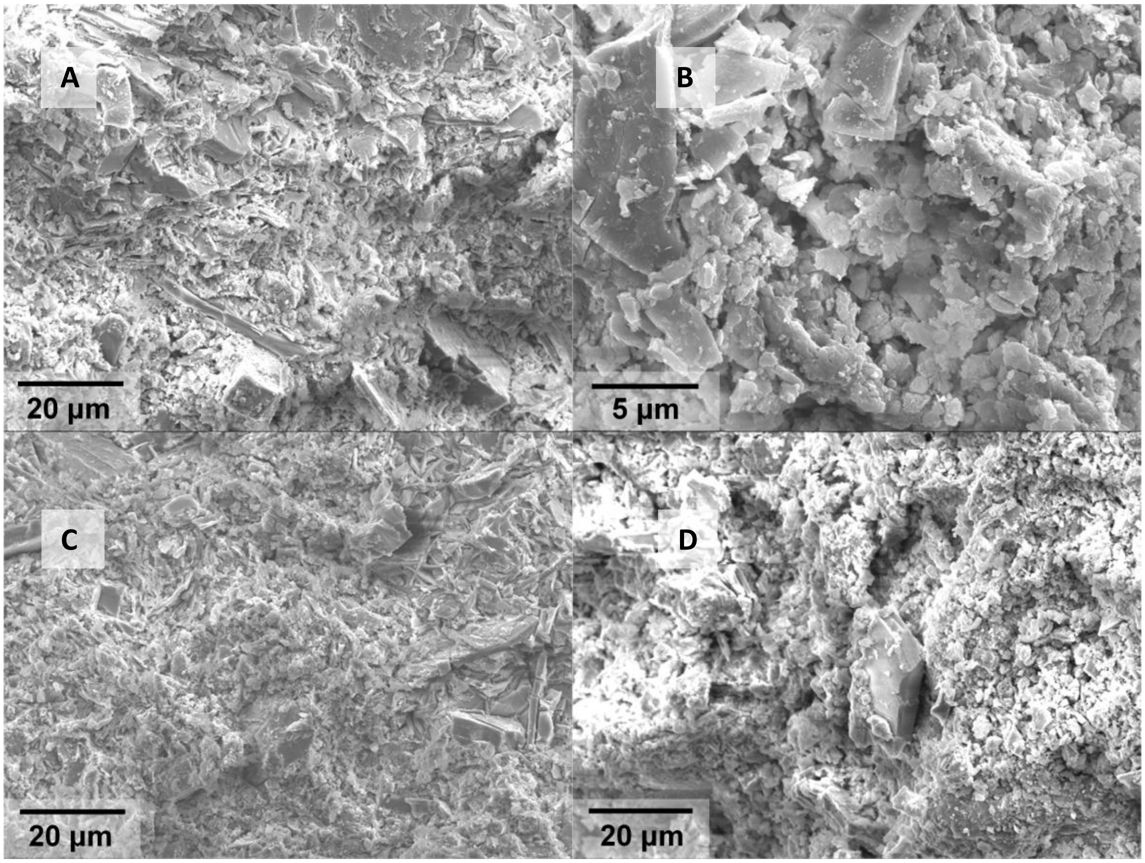

Figure L-2 SEM of 10wt% NaPC/Mars-1a. SEM micrographs of Sample 301 post-test fracture surface. This sample was a 10wt% NaPC-Mars-1a hybrid quasi-statically compressed to 270MPa inside a rigid lateral boundary.

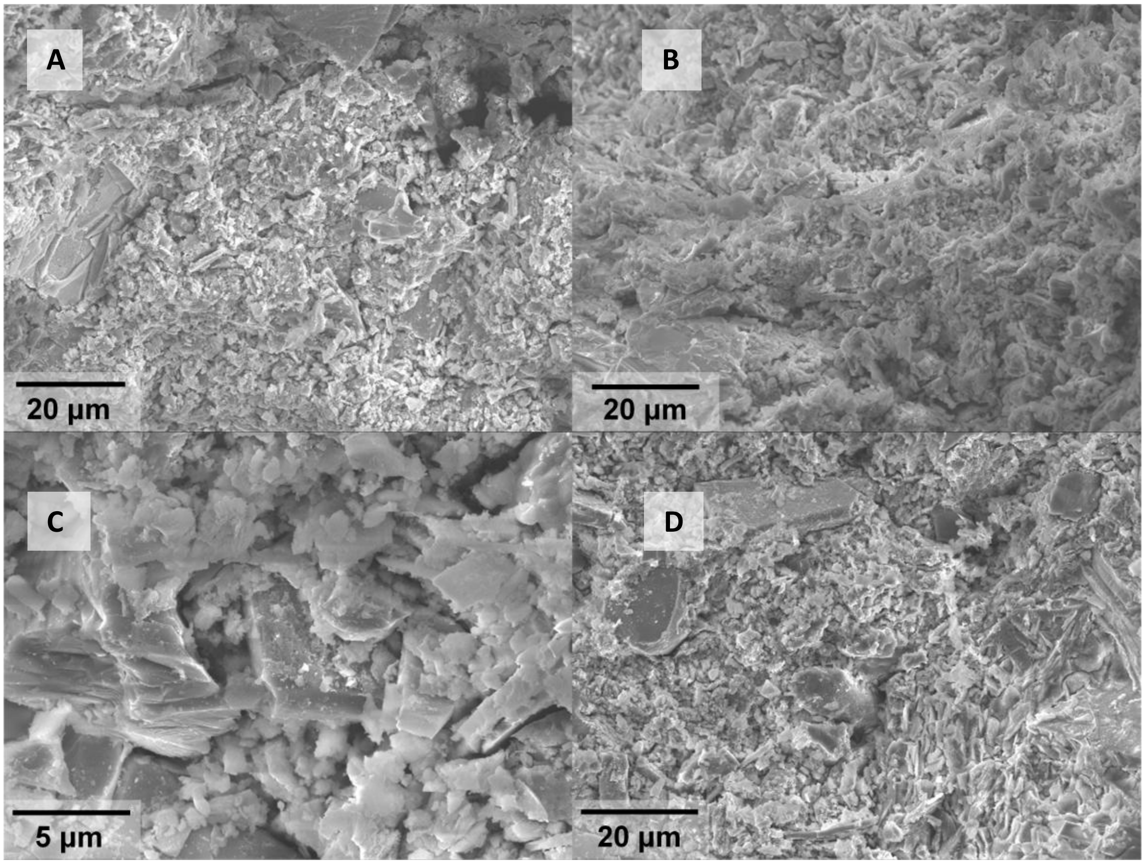

Figure L-3 SEM of 20wt% NaPC/Mars-1a. SEM micrographs of Sample 303 post-test fracture surface. This sample was a 20wt% NaPC-Mars-1a hybrid quasi-statically compressed to 270MPa inside a rigid lateral boundary.

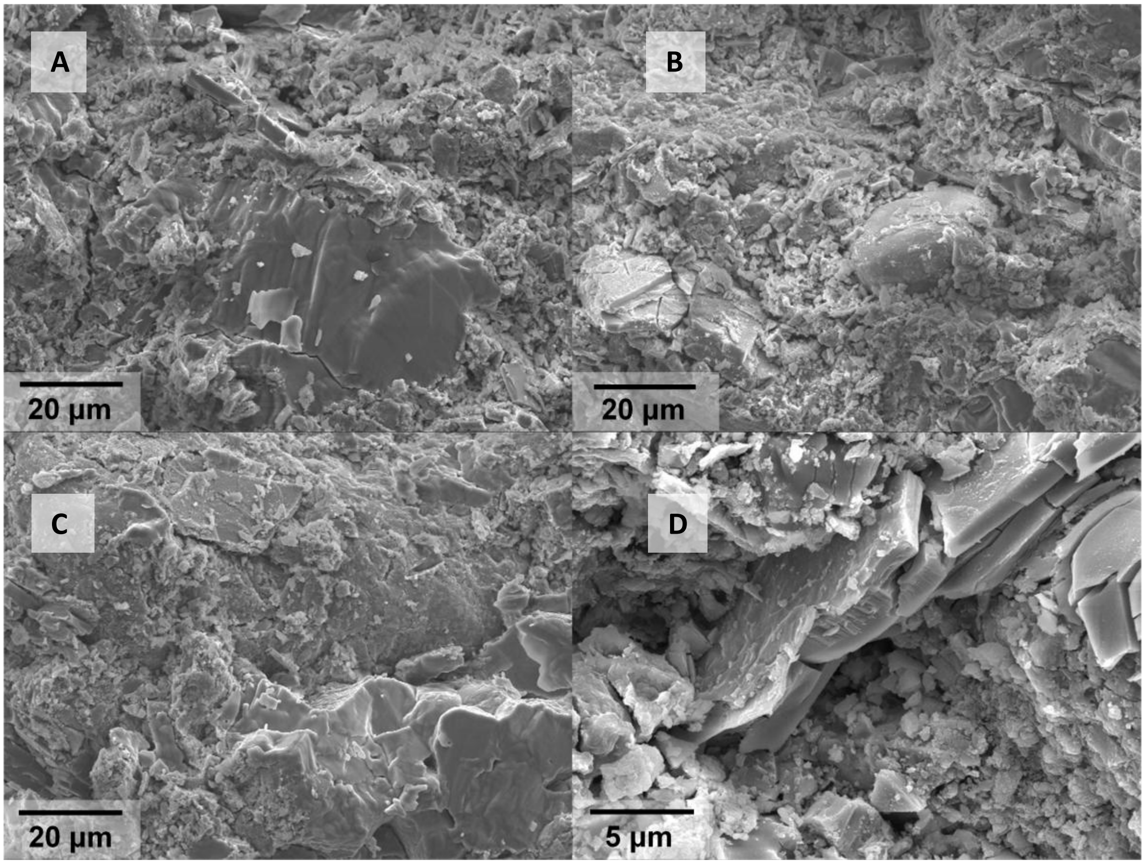

Figure L-4 SEM of 40wt% NaPC/Mars-1a. SEM micrographs of Sample 305 post-test fracture surface. This sample was a 40wt% NaPC-Mars-1a hybrid quasi-statically compressed to 270MPa inside a rigid lateral boundary.